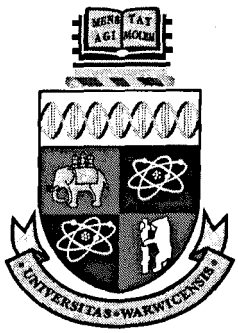

An Investigation into Methods to aid the Simulation of Turbulent Separation Control

by

Adam Preece

A thesis submitted in partial fulfilment of the requirements
for the degree of
Doctor of Philosophy in Engineering

Supervisors: Prof. Peter W. Carpenter
and Dr. Yongmann M. Chung

University of Warwick, School of Engineering
Fluid Dynamics Research Centre
Submitted: 22nd May 2008, Revised & Resubmitted: 22nd August 2008

In memory of

Professor Peter W. Carpenter

(1942-2008)

Contents

List of Figures

List of Tables

Acknowledgments

Any acknowledgments must begin with special thanks for my supervisors Prof. Peter Carpenter & Dr. Yongmann Chung without whose help this work would not have even come close to completion. Sadly, Peter passed away before I managed to submit this work so for this reason, I have dedicated this thesis to his memory. Thankfully, Yongmann stepped in to supervise my work for the actual submission and, even though he was snowed under with marking, still managed to read every chapter and offer suggestions.

Thanks must also go to Prof. Paul Tucker for his help as supervisor in my first year and his continuing advice in the development of his NEAT code.

I'd also like to thank everyone in the School of Engineering who's made this possible even just in allowing me to bounce my ideas off them! Gwilym & Novak for their help in getting my head around LaTeX & JabRef, Paddy for helping with my circular cylinder validation work & writing work, Mark E for general encouragement and Mark B for allowing me to clear up my own mind by discussing my work with someone else (as well as by climbing!). Thanks to Karen for help with formatting the thesis and the early morning chats over tea. And, of course, not to forget Juice for working together on implementing both the Immersed Boundary Methods and the turbulent inflow simulations.

Finally, but most importantly, I want to thank my family & friends without whose support, I would have failed long go. Thanks must go to my parents for always believing I could do it, my fiancée Milla for providing a calm voice (and plenty of tea!) when I needed it and Wallace for providing a crazy distraction at the right times!

This research has been funded by the EPSRC and the European AEROMEMS II project.

Declaration

This thesis, and the material in it, is my own work. It has not been submitted for a degree at any other university.

As part of the work carried out, the following paper was published:

- Preece *et al.* (2004)

Abstract

The reduction of drag on commercial aircraft is an active field of study especially with environmental pressures to reduce the carbon emissions associated with climate change. To this end, the AEROMEMS-II project was commissioned by the EU with a view to investigate methods for reducing drag by using MEMS devices for controlling separation. One method for investigating flow control devices is to use the field of Computational Fluid Dynamics (CFD) to simulate the flow interactions produced in flow control applications and assess their effect.

Simulating such flows can be computationally expensive so a number of methods have been investigated here to assess their use in flow control simulation applications. The first of these is the Immersed Boundary Method (IBM) which allows complex geometries to be simulated using simple cartesian grid CFD codes. IBMs are found to reduce requirements whilst maintaining flow resolution and accuracy.

Next is the use of turbulence modelling with wall functions to reduce the need for fine grids near any solid surfaces. This method is found to work well and can allow the grid spacing near the wall to be 100 times coarser than with no wall functions applied. Finally, Detached Eddy Simulation (DES) has been considered as a method for allowing unsteady flow control structures to be simulated without being damped by conventional turbulence modelling. Each of these methods is presented, implemented and validated against known flow cases to assess their abilities fully.

All three methods have then been applied together to a known experimental turbulent flow-control set-up at the University of Lille (fellow partners in the AEROMEMS-II project) in order to assess the feasibility of using all of these methods together to simulate flow control. All three of these methods are seen to work well together although not always with the same effect.

Abbreviations

- CD: Central Differencing *A method for approximating flow gradients using nodes either side of a desired node*
- CFD: Computational Fluid Dynamics *The use of numerical simulations solved using computer hardware to simulate fluid flows*
- DES: Detached Eddy Simulation *The use of turbulence modelling near walls and LES away*
- DNS: Direct Numerical Simulation *The use of sufficiently fine grids to resolve all significant length scales within a turbulent flow*
- EASM: Explicit Algebraic Stress Model *A turbulence model which approximates the turbulent Reynolds stresses directly. Detailed in Gatski and Speziale (1993)*
- HWA: Hot-Wire Anemometry *The use of the cooling characteristics of a small length of electrically conducting wire to estimate the velocity over the wire*
- IBM: Immersed Boundary Method *The use of body forces to produce surface geometries not coincident with the computational mesh*
- ILES: Implicit Large Eddy Simulation *An LES simulation without an SGS model the sub-grid scale eddies being modelled by the natural numerical dissipation within the code.*
- LDA: Laser Doppler Anemometry *An experimental method involving the use of laser doppler methods to measure the velocity of particles added to the flow*
- LES: Large Eddy Simulation *The use of a fine grid to model the largest turbulent eddies and a turbulence model to resolve the sub-grid scale turbulence*

- PIV: Particle Image Velocimetry *An experimental method involving taking rapid snapshots of flow-borne particles in order to estimate the velocity of the flow around those particles*
- RANS: Reynolds-Averaged Navier-Stokes (equation) *Usually referring to the use of Reynolds-Averaging to simplify the Navier-Stokes equations in order to use turbulence modelling*
- S-A Model: Spalart-Allmaras model *A one equation RANS turbulent model solving for a modified eddy-viscosity as detailed in Spalart and Allmaras (1994)*
- SGS: Sub-Grid Scale *Usually pertaining to a model used in LES to approximate the turbulent dynamics below the grid scale*
- SJ: Synthetic Jet *A jet flow produced by entrainment caused by an zero-net mass-flow oscillatory jet output*
- URANS: Unsteady Reynolds-Averaged Navier-Stokes (equation) *As for RANS but including the unsteady derivative*

Nomenclature

General Variables

x	Coordinate in the streamwise direction
y	Coordinate in the wall-normal direction
z	Coordinate in the cross-stream direction (normal to both x & y)
$u(x,y,z,t)$	Unsteady velocity in the x direction
$v(x,y,z,t)$	Unsteady velocity in the y direction
$w(x,y,z,t)$	Unsteady velocity in the z direction
$U(x,y,z)$	Time-averaged velocity in the x direction
$V(x,y,z)$	Time-averaged velocity in the y direction
$W(x,y,z)$	Time-averaged velocity in the z direction
$u'(x,y,z,t)$	Fluctuating velocity in the x direction
$v'(x,y,z,t)$	Fluctuating velocity in the y direction
$w'(x,y,z,t)$	Fluctuating velocity in the z direction
t	Time
T	Time averaging period

Physical Fluid Variables

μ	Molecular viscosity
ν	Kinematic viscosity
ρ	Air density

Boundary Layer Properties

U_∞	Freestream velocity
U_e	Boundary layer edge velocity

δ	Displacement thickness
Θ	Momentum thickness
δ^{**}	Kinetic energy thickness
H	Shape factor, δ^*/Θ
H_1	Shape factor, Θ/δ^{**}
H^*	Modified Shape factor as given in Eqn. 2.22
y^+	Non-dimensional y-coordinate (in wall units)
u^+	Non-dimensional velocity (in wall units)
u_τ	Friction velocity
τ_w	Wall shear stress
Θ	Momentum thickness
Θ	Momentum thickness

Turbulence Variables

$\overline{u'^2}$	Streamwise normal Reynolds stress
$\overline{v'^2}$	Wall-normal Reynolds stress
$\overline{w'^2}$	Cross-stream normal Reynolds stress
$\overline{u'v'}$	Reynolds shear stress

Flow Control Variables

α	Skew angle of jet in Godard and Stanislas (2006a)
β	Pitch angle of jet in Godard and Stanislas (2006a)
Φ	Jet diameter in Godard and Stanislas (2006a)
L	Distance between two jets of a system in Godard and Stanislas (2006a)
λ	Distance between adjacent systems in Godard and Stanislas (2006a)

VR Velocity ratio in Godard and Stanislas (2006a)

Numerical Variables

δx Size of grid cell in x-direction

δy Size of grid cell in y-direction

δz Size of grid cell in z-direction

a_P Numerical coefficient for cell, P

a_E Numerical coefficient for cell to the east of cell P (I.e. $i+1$)

a_W Numerical coefficient for cell to the west of cell P (I.e. $i-1$)

a_N Numerical coefficient for cell to the north of cell P (I.e. $j+1$)

a_S Numerical coefficient for cell to the south of cell P (I.e. $j-1$)

a_F Numerical coefficient for cell to the front of cell P (I.e. $k+1$)

a_B Numerical coefficient for cell to the back of cell P (I.e. $k-1$)

S_ϕ Source term for variable ϕ at cell P

Chapter 1

Introduction

1.1 The Political Climate

The impact of air travel on our environment is of the utmost importance in today's political climate. From demonstrations about a third runway at Heathrow to the still much debated impact of carbon emissions on the global climate, the use of commercial aircraft seems to attract controversy at every turn.

Added to this is the fact that the number of air passengers in the UK alone has exploded from 4 million in 1954 to 228 million in 2005. With no sign that these numbers will not continue to increase at a similar rate, the commercial aircraft manufacturers are under increasing pressure to make their aircraft more efficient, produce less emissions and all with less noise. One major area for increasing aircraft efficiency is to reduce the overall drag hence drag reduction is an active area of research.

In order to approach this problem of drag reduction, a number of research programs

have been funded with the intention of investigating novel methods of drag reduction. In particular, the AEROMEMS and AEROMEMS-II projects funded by the European union have been involved with the use of small jets to control turbulent separation and reduce drag as reported in Warsop (2005). The current work has been produced in conjunction with the AEROMEMS-II project.

1.2 The Need for Computational Tools

As computational resources have become more powerful and prolific, the use of computational tools has become an essential part of the research and development process. To this end, the development of computational methods to aid the simulation of flow structures has become a vital field of study.

Whilst computing power has increased greatly, the ability to model a fully turbulent flow over an aircraft's wing at high Reynolds numbers is still unfeasible within a reasonable time-frame as covered in Spalart (2000). For this reason, any computational method which improves accuracy or reduces computational effort is worth investigating.

With these factors in mind, the purpose of this thesis has been to examine a number of recent methods within the field of Computational Fluid Dynamics (CFD) and consider their possible application within the context of turbulent separation control.

1.3 The Scope & Content of this Work

The work contained herein is arranged in the following way. Firstly, a review of the literature relevant to turbulent separation control is covered in Chapter 2. This includes

both experimental and computational studies of steady and unsteady jets being used to control turbulent separation and provides context for the following work.

Chapter 3 considers the computational methods and CFD code used in this work as these are key to the subsequent validations. In order to test the accuracy of the code, a number of base-line simulations were performed to test its performance.

The main body of work is contained in Chapters 4, 5 and 6 in which the computational methods are investigated. Each of these chapters presents the need for the method and also contains a brief history. The methods are then validated against some well-established cases.

These begin with Chapter 4 in which the Immersed Boundary Method (IBM) is presented and validated using the case of circular cylinder flow. Novel work in this area has been done in applying the IBM to a SIMPLE pressure-correction code and in doing so, a new implementation involving coefficients has been formulated.

Chapter 5 presents the turbulence modelling used and investigates the use of wall functions to improve the accuracy of such models on a coarse grid. A novel implementation of the wall functions method is also presented allowing the method to work alongside the IBM. Testing of the wall functions method has been done using the case of a flat plate turbulent boundary layer.

Finally, Chapter 6 considers Detached Eddy Simulations and provides a qualitative investigation into their use for a backward-facing step flow.

In addition to this work, Chapter 7 provides a study of employing all of the methods covered in a typical flow control situation. This chapter is simply to provide a feasibility study of combining the previously studied methods into one simulation. To the author's knowledge, such a study has not yet been completed and provides an initial look at how

such methods could work together.

Finally, Chapter 8 brings together any conclusions that can be drawn from the previous chapters and presents some ideas for further work.

Chapter 2

Literature Review of Turbulent Separation Control

The content of this chapter presents some background theory in addition to a review of the relevant literature into the area of turbulent boundary-layer flow control in order to provide a setting for the work that follows. The chapter begins by examining turbulent boundary layer properties and the work that has been done to characterize them. Next, separated flows are considered with research into the boundary-layer characteristics under separation being presented. Finally, a review into the works on separation control using steady and unsteady jets is covered with emphasis being placed on the work done at the Laboratoire de Mécanique de Lille as part of the AEROMEMS-II project.

Literature relevant to specific methods covered later will be presented at the beginning of the relevant chapters. For example, research into immersed boundary methods is not presented here but at the beginning of Chapter 4.

2.1 Turbulent boundary-layers with zero pressure gradients

2.1.1 Turbulence

The boundary-layer manifests itself physically as a thin region of fluid in contact with any solid surface exposed to a flow. For typical aeronautical applications, this thickness is observed to be typically of the order of $0.001 - 0.01L$ where L is some characteristic length scale in the main flow direction e.g. the chord of a wing section. This is covered in some depth in Houghton and Carpenter (2003).

A major characteristic of turbulent boundary-layers is that they are inherently unsteady even when based on flows that are steady by nature. The velocity within a turbulent boundary-layer can be decomposed into a mean and fluctuating component such that:

$$u(t) = U + u'(t) \tag{2.1}$$

where $u(t)$ is the instantaneous velocity, U is the mean velocity and $u'(t)$ is the fluctuating velocity. The mean velocity, U is defined as:

$$U = \lim_{T\to\infty} \frac{1}{T} \int_0^T u(t)dt \tag{2.2}$$

where U denotes a time average of $u(t)$ and T is the period over which the averaging takes place. Therefore, the fluctuating velocity can be found as:

$$u'(t) = u(t) - U \tag{2.3}$$

2.1.2 The Velocity Profile

This velocity profile is shown graphically in Figure 2.1. Part (a) of the figure shows the instantaneous unsteady velocity profile across a turbulent boundary-layer, part (b) shows the mean velocity profile and part (c) shows the fluctuating velocity profile. Although there are analytical solutions for the Navier-Stokes equations for some laminar boundary-layers, no such solutions exist for turbulent flow because of their complex, non-linear behaviour. However, the observations of Prandtl (1904) lead to the approximation of the mean velocity profile by an inverse power law. Hence, for a turbulent boundary-layer, the mean velocity, U, at some height, y, above the wall is given approximately by:

$$\frac{U}{U_\infty} = \left(\frac{y}{\delta}\right)^{\frac{1}{n}} \tag{2.4}$$

where n is the power of the profile.

As one examines the flow closer to the wall it is clear that the turbulent fluctuations will eventually be damped out by the proximity of the solid wall. This leads to the assessment that the layer of the fluid directly in contact with the surface is dominated by viscous effects. For Newtonian fluids, this results in the velocity varying linearly close to the wall. As the fluid in contact with the wall remains fixed to the surface by viscosity, it is assumed that the velocity there is the same as the wall velocity (the 'no-slip condition').

This gives the following relation for the velocity in the immediate vicinity of the wall as:

$$u^+ = y^+ \tag{2.5}$$

where u^+ and y^+ are the velocity and wall distance respectively in wall units and defined as:

$$u^+ = \frac{u}{u_\tau} \tag{2.6}$$

$$y^+ = \frac{\rho u_\tau y}{\mu} \tag{2.7}$$

where ρ is the fluid density and u_τ is known as the friction velocity defined as:

$$u_\tau = \sqrt{\frac{\tau_w}{\rho}} \tag{2.8}$$

τ_w is the wall shear stress and is defined as:

$$\tau_w = \mu \left(\frac{dU}{dy} \right)_{wall} \tag{2.9}$$

The near-wall layer in which the velocity distribution is linear is known as the viscous sub-layer but only exists up to a distance of roughly $y^+ = 5$ from the wall. Near the wall but well above the viscous sub-layer, the boundary-layer is unrestricted by the surface and so the turbulent stresses dominate over the viscous stresses. In this region, the velocity profile is found experimentally to follow a logarithmic relation such as:

$$u^+ = A \ln y^+ + B \tag{2.10}$$

A number of values for the constants A and B have been found but it is generally accepted that they take the approximate values of 2.54 and 5.56 respectively as covered in Houghton and Carpenter (2003). This region of fully-developed turbulent flow is known as the log-law region.

In between the viscous sub-layer and the log-law region there exists a layer in which both viscous and inertia effects have a similar magnitude. This region is known as the buffer layer and is presented as a blended region between the viscous sub-layer and log-law region profiles. These relationships are known collectively as the law of the wall and are given in Figure 2.2 below. The initial formulation of the Law of the Wall was derived from experiments on pipe flow with the above formulation being proposed by Ludwieg and Tillmann (1949). See Coles (1956) for more detail.

2.1.3 Boundary-layer Development along a flat-plate

It has been mentioned that the velocity profile itself remains largely unchanged in the streamwise direction although it will experience a growth in the wall normal direction as the retarding effect of the wall causes the boundary-layer thickness to grow. There is a problem, however, with the calculation of the boundary-layer thickness. There is no clearly defined edge to the layer as the velocity profile tends slowly towards the freestream velocity only fully reaching the freestream value at infinity. Therefore it is often more practical to assess other properties from the velocity profile which relate directly to the fluxes of certain properties through the boundary-layer profile.

The first such parameter is the displacement thickness which is a measure of the mass flux through the boundary-layer profile. If the profile is integrated in the wall-normal direction, the defect (i.e. the amount of mass flux that is lost due to the effects

of flow retardation as it approaches the wall) can be calculated. The displacement thickness can then be thought of as the height through which the surface would need to be moved in order to preserve the mass flux through the profile at that plane assuming that the boundary-layer profile is replaced with the edge velocity all of the way to the wall. This also means that the displacement thickness is a measure of the mass-flux lost as a result of the boundary layer being retarded by the wall.

The displacement thickness is usually denoted by δ^* and defined by:

$$\delta^* = \int_0^\infty \left(1 - \frac{u}{U_e}\right) dy \tag{2.11}$$

where U_e is the velocity at the edge of the boundary layer.

If one considers a similar property but concerned with the momentum flux through the area (and hence measures the momentum lost in the boundary layer), another property known as the momentum thickness (denoted by θ) can be derived as:

$$\theta = \int_0^\infty \frac{u}{U_e}\left(1 - \frac{u}{U_e}\right) dy \tag{2.12}$$

Likewise, a thickness quantifying the kinetic energy flux is denoted by δ^{**} and defined as:

$$\delta^{**} = \int_0^\infty \frac{u}{U_e}\left(1 - \left(\frac{u}{U_e}\right)^2\right) dy \tag{2.13}$$

A key development in the analysis of how the boundary-layer grows was performed by von Kármán in the early twentieth century. This is covered in more depth in Houghton and Carpenter (2003). The approach was to consider a thin slice of boundary-layer and examine the momentum fluxes around this slice. By integrating

these momentum fluxes around the slice, an equation representing the development of the boundary-layer along the plate is presented. This is given as:

$$\frac{\tau_w}{\rho} = \frac{d}{dx}(U_e^2\theta) + \delta^* U_e \frac{dU_e}{dx} - \rho U_e V_s \tag{2.14}$$

where V_s is any suction applied at the surface. This equation is known as the Kármán momentum integral equation.

In the case of no surface suction, the suction velocity V_s will be zero. Also, if assuming the case of zero pressure gradient, the edge velocity U_e will remain constant along the plate (and be equal to the freestream velocity U_∞). This simplifies the momentum integral equation to:

$$\frac{\tau_w}{\rho} = U_\infty^2 \frac{d\theta}{dx} \tag{2.15}$$

This simplified equation can be used along with empirical relations for drag coefficient in order to produce a semi-empirical relationship for the development of the boundary-layer along the plate without any pressure gradient.

Manipulating Equation (2.15) and assuming the boundary layer follows the seventh power-law profile in Equation (2.4) with $n = 1/7$ gives a relation for the above thicknesses in terms of the boundary-layer thickness as given below:

$$\delta^* = 0.125\delta \tag{2.16a}$$

$$\theta = 0.0973\delta \tag{2.16b}$$

$$\delta^{**} = 0.175\delta \tag{2.16c}$$

Further information regarding this derivation can be found in Houghton and Carpenter (2003). Although providing information about the properties of a boundary-layer velocity profile in their own right, the integral thicknesses can also be combined to provide further quantification of the boundary-layer. For example, one aspect that the displacement thickness does not reveal is whether the boundary-layer is 'biased' more towards the wall (as in a turbulent profile) or further away from the wall (as in a laminar profile) By calculating a ratio between two integral thicknesses, a shape factor, H is defined as:

$$H = \frac{\delta^*}{\theta} \tag{2.17}$$

This shape factor is constant providing the velocity profile is not being acted upon by a pressure gradient or surface suction. For laminar boundary-layers, the shape factor is given in pages 412-414 of Houghton and Carpenter (2003) as approximately:

$$H \approx 2.7 \tag{2.18}$$

However, for a turbulent boundary-layer, using the power-law approximation, gives the shape factor as roughly:

$$H = \frac{0.125\delta}{0.0973\delta} \approx 1.28 \tag{2.19}$$

These shape factors measure, in quantitative terms, the 'fullness' of the boundary-layer. That is, if the displacement thickness (how much mass flux is lost through the boundary-layer) is large compared with the momentum thickness (how much momentum flux is lost through the boundary-layer) then a higher shape factor will result. However,

as the amount of momentum through the boundary-layer increases for a given displacement thickness (as is the case for a turbulent boundary-layer) then the shape factor reduces. This makes the shape factor useful in assessing the state of the boundary-layer. For example, the shape factor starting to increase, may be an indication that the boundary-layer may be starting to re-laminarise or may be under an adverse pressure gradient.

This chapter will now consider the conditions that give rise to turbulent boundary-layer separation and how calculating the above parameters can allow a more thorough assessment of the state of the boundary-layer.

2.2 Turbulent boundary-layers in adverse pressure gradients

Although the previous section examined the behaviour of turbulent boundary-layers without the effect of streamwise pressure gradients, this case is clearly a special one. All aerodynamic flows of engineering significance have some form of pressure distribution around them, so leading to pressure gradients acting on the boundary-layers in the immediate vicinity of such objects.

A classic example of this is an aerofoil. The air approaches the aerofoil and slows down as it approaches the stagnation point on the leading edge. The air then splits around the aerofoil section and is forced to speed up in order to preserve continuity. This in turn causes the pressure to decrease along the surface in response. Past the thickest point of the aerofoil, the flow decelerates towards the freestream velocity as it approaches the trailing edge, so causing the pressure to again rise to balance this. It can be seen from this example that generally, up to the point of maximum thickness, the pressure is dropping so producing a negative pressure gradient. Likewise, towards the trailing edge, the pressure is increasing so giving rise to a positive pressure gradient.

A brief summary of the effect of these pressure gradients on the flow within the boundary-layer will now be given.

2.2.1 Theory

Imagine a small element of fluid $\delta x \delta y$ within a turbulent boundary-layer as shown in Figure 2.3. Acting upon this element are many different forces. On the top face, shear stresses act to speed up the element whilst on the bottom fact, shear stresses act to

slow down the element as it travels through the boundary-layer. This gives rise to the boundary-layer development in the stream-wise direction as detailed above.

For turbulent boundary-layers these shear stresses are more complex than for laminar boundary-layers in that the fluctuating velocities produce turbulent stresses which vary with time. By following the Reynolds averaging process (see Chapter 5), these turbulent stresses, unchanging with respect to time, are many times larger in magnitude than the laminar shear stresses. This is the effect that causes a turbulent boundary-layer to grow more quickly than its laminar counterpart as shown in Houghton and Carpenter (2003).

However, the force which has the most effect when considering boundary-layer separation is the pressure gradient across the element. If the pressure on the left-hand face is given by p then the total pressure force on the element will be given by the following relation:

$$F_p = p\,\delta y - \left(p + \delta x \frac{\partial p}{\partial x}\right)\delta y \tag{2.20}$$

which simplifies to:

$$F_p = -\frac{\partial p}{\partial x}\delta x \delta y \tag{2.21}$$

where F_p is the pressure force positive in the x direction. It is clear, therefore, that the pressure force on an element in a boundary layer is acted upon by a force directly proportional with the pressure gradient at that point.

This pressure force has the effect of the retarding the element as it travels downstream if the gradient is positive or accelerating the element if the gradient is negative.

To avoid confusion, a negative pressure gradient is known as a favourable pressure gradient to denote the effect it has on the boundary-layer. Conversely, a positive pressure gradient is known as an adverse pressure gradient as it acts against the boundary-layer. (However, one could argue that if one was trying to achieve separation, a positive pressure gradient should be known as favourable!)

The phenomenon of separation is known to occur when the pressure gradient is excessively adverse over a sufficient distance. This can be explained by considering the fluid 'layers' across a boundary-layer profile as it travels downstream. At the start of the adverse-pressure-gradient region, the profile would probably look very similar to the velocity profiles detailed in the previous section. As the profile convects downstream, all of the layers across the profile are retarded by the pressure gradient.

Unfortunately, the layers closest to the wall will have less momentum to begin with than the layers towards the edge of the boundary-layer as they are closest to the retarding effect of the wall. This means that at some point downstream, the velocity gradient at the wall (and hence the wall shear stress) will become zero. This point on the surface is known as the separation point and downstream of this point, the flow near the wall will begin to flow back upstream. If a streamline is drawn from the separation point and following the point on the profile at which the boundary-layer above has an equal mass flow to the boundary-layer before separation, then the fluid flow near the wall becomes separated into two regions. The region closest to the wall is now a recirculating region of fluid known as the separation region. Above this and below the freestream flow, the boundary layer still exists but is said to be separated from the wall.

Unfortunately, there exist no analytical solutions to the flow within a turbulent boundary-layer acting under a non-zero pressure gradient. This has led to active research both experimentally and (more recently) computationally to try and ascertain

what criterion can be used to quantify separated flows, what effects separation has on a turbulent boundary-layer and how it can be better predicted. It is the use of computational methods in order to predict separation and simulate separation-control methods that is the main aim of this present work.

In order to better understand the physical behaviour of separation on turbulent boundary-layers, a summary of the experimental studies into this area will now be covered.

2.2.2 Experimental Studies

Although the previous section details in qualitative terms the effects of the pressure gradient on a typical boundary-layer, a review of the experimental studies done in this area is necessary to begin quantifying the problem.

In any flow experiencing a pressure gradient, there are a number of regions within the flow domain. To begin with, there is always a 'development region'. This is where the boundary-layer develops along a solid surface. With no pressure gradient present, the boundary-layer will develop as considered in the previous section. However, if a non-zero pressure gradient exists the boundary-layer will be different to the general case.

For a negative or 'favourable' pressure gradient, the velocity at the edge of the boundary, U_e will be increasing due to pressure-velocity coupling. As the pressure accelerates the boundary-layer, the profile becomes fuller with more momentum being added to the near-wall flow. This causes the thickness of the layer to reduce in order to conserve mass-flux and as a result also increases the wall shear stress as the velocity gradient at the wall increases. Because the wall shear stress is increasing, a boundary-

layer is actually less likely to separate under a favourable pressure gradient than under no pressure gradient at all. For this reason, the case of a favourable pressure gradient will not be examined.

The adverse pressure gradient, on the other hand, causes more complex effects. Until the point of separation, the velocity profile becomes retarded by the pressure gradient thus becoming less full with the near-wall velocity being retarded mostly due to it being further from the mainstream flow. This can be seen in many experimental works especially Spalart and Watmuff (1993), Dengel and Fernholz (1990) and Alving and Fernholz (1996).

Although the overall boundary-layer profile changes shape dramatically when plotted using conventional coordinates, the near-wall velocity profiles are observed to maintain the law-of-the-wall behaviour detailed previously. As the wall shear stress is decreasing more rapidly due to the pressure gradient, until the point of separation, (where $\tau_w = 0$ and hence $y^+ = 0$ & $u^+ = \infty$) the dimensionless near-wall behaviour is maintained as shown in Samuel and Joubert (1974). However, because they do not cover the viscous sub-layer region due to measurement resolution it can be safely assumed that if the profile immediately above the buffer layer follows a good logarithmic behaviour then the viscous sub-layer is likely to be accurately followed.

In terms of the development in the streamwise direction, the overall retardation of the velocity profile causes the boundary-layer thickness to increase in order to conserve mass and so the other boundary-layer thicknesses (displacement thickness etc.) increase accordingly. Recalling that the shape factor, H, provides a measure of the fullness of the profile by comparing the displacement thickness with the momentum thickness, it is clear that the retarded profile will result in an increasing shape factor as observed in Samuel and Joubert (1974). This implies that an adverse pressure gradient will cause

an increase the displacement thickness at a faster rate than the increase in momentum thickness. The work by Dengel and Fernholz (1990) observed this behaviour in their work.

The retardation of the boundary-layer also has the effect of causing the wall shear stress to drop at a quicker rate as the velocity gradient at the wall decreases. As mentioned previously, once the wall shear stress has fallen to zero, the boundary-layer separates as the negative wall shear stress downstream of this point denotes a region of recirculating flow forcing the boundary-layer to leave the surface. This increased drop in wall shear stress can be illustrated by the work of Samuel and Joubert (1974). Their results show various boundary-layer properties from the positions $x = 1.04m$ to $x = 3.39m$. This streamwise distance equates to the Reynolds number based on x increasing by a factor of 3.26. Over this distance, the drag coefficient is observed to decrease from 2.75×10^{-3} to 0.68×10^{-3} thus decreasing by a factor of roughly 4.

As the drag coefficient of a boundary-layer without a pressure gradient varies by the inverse of the fifth root of the Reynolds number, this gives the drag coefficient as decreasing by a factor of 1.27. This can be seen in Houghton and Carpenter (2003). This is around a third of the rate at which the adverse pressure gradient results decrease. Therefore, just for the example of the work by Samuel and Joubert (1974) it is not uncommon to see the drag coefficient decrease 5-10 times quicker in a moderate adverse pressure gradient.

Once the wall shear stress reaches zero, the boundary-layer behaviour becomes much more complex. The boundary-layer separates from the surface at the point of zero shear stress and is moved away from the surface by the recirculating fluid in contact with the wall. This is observed in many works including Ruderich and Fernholz (1986), Alving and Fernholz (1996) and Song *et al.* (2006). However, perhaps one of the best works

for considering the flow behaviour at the exact point of separation is that by Dengel and Fernholz (1990). Here an adverse pressure gradient is applied to the boundary-layer and carefully varied to cause the approach and onset of separation. The skin friction was measured by Preston tubes in the upstream portion of the flow whilst pulsed-wire probes were used where separation was observed.

An important point to note is that like most other properties of the turbulent boundary-layer, the separation point is unsteady with respect to time. In quantifying separation, an upstream-flow parameter is often employed providing a estimate of the fraction of time in which the flow is spent travelling back upstream. If this parameter equals 1.0, the flow is always travelling back upstream, if it is 0.0, the flow is always downstream and if it is 0.5, the flow spends an equal amount of time flowing upstream and downstream.

This upstream-flow parameter is also found to vary strongly with distance from the wall. Dengel and Fernholz (1990) show that the intermittency increases exponentially as one approaches the wall. This has the problem that it makes an estimate of an exact value for intermittency at the wall difficult to estimate by extrapolation. However, it was observed by Simpson *et al.* (1981) that the point of maximum intermittency does not lie at the wall but simply very close to it. They observed that the maximum point was at roughly $y/\delta = 0.01$ whilst Dengel and Fernholz (1990) did not have any readings below around 4mm which for a boundary-layer thickness of roughly 80mm only equates to $y/\delta \approx 0.05$.

Up until now, only the mean velocity profile has been examined and so it is intuitive that the pressure gradient and subsequent separation have an effect on the velocity fluctuations. A number of works have employed experimental methods to investigate these velocities and their resulting Reynolds stresses. These works include Dengel and

Fernholz (1990), Alving and Fernholz (1996) and Song *et al.* (2006) and consider the separation of flow through a two-dimensional geometry. The three Reynolds stresses present in a two-dimensional geometry consist of the streamwise normal Reynolds stress, $\overline{u'^2}$, the wall normal Reynolds stress, $\overline{v'^2}$ and the Reynolds shear stress, $\overline{u'v'}$

It is observed in Song *et al.* (2006) that as soon as the flow begins to separate, the peak in the streamwise normal Reynolds stress, $\overline{u'^2}$ moves from being very close to the wall and starts to move away from the wall. The magnitude of this peak also begins to grow. Moving downstream, the peak grows in magnitude and moves further away from the wall. Eventually, the peak begins to diffuse into the overall boundary-layer distribution for $\overline{u'^2}$ as the layer begins to reattach itself. Similar behaviour is also observed for the other Reynolds stresses $\overline{v'^2}$ and $\overline{u'v'}$.

Of particular interest to the current work is the research done at the University of Lille into the effects of an adverse pressure gradient on a turbulent boundary layer and this will now be covered.

2.2.3 The Lille Bump

As part of the AEROMEMS-II project given in Warsop (2005), the University of Lille conducted experiments examining methods for the supression of separation. In their work, a long wind-tunnel is used such that the boundary-layer is allowed to develop over 15 metres before approaching the test section. The boundary-layer then experiences a favourable pressure gradient followed by an adverse pressure gradient as a result of a 'bump' placed in the lower part of the working section. This bump has been designed such that it models a boundary-layer approaching separation over the rear of an aerofoil surface without actually separating. Figures 2.4 and 2.5 show this set-up whilst Table

2.1 gives coordinates for the bump geometry.

Over recent years, a number of studies have been published by the team at Lille as work has progressed. The first work relevant to the current study can be found in Bernard *et al.* (2003). Here the velocity details of the flow are given by using hot-wire anemometry and the pressure at the surface of the bump is given by micromanometer transducers.

The bump starts at 15.5m from the beginning of the wind-tunnel base plate and ends at 19m. The wind tunnel cross section is $1 \times 2m^2$. The maximum velocity through the tunnel is $10ms^{-1}$ so allowing Reynolds numbers (based on momentum thickness) of 2×10^4 to be reached. There is little pressure gradient in the 15m run-up section of the tunnel with a value of -0.53Pa/m at $10ms^{-1}$ being recorded.

The shape of the bump was computed by Dassault Aviation using $k-\varepsilon$ modelling in order to bring the flow behind the bump to the point of separation without actually separating. This was done to avoid any three-dimensional perturbations associated with separated flow and so allow the effects of various flow control devices to be more accurately analysed. As mentioned previously, the coordinates of the bump are given in Table 2.1.

The flow over the bump was run with the pressure and velocity profiles being recorded for later analysis. From these data a number of parameters were calculated. Firstly the external velocity at the edge of the boundary-layer increases to a maximum over the bump before reducing to the freestream value given at the inlet. This is to be expected as the flow speeds up to conserve mass over the bump.

With regard to integral lengths, displacement, momentum and kinetic energy thicknesses were all calculated and showed a steady increase over the rear of the bump. Using these parameters to calculate shape factors gave a more accurate estimate for how close

the boundary-layer was to separation. The modified shape factor was used as given in Schlichting (1979) as:

$$H^* = 0.5442 H_1 \sqrt{\frac{H_1}{H_1 - 0.5049}} \tag{2.22}$$

where H_1 is the shape factor θ/δ^{**}.

Over the rear of the bump, a minimum shape factor, H^* of 0.85 was found. As it is proposed that a modified shape factor of less than 0.761 indicates the boundary-layer is prone to separation, it is clear that the bump boundary-layer is close to separation.

The pressure distribution over the bump was found to follow the relationship shown in Figure 2.6. There is good agreement between the measured results from the pressure transducers and the computed results carried out by Dassault Aviation. It is clear that the pressure drops to a minimum over the apex of the hump where the velocity has increased to a maximum. As the flow reduces speed over the rear of the bump, the pressure rises again so placing the boundary-layer in this rear region under an adverse pressure gradient. This research is covered in greater depth later in Chapter 7 when it is compared with the simulations of the current work.

2.2.4 Computational Studies

The explosion of computational power in recent decades has lead to a huge increase in computational studies of turbulent boundary-layers in adverse pressure gradients and subsequent separation. One of the earliest of these studies was that of Spalart and Watmuff (1993) in which a low-Reynolds number turbulent boundary-layer in an adverse pressure gradient was investigated both experimentally and computationally. Direct Numerical Simulation was used as this uses no turbulence approximations and

relies on fine grid resolution to model any turbulent structures. This resulted in the Reynolds number based on momentum thickness being around 600.

The recent NASA-CFDVAL2004 validation conference on synthetic jets and turbulent separation control held at the Langley Research Centre provided an excellent opportunity to compare various computational methods and approximations on identical cases. This conference is of special significance to the present work as the author completed some synthetic jet simulations that were included in the proceedings.

The conference consisted of three cases with one of these involving the modelling of flow over a hump with a synthetic jet being applied for the purpose of flow control. Most of the works from this case were published recently in the AIAA Journal and are detailed in Rumsey *et al.* (2006). Only the uncontrolled separation cases will be considered in this section with the controlled case being considered later in Section 2.4.

The case set-up was based on the work by Seifert and Pack (2002) which employed a Glauert-Goldschmied type body, that is an aerofoil with a convex leading portion and a concave trailing portion. The model is 584mm wide, 53.7mm high and the length of the hump from the front to the back is 420mm. The Reynolds number based on chord length was $Re = 9.29 \times 10^5$ which equates to a Mach number of 0.1.

In total, there were 13 contributors who ran 56 separate cases for the conference. The simulations were run mainly using RANS/URANS although a few did use blended RANS-LES results and even DNS. Grids were supplied by the conference organisers to avoid issues of grid resolution between submissions. The supplied structured and unstructured grids all had somewhere in the region of 50,000-250,000 nodes.

Overall, the results produced gave a reasonable agreement with the pressure distribution although the error was consistent between all submissions. This suggested that there may be blockage effects that need to be accounted for in the experimental

wind-tunnel set-up. The location of the separation point was well calculated by all submissions which indicates that the turbulence models are well adjusted to calculate the point of zero wall shear stress. However, the reattachment length is less accurately predicted (roughly 10-20% too long) This could be as a result of under-prediction in the turbulent shear stress in the separated region where most submissions only predicted the magnitude as around 25% of the actual experimental measurements. This lack of turbulent shear stress would probably slow down the turbulent mixing from the outer regions of the boundary-layer down towards the wall so delaying reattachment.

Another issue that may affect the accuracy of a separation simulation is the order of the turbulence model being used. For example, the work of Morgan *et al.* (2006) focussed on using High Order RANS (HO-RANS) $k-\varepsilon$ modelling to model flow over the flow-control case geometry. On initial inspection, simulations showed that using a second-order $k-\epsilon$ model limited the overall simulation to second-order even if the base code used a sixth order method. The HO-RANS method therefore allows the base code to achieve higher accuracy compared to the second-order method.

However, it should be noted that the biggest contribution made by this work was found during grid-refinement studies. It was shown that the HO-RANS simulations provided similar results to the lower-order model using a grid four times larger. This suggests that whilst the validity of RANS modelling for the highly unsteady flows encountered in flow-separation control systems is debatable, the use of HO-RANS will inevitably provide a significant saving in computational resources as compared with the more standard second-order method.

Inlet boundary conditions can also have a significant effect on the final separation characteristics. For example, whilst it is fairly simple to add random numbers to a mean velocity profile and adjust the fluctuation amplitudes to match the RMS fluctuations

observed in turbulent boundary layers, the correlation between the various fluctuations will still be zero. This is because, if u' and v' vary independently, the correlation $\overline{u'v'}$ (and hence the turbulent shear stress) will be zero.

One work which emphasises this point is that of Persson *et al.* (2005) and Persson *et al.* (2006). It was observed for the DES simulations that the estimated level of turbulent viscosity at the inlet had a significant effect on the downstream flow. Similarly, it was also observed that varying the development length before the hump also had significant effect. To quote Persson *et al.* (2005):

> *For the DES calculations, improved agreement with the experimental data was also obtained for the long inflow section suggesting that the resolvable structures in the boundary-layer are not negligible.*

This sensitivity of the downstream simulation to the inlet eddy viscosity was also experienced in the current work and is covered later in Chapter 5.

In summary, the largest factor to consider when modelling turbulent separation seems to be the ability of the simulation to model the fluid structures (turbulent and otherwise). Therefore, grid/surface resolution and turbulent treatment are key aspects to any separation prediction. Now, the use of a number of methods for controlling separation will be considered starting with the use of steady jets.

2.3 Separation control using steady jets

One way of controlling separation is to introduce momentum into the flow so making the boundary layer less prone to separation. This can be done in a variety of ways but one efficient way to achieve this is to introduce streamwise vorticity which has the effect of bringing higher momentum flow from the edge of the boundary layer down towards the wall.

2.3.1 Previous Studies

Much of the work in the area of steady jet separation control has been done by James Johnston of Stanford University. His research has been concerned with the use of pitched & skewed jets to induce streamwise vorticity in order to control turbulent separation. Key works include Johnston and Nishi (1990), Compton and Johnston (1992), Johnston (1999) and Johnston *et al.* (2002).

The best of these works that explain the general principles of pitched & skewed jets is given in Johnston and Nishi (1990). This consists of an experimental study using a wind tunnel with a variable upper surface to allow varying pressure gradients to be applied. The boundary-layer in question develops along a flat plate and proceeds past a trip in order to ensure turbulence. An array of variable geometry jets is placed a suitable distance downstream. These consist of circular holes in the lower surface of the tunnel which allow a plug to be fitted having a hole drilled through at the desired pitch angle of the jet (in this case 45 degrees). The skew angle can then be adjusted by rotating the 'plug' in the jet hole.

A number of geometries were investigated, specifically, a co-rotating system (all jets skewed the same way) and three counter-rotating systems (investigating different

combinations of jets paired together).

The resulting vortices were shown to produce peaks in the drag coefficient (and hence wall shear stress) directly under the vortices as a result of the sideways motion being imparted on the flow underneath the vortex. Between two counter-rotating vortices there seems to be either an increase or decrease in wall shear stress depending on whether the flow is being forced down or up between the vortices. However, on average, the wall shear stress is increased by the presence of the vortices. This is confirmed by the mean velocity profile downstream of the jets as shown in Johnston and Nishi (1990). The jet results in an increase of the velocity profile at the wall but does result in a reduced velocity profile at the edge of the boundary-layer. This shows the transfer of momentum from the outer part of the layer to the near-wall region which is of interest for separation control.

Compton and Johnston (1992) continues this work and looks to visualise the results using a five-hole pressure probe. The resulting visualisations, including vector and vorticity plots, show that the proposals of Johnston and Nishi (1990) were well founded. The vortices produced by the pitched & skewed jets are shown to travel and grow downstream so bringing the outer flow nearer the wall.

The work detailed in Johnston *et al.* (2002) investigates the effects of the jet geometry by considering a number of different nozzle shapes leading up to the outlet of the jet itself. A smoothly contoured nozzle was compared with one using a sharp step and whilst little difference was observed downstream, the sharp step nozzle produced more turbulence near the orifice. This was thought to be due to shear layer instability within the nozzle before the jet orifice.

2.3.2 Lille work on steady jets

Godard and Stanislas (2006b) considers the application of fully round steady jets and their effects on the boundary layer. This work was similar in nature to the earlier works of Johnston and Nishi (1990) and Compton and Johnston (1992) although the focus is to measure the change in wall shear stress due to the induced vortices. The optimization study varied the following parameters; the skew angle of the jet, α, the pitch angle of the jet, β, the jet diameter, Φ/δ, the spanwise distance between two jets of a system, L/Φ, the spanwise distance between each system, λ/Φ and the velocity ratio, VR. A diagram of the set-up is given in Figure 2.7.

Considering first the co-rotating system, the round jets appear to work reasonably well at low velocity ratio (around 1.6). Obviously as the velocity ratio is increased, the performance of the jets increases although in the co-rotating case, the velocity also varies the migration of the vortices in the spanwise direction. The skew angle of the jets makes little difference between 45 and 90 degrees confirming the previous work of Compton and Johnston (1992), although a value of 60 degrees seemed to give the best efficiency.

As with the slotted jets, decreasing the distance between the jets improves the performance, most likely because the vortices are working better together and less in isolation. Increasing the number of jets has the effect of reducing the spanwise variation of the peak wall shear stress although this does not result in an overall increase in performance.

For the counter-rotating case, the velocity ratio is also effective from low ratios and increasing ratio results in a greater performance. The increase in performance is significant up to around 3 but then slows down up to around 6 (the maximum tested).

The skew angle has little effect on the performance, especially at the higher velocity ratios. As to be expected, as the distance between jets is increased, the interaction between the two vortices of a system reduces and so the overall performance is reduced.

Again, the starting and final optimum parameters for the co-rotating and counter-rotating cases are shown in Tables 2.2 and 2.3 respectively. Now, research covering the use of synthetic jets for flow control will be covered.

2.4 Separation control using synthetic jets

2.4.1 Previous Studies

An unsteady jet is simply defined as a jet whose velocity characteristics vary with respect to time. They can be classified in a number of ways and, indeed, this sometimes leads to confusion as to which jet is being used. For the purpose of this work, two main groups of unsteady jets are considered. The first main group considers all jets which only expel air periodically but without any suction phase at all. These will be known as 'pulsed jets'. The other group considers all jets which have a suction phase equal in magnitude to the expulsion phase so imparting no net mass-flux to the flow. These are to be known as 'synthetic jets' but are also known in the literature as 'zero-net-mass-flux jets'.

In short, these jets work by the principle of generating a vortex pair or ring from the jet orifice as the flow is expelled from the jet. As the flow starts to reverse and flow back into the jet on the suction stroke, these vortices continue to travel away from the jet if the original momentum imparted by the synthetic jet is sufficient. If the average flow field is recorded a net mass-flux away from the jet is evident as a result of the vortex streaming.

The finer principles of synthetic jets are a complete field of study within itself and so will not be covered in greater depth here. However, some research has been done in this area for the current work as part of the NASA-CFDVAL conference and this has been published in Preece *et al.* (2004) and later in Rumsey *et al.* (2006). In addition, there is the excellent review on synthetic jets given in Glezer and Amitay (2002).

With regard to using such synthetic jets for flow control, a number of works, both experimental and computational, have been completed considering the effect of synthetic

jets on flow separation. Following the development of the synthetic jet in the 1980s, it was not long before their use as a flow control device was being investigated. Early works by Seifert *et al.* (1993) and Hassan and JanakiRam (1998) performed some basic studies on the effects of using a synthetic jet on an aerofoil flow and came to the initial conclusion that the jets could produce a significant increase in lift and reduction in drag.

It was not until the late 1990s that the attention of Glezer and Amitay turned towards the use of synthetic jet for flow control after many years of studying jets in isolation. These works began with Amitay *et al.* (2001) in which case an unconventional aerofoil was used as a test case for synthetic jet control.

This aerofoil took the form of a cylinder on which a synthetic jet was mounted. An aerodynamic fairing was then used at the rear of the cylinder in order to streamline the flow and produce a roughly aerofoil shape. This had the advantage of allowing the position of the jet to be moved relative to the flow direction and the rear fairing. For this case they found that the flow would separate for angles of attack greater than five degrees in the uncontrolled case. However, in using a synthetic jet near the leading edge flow attachment would be retained for angles of attack of up to 17.5 degrees.

Following on from this study, further works have been published in Amitay *et al.* (2001), Amitay and Glezer (2002), Amitay *et al.* (2004), Glezer *et al.* (2005) and Amitay and Glezer (2006). These consider a number of aspects involved in flow control but mainly look at the frequency of the synthetic jet. In particular, Amitay *et al.* (2004) considers the effect of pulse modulation on the overall flow.

More recently, a variety of other works considering the use of synthetic jets for flow-control were produced including Melton and Yao (2006), Suzuki (2006) and Rumsey *et al.* (2006).

The experimental study of Melton and Yao (2006) considers zero-net-mass-flux

jets being applied at a number of positions on the surface of a flapped supercritical aerofoil. Amplitude modulation of the signal was also considered and found to produce similar gains for only 30% of the momentum required for the purely sinusoidal signal.

The work of Suzuki (2006) similarly considers the effects of a synthetic jet on the flow over a bump by examining the effect of jet position and frequency. This work is computational and employs a mesh fine enough to allow Direct Numerical Simulation (DNS). It was found that the position of the jet was of the utmost importance of shifting the centroid of vorticity production so reducing drag and increasing lift.

Finally, the computational studies completed at the NASA-CFDVAL conference (as mentioned previously) were presented in Rumsey *et al.* (2006). One case covered in this conference considered the flow over a hump with a synthetic jet flow being used to control this flow and was of especial significance to the current work as it considered the computational issues to be addressed in simulating separation control.

It was found in Rumsey *et al.* (2006) that whilst most simulations agreed with one another reasonably well, they did not agree as closely with the experimental results. In particular, the reattachment point was poorly predicted. In defence of the simulations however, it was proposed that the effect of end plates on the original experimental results was not as negligible as first thought. These thoughts were backed up by the fact that simulations which took end plate effects into account were closer to the final experiments. Whilst Rumsey *et al.* (2006) contains a summary of the results for the CFDVAL04 conference, other papers published by the respective authors were presented in the same volume.

2.4.2 Lille work using Unsteady Jets

Unfortunately, research into the area of synthetic jet flow control on the Lille bump apparatus has yet to be performed. However, work considering the use of pulsed jets was published by Kostas *et al.* (2007), the main difference between pulsed jets and synthetic jets being that there is no suction phase for a pulsed jet. This results in the pulsed jet introducing a net mass flux to the flow and so would require some source of higher pressure air.

In the work by Kostas *et al.* (2007), a number of pulsed jets were applied to the Lille bump geometry and their effect on the flow assessed. As with the steady jet case, both counter-rotating and co-rotating configurations were investigated. The duty cycle (i.e. what percentage of the cycle the jet is active for) and the frequency were varied and the effects on the skin friction and flow structures were examined.

In general, it was found that the net mass flow increased the mean wall shear stress and that for higher frequencies, quasi steady flow structures were found to develop far downstream of the jets. Further details regarding this work will be covered in greater depth in Chapter 7 where they are compared with the numerical simulations produced in the current work.

2.5 Conclusions

Much theoretical and experimental research has been completed over the last hundred years into the field of turbulent boundary layers, their behaviour in pressure gradients and efforts to control this behaviour. In addition, the comparatively recent development of computing technologies have now added computational tools to the research methods available to allow such flows to be investigated further.

Recent validation conferences and independent studies of turbulent separation control using computational methods provide a framework from which further research can be conducted. To this end, the purpose of the present thesis is to investigate such methods and consider their validity in simulating turbulent flow control.

The next chapter will now cover the computational code used and validate the code against a well-known case.

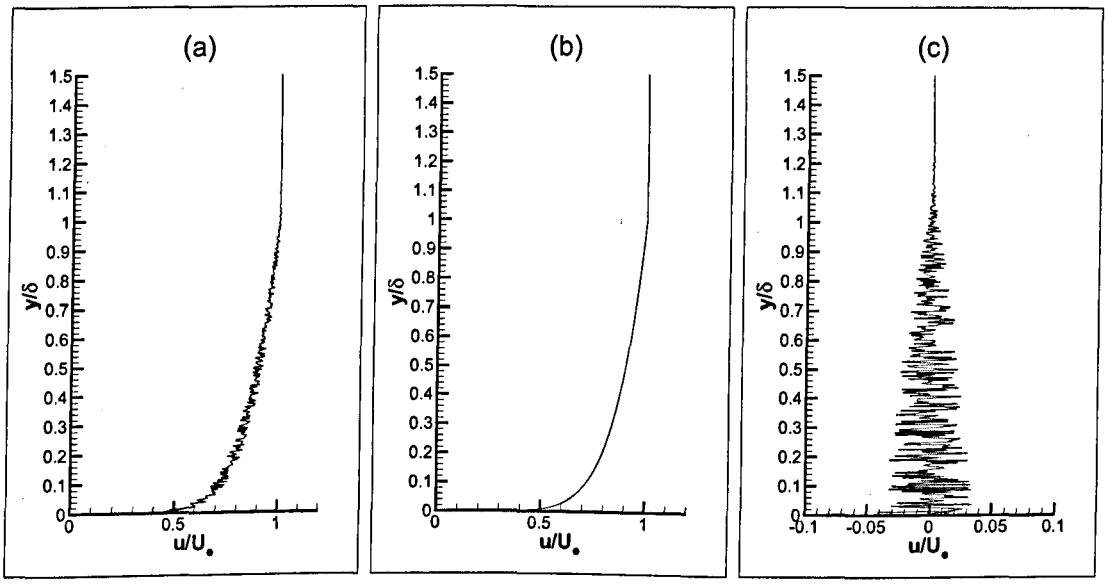

Figure 2.1: A typical turbulent velocity profile. (a) Overall profile, u, (b) Mean profile, U, (c) Fluctuating profile, u'

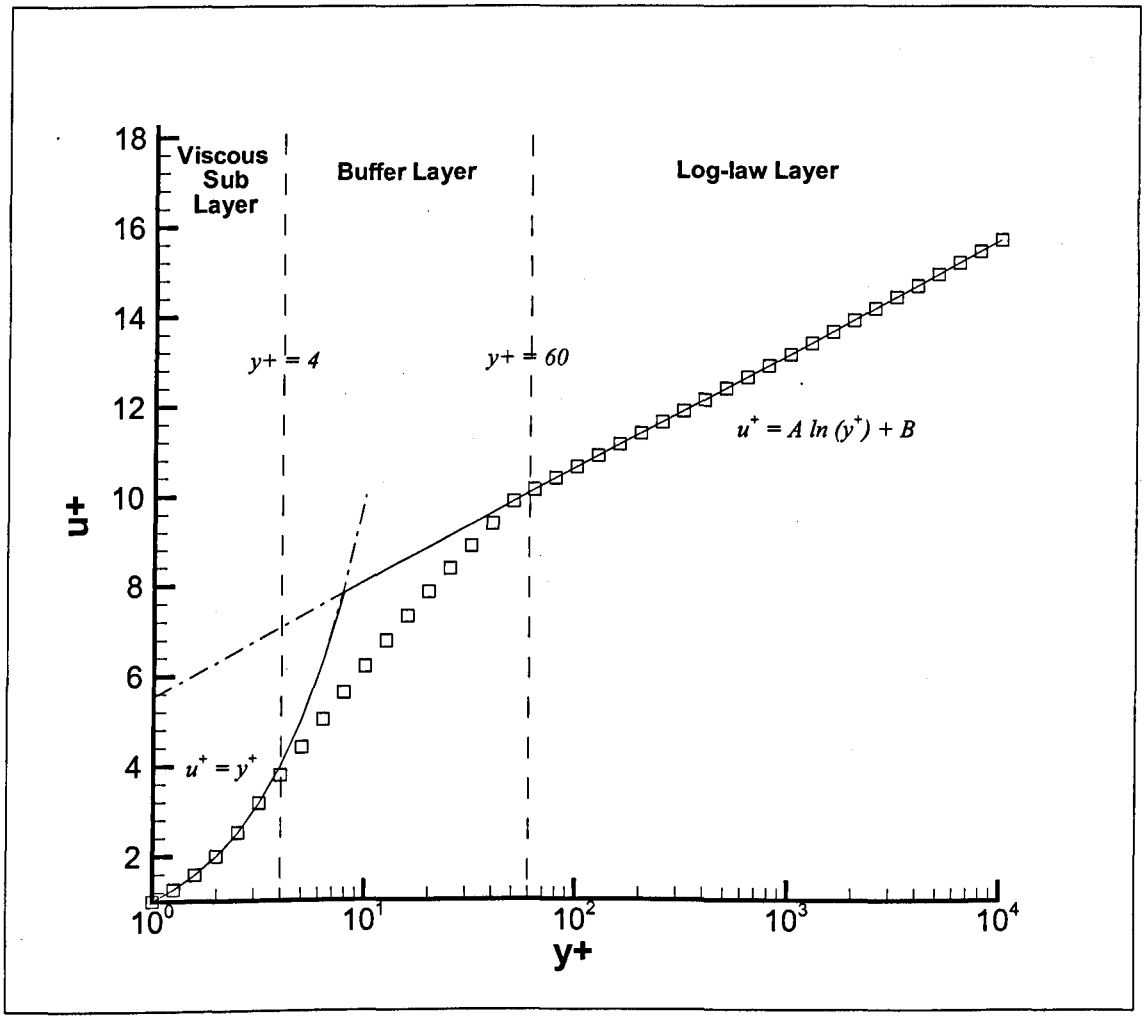

Figure 2.2: Law of the Wall □: typical boundary-layer profile

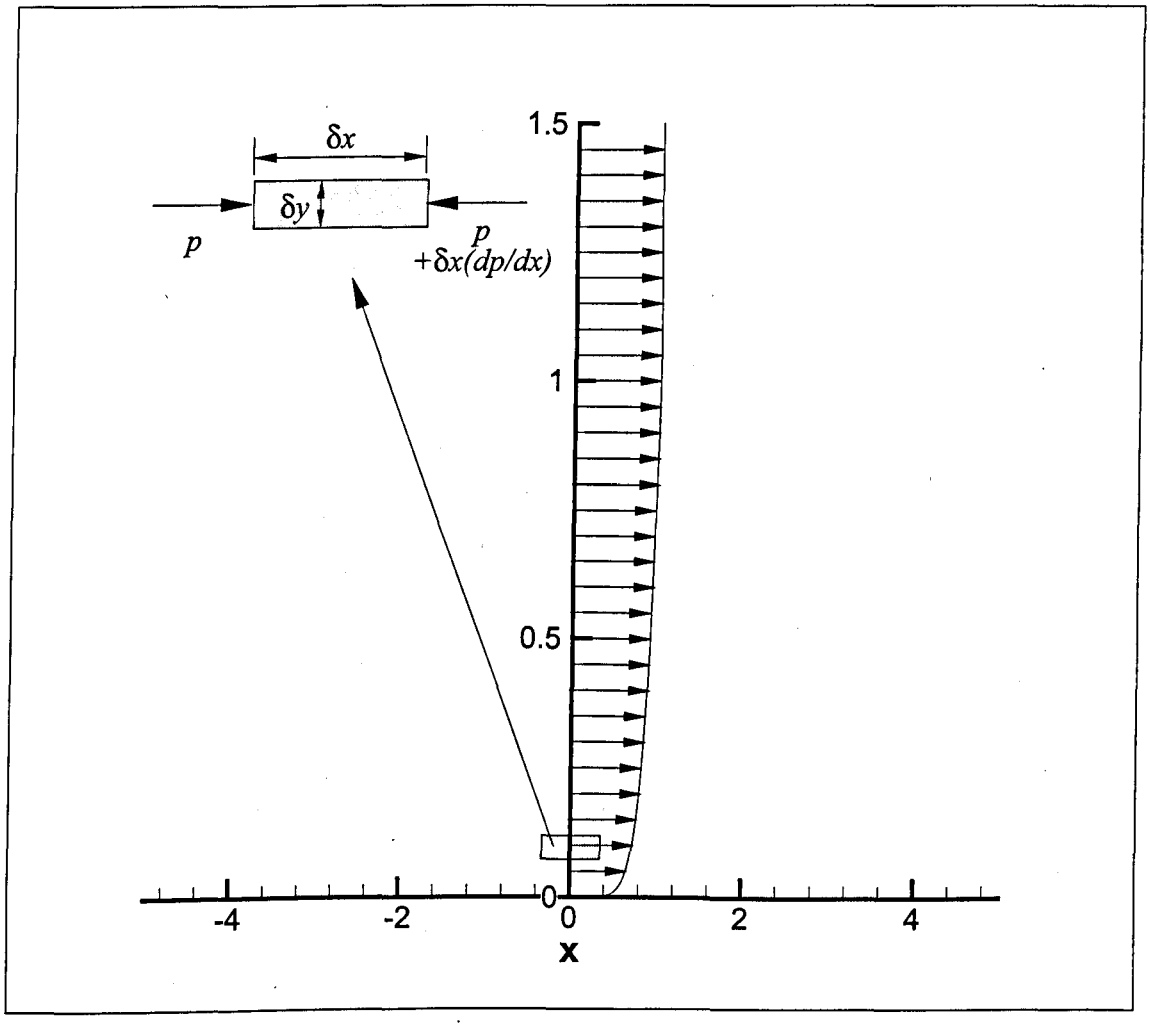

Figure 2.3: The effects of pressure on a small element of fluid

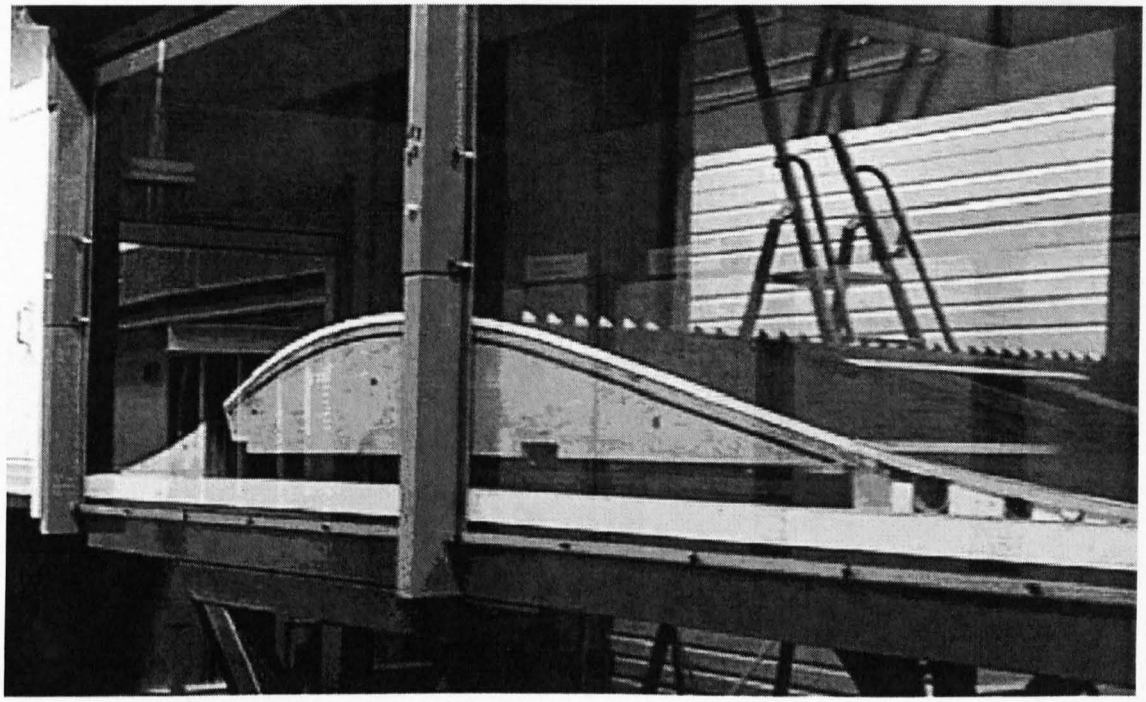

Figure 2.4: The 'bump' test section at the University of Lille

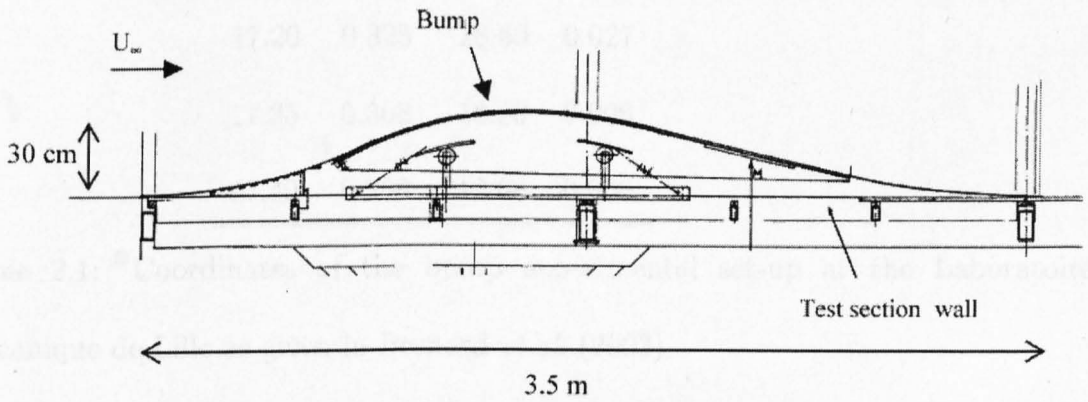

Figure 2.5: A schematic of the Lille bump set-up

x (m)	y (m)	x(m)	y (m)
15.50	0.000	17.60	0.258
15.60	0.002	17.63	0.251
15.80	0.014	17.80	0.207
16.00	0.044	17.90	0.181
16.20	0.099	18.00	0.155
16.40	0.178	18.20	0.102
16.60	0.257	18.24	0.093
16.80	0.310	18.40	0.058
17.00	0.331	18.58	0.031
17.20	0.325	18.60	0.027
17.35	0.308	18.80	0.006
17.40	0.300	19.00	0.000

Table 2.1: Coordinates of the bump experimental set-up at the Laboratoire de Mécanique de Lille as given in Bernard *et al.* (2003)

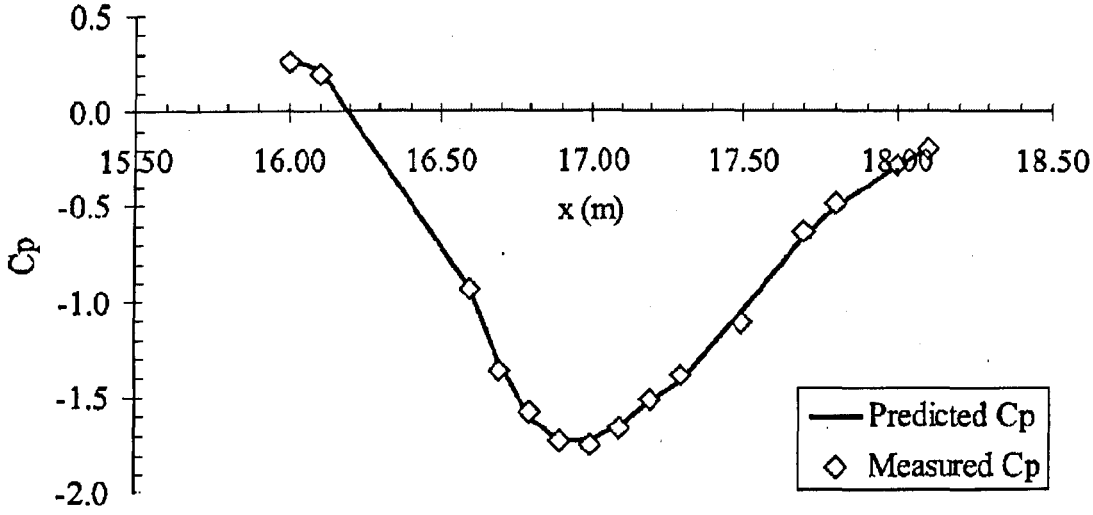

Figure 2.6: The uncontrolled pressure distribution over the Lille bump as given in Bernard *et al.* (2003)

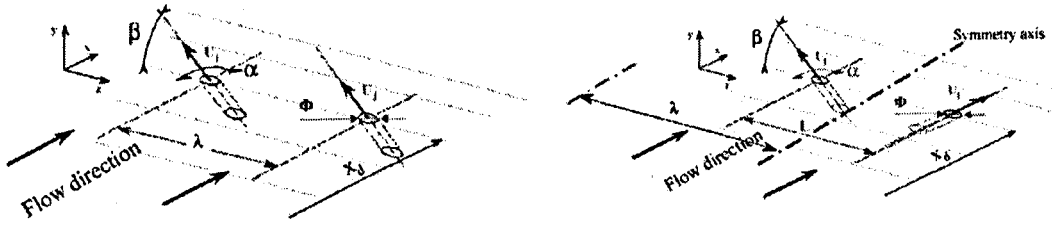

Figure 2.7: The experimental set-up of Godard and Stanislas (2006b) for co-rotating (left) and counter-rotating (right) systems

Parameter	Starting Value	Optimized Value
VR	1.6-4.7	4.7
α	90	45-90
β	45	45
Φ/δ	0.036	0.036
λ/Φ	16.7	6

Table 2.2: Parameters for the optimization study of the co-rotating jet system detailed in Godard and Stanislas (2006b)

Parameter	Starting Value	Optimized Value
VR	1.6-4.7	¿3.1
α	45	45-90
β	45	45
Φ/δ	0.036	0.036
L/Φ	23	15

Table 2.3: Parameters for the optimization study of the counter-rotating jet system detailed in Godard and Stanislas (2006b)

Chapter 3

Numerical Methods

This chapter considers the CFD code used in the present work. The development and features of the code are considered as is the discretization and solution methodology. Finally, some testing of the code is ventured by simulating the flow over a backward-facing step.

3.1 Code Features

The current work employs the NEAT code presented in Tucker (2001). Further work relevant to this research was done in the development of the code by Drs. Alexandre Jouvray and Yan Liu as given in Jouvray and Tucker (2005) and Tucker *et al.* (2003).

The code itself is based on a rectilinear coordinate system although versions of the code to simulate polar coordinate systems are available and again, given in Tucker (2001). The coordinate systems for the pressure and velocity components are located

on a staggered grid system as shown in Figure 3.2 below.

The need for a staggered grid system is due to the fact that if there is a checker-board pressure distribution of high-low pressures, these will result in zero gradients with a co-located grid. This means that for a staggered grid, the pressure is calculated at the regular grid nodes, whilst the velocities are calculated on the cell faces. More information on this is given in Harlow and Welch (1965).

3.1.1 Discretization

Once the domain has been discretized with a suitable grid mesh, a number of partial differential equations (or PDEs) need to be solved (including the Navier-Stokes equations) in the process of finding a flow solution. This process involves using the Finite Volume Method which considers each cell as a finite volume and takes into account the various flow fluxes across the cell faces. This procedure reduces all PDEs in the solution down to the general form:

$$a_P\phi_P = a_W\phi_W + a_E\phi_E + a_N\phi_N + a_S\phi_S + a_F\phi_F + a_B\phi_B + S_\phi \tag{3.1}$$

where the geographical notation is used to denote the effects of a number of adjacent cells on a cell in question. The variable ϕ denotes a general flow variable such as velocity, pressure or temperature. a denotes the coefficients of the equation where the subscript P represents the cell of interest at (i, j, k), E is the point to the east, $(i+1, j, k)$, N is the point to the north, $(i, j+1, k)$, F is the point to the front, $(i, j, k+1)$ and so forth. The term, S_ϕ is the source term for cell P for the variable S_ϕ. This geographical notation is used in a number of works but was used, in particular, in Tucker (2001). For brevity, this general equation is often abbreviated to:

$$a_P\phi_P = \sum a_{NB}\phi_{NB} + S_\phi \tag{3.2}$$

where NB denotes the neighbouring points. This geographical notation for the partial differential equations involved with fluid flow will be used for the remainder of this work.

3.1.2 Differencing Schemes

When solving the Navier-Stokes equations, it is necessary to estimate the flow properties at the faces of the cells and the local gradients of these properties in order to allow the various terms to be calculated. These flow properties are then used to calculate the coefficients, a & source term S as given in Eqn. 3.2 above. This is done in a number of ways and these will be briefly covered. However, the underlying integration of the Navier-Stokes equations over the finite volumes of the solution mesh is complex and will not be covered in greater detail here.

Consider a simple one-dimensional system divided into a number of cells as shown in Figure 3.1. Capital letters denote cell centres whilst lower-case letters signify cell faces.

Standard central differencing is based on the assumption that the value of the flow property, ϕ on the faces e and w of the cell is given by:

$$\phi_e = (\phi_P + \phi_E)/2 \tag{3.3a}$$

$$\phi_w = (\phi_W + \phi_P)/2 \tag{3.3b}$$

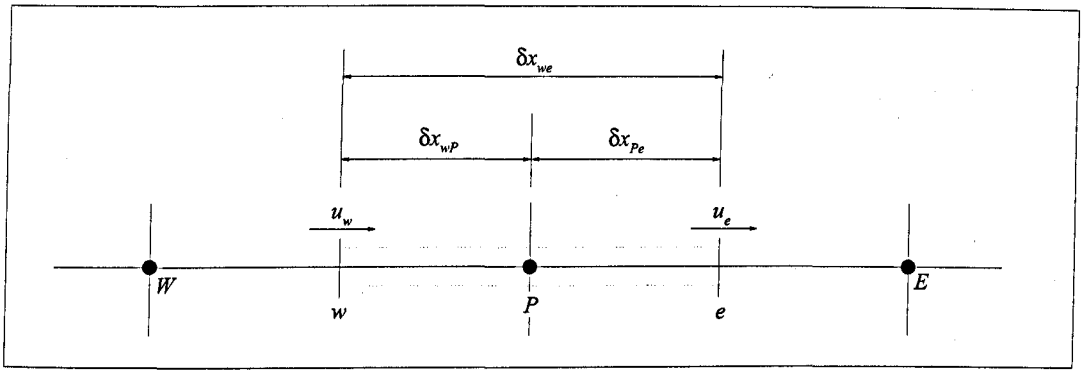

Figure 3.1: A simple one-dimensional system

where ϕ_P, ϕ_W and ϕ_E are the values of ϕ at the points P, W and E. This scheme has the advantage of being simple to implement and second-order accurate. However, the disadvantage is that for high Peclet numbers, oscillations are introduced to the flow. The Peclet number provides a measure of the convective terms relative to the diffusive terms and as such is sometimes referred to as the cell Reynolds number. It is defined as:

$$Pe = \frac{\rho u}{\Gamma/\delta x} \tag{3.4}$$

where Γ is the diffusion coefficient (based on the viscosity)

The Peclet number provides a relative measure of the ratio of convection to diffusion. For $Pe = 0$, there is pure diffusion with no convection whilst $Pe \rightarrow \infty$ denotes a flow completely dominated by convection. A problem arises with the standard central differencing method for $Pe > 2$ as the coefficients of the equations will start to become negative so violating the boundedness of the solution. This leads to oscillations or 'wiggles' being seen in the flow. Whilst it is almost impossible to maintain Peclet numbers of less than 2 for all but the lowest-Reynolds number flow, experience shows that Peclet

numbers can be of the order of 10^3 before serious numerical instability is introduced. More information regarding Peclet numbers can be found on page 112 of Versteeg and Malalasekera (1995).

Another scheme of use is First Order Upwind differencing. This is simpler than the central difference scheme in that the cell face properties are given by:

$$\phi_e = \phi_P \tag{3.5a}$$

$$\phi_w = \phi_W \tag{3.5b}$$

for a flow from left to right or:

$$\phi_e = \phi_E \tag{3.6a}$$

$$\phi_w = \phi_P \tag{3.6b}$$

for a flow from right to left. This is based on the assumption that for high Peclet numbers the cell faces will become more dependent on the flow properties upwind of the face than of the flow properties downwind. This has the advantage of simplicity and stability but introduces high levels of numerical diffusion into the flow due to it being of first order.

Hybrid differencing attempts to employ both standard central differencing and upwind differencing in a hybrid scheme choosing a central differencing scheme for low Peclet numbers whilst switching to upwind differencing for the higher Peclet numbers. This is useful for flows in which Peclet numbers are of the order of 10 but faster flows would simply end up using upwind differencing so negating the use of a hybrid scheme.

However, hybrid differencing is only as good as either central or upwind differencing so will either have issues with dissipation or diffusion depending on the local Peclet numbers. This can be avoided if a higher-order method is used but does have the disadvantage of requiring the solver to be modified to accept information for cells further away than those adjacent to a cell in question.

The Quadratic Upstream Interpolation for Convective Kinetics (or QUICK) scheme of Leonard (1979) is just such a method and works by using the two nodes either side of the face in question plus an additional node upstream of the face to estimate the face value. These additional nodes are given the labels WW denoting the cell two nodes to the left and EE as the cell two nodes to the right.

For flow travelling from west to east this is given by the relation:

$$\phi_w = \frac{6}{8}\phi_W + \frac{3}{8}\phi_P - \frac{1}{8}\phi_{WW} \tag{3.7a}$$

$$\phi_e = \frac{6}{8}\phi_P + \frac{3}{8}\phi_E - \frac{1}{8}\phi_W \tag{3.7b}$$

In contrast for the flow travelling from east to west the following relation is used:

$$\phi_w = \frac{6}{8}\phi_P + \frac{3}{8}\phi_W - \frac{1}{8}\phi_E \tag{3.8a}$$

$$\phi_e = \frac{6}{8}\phi_E + \frac{3}{8}\phi_P - \frac{1}{8}\phi_{EE} \tag{3.8b}$$

However, this scheme has two main problems. Firstly, the coefficients for WW and EE are negative so are prone to set the overall coefficients negative inducing some instability into the simulation. Secondly, for a code based on a tri-diagonal solver, this method requires significant modifications in order to accept the influence of the WW and EE points on the flow solution.

In order to alleviate these problems, a modification of the QUICK method was proposed by Hayase *et al.* (1992) and involves placing the problematic WW or EE terms into the source term. This is given as:

$$a_W = D_w + \alpha_w F_w \tag{3.9a}$$

$$a_W = D_e - (1-\alpha_e)F_e \tag{3.9b}$$

$$\begin{aligned} S = {} & \frac{1}{8}(3\phi_P - 2\phi_W - \phi_{WW})\alpha_w F_w \\ & + \frac{1}{8}(\phi_W + 2\phi_P - 3\phi_E)\alpha_e F_e \\ & + \frac{1}{8}(3\phi_W - 2\phi_P - \phi_E)(1-\alpha_w)F_w \\ & + \frac{1}{8}(2\phi_E + \phi_{EE} - 3\phi_P)(1-\alpha_e)F_e \end{aligned} \tag{3.9c}$$

where the coefficients D and F are the contributions due to diffusion and convection respectively and α_w and α_e are defined as:

$$\alpha_w = 1 \quad \text{and} \quad \alpha_e = 0 \quad \text{for} \quad u_{local} > 0 \tag{3.10a}$$

$$\alpha_w = 0 \quad \text{and} \quad \alpha_e = 1 \quad \text{for} \quad u_{local} < 0 \tag{3.10b}$$

For the purposes of this work, simulations were initially run using Upwinding as this provides a stable starting point. The simulation was then run using standard central differencing if stability could be maintained. If not, this QUICK method was used to provide a more stable solution.

3.1.3 The TDMA Solver

The code solver is based on the standard Tri-Diagonal Matrix Algorithm (TDMA) as detailed in Patankar (1980). This has the benefit of simplifying the solution by only linking a cell with those cells in contact by exploiting the tridiagonal properties of the coefficient matrices.

The TDMA solver can be thought of as dividing a multi-dimensional problem into a series of sweeps in each coordinate direction. A recursive relation for a distribution of ϕ in the x direction can be given as:

$$a_i\phi_i = b_i\phi_{i+1} + c_i\phi_{i-1} + d_i \tag{3.11}$$

where a, b, c and d are the coefficients and source terms for ϕ_i relative to its surrounding nodes. For the geographic notation used previously, these coefficients would correspond to:

$$a_i = a_p \tag{3.12a}$$

$$b_i = a_e \tag{3.12b}$$

$$c_i = a_w \tag{3.12c}$$

$$d_i = \text{remaining coefficients \& nodes + other sources} \tag{3.12d}$$

The problem now arises that every node is dependent on nodes either side so the following relation is sought:

$$\phi_i = P_i\phi_{i+1} + Q_i \tag{3.13}$$

It then follows that at the point to the left of i, the following relation holds equally:

$$\phi_{i-1} = P_{i-1}\phi_i + Q_{i-1} \tag{3.14}$$

Substituting Equation 3.14 into 3.11 to get rid of ϕ_{i-1} gives the recurrence relations P & Q as:

$$P_i = \frac{b_i}{a_i - c_i P_{i-1}} \tag{3.15a}$$

$$Q_i = \frac{d_i + c_i Q_{i-1}}{a_i - c_i P_{i-1}} \tag{3.15b}$$

This allows P and Q at i to be found in terms of P and Q at point $i-1$. To start the process, P and Q need to be found at point $i = 1$ then the distributions of P and Q can be found by forward substitution.

Assuming that $c_1 = 0$, as $i = 1$ is at the boundary of domain this gives P and Q there as:

$$P_1 = \frac{b_1}{a_1} \tag{3.16a}$$

$$Q_1 = \frac{d_1}{a_1} \tag{3.16b}$$

By cycling from $i = 2$ to $i = N$, the remaining values of P and Q are found by forward substitution. Given ϕ at point N it is now possible to use Equation (3.14) to back-substitute the known values of P and Q to find the distribution of ϕ. This process is then repeated in each of the coordinate directions so that the entire domain is solved.

This solver has the advantage of being simple to implement and efficient to use as it assumes that only immediately adjacent cells have an effect on any particular cell

in question (i.e. the coefficient matrices are highly tri-diagonal). However, this has the disadvantage that higher-order differencing methods such as Quadratic Upwinding (QUICK) and higher-order central differencing cannot be used directly although a solution to this problem was presented in the previous section.

3.1.4 The SIMPLE Algorithm

Pressure-velocity coupling is achieved using the Semi Implicit Method for Pressure-Linked Equations (SIMPLE) as detailed in Patankar and Spalding (1972). The SIMPLE algorithm works as follows. Consider the discretized momentum equations in the x and y directions as:

$$a_{i,J}u_{i,J} = \sum a_{nb}u_{nb} + (p_{I-1,J} - p_{I,J})A_{i,J} + b_{i,J} \quad (3.17a)$$

$$a_{I,j}v_{I,j} = \sum a_{nb}v_{nb} + (p_{I,J-1} - p_{I,J})A_{I,j} + b_{I,j} \quad (3.17b)$$

where $A_{i,J}$ is the area of the cell and $b_{i,J}$ is the sum of the other source terms.

Firstly, the pressure field is guessed and stored as p^*. If this is used in the above momentum equations, it yields the guessed velocity field, u^* and v^* thus:

$$a_{i,J}u^*_{i,J} = \sum a_{nb}u^*_{nb} + (p^*_{I-1,J} - p^*_{I,J})A_{i,J} + b_{i,J} \quad (3.18a)$$

$$a_{I,j}v^*_{I,j} = \sum a_{nb}v^*_{nb} + (p^*_{I,J-1} - p^*_{I,J})A_{I,j} + b_{I,j} \quad (3.18b)$$

It therefore follows that there exists some correction distribution for u, v and p which, when applied to the guessed fields, yields the correct distributions of these variables. Therefore:

$$u = u^* + u' \tag{3.19a}$$

$$v = v^* + v' \tag{3.19b}$$

$$p = p^* + p' \tag{3.19c}$$

where u, v and p are the exact velocity & pressure distributions, u^*, v^* and p^* are the guessed velocity and pressure distributions and u', v' and p' are the correction velocity & pressure distributions. If a guessed field is subtracted from an exact field, a correction field is produced. Therefore subtracting Eqns. (3.18a) & (3.18b) from Eqns. (3.17a) & (3.17b) gives the equations for the correction field thus:

$$a_{i,J}u'_{i,J} = \sum a_{nb}u'_{nb} + (p'_{I-1,J} - p'_{I,J})A_{i,J} \tag{3.20a}$$

$$a_{I,j}v'_{I,j} = \sum a_{nb}v'_{nb} + (p'_{I,J-1} - p'_{I,J})A_{I,j} \tag{3.20b}$$

These are the correction formulae. The main approximation of the SIMPLE algorithm is that the above terms $\sum a_{nb}u'_{nb}$ and $\sum a_{nb}v'_{nb}$ can be neglected as all of the coefficient contributions should roughly balance anyway. This gives the velocity corrections as:

$$u'_{i,J} = d_{i,J}(p'_{I-1,J} - p'_{I,J}) \tag{3.21a}$$

$$v'_{I,j} = d_{I,j}(p'_{I,J-1} - p'_{I,J}) \tag{3.21b}$$

where $d_{i,J} = \frac{A_{i,J}}{a_{i,J}}$ & $d_{I,j} = \frac{A_{I,j}}{a_{I,j}}$. These can then be substituted into Eqns. (3.19a)-(3.19c) to give the actual velocity distributions:

$$u_{i,J} = u^*_{i,J} + d_{i,J}(p'_{I-1,J} - p'_{I,J}) \quad (3.22a)$$

$$v_{I,j} = v^*_{I,j} + d_{I,j}(p'_{I,J-1} - p'_{I,J}) \quad (3.22b)$$

$$u_{i+1,J} = u^*_{i+1,J} + d_{i+1,J}(p'_{I,J} - p'_{I+1,J}) \quad (3.22c)$$

$$v_{I,j+1} = v^*_{I,j+1} + d_{I,j+1}(p'_{I,J} - p'_{I,J+1}) \quad (3.22d)$$

This implies that if a pressure correction field, p', can be found, then the velocity field can be corrected to take into account the effects of pressure.

By considering a discretized form of the continuity equation, thus:

$$[(\rho uA)_{i+1,J} - (\rho uA)_{i,J}] + [(\rho vA)_{I,j+1} - (\rho vA)_{I,j}] \quad (3.23)$$

Substituting the above relations Eqns. (3.22a)-(3.22d) into Eqns. (3.23) and simplifying gives the equation for pressure correction as:

$$a_{I,J}p'_{I,J} = a_{I+1,J}p'_{I+1,J} + a_{I-1,J}p'_{I-1,J} + a_{I,J+1}p'_{I,J+1} + a_{I,J-1}p'_{I,J-1} + b'_{I,J} \quad (3.24)$$

where the coefficients are given as:

$$a_{I,J} = (\rho dA)_{I,J} \quad (3.25a)$$

$$a_{I+1,J} = (\rho dA)_{i+1,J} \quad (3.25b)$$

$$a_{I-1,J} = (\rho dA)_{i,J} \quad (3.25c)$$

$$a_{I,J+1} = (\rho dA)_{I,j+1} \quad (3.25d)$$

$$a_{I,J-1} = (\rho dA)_{I,J} \quad (3.25e)$$

$$b'_{I,J} = (\rho u^*A)_{i,J} - (\rho u^*A)_{i+1,J} + (\rho v^*A)_{I,j} - (\rho v^*A)_{I,j+1} \quad (3.25f)$$

In summary, the overall SIMPLE algorithm consists of the following stages:

1 Use the previous pressure field, p as the guessed pressure field, p^*

2 Solve the u and v momentum equations to find a guessed velocity field, u^* and v^*

3 Use this guessed velocity field to solve the pressure correction field, p' as given in Eqn. 3.24

4 Use the pressure correction field to find the actual velocity field using the correction relations given in Eqns. 3.22a-3.22d

5 Use the pressure correction field to correct the previously guessed pressure field

It should be noted that this method is prone to numerical instability and so is usually accompanied by some form under-relaxation such that:

$$u^{new} = \alpha_u u^{new} + (1 - \alpha_u)u^{old} \tag{3.26a}$$

$$v^{new} = \alpha_v v^{new} + (1 - \alpha_v)v^{old} \tag{3.26b}$$

$$p^{new} = \alpha_p p^{new} + (1 - \alpha_p)p^{old} \tag{3.26c}$$

where α_u, α_v and α_p are the under-relaxation factors for u, v and p respectively and can take any value between 0 and 1. However, if a value of $\alpha = 1$ is selected, the system is no longer under-relaxed and so may be unstable. Conversely, if $\alpha = 0$ is selected, no correction will be applied and so the solution will not progress. For the purpose of this thesis, values were chosen to be between $\alpha = 0.4$ and $\alpha = 0.7$.

In general, grid compression is achieved using a geometric progression scheme and is represented by:

$$\Delta x_i = E_x \Delta x_{i-1} \tag{3.27}$$

where Δx_{i-1} and Δx_i are the grid spacings at points i and $i-1$ respectively and E_x is the expansion factor. This factor can be less than unity for compressing meshes or greater than unity for expanding meshes. In general, values for E_x are chosen between (1/1.3) and 1.3.

3.2 Code Validation

For the purpose of code validation, the well-documented case of laminar flow over a backward-facing step has been considered. The reason for using this case is that the flow is dominated by a single, two-dimensional vortex in contact with the step which can be characterised by a single length scale known as the 'recirculation length'. For this reason, this flow has been used as a code validation case by a number of people including Kim and Moin (1985), Le and Moin (1991) and Chung *et al.* (2003). Experimental work for the backward-facing step has also been completed by Armaly *et al.* (1983).

The code is used in two-dimensional mode without any turbulence treatment and applied to Reynolds numbers ranging from 125 to 500. This Reynolds number is determined by:

$$Re = \frac{U_{ave} h}{\nu} \tag{3.28}$$

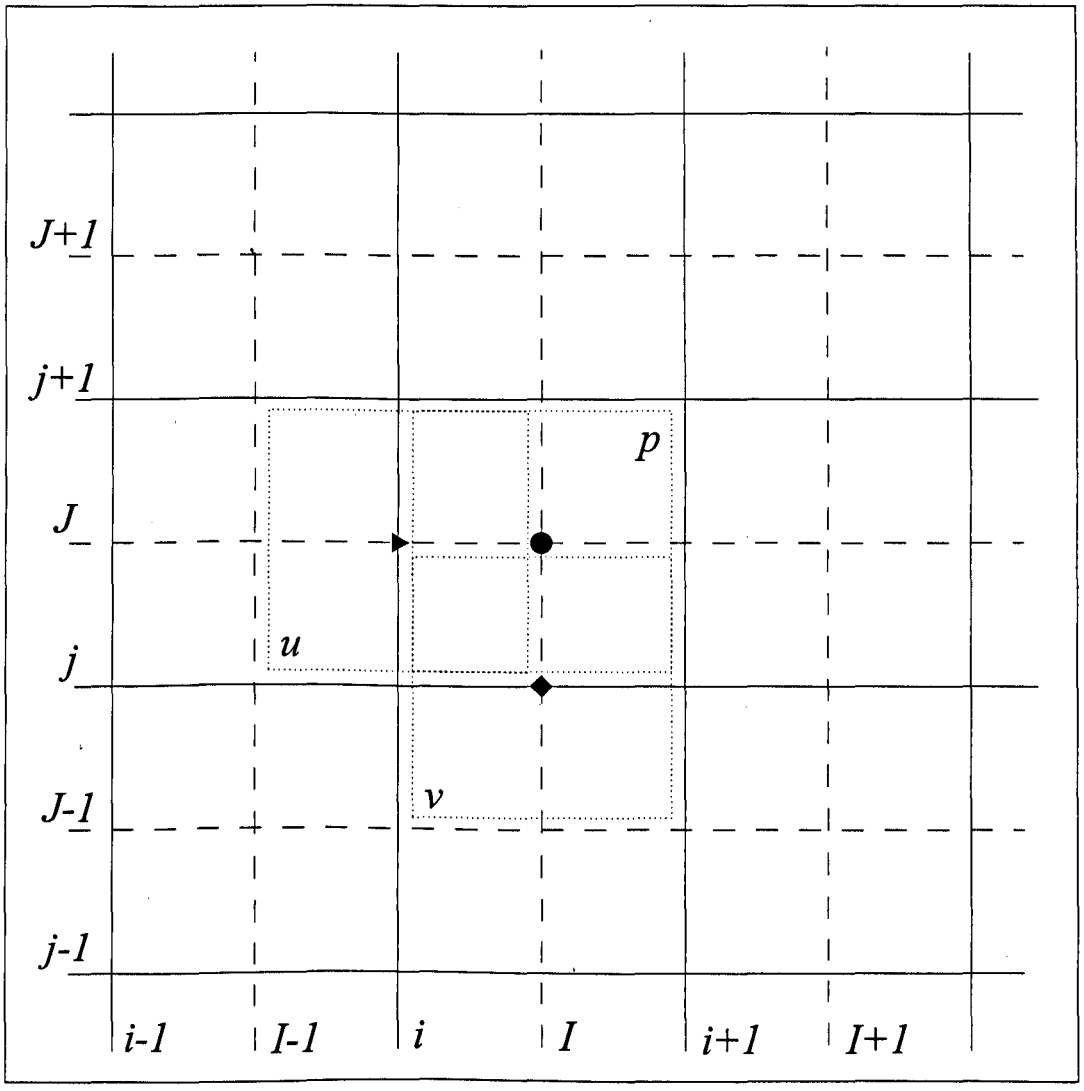

Figure 3.2: The Staggered Grid System. Capital letter labels denote centres of the pressure grid. Lower-case letter labels denote staggered cell centres for u & v grids.

where U_{ave} is the bulk mean velocity, h is the step height and ν is the kinematic fluid viscosity.

The flow problem was set-up in a two-dimensional domain $30m$ long by $2m$ high with a step height of $1m$, thus equating to an expansion ratio of $2:1$. The step was located $10m$ into the domain so leaving $20m$ downstream for the separated region to develop. A grid mesh of 380 nodes in the streamwise direction, was used to discretize the domain. Grid expansions were also used in the x direction in order to resolve the flow close to the vertical surface of the step. In the wall-normal y direction, geometric grid expansions were used to compress the grid of 100 nodes near the walls of the channels both leading up to and away from the step. This mesh is shown in Figure 3.3.

The main problem with this grid mesh is that it leads to many wasted grid nodes downstream of the step along the centre of the channel where not much would be expected to happen. However, this is a generic drawback of using rectilinear codes to solve such a problem.

Although these flows are known to be steady in time for the lowest Reynolds numbers, all simulations were run using unsteady methods. In order to measure the time a simulation has been run in realistic terms, a non-dimensional time-scale T is defined as:

$$T = \frac{U_{ave}t}{x_{max}} \tag{3.29}$$

where t is actual time (in s), U_{ave} is the average flow speed (in ms^{-1}) and x_{max} is the length of the domain (in m). The parameters used for each of the cases are given in Table 3.1. It can be seen from this table that all simulations were run for at least $30T$ thus allowing the flow to have travelled the length of the domain more than 30 times

before terminating.

The results for these simulations are given below in Figure 3.4 which shows stream-trace plots of the flow within the domain. The recirculation length is defined as the distance of the reattachment point from the step and is measured in step-heights (in this situation this is simplified by the step height being unity). The results in Figure 3.4 show an almost linear increase in x_r at least for lower Reynolds numbers. This behaviour is observed in the experimental results of Armaly *et al.* (1983). Values for the recirculation length are also given in Table 3.1.

For comparison with other works, these results are plotted in Figure 3.5. As can be seen, all results have good agreement with one another up to around $Re = 350$. Above this Reynolds number, the relations start to break down with the simulations generally under-estimating the recirculation length. This can be explained by the nature of the flow becoming three-dimensional at a Reynolds number of around 500 so leading to increasing inaccuracies being produced by a two-dimensional simulation. In conclusion, it has been seen that the base code compares well to a selection of other works.

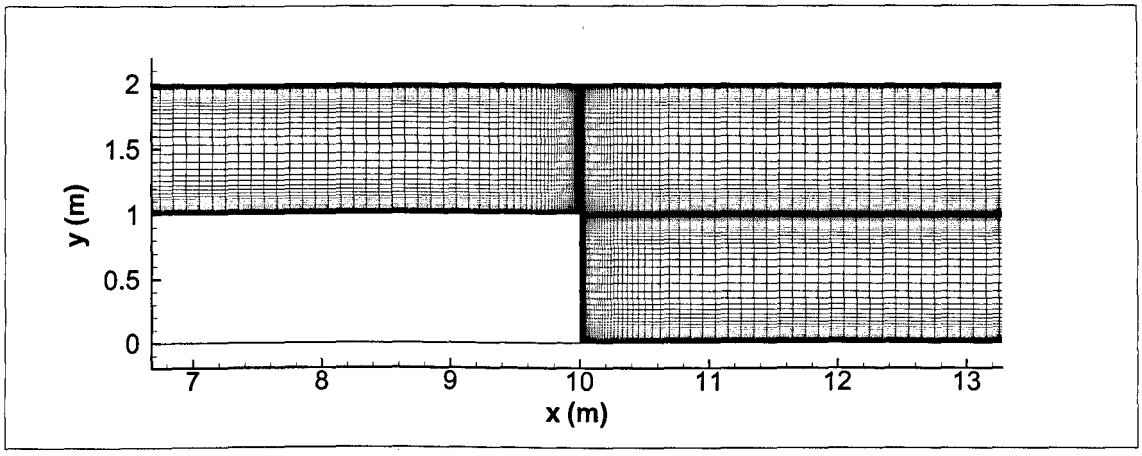

Figure 3.3: The grid mesh chosen for the backward-facing step flow

Code Number	Case	$U_{ave}(ms^{-1})$	T	x_r
MT01-02-A01	$Re = 125$	0.91×10^{-3}	30.3	3.49
MT01-02-A02	$Re = 250$	1.82×10^{-3}	30.3	5.91
MT01-02-A03	$Re = 375$	2.73×10^{-3}	34.1	7.84
MT01-02-A04	$Re = 500$	3.64×10^{-3}	60.6	9.21

Table 3.1: Parameters & Results for the case of the backward-facing-step

3.3 Conclusions

Now that the code itself has been presented and validated, a detailed assessment of the methods to be covered in this thesis will begin with the chapter on Immersed Boundary Methods. This will be followed by the chapter on turbulence modelling using wall functions which then follows on to the chapter about detached eddy simulation.

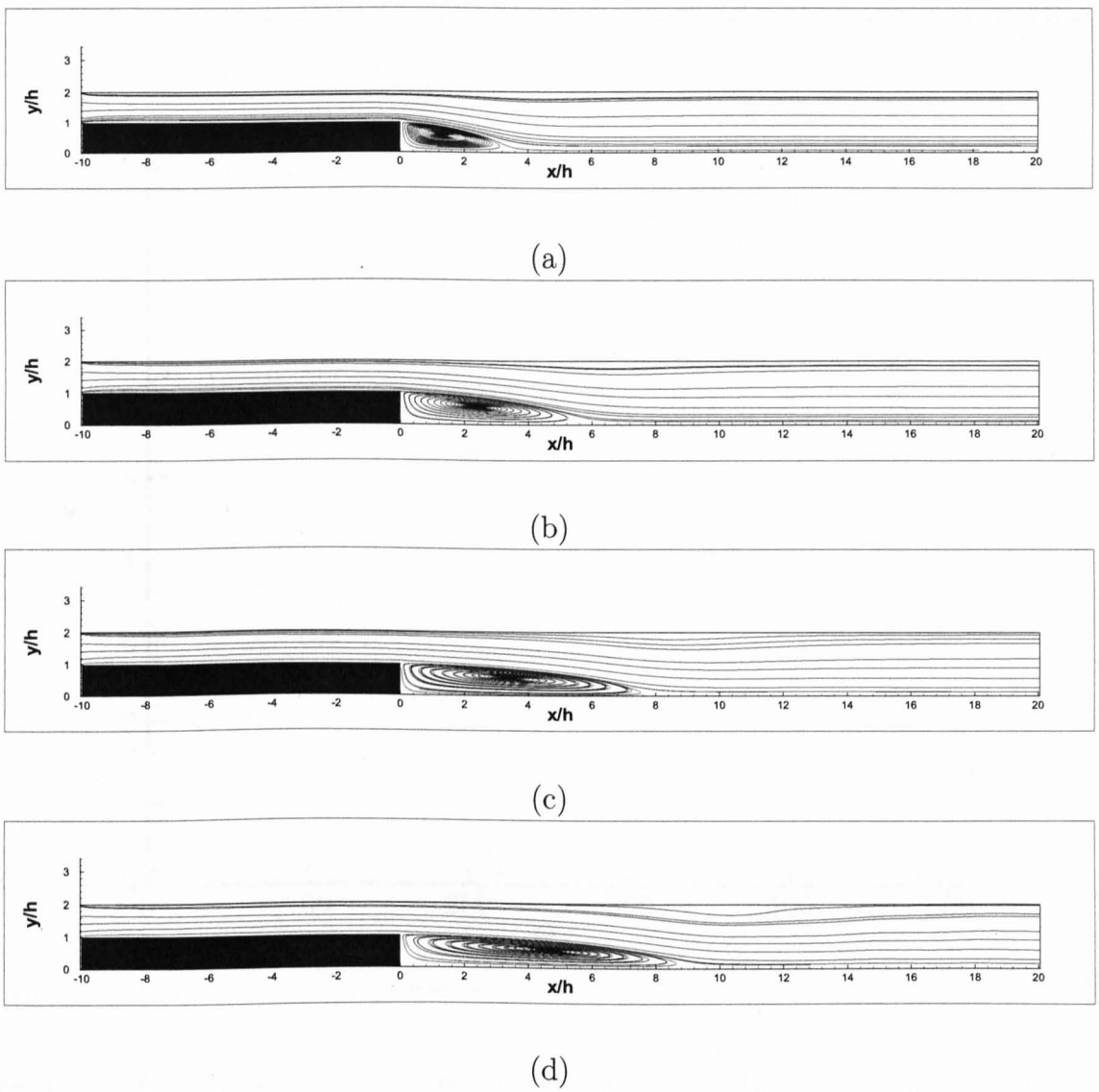

Figure 3.4: Stream-trace results for the backward-facing step flows. (a): Re=125, (b): Re=250, (c): Re=375, (d): Re=500

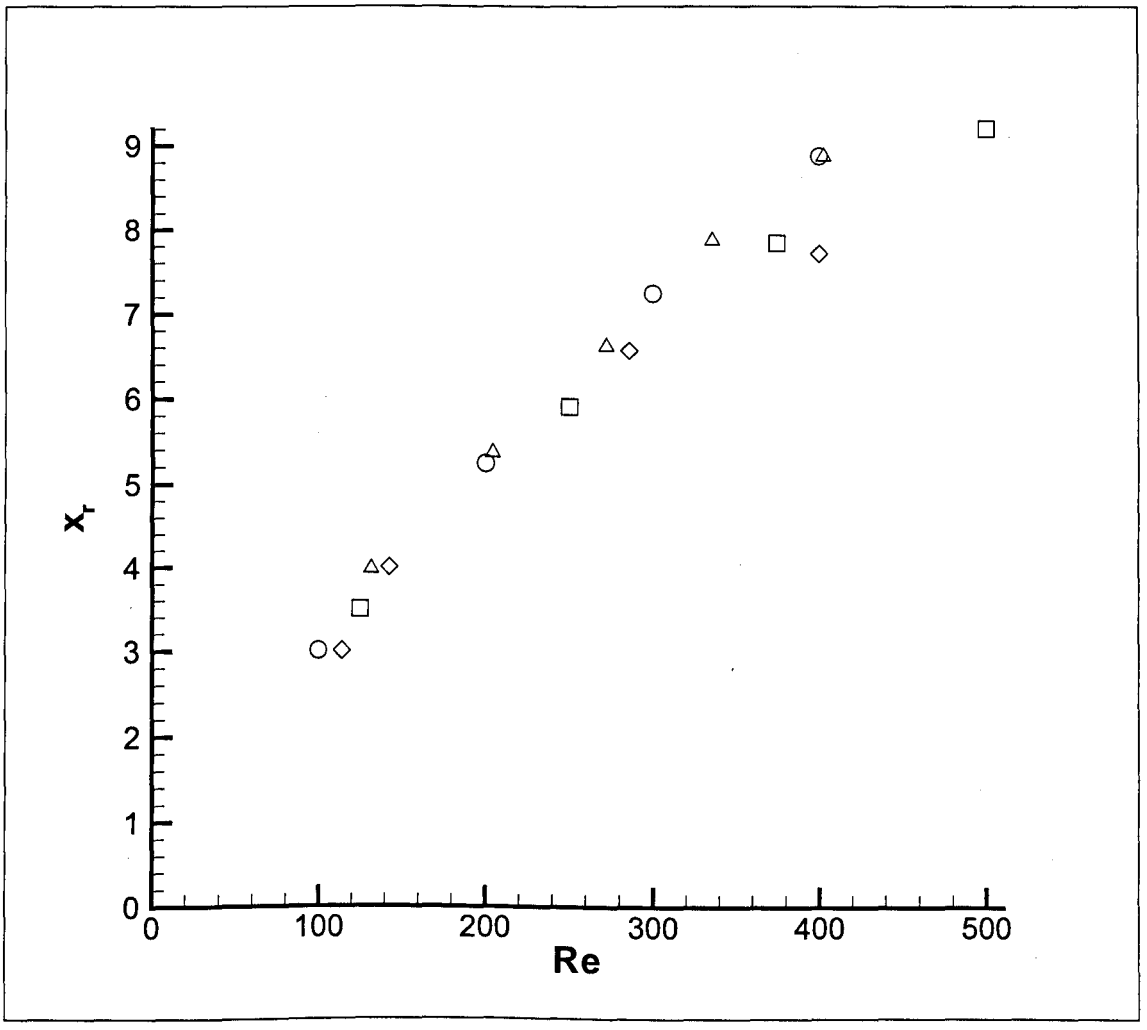

Figure 3.5: Comparison of recirculation lengths against Reynolds number for various works. □: Current Work (NEAT), ◇: Armaly *et al.* (1983), ○: Kim and Moin (1985), △: Le and Moin (1991)

Chapter 4

Immersed Boundary Methods

The modelling of complex geometries and curved shapes has always been of interest in the field of Computational Fluid Dynamics. Conventionally, in order to model a curved or complex shape, either curvilinear or unstructured grid systems would be used to fit the computational mesh exactly to the body. Figure 4.1 shows an example of using (a) curvilinear grids and (b) unstructured grids to model such geometries. This results in very simple application of the boundary conditions because the faces of the grid are coincident with the solid surface. The overall complexity of the code, however, is greatly increased so as to deal with the transformed coordinates and grid systems. One solution is to use a code based on a cartesian grid system and employ some form of Immersed Boundary Method to create a surface not coincident with the grid mesh.

This chapter will begin with a brief history of the development of such methods before covering the related theory. A novel implementation of the IBM within a SIMPLE pressure-correction based method is covered followed by a validation against circular cylinder flow at two Reynolds numbers.

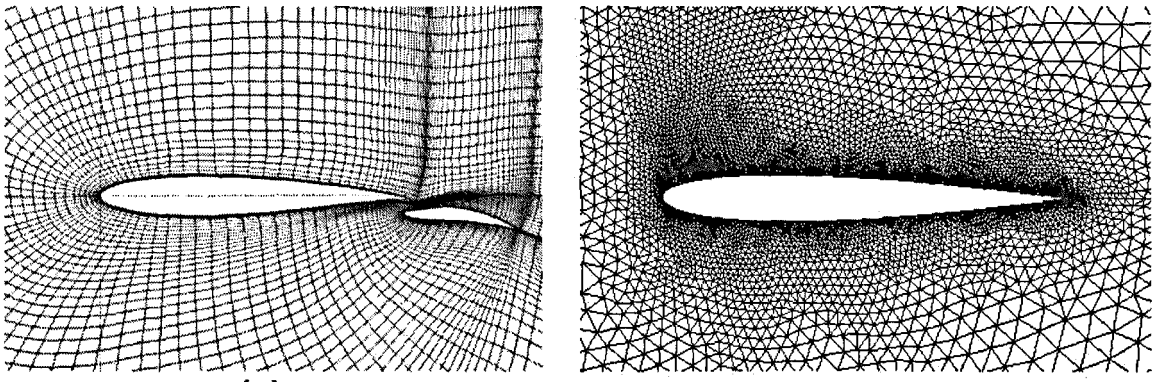

Figure 4.1: Modelling a complex geometry using (a) Curvilinear grids (b) Unstructured grids

4.1 History

In recent years there has been an upsurge in the use of Immersed Boundary Methods to model complex shapes using CFD codes based on cartesian grids. This has the benefit of using a simple rectilinear grid and the associated solution methods to model geometries previously only possible using one of the aforementioned grid systems. The problem with using a cartesian grid to model a complex geometry is that most of the fluid volumes through which the surface passes will generally not have cell centres that coincide exactly with the surface geometry. This causes a problem in that the boundary condition of zero velocity normal or tangential to the surface needs to be enforced somewhere between the grid nodes.

This problem was first addressed by Peskin (1972) in his work on flows around heart valves. Using a cartesian grid, it was found that the position and motion of the heart walls could be modelled by introducing an additional forcing term within the governing equations at the cells along the immersed boundary. This forcing term would then have

the effect of forcing these cells to negative values, thus resulting in the boundary being interpolated somewhere between the fluid node and the immersed boundary node.

Throughout the 1970s and 1980s this method was little used, probably because computing power was insufficient to solve anything other than very low Reynolds number flows and geometries. The rapid increase in computing power in the 1990s resulted in a far greater number of flows being available for study by CFD making desirable more efficient methods for modelling complex geometries. Much initial work on the immersed boundary method was done in the 1990s by Mohd-Yusof (1997) who looked into various methods of forcing available for Immersed Boundary Methods and the benefits/downfalls of such methods. Although Mohd-Yusof (1997) was concerned with implementing an IBM within a spectral code to take advantage of the high-order accuracy of such a code, the forcing functions introduced are still the basis of modern direct-forcing methods. Following this initial study, the works of Fadlun *et al.* (2000), Kim *et al.* (2001) and Tseng and Ferziger (2003) have all made important contributions to the field.

Fadlun *et al.* (2000) looked into different methods of implementing the IBM. Firstly two forcing methods were covered: namely feedback forcing and direct forcing. It was found that direct forcing was preferable, as it does not require any arbitrary constants to be calibrated beforehand, and has more relaxed stability constraints. For example, recalling the definition of the CFL number as $(U_\infty dt/dx)$ it was found that $CFL < 1.5$ was required for direct forcing rather than $CFL < 0.025$ being required for feedback forcing.

Three different interpolation methods were also covered. These were stepwise (no interpolation), volume fraction weighting and linear interpolation. The main difference, however, between this work and other works on the IBM is that the first node *outside* the boundary is not solved, but simply set to the required value.

As examples, the cases of a vortex-ring formation from a nozzle, the flow around a cylinder and the flow within a moving-piston/cylinder assembly are all investigated. These all perform well and established the benefits of using the IBM in modelling complex two- and three-dimensional boundaries, as well as moving boundaries.

An important improvement to the IBM was proposed by Kim *et al.* (2001). This involved applying mass sources and sinks near the immersed cells in order to preserve continuity at the boundary. This method was validated against a square block angled at 45 degrees to the flow, and the flows around a circular cylinder and a sphere. The work employs a similar method to that proposed by Mohd-Yusof (1997), and involves a second-order-accurate interpolation scheme.

The main proposal of their work was to employ mass sources and sinks near the ghost cells in order to preserve continuity. It is simple to see that in forcing the desired velocity at the ghost cell, little thought is given to conserving mass within that control volume. A mass source is applied at the ghost cell in order to conserve continuity.

Although the results without the mass sources show good agreement with body-fitted grid and experimental results, inaccuracies in areas of high continuity violation (namely the stagnation regions) are found, and instability of the method is experienced with increasing Reynolds number. Applying mass sources has the effect of improving the accuracy of the surface resolution near stagnation regions and improves the stability.

This work was recently investigated and added to by Huang and Sung (2005). The same test cases of an angled square block and a circular cylinder were examined in order to test a new mass source/sink formulation. During the derivation of the mass source in Kim *et al.* (2001), an assumption was made that the boundary crossed grid points. A more general case results in a mass source derivation which is more complete.

Huang and Sung (2005) found slightly better agreement for all drag and lift co-

efficients for the flows around a circular cylinder. An almost perfect modelling of the cylinder surface was also achieved. The few points that did not follow the surface using the method of Kim *et al.* (2001) were corrected by a fuller approximation incorporating mass sources.

Further development of the method was shown by Tseng and Ferziger (2003), where a number of methods for interpolating the immersed boundary velocities were considered. Here, linear and quadratic planes were proposed in order to assess the effect of interpolation on the final results. The key point of this work is the investigation of the use of Immersed Boundary Methods with Large Eddy Simulation for higher Reynolds number flows. The application of the IBM to geophysical fluid dynamics flows are also considered.

This chapter is organised as follows. Firstly, the basic principles behind Immersed Boundary Methods are covered and a number of different methods for surface approximation and forcing are introduced. A novel method using coefficients calculated beforehand at each ghost cell is covered. This was formulated in order to reduce the computational effort necessary for the Immersed Boundary Method during the simulation.

Further original work was also completed in the implementation of the immersed boundary method within a pressure-correction based code (see Section 3.1.4) as opposed to the fractional-step or spectral codes used in previous works. This involved directly implementing the immersed boundary method within the solver detailed in Chapter 3.

In order to test these implementations, a number of test cases are then shown and validated. Finally, some conclusions are drawn as to the overall benefits and drawbacks of IBM.

4.2 Theory

Imagine a complex geometry superimposed on a conventional non-staggered rectilinear grid as shown in Figure 4.2. The nodes are divided into three groups. Firstly, fluid nodes are defined as cells which have their centre outside the object surface and are within the fluid domain. Next, solid cells are those which lie entirely within the surface. Finally, ghost cells are defined as those cells which lie on the boundary but have their cell centres within the solid domain. As shown below, sometimes solid cells near the boundary are also chosen as ghost cells.

An example of this can be seen clearly in Figure 4.2 as the ghost cells at (i, j) and $(i-1, j-1)$ which have the boundary passing through and have their cells centres within the solid domain. The cell at $(i+1, j+1)$ is *not* a ghost cell however, because, although it lies on the surface, the cell centre lies outside the surface in the fluid domain. For this reason the cell at $(i+1, j)$ has been chosen as a ghost cell instead.

The computational nodes generally do not coincide with the surface, so the boundary condition at the surface needs to be implicitly imposed. As already mentioned, this is done by setting the flow property (e.g. velocity or temperature) at the ghost cells to some value compensating for the flow property just outside the boundary.

Consider the ghost cell at (i, j) in Figure 4.2. The flow properties here necessary to force the flow properties to zero at the boundary will be some function of the flow properties outside the boundary. If the flow property is positive outside the boundary, the immersed boundary node will generally need to be negative in order to counter the exterior flow, implying that the zero contour is somewhere between the two nodes. If this process is performed in order to set the velocity in all directions to be zero at the immersed boundary, then it is obvious that the zero velocity contours will coincide with

the desired boundary shape, so effectively imposing that shape upon the flow.

The process of calculating the value of the flow property at the immersed boundary node with respect to the external fluid nodes is known as 'reconstruction', and there are a wide variety of methods for reconstruction. For the purpose of this work, however, four methods have been used. These are:

- Solid Block Reconstruction
- Simple Linear Reconstruction
- Full Linear Reconstruction
- Quadratic Reconstruction

Each of these methods will now be considered in greater depth, with a full derivation of the governing relationships.

4.2.1 Solid Block Reconstruction

By setting the immersed boundary node to have zero velocity irrespective of the local flow, the geometry is being simply modelled using a crude block approximation. This can be written as:

$$\phi_G = 0 \tag{4.1}$$

where ϕ_G is some fluid property at the ghost cell namely velocity but could also be some other property such as pressure or temperature. This method has the benefit of being very simple to implement and invariably being as stable as the base simulation.

The surface itself, however, will only ever be approximated by a crude step approximation. The accuracy of the surface approximation then becomes completely dependent on the grid spacing surrounding the shape and so, to the extent that, a complex shape will end up being approximated by a simple block as the grid is coarsened.

The solid-block approximation is nevertheless a good starting point. It does not produce any additional instabilities, so allows a base simulation to be set up appropriately before moving on to the more complex reconstruction methods.

4.2.2 Simple Linear Reconstruction

This method takes the flow property ϕ to vary linearly directly between the immersed boundary node and the closest fluid node. Shown in Figure 4.3, X_1 is defined as the fluid node above/below the ghost cell if the surface is roughly horizontal or left/right if the surface is roughly vertical. O is defined as the point on the surface which crosses the line between X_1 and G.

A relation for the ghost-cell flow property, ϕ becomes:

$$\phi_G = C_{X1}\phi_{X1} + C_O\phi_O \tag{4.2}$$

where C_{X1} and C_O are the coefficient contributions of ϕ at points X_1 & O to point G and for this method can be defined as:

$$C_{X1} = -\frac{d_{GO}}{d_{GX1} - d_{GO}} \tag{4.3}$$

$$C_O = 1 + \frac{d_{GO}}{d_{GX1} - d_{GO}} \tag{4.4}$$

where d_{GX1} and d_{GO} are the distances between G & X_1 and G & O respectively. It is clear, however, that the selection of point X_1 is important. If X_1 lies too close to boundary, then the term $d_{GX1} - d_{GO}$ tends to zero resulting in very large coefficients. Experience and Tseng and Ferziger (2003) have shown that in this case it is best to do one of the following.

Firstly there is the option of setting this X_1 point to become a ghost point and setting the coefficients here to zero as it is so close to the boundary. This will result in a slight shift in the local surface position but will result in a completely stable solution there. The second option is to pick the next closest fluid node as the X_1 point and recalculate the coefficients. This will result in reduced accuracy because of the assumption of a linear distribution over a greater distance, but it does have the benefit of greater stability.

4.2.3 Full Linear Reconstruction

The basis of this method is to assume that the flow property ϕ follows a linear plane near the ghost cell in question. This is shown in Figure 4.4. O is defined as the closest point on the boundary to G and X_1 & X_2 are chosen in order to make a triangle GX_1X_2 containing O. The values of ϕ at X_1 and X_2 are known and the desired value of ϕ at O is also known. A linear plane can therefore be defined that passes through each of these three points. Recall the definition for a linear plane:

$$\vec{r} \cdot \vec{N} = \vec{a} \cdot \vec{N} \tag{4.5}$$

where $\vec{r}$ is the general vector to a point on the plane, $\vec{N}$ is a vector normal to the plane and $\vec{a}$ is a known point on the plane.

In previous works but especially the work of Tseng and Ferziger (2003) the ghost cell properties, ϕ_G are found by substituting all node positions and flow properties at the surrounding nodes into the above vector equation and solving for every ghost cell and repeating this process for every timestep.

In order to reduce this effort, a new formulation is proposed. This involves finding a general solution to the vector relationship given in Eqn. (4.5) by assuming that if the ghost cells remain stationary, the contributions of the surrounding fluid nodes can be simplified to a coefficient form. This has the advantage of allowing these coefficients to be calculated at the beginning of the simulation so that they can be easily used during the solution process.

Writing Eqn. (4.5) in column vector form gives:

$$\begin{pmatrix} x \\ y \\ \phi \end{pmatrix} \cdot \begin{pmatrix} N_x \\ N_y \\ N_\phi \end{pmatrix} = \begin{pmatrix} a_x \\ a_y \\ a_\phi \end{pmatrix} \cdot \begin{pmatrix} N_x \\ N_y \\ N_\phi \end{pmatrix} \tag{4.6}$$

Taking the positions of the points as (x_O, y_O), (x_{X_1}, y_{X_1}) and (x_{X_2}, y_{X_2}) respectively, and the values of ϕ at the points to be ϕ_O, ϕ_{X_1} and ϕ_{X_2}, the terms of the vector equation become:

$$N_x = y_{OX_1}\phi_{OX_2} - \phi_{OX_1}y_{OX_2} \tag{4.7a}$$

$$N_y = x_{OX_2}\phi_{OX_1} - \phi_{OX_2}x_{OX_1} \tag{4.7b}$$

$$N_\phi = x_{OX_1}y_{OX_2} - x_{OX_2}y_{OX_1} \tag{4.7c}$$

and

$$x_{OX_1} = x_{X_1} - x_O \tag{4.8a}$$

$$x_{OX_2} = x_{X_2} - x_O \tag{4.8b}$$

$$y_{OX_1} = y_{X_1} - y_O \tag{4.8c}$$

$$y_{OX_2} = y_{X_2} - y_O \tag{4.8d}$$

$$\phi_{OX_1} = \phi_{X_1} - \phi_O \tag{4.8e}$$

$$\phi_{OX_2} = \phi_{X_2} - \phi_O \tag{4.8f}$$

As the immersed cell of interest is at point G, we can find the value of ϕ at this point by the following relation:

$$\phi_G = C_{X_1}\phi_{X_1} + C_{X_2}\phi_{X_2} + C_O\phi_O \tag{4.9}$$

Substitution of the above relations gives the coefficients C_{X_1} and C_{X_2} as:

$$C_{X_1} = \frac{(y_O - y_G)x_{OX_2} - (x_O - x_G)y_{OX_2}}{x_{OX_1}y_{OX_2} - x_{OX_2}y_{OX_1}} \tag{4.10a}$$

$$C_{X_2} = \frac{(x_O - x_G)y_{OX_1} - (y_O - y_G)x_{OX_1}}{x_{OX_1}y_{OX_2} - x_{OX_2}y_{OX_1}} \tag{4.10b}$$

As these coefficients only depend on the positions of O, G, X_1 and X_2, they can be calculated before the start of the simulation, stored and then used quickly during the solution process. This new formulation has the advantage of ease of implementation and reduction in computational effort required during the solution. However, this method does not allow the simulation to model moving boundaries as it is built on the assumption the positions of the nodes relative to the boundary are unchanging.

It is easy to see that, for any given geometry and grid, C_{X_1} and C_{X_2} are both constant as they only depend on local node positions and not the flow property, ϕ. It is also reasonably easy to see that both coefficients should always be negative. If $\phi_{X_1} = 0$ and $\phi_O = 0$ then the pivot line for $\phi = 0$ is as shown in Figure 4.5(a). This means that ϕ_G will always be opposite in sign to ϕ_{X_1} and so C_{X_1} must be negative. Likewise, by the same argument, C_{X_2} must be negative, as shown in Figure 4.5(b).

A note should be made at this point about the stability of this method. As with the simple linear method, if O gets close to X_1 or X_2 then the method will produce very large coefficients for that point. This is also true if O approaches the line between X_1 and X_2. This is because the plane was defined using the vector normal to the plane, which in turn was calculated by the cross product of vector OX_1 and OX_2. As O moves closer to the line X_1X_2 then, there becomes an infinite number of planes that can pass through O, X_1 and X_2 thus causing unstable coefficients. These characteristics are shown in Figure 4.6. The solution to this is as with the simple linear method, to move X_1 or X_2 or set X_1 or X_2 as a new ghost cell.

4.2.4 Quadratic Reconstruction

This method is similar to the full linear reconstruction and is given in Tseng and Ferziger (2003) except that it is assumed that ϕ takes the distribution:

$$\phi = a_0 + a_1x + a_2y + a_3x^2 + a_4xy + a_5y^2 \tag{4.11}$$

By using the positions and values of ϕ at the five nearest fluid nodes and the boundary point, the coefficients can be found from the matrix equation:

$$a = B^{-1}\phi \tag{4.12}$$

where:

$$B = \begin{bmatrix} 1 & x_O & y_O & x_O^2 & x_O y_O & y_O^2 \\ 1 & x_{X_1} & y_{X_1} & x_{X_1}^2 & x_{X_1} y_{X_1} & y_{X_1}^2 \\ \cdots & \cdots & \cdots & \cdots & \cdots & \cdots \\ 1 & x_{X_5} & y_{X_5} & x_{X_5}^2 & x_{X_5} y_{X_5} & y_{X_5}^2 \end{bmatrix} \tag{4.13}$$

$$\phi = \begin{bmatrix} \phi_O \\ \phi_{X_1} \\ \vdots \\ \phi_{X_5} \end{bmatrix} \tag{4.14}$$

Assuming that the value of ϕ at any point can be written as a weighted combination of the values of ϕ at the nearby points, a relation for ϕ is given by:

$$\phi = C_{X_1}\phi_{X_1} + C_{X_2}\phi_{X_2} + C_{X_3}\phi_{X3} + C_{X_4}\phi_{X_4} + C_{X_5}\phi_{X_5} + C_O\phi_O \tag{4.15}$$

The coefficients can then be found from the above matrix equation.

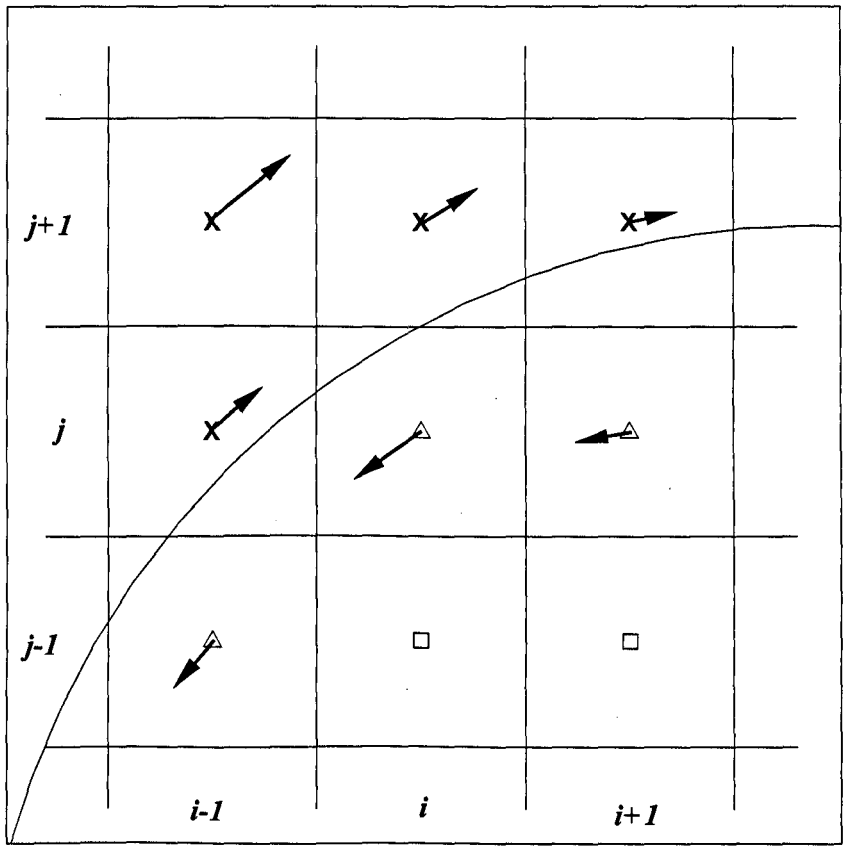

Figure 4.2: The Immersed Boundary Method: × Fluid cell, □ Solid Cell, △ Ghost Cell

4.3 Applying the boundary conditions

Once the coefficients for each ghost cell have been ascertained, the flow properties at the ghost cells need to be calculated and applied. Most methods covered in the previous section incorporate some form of forcing term within the original flow equations at the ghost cell. This effectively maintains the ghost cell as a fluid node and so means that the flow properties there are open to influence from fluid nodes outside of the solid surface.

In this study, a SIMPLE pressure-correction code is being used so allowing each velocity and pressure component to be solved separately. This means that each ghost cell can be applied sequentially for each velocity and for the pressure and as a TDMA

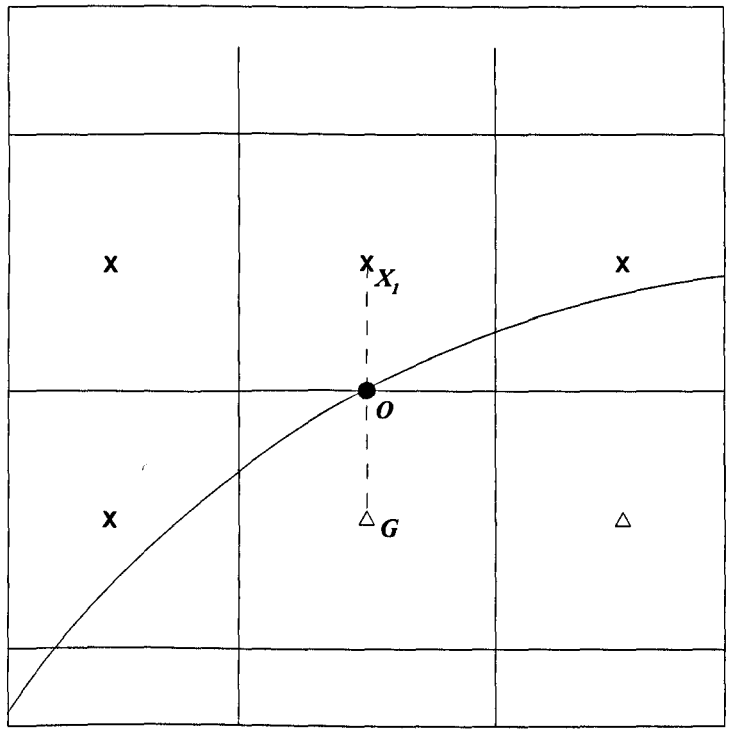

Figure 4.3: Simple Linear Reconstruction

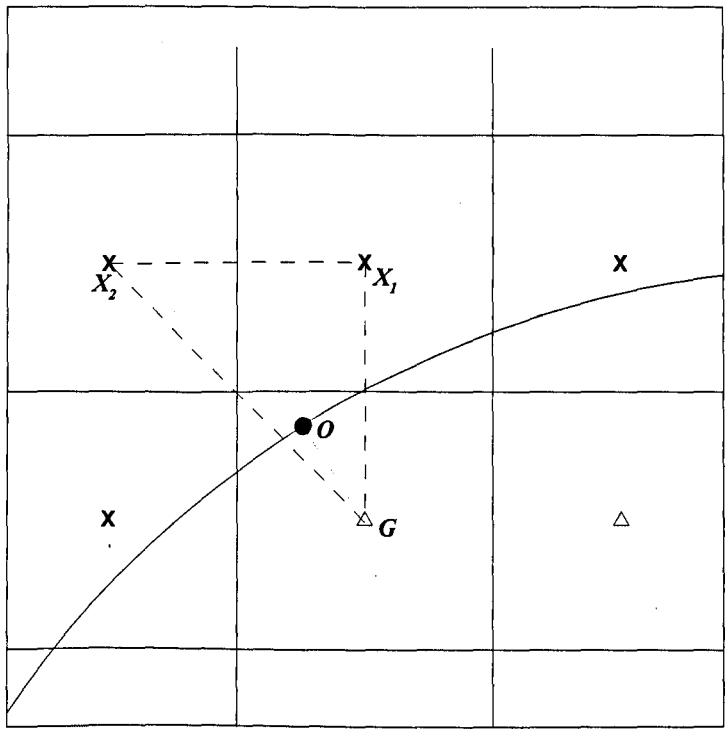

Figure 4.4: Full Linear Reconstruction

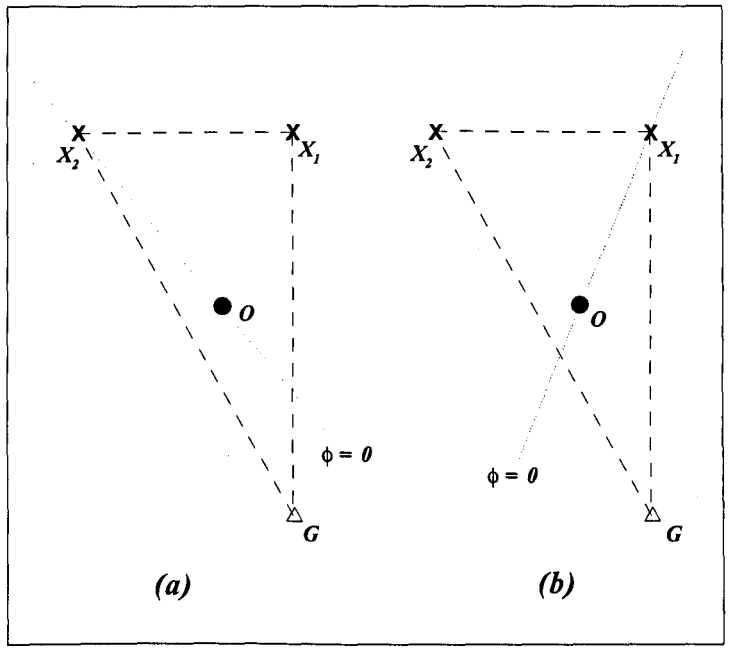

Figure 4.5: Why the coefficients are negative

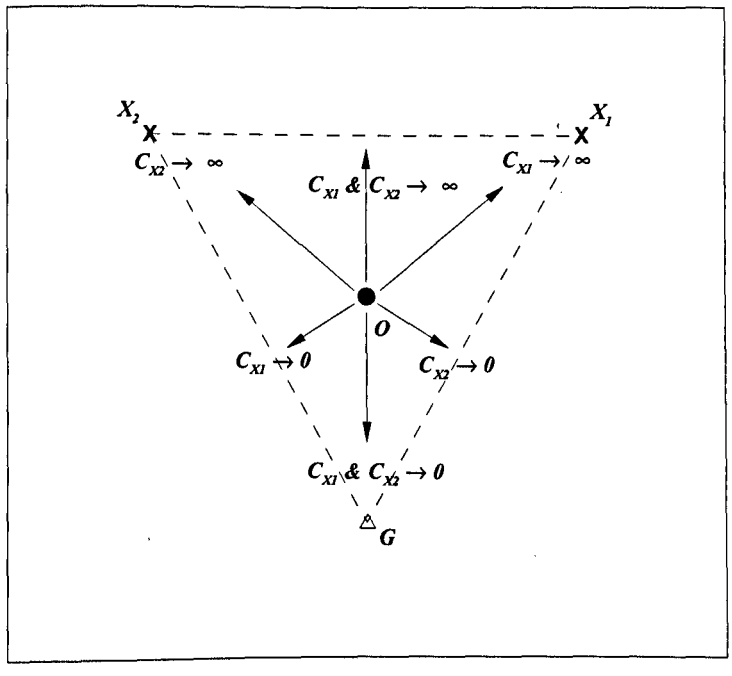

Figure 4.6: The behaviour of the coefficients

solver subroutine is to be used, the ghost cell properties can be applied directly within that solver.

In order to take advantage of this, an original method for applying the ghost cell values has been proposed. This involves isolating the ghost cells numerically by setting all local coefficients to zero and then applying the required ghost cell property using the source term. This can be seen by first considering the discretized flow equation:

$$A_p\phi_p = A_n\phi_n + A_s\phi_s + A_e\phi_e + A_w\phi_w + S_\phi \tag{4.16}$$

The coefficients at the ghost cell are then set as $A_p = 1$, $A_n, A_s, A_e, A_w = 0$ and $S_\phi = \phi_G$. This has the effect of allowing the ghost cells to be isolated from local nodes and allows them to be forced exactly without any additional instability criterion being produced. Considering the flow solver equations as given in Section 3.1.3 this leads to the relationship:

$$\phi_p = \phi_G \tag{4.17}$$

To allow the ghost cell values to continually update the position of the boundary, this process is updated for every sweep of the solver algorithm. This means that at most, the ghost cell values of velocity or pressure should never be more than one sub-iteration behind the main fluid simulation. This has the advantage over the other methods detailed as it allows the ghost cell properties to be adjusted almost as quickly as the flow solution is calculated so preserving a more accurate surface.

4.3.1 Pressure Treatment

When first applying the immersed boundary method, the pressure was originally allowed to vary according to the local flow field without any interference from the method. Whilst this produced acceptable results, there were areas of high pressure within the surface as a result of continuity violations due to ghost cell values being forced directly.

As mentioned previously, this is to be expected as the ghost cells will be automatically adjusted to suit the local flow without regard for any preservation of continuity.

A more straightforward method was formulated based on the ideas of Tseng and Ferziger (2003). This method assumed that the pressure would not vary appreciably in the wall normal direction and so the pressure at the ghost cells could be set to a value depending on the local pressure field.

This was done by using two external fluid nodes, X_1 and X_2 (Figure 4.4) as covered in the full linear method detailed in Section 4.2.3. The pressure at the ghost cell is then taken to be a weighted combination of the pressures at points X_1 and X_2. For example, if the surface point lies on the line between the ghost cell and point X_1 then the pressure at the ghost cell will equal the pressure at X_1. Likewise, if the surface lies on a line between X_2 and G, the pressure there will then be applied to the ghost cell. Between these two extremes, the pressure is a weighted combination of the two.

This method was found to eliminate large pressure spots within the surface and so allowed a much more accurate surface to be modelled. It also made a large difference in measuring the pressure coefficient at the surface as large internal pressures were now no longer present.

4.3.2 The Staggered Grid Formulation

Up until this point, it has been assumed that ghost cells for all of the velocity components and the pressure have been coincident. However, for the code used in this work (and for many codes being used in research and industry) a staggered grid system is used for the ease of pressure convergence.

This does not preclude the use of immersed boundary methods but does require additional work to be done. The main change is that the ghost cell positions and coefficients need to be calculated for each grid system at the beginning of the simulation. For a typical three dimensional simulation, this equates to three velocity components and a pressure grid so requiring four times more effort in calculation. These parameters will also need storage for later use so increasing the memory requirements for these parameters by a factor of four. However, considering that even a complex geometry and fine grid will only require around ten minutes to initialize itself then this increase in time required is negligible compared to the overall time of the simulation.

4.4 Validation

This section discusses the validation of the above IBMs using a number of different test cases. The flow around a circular cylinder is a good test of the Immersed Boundary Method as it allows the evaluation of the modelling of a surface at every possible angle to the grid mesh. In addition, many other works have employed this as a validation case namely Liu *et al.* (1998), Ye *et al.* (1999), Kim *et al.* (2001), Tseng and Ferziger (2003), & Huang and Sung (2005)

Two cases have been run in order to test the ability of the IBM to handle different flow regimes. Firstly, the case of Reynolds number (based on cylinder diameter) at 40 is run to test the method on a steady laminar flow. Secondly, the flow at a Reynolds number of 100 is run in order to test the method for an unsteady flow. The exact dimensions of the problem domain are shown in Figure 4.7. The cylinder diameter is 1.58mm and the freestream velocity is varied from 0.368m/s for the $Re = 40$ case to 0.92m/s for the $Re = 100$ case. The results for the $Re_D = 40$ case will now be considered followed by the unsteady results of $Re_D = 100$.

4.4.1 Steady Flow around a circular cylinder ($Re_D = 40$)

The flow around a circular cylinder at a Reynolds number based on diameter (Re_D) of 40 has been well documented both experimentally and numerically over the years. The work by Taneda (1956) is especially relevant and details how the flow at this Reynolds number consists of two entrained vortices trapped behind the cylinder. This is shown photographically in Figure 2(a) of Taneda (1956) and has been reproduced in Figure 4.8. From this figure, it can be seen that the dimensionless wake length L_w/D is around 2.3.

The drag on circular cylinders in this regime has also been well documented, and can be quantified by the drag coefficient, C_D as:

$$C_D = \frac{F_D}{\frac{1}{2}\rho U_\infty^2 l D} \tag{4.18}$$

where F_D is the total drag force, ρ is the air density, U_∞ is the freestream velocity D is the cylinder diameter and l is the length of the cylinder span. In the region of $Re_D = 40$ the drag coefficient decreases steadily, as shown in Figure 4.9. For $Re_D = 40$, the drag coefficient is estimated to be around 1.6.

To simulate this case, the four different immersed boundary methods were employed on four different grids, in order to investigate both the accuracy of the methods and how they compare when the grid is coarsened. The grid system is generally square in the vicinity of the cylinder with grid expansions, and contractions occuring around this uniform region in order to save computational resources. The grid set-up is shown in Figure 4.10.

In detail; the computational domain extends 15 diameters upstream and 35 diameters downstream, whilst extending 15 diameters either side of the cylinder in the cross-stream direction. The uniform region around the cylinder extends 2.5 diameters upsteam and downstream and 1.5 diameters either side of the cylinder in the cross-stream direction.

The grid dimensions investigated consisted of 5, 10, 15 and 20 nodes across the diameter of the cylinder. Further details of these grids are given in Table 4.1

Beginning with the finest grid, (i.e. 20 nodes across the diameter), Figure 4.11 shows some initial results for the overall flow pattern around the cylinder for each of the methods. It is clear that there is little difference in results far away from the cylinder

Table 4.1: Grid Properties

	Nodes/Diameter	Uniform Mesh	Total Mesh	Mesh count
Grid 01	5	25×15	76×38	2888
Grid 02	10	50×30	151×76	11476
Grid 03	15	75×45	228×114	25992
Grid 04	20	100×60	301×152	45752

surface. There is a slight difference in the wake length between the methods, with the values varying from 2.35 for solid block and simple linear methods, down to 2.3 and 2.29 for full linear and quadratic methods respectively.

With regard to the forces on the cylinder, the pressure coefficient distribution for this fine grid system is shown in Figure 4.12. For the purpose of this work, the pressure coefficient is defined as:

$$C_p = \frac{p - p_s}{\frac{1}{2}\rho U_\infty^2} \tag{4.19}$$

where p_s is the stagnation pressure at the front of the cylinder.

The results all lie fairly close, although the results for the solid block approximation are slightly higher than the other immersed boundary methods. This is shown out in the pressure drag coefficients which are calculated to vary from 1.66 for the solid block approximation through 1.61 for the simple linear method to around 1.58 for both the full linear and the quadratic methods.

It should be noted that these pressure drag coefficients are calculated using the above detailed pressure distributions so sum-up the pressure forces around the surface

of the cylinder. The surface forces in the streamwise, x-direction are then taken to be components of the pressure drag force. However, this coefficient does not take into account the drag forces produced by surface friction.

It appears that the fine grid offers very similar results, regardless of the immersed boundary method used. This provides a starting point from which a coarsening of the grid can take place and the respective results compared. Running the coarser grids yields the pressure distributions shown in Figures 4.13-4.15. Compared to the fine grid results in Figure 4.12 it can be seen that the coarser the grid gets, the more divergence there is between the different methods. This is intuitive as, for any immersed boundary methods, there will come a grid that is so coarse that realistic answers are no longer produced.

It is also interesting to note that the higher the order of the method, the less the results change as the grid becomes coarser. This is shown in the pressure distributions given in Figures 4.16 - 4.19, where each method is shown in isolation with the different grids available for comparison. This is a key feature of IBMs as any method will produce an adequate result if the grid is fine enough. The higher the order of IBM, the more robust the solution becomes for a coarser grid.

Calculating drag coefficients from these pressure distributions, a summary of the results can be seen in Figure 4.20 and Table 4.2. It is clear from these results that the higher the order of the method, the closer the result comes to estimating the correct drag coefficient which is shown by the dashed line in Figure 4.20 and was taken from Tritton (1977) reproduced in Figure 4.9. In fact, for the simple solid block approximation, the drag coefficient is the least accurate even for the finest grid case. On the other hand, the full linear and quadratic IBMs produce accurate results for even the $n/D = 10$ grid system.

Study	C_D	L_w/D
Solid Block Approximation	1.66	2.35
Simple Linear IBM	1.61	2.35
Full Linear IBM	1.58	2.30
Quadratic IBM	1.58	2.29
Other works		
Taneda (1956)	-	2.27
Huang and Sung (2005)	1.56	2.27
Tseng and Ferziger (2003)	1.53	2.21
Kim *et al.* (2001)	1.51	-
Ye *et al.* (1999)	1.52	2.27

Table 4.2: Table of results for Re=40 for the finest grid spacing (D/20)

4.4.2 Unsteady Flow around a circular cylinder ($Re_D = 100$)

For the $Re_D = 100$ case the flow is more complex. Although still laminar, at this Reynolds number the previously entrained vortices become unstable and start to shed alternately from the top and bottom surfaces of the cylinder. This effect is shown in the sequence of vorticity contour plots shown in Figure 4.21, and it is clear that vortices of opposing polarity are shed alternately downstream.

This shedding is dominated by a single shedding frequency which can be characterised by the Strouhal number thus:

$$St = \frac{fD}{U} \tag{4.20}$$

where f is the shedding frequency, D is the diameter of the cylinder and U is the freestream velocity.

This case has been well documented by Williamson and Brown (1998), who proposed the following relationship between Reynolds number and Strouhal number for the interval of $50 < Re_D < 200$:

$$St = 0.285 - \frac{1.3897}{\sqrt{Re_D}} + \frac{1.8061}{Re_D} \tag{4.21}$$

This yields a Strouhal number of around 0.165 for the $Re_D = 100$ case. The purpose of using the $Re_D = 100$ case for validation of the Immersed Boundary Method is to assess the ability of the surface definition to be maintained, even when the local velocity is constantly changing as would be the case within a turbulent separation control situation.

Initial results using the finest grid are shown in Table 4.3 below. The first point of interest is that the Strouhal number does not seem very sensitive to the IBM being used. This would make sense, in that the IBM method is concerned with modelling the surface more accurately yet the shedding of vortices is largely a factor of the flow around the object. For example, a square or hexagonal cylinder of similar dimensions is likely to shed vortices at a similar frequency to the circular cylinder case. The Strouhal numbers are all within 5% of the value predicted by Williamson and Brown (1998).

The time-averaged drag coefficient, $(C_D)_{ave}$, shows more variation with over-estimated values for the solid-block approximation whilst the higher order methods improve this result. However even the quadratic method still over-estimates the value by around 6% of the closest results, those given in Lai and Peskin (2000). Finally, whilst there is no actual lift produced by this flow, (as the flow is symmetrical in y making the mean lift coefficient over time is zero) the root mean square (RMS) values for the time varying lift coefficients, $(C_L)_{rms}$, have been calculated. This is done in the same way as for the drag coefficients but using the force contributions in the y-direction instead. The results given for $(C_L)_{rms}$ are promising with the solid-block approximation over-estimating the value whilst the quadratic method is very close to the results given by Lai and Peskin (2000) and Dias and Majumdar (1999).

In general, then, it can be seen that the higher the order of the method, the more accurately each of the parameters tends to be calculated. Considering the effects of grid refinement, the above results have been duplicated and are shown in Figures 4.22-4.24. Figure 4.22 shows the change in Strouhal number for the given Immersed Boundary Methods over a series of grid meshes as given in the previous section. It is clear that as the grid is refined, the Strouhal number settles down towards the value given in Williamson and Brown (1998) shown by the dashed line. There is little difference

Study	St	$(C_D)_{ave}$	$(C_L)_{rms}$
Grid D/20			
Solid Block Approximation	0.154	1.77	0.35
Simple Linear IBM	0.159	1.63	0.31
Full Linear IBM	0.154	1.59	0.31
Quadratic IBM	0.160	1.54	0.28
Tseng and Ferziger (2003)	0.164	1.42	0.29
Kim *et al.* (2001)	0.165	1.33	-
Lai and Peskin (2000)	0.165	1.45	0.33
Dias and Majumdar (1999)	0.171	1.40	0.28
Williamson and Brown (1998)	0.166	-	-

Table 4.3: Table of results for Re=100 for the finest grid spacing (D/20)

between the methods themselves although this difference does increase as the grid is coarsened.

Another point of note is that for the coarsest grid, the simple linear method was unstable. This is most likely due to the fact that with few ghost cells, each one has more effect on the overall simulation. However, for the simple linear method, these ghost cells are only influenced by one fluid node. This lack of control is likely to cause the simulation to be less stable so explaining why the full linear and quadratic methods are fully stable even for such a coarse grid.

Considering the drag coefficients, Figure 4.23 shows the effect of the grid refinement

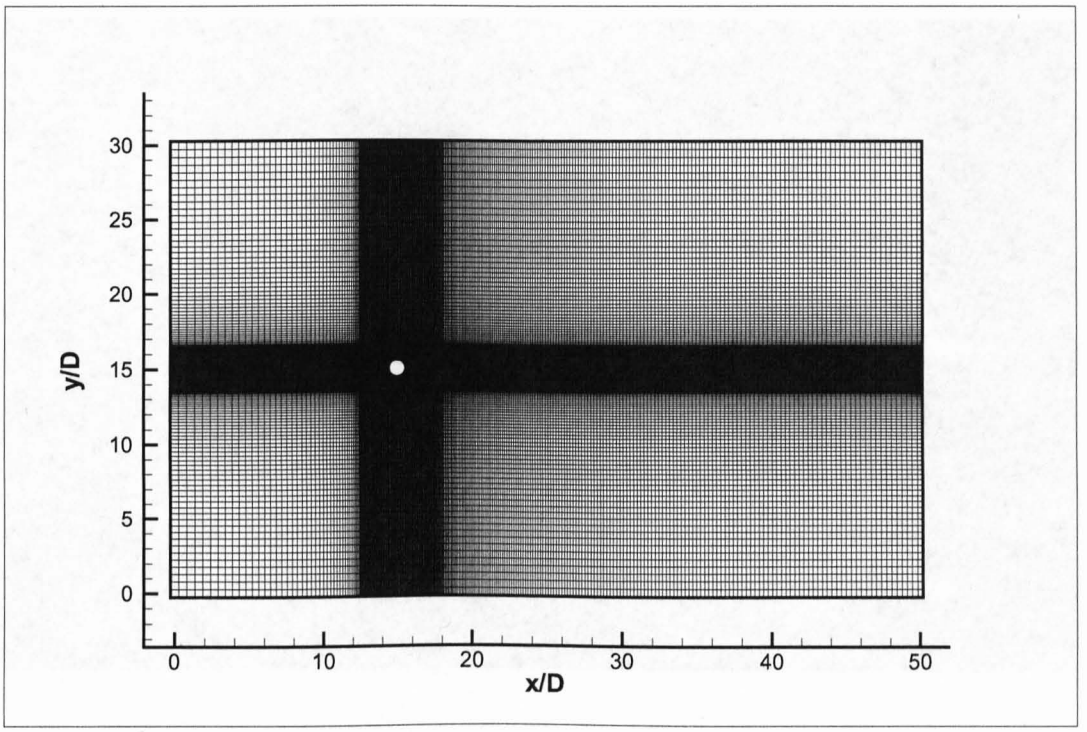

Figure 4.7: Set-up for the circular cylinder validation simulations

and this seems to indicate that the drag coefficients have converged on a final value for the finest grids. As with the results for $Re = 40$, the final drag coefficient is much reduced as a higher order IBM is used. In fact, the full linear and quadratic method results are actually very similar.

Finally, the lift coefficients given in Figure 4.24 show a very similar result to the drag coefficients although there is a slight undershoot with the finest grid slightly higher than the previous grid results. This is very small and is probably due to other computational factors rather than simply the IBM used.

In general, it is seen that the benefits of using an Immersed Boundary Method are maintained even for an unsteady flow, and that the simulation is not made unstable by the addition of such a method.

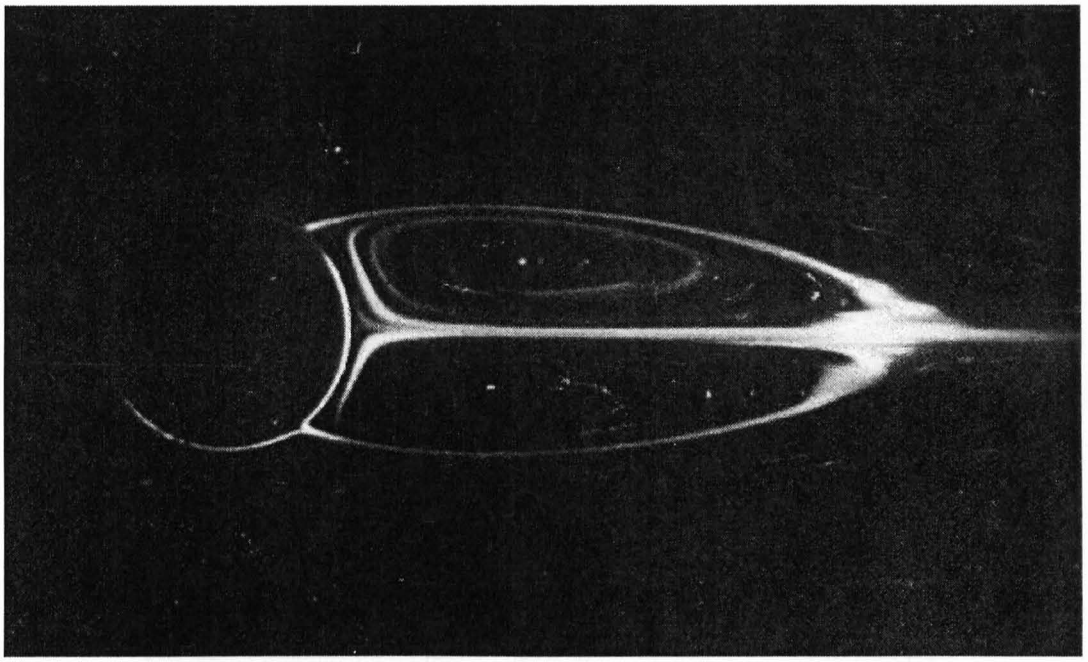

Figure 4.8: Experimental Results of flow around a circular cylinder at $Re_D = 41$ (Taken from Taneda (1956))

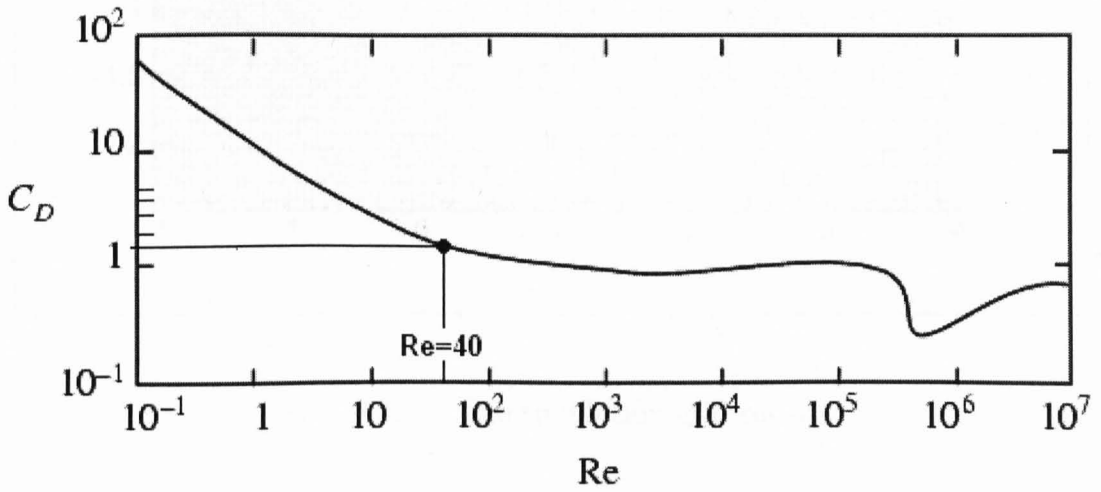

Figure 4.9: Drag coefficients for a circular cylinder with $10^{-1} < Re_D < 10^7$ (Taken from Tritton (1977))

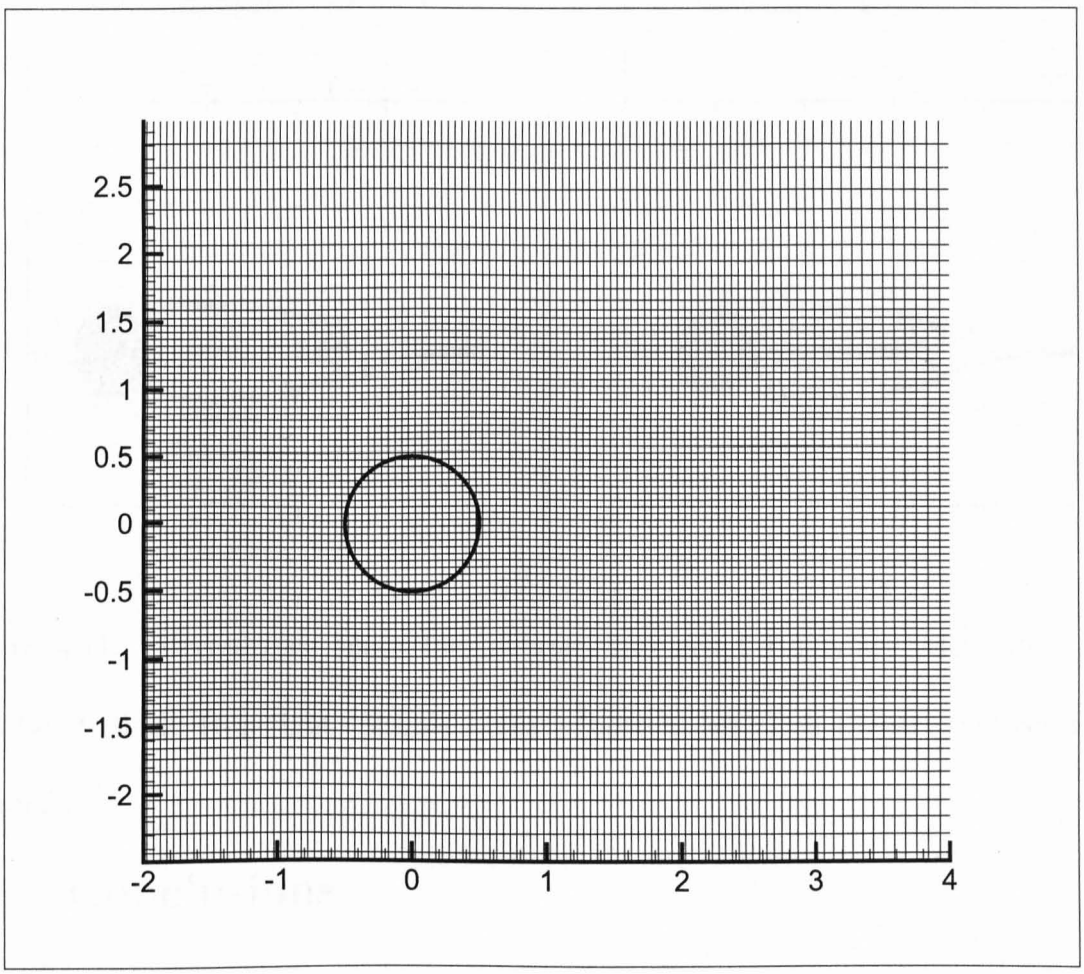

Figure 4.10: The simulation grid set-up

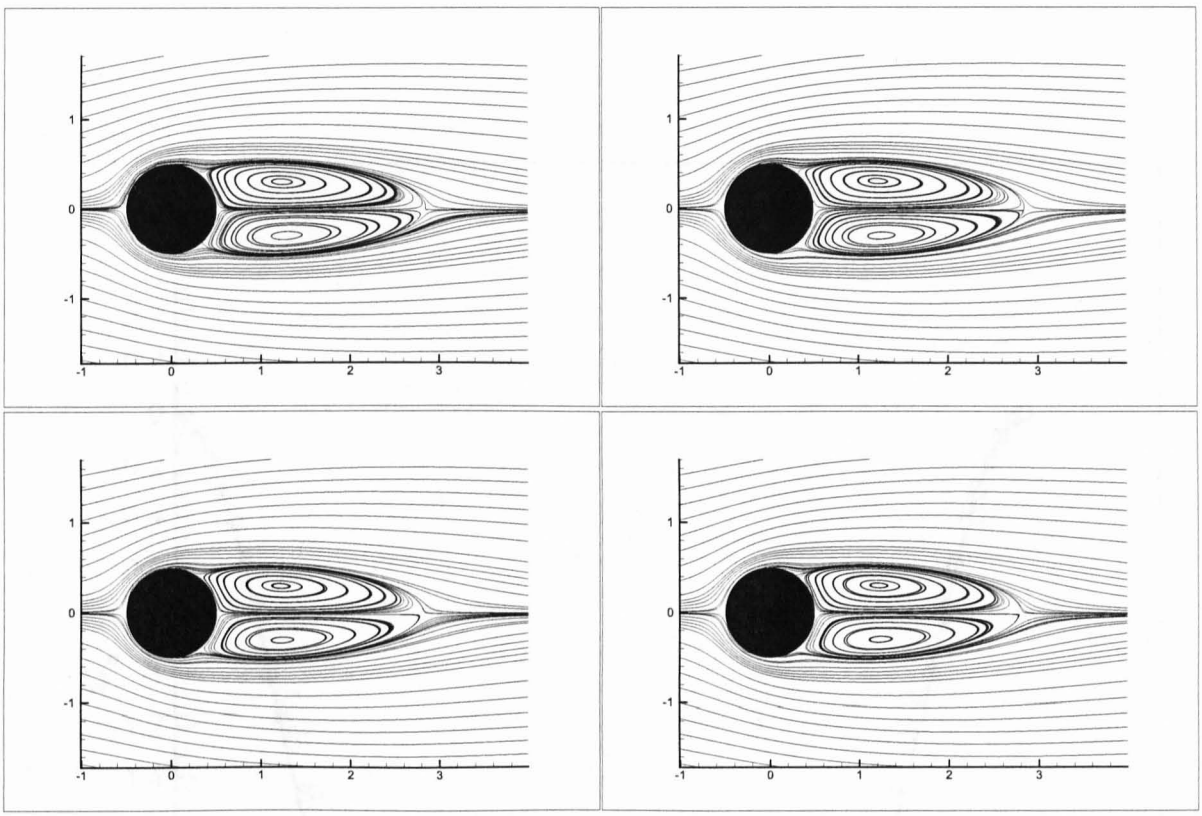

Figure 4.11: Streamtrace plots for different Immersed Boundary Methods: (top-left) Solid Block, (top-right) Simple Linear, (bottom-left) Full Linear, (bottom-right) Quadratic

4.5 Conclusions

A brief history of the development of Immersed Boundary Methods has been presented followed by an in depth breakdown of the theory behind such methods. A validation case of the flow around a circular cylinder was then given for steady flow ($Re = 40$) and unsteady flow ($Re = 100$).

In general, it was seen that for any given grid mesh, an Immersed Boundary Method will bring the results closer to their final converged value with the higher order

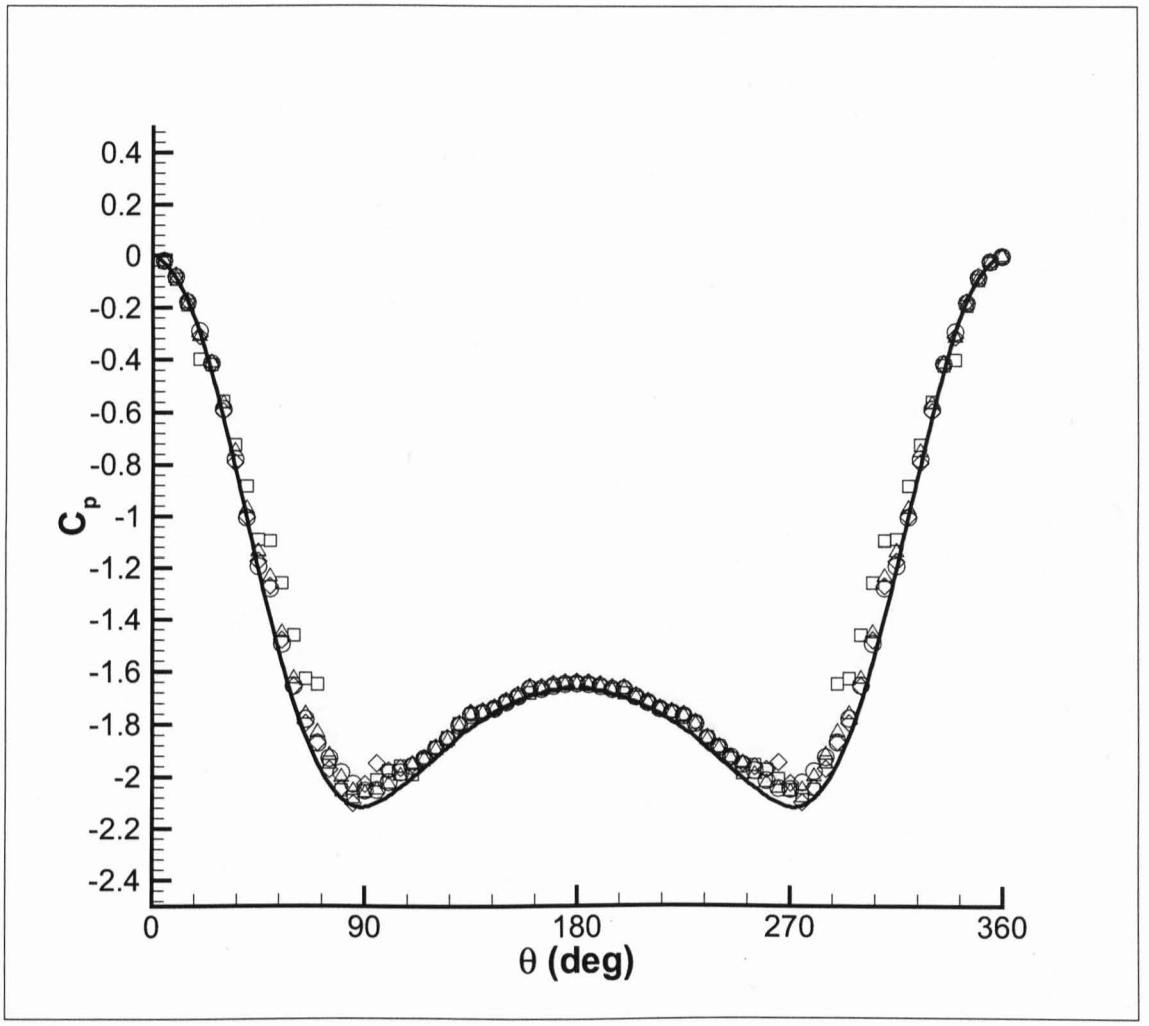

Figure 4.12: Pressure Distribution around the cylinder at $Re_D = 40$ for the finest grid, G04 (D/20) □ Solid Block △ Simple linear, ◇ Full linear, ○ Quadratic, Solid Line: Body fitted computation of Tseng and Ferziger (2003)

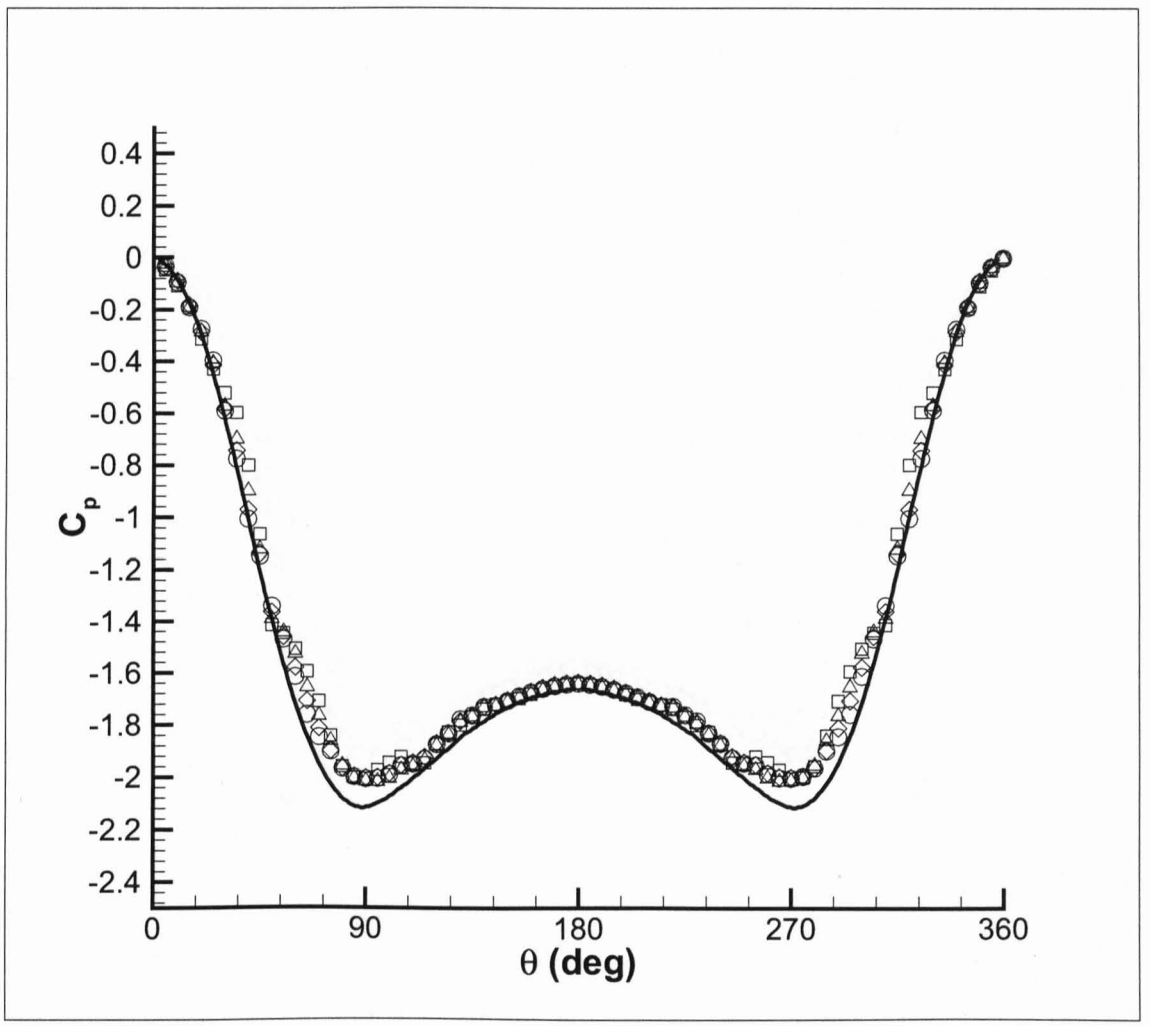

Figure 4.13: Pressure Distribution around the cylinder at $Re_D = 40$ for the intermediate-fine grid, G03 (D/15) □ Solid Block △ Simple linear, ◇ Full linear, ○ Quadratic, Solid Line: Body fitted computation of Tseng and Ferziger (2003)

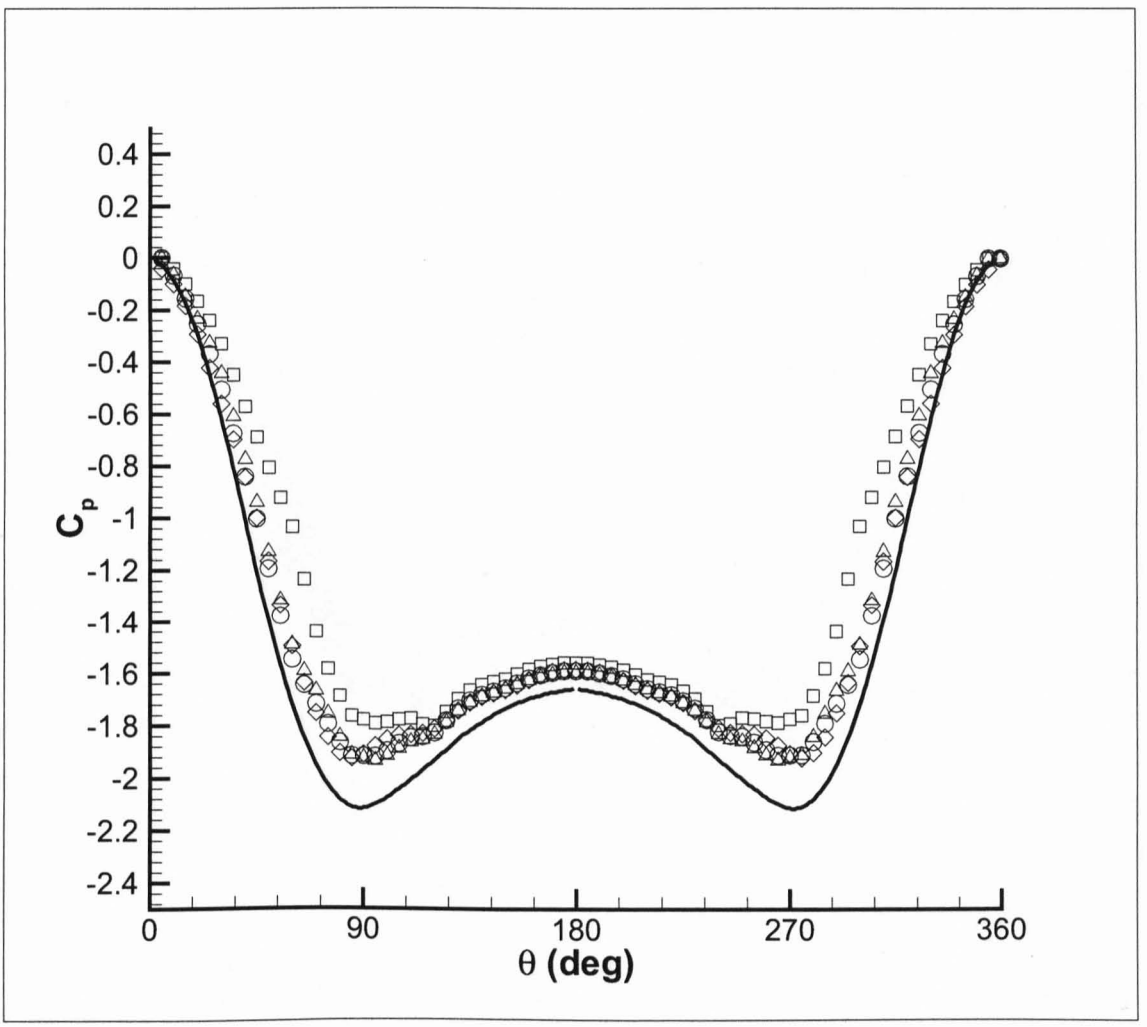

Figure 4.14: Pressure Distribution around the cylinder at $Re_D = 40$ for the intermediate-coarse grid, G02 (D/10) □ Solid Block △ Simple linear, ◇ Full linear, ○ Quadratic, Solid Line: Body fitted computation of Tseng and Ferziger (2003)

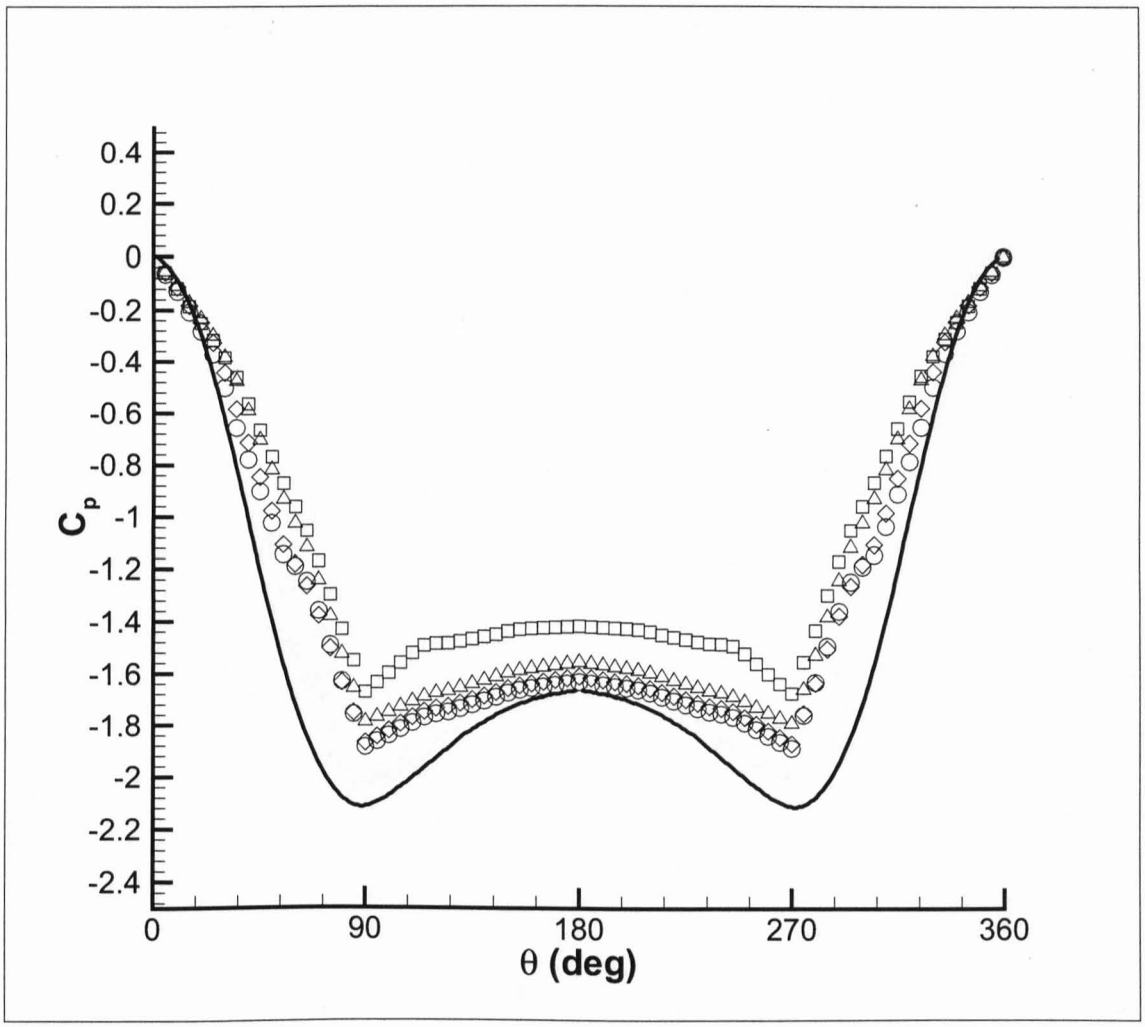

Figure 4.15: Pressure Distribution around the cylinder at $Re_D = 40$ for the coarsest grid, G01 (D/5) □ Solid Block △ Simple linear, ◇ Full linear, ○ Quadratic, Solid Line: Body fitted computation of Tseng and Ferziger (2003)

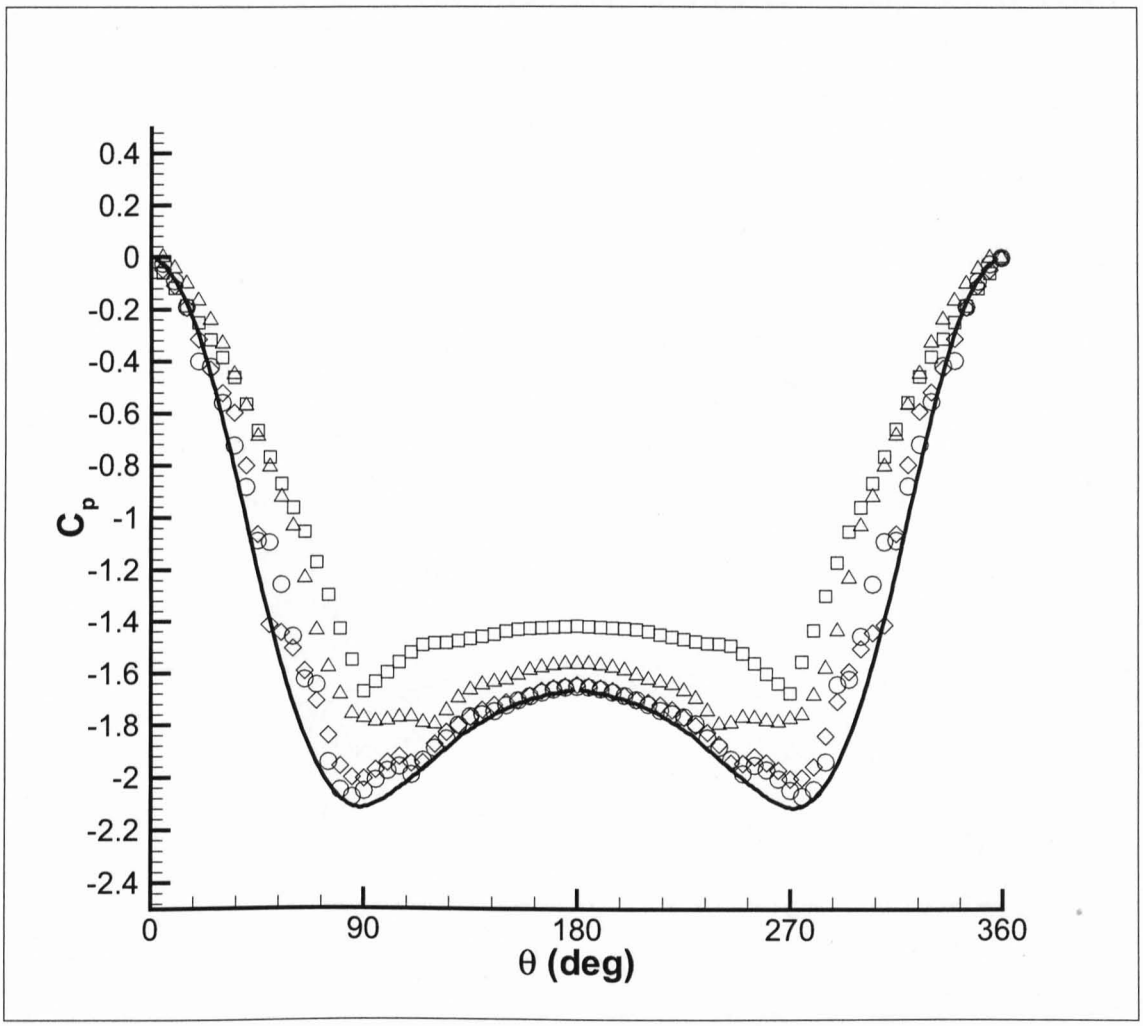

Figure 4.16: Pressure Distribution around the cylinder at $Re_D = 40$ for the solid block approximation: □ Grid 01 (D/5) △ Grid 02 (D/10), ◇ Grid 03 (D/15), ○ Grid 04 (D/20), Solid Line: Body fitted computation of Tseng and Ferziger (2003)

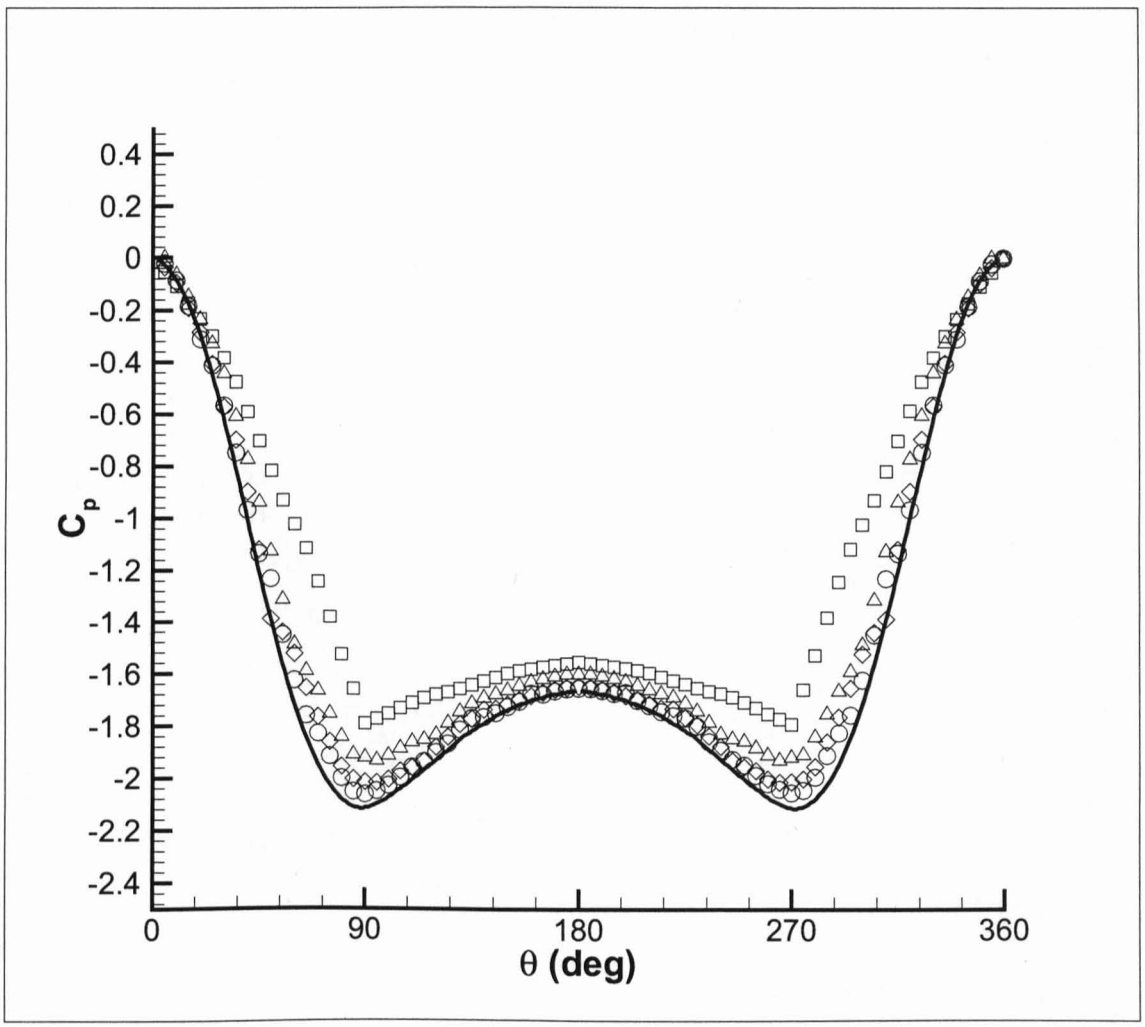

Figure 4.17: Pressure Distribution around the cylinder at $Re_D = 40$ for simple linear method: □ Grid 01 (D/5) △ Grid 02 (D/10), ◇ Grid 03 (D/15), ○ Grid 04 (D/20), Solid Line: Body fitted computation of Tseng and Ferziger (2003)

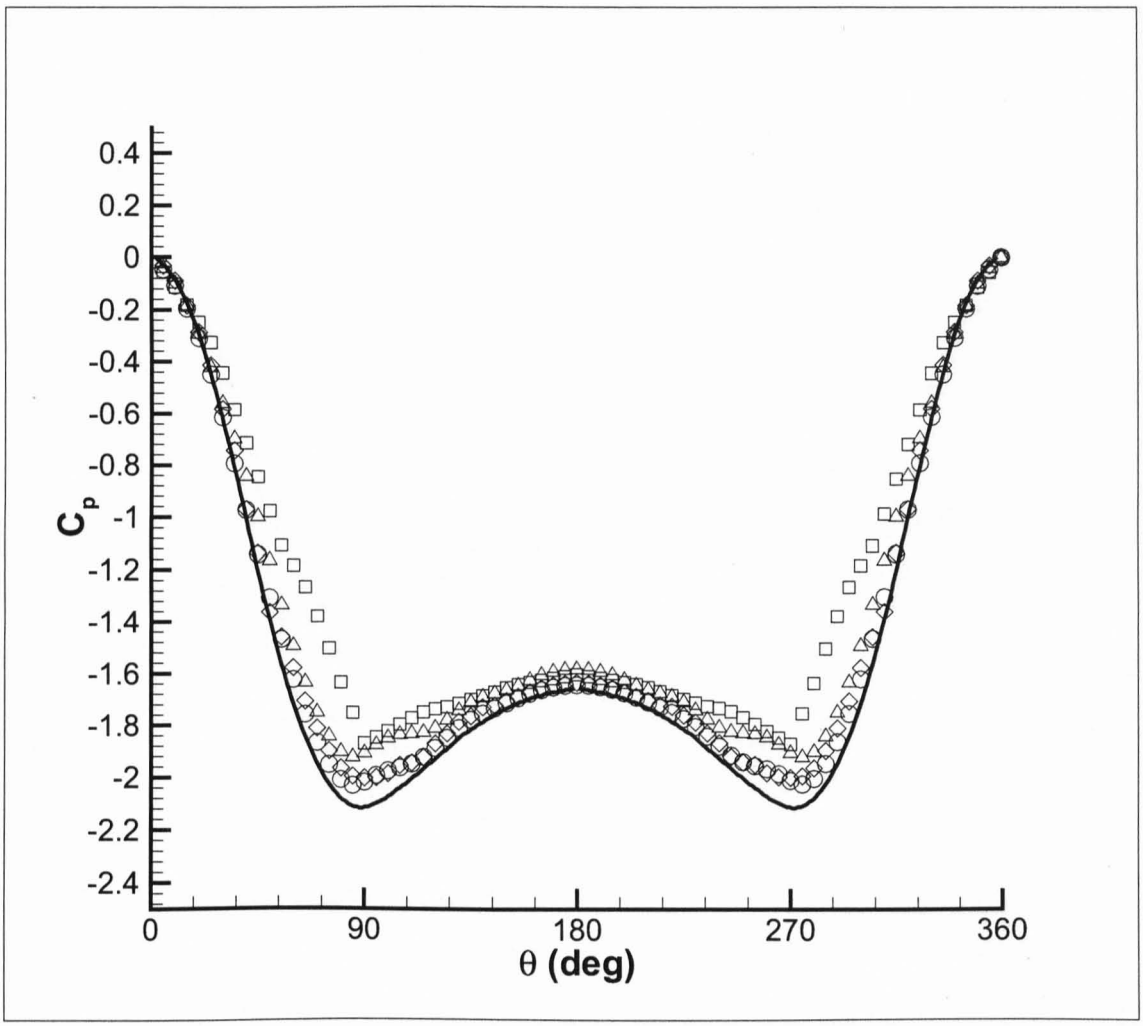

Figure 4.18: Pressure Distribution around the cylinder at $Re_D = 40$ for the full linear method: □ 718 Grid 01 (D/5) △ Grid 02 (D/10), ◇ Grid 03 (D/15), ○ Grid 04 (D/20), Solid Line: Body fitted computation of Tseng and Ferziger (2003)

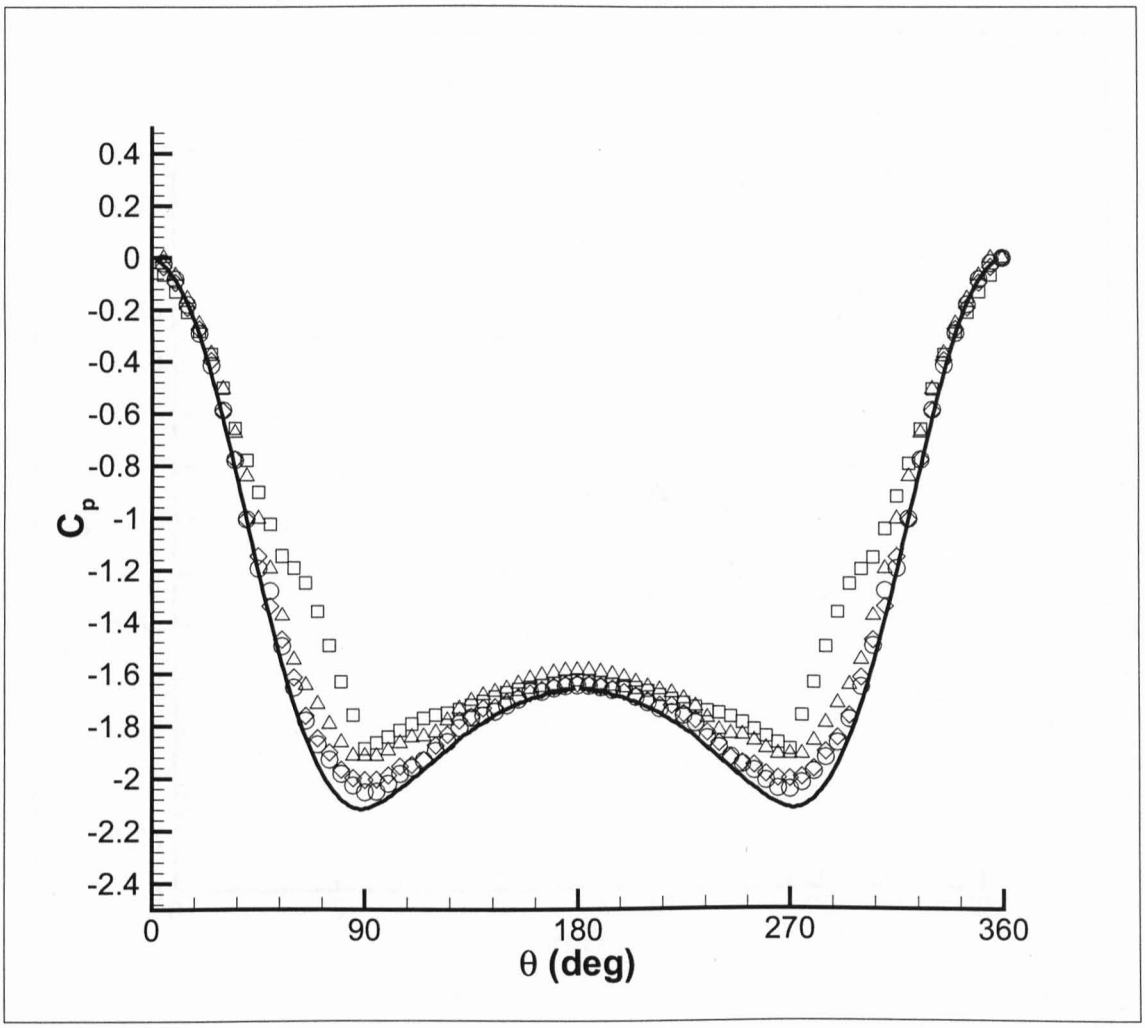

Figure 4.19: Pressure Distribution around the cylinder at $Re_D = 40$ for the quadratic method: □ Grid 01 (D/5) △ Grid 02 (D/10), ◇ Grid 03 (D/15), ○ Grid 04 (D/20), Solid Line: Body fitted computation of Tseng and Ferziger (2003)

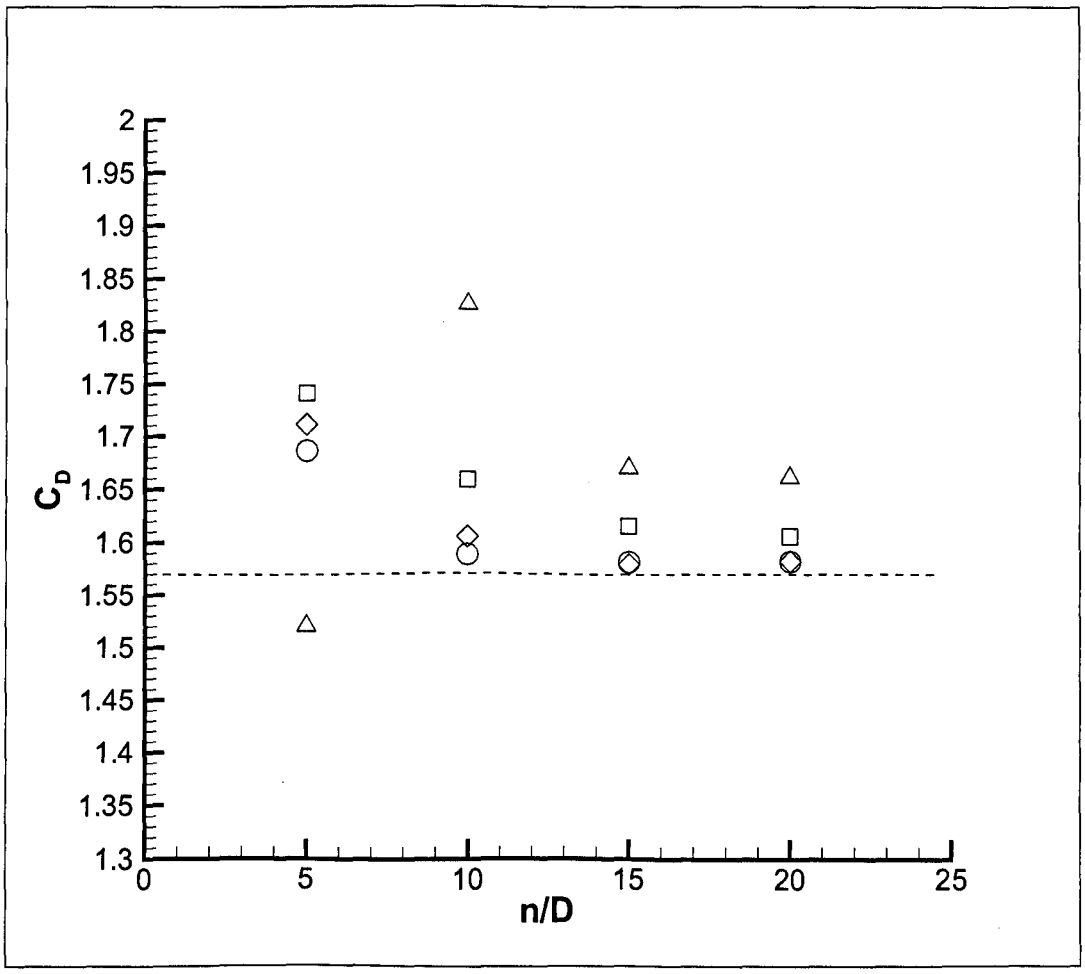

Figure 4.20: Drag coefficient sensitivity to grid mesh & IBM △ Solid Block Approximation, □ Simple Linear Method, ◇ Full Linear Method, ◯ Quadratic Method, Dashed Line: Results from Tritton (1977)

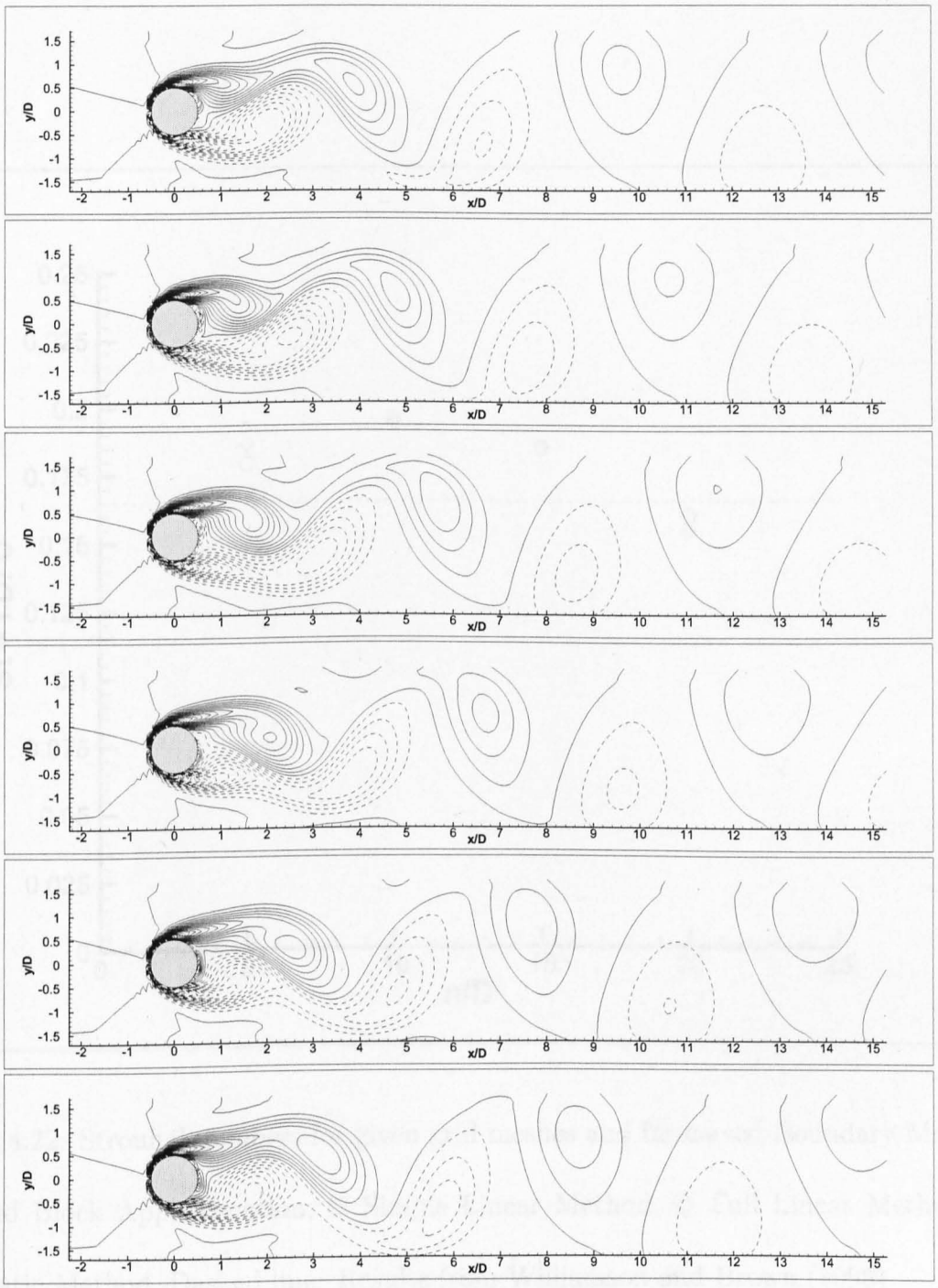

Figure 4.21: Vorticity contours showing a complete cycle of vortex shedding from a cylinder at $Re = 100$. (solid lines: clockwise, dashed lines: anti-clockwise)

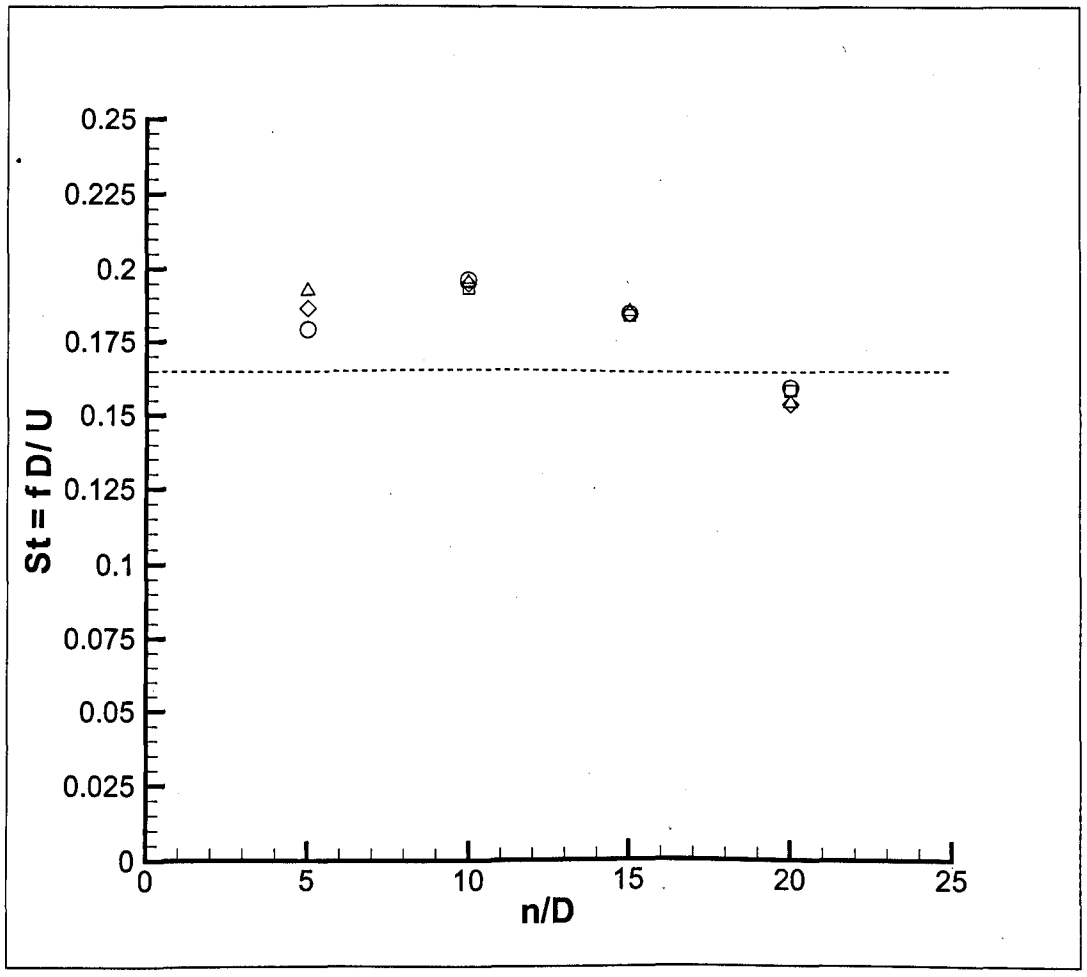

Figure 4.22: Strouhal numbers for given grid meshes and Immersed Boundary Methods △ Solid Block Approximation, □ Simple Linear Method, ◇ Full Linear Method, ○ Quadratic Method, Dashed line: Results from Williamson and Brown (1998)

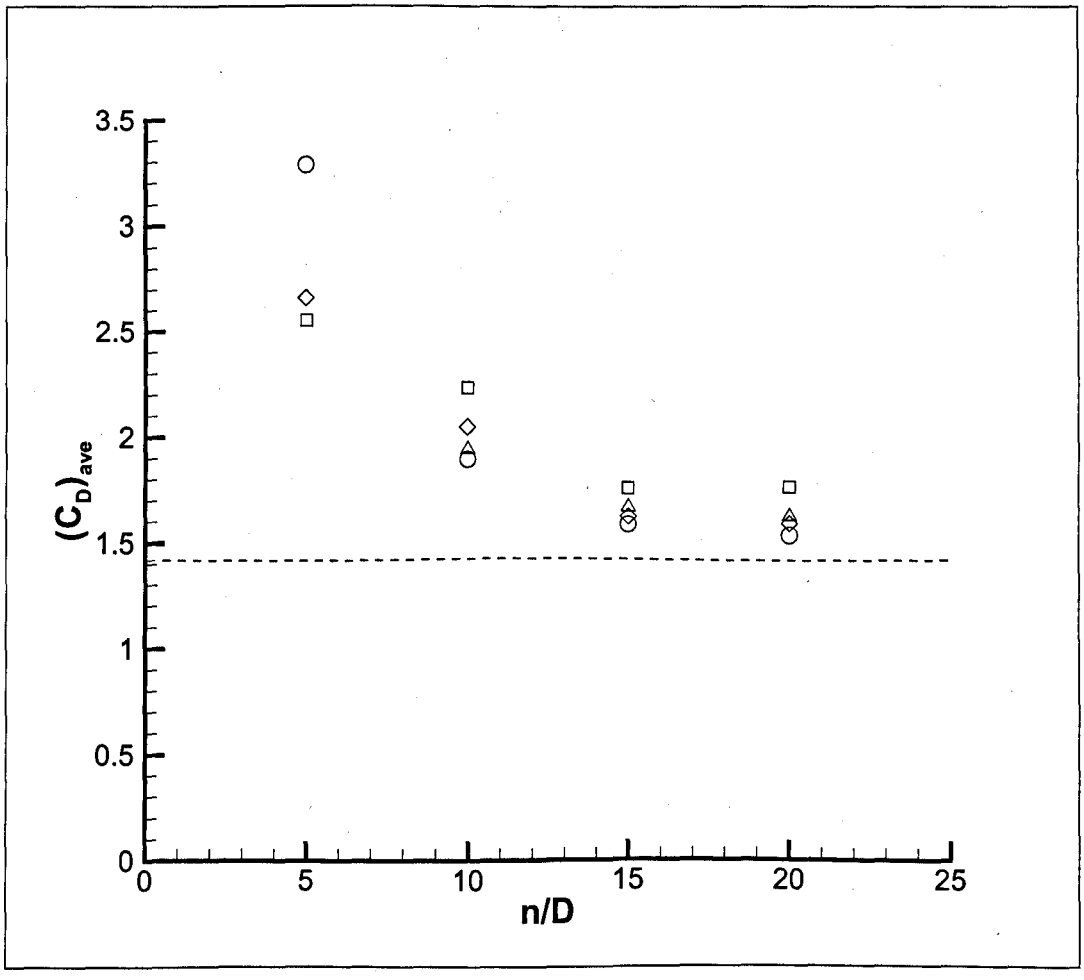

Figure 4.23: Average drag coefficients for given grid meshes and Immersed Boundary Methods □ Solid Block Approximation, △ Simple Linear Method, ◇ Full Linear Method, ○ Quadratic Method, Dashed line: Results from Tseng and Ferziger (2003)

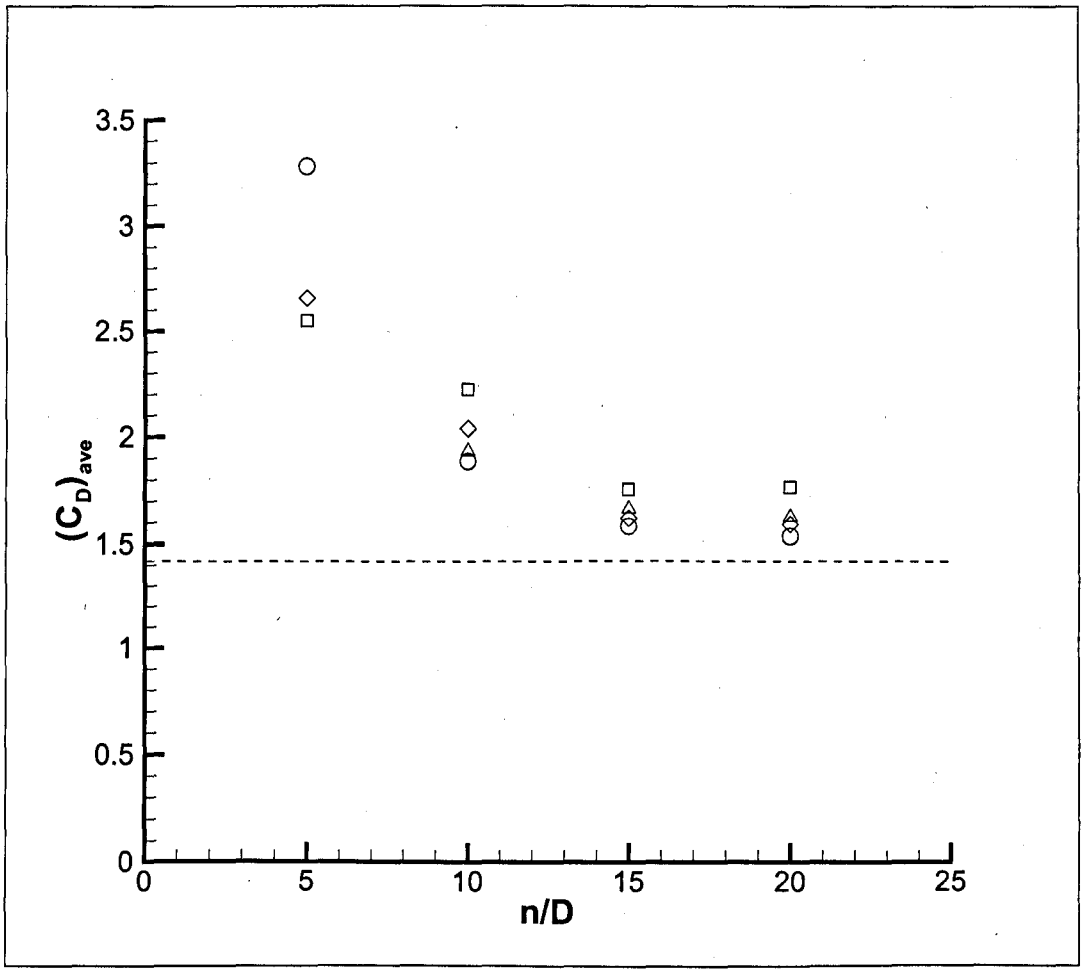

Figure 4.24: RMS lift coefficients for given grid meshes and Immersed Boundary Methods □ Solid Block Approximation, △ Simple Linear Method, ◇ Full Linear Method, ○ Quadratic Method, Dashed line: Results from Tseng and Ferziger (2003)

methods being more effective than the lower order methods. However, this is more true for properties related to the surface flow such as lift or drag coefficients whilst parameters dependent of the total flow around the cylinder such as the recirculation length or shedding frequency were less dependent on the method used. In general, this has the clear advantage of allowing a more accurate simulation to be produced for any particular grid mesh even if the grid only possesses 10 nodes across the object diameter.

As for the novel implementations of the IBM given in this chapter, the results produced for the simulations performed are comparable in accuracy to other published results. This means that the use of coefficients to calculate the ghost cell properties and the implementation of these ghost cell properties directly within the flow solver produce acceptable results. This is achieved without reducing the stability of the simulation although the method remains easy to implement.

Chapter 5

Turbulence Modelling using Wall Functions

With present computing technologies, resolving the extremely complex mechanics of turbulence would take far too long to be of any realistic use. This chapter considers certain methods that can be used in order to simplify the representation of turbulence using engineering CFD and allow accurate results to be produced in a reasonable time frame.

The chapter begins with presenting the need for turbulence modelling followed by an in-depth study of one turbulence model, that of Spalart and Allmaras (1994). This model was chosen as it was to later form the basis for Detached Eddy Simulations (DES) to be covered in Chapter 6. Tests of this model are then done against a turbulent flat plate boundary layer flow and a number of issues influencing its accurate use are considered such as boundary conditions and grid resolution.

A wall-functions approach is then presented as an extension to the basic model of Spalart and Allmaras (1994). This method is based on the work of Kalitzin *et al.* (2005) but has been implemented in an original way to allow its application alongside the immersed boundary method. Finally, the wall functions method is also applied to a turbulent flat plate boundary layer flow and its validity is discussed.

5.1 The need for turbulence modelling

In the field of computational fluid dynamics, turbulent flow represents a very serious challenge. The large range of length and time scales within even modest turbulent flows makes simulation of flows of engineering significance unfeasible using present computing technologies.

Direct numerical simulation (DNS) of turbulent flows has been achieved for very simple cases of modest Reynolds number and allow all turbulent flow structures to be resolved. However these are of little use when considering the typical flows found in most aerospace engineering applications.

Take, for example, the flow over a typical aircraft where the Reynolds number is of the order of 10^8. The grid resolution required to resolve the fine scale turbulence within the boundary layer will require grid spacings in the wall normal direction of around 1 μm. In all, this leads to the number of grid nodes being of the order of 10^{20} (i.e. one hundred, million, billion nodes) This large number of grid nodes leads to somewhere in the region of 10^{20} Floating Point OPerations (or FLOPS) being required for every timestep to be calculated. In order to resolve the time scales involved within the flow, it will probably be necessary to use somewhere in the region of 10^4 timesteps. This means that the total number of FLOPS for the simulation will be of the order of 10^{24}. At the time of writing, the fastest supercomputer in the world, Blue Gene, is capable of calculating around 300 Tflops/s (that is 3×10^{14} flops/s) Even at this speed, 10^{24} FLOPS would still take 3×10^9 seconds or approximately 100 years. A similar analysis is given in Spalart (2000).

In order to get at least some idea of turbulent flows for higher Reynolds numbers, a number of turbulent treatments have been developed. First and foremost are RANS

turbulence models which endeavour to model the apparent increase in viscosity produced by turbulence by modelling an eddy viscosity, typically of the order of 100-1000 times larger than molecular viscosity. The number of models under this banner are manifold and each has its own merits and downfalls. By far the most popular turbulence model is the $k-\varepsilon$ model of Launder and Spalding (1974) which solves equations for the turbulent kinetic energy, k, and the turbulent dissipation, ε in order to calculate a value for the eddy viscosity. This model is well validated and has been used extensively in industry for decades. Whilst far from adequate for investigating fully unsteady turbulence, it allows reasonable approximations of the time averaged behaviour of turbulent flows, something which is very important for estimating average aerodynamical loadings. The principles of turbulence modelling will now be covered.

5.2 Approaching turbulence treatment

The unsteady incompressible continuity and Navier-Stokes equations with constant viscosity are given in Eqns. (5.1) and (5.2) respectively

$$\frac{\partial u_i}{\partial x_i} = 0 \tag{5.1}$$

$$\frac{\partial u_i}{\partial t} + u_j \frac{\partial u_i}{\partial x_j} = -\frac{1}{\rho}\frac{\partial p}{\partial x_i} + \frac{\partial}{\partial x_j}\left(\nu \frac{\partial u_i}{\partial x_j}\right) \tag{5.2}$$

where the Einstein convention has been used.

The unsteady velocity and pressure is then defined as the sum of an average component and a fluctuating component with a time average of zero as shown in Eqns. (5.3a) and (5.3b)

$$u_i = U_i + u_i' \tag{5.3a}$$

$$p_i = P_i + p_i' \tag{5.3b}$$

By substituting Eqns. (5.3a) and (5.3b) into the Navier-Stokes equations, Eqns. (5.1) and (5.2) and averaging over time, the following equations are obtained:

$$\frac{\partial U_i}{\partial x_i} = 0 \tag{5.4}$$

$$\frac{\partial U_i}{\partial t} + U_j \frac{\partial U_i}{\partial x_j} = -\frac{1}{\rho}\frac{\partial P}{\partial x_i} + \frac{\partial}{\partial x_j}\left(\nu \frac{\partial U_i}{\partial x_j} - \overline{u_i' u_j'}\right) \tag{5.5}$$

Although the continuity equation given in Eqn. (5.4) is unchanged the momentum equations in Eqn. (5.5) contains extra terms, $-\overline{u_i' u_j'}$. These terms have the effect of adding additional stresses into the flow and as such are known as 'Reynolds Stresses' whilst these equations are known as the 'Reynolds Averaged Navier-Stokes' or RANS equations. However, there is now a problem of closure as there are extra terms which need to be approximated in order for the equations to be solved. One way to gain closure is to model the Reynolds Stresses and this will now be covered.

5.2.1 Turbulence Modelling

Recall, that Newton's law of viscosity defines the viscous stresses in a Newtonian fluid as:

$$\tau_{ij} = 2\mu S_{ij} = \mu\left(\frac{\partial u_i}{\partial x_j} + \frac{\partial u_j}{\partial x_i}\right) \tag{5.6}$$

In Boussinesq (1877) proposed that the Reynolds stresses could be written in the same way, i.e.

$$\tau_{ij} = -\rho\overline{u_i' u_j'} = \mu_t\left(\frac{\partial U_i}{\partial x_j} + \frac{\partial U_j}{\partial x_i}\right) \tag{5.7}$$

where μ_t is the 'eddy viscosity'. This essentially simplifies the closure problem into one unknown eddy viscosity. A turbulence model can then be used to find the distribution of μ_t within the domain and thus estimate the Reynolds Stresses.

One way of using the RANS equations is to model the Reynolds Stresses directly. There are a series of turbulence models which come under the banner of Reynolds Stress Models (RSM). These models result in solving equations for each of the six Reynolds

stresses and are therefore more computationally expensive than eddy viscosity models. However, these models work much better where there are complex anisotropic stresses in the flow where the eddy viscosity approximation starts to break down.

If the eddy viscosity approximation is adequate, then one of a number of eddy viscosity turbulence models can be used. The mixing length model, first proposed by Prandtl approximates the eddy viscosity using:

$$\mu_t = l_m^2 \left| \frac{\partial U}{\partial y} \right| \tag{5.8}$$

where l_m is some characteristic mixing length within the flow and varies depending on the flow type. For a boundary layer, this is typically the wall distance $l_m = \kappa y$.

As mentioned previously, another eddy viscosity model which is commonly used is the $k - \varepsilon$ model. This model approximates the eddy viscosity using the relation:

$$\mu_t = \rho C_\mu \frac{k^2}{\varepsilon} \tag{5.9}$$

where C_μ is a dimensionless constant, k is the turbulent kinetic energy and ε is the turbulent dissipation. As there is no algebraic approximation for k and ε an extra transport equation for each of these properties needs to be solved. For this reason, this model is classed as a two-equation model.

An important eddy viscosity model of recent years is the Spalart-Allmaras turbulence model of Spalart and Allmaras (1994) and it is this model which will now be covered in greater detail.

5.3 The Spalart-Allmaras (S-A) Turbulence Model

The basic premise behind the Spalart-Allmaras turbulence model (known hereafter as the S-A model) is to solve a single equation for eddy-viscosity within the flow domain. In Spalart and Allmaras (1994), a turbulence model equation for the modified eddy viscosity (denoted by $\tilde{\nu}$) is developed.

This modified eddy viscosity, $\tilde{\nu}$, is equal to the overall eddy viscosity, ν_t, everywhere in the domain except near the wall. As shown in Spalart and Allmaras (1994), ν_t, equals $\kappa y u_\tau$ within the log layer but not within the buffer or viscous sublayer. However, the modified viscosity, $\tilde{\nu}$, equals $\kappa y u_\tau$ all the way to the wall. This has the benefit of making sure the eddy viscosity remains stable near the wall and precludes the need for damping functions for $\tilde{\nu}$.

In Spalart and Allmaras (1994), the model is developed stage by stage in order to show how each of the various terms represent the turbulence mechanisms involved. The full turbulence model contains terms for dealing with free shear flows, boundary-layer flows, near wall flows and laminar transition. For the purpose of this work, however, the laminar transition parts of the model are ignored.

Recall, the Reynolds stresses are related to the shear rate and eddy-viscosity by the relation:

$$-\overline{u_i' u_j'} = 2\nu_t S_{ij} \tag{5.10}$$

For the S-A model, the modified eddy viscosity, $\tilde{\nu}$ is defined as:

$$\nu_t = \tilde{\nu} f_{v1} \tag{5.11}$$

c_{b1}	c_{b2}	σ	c_{w1}	c_{w2}	c_{w3}
0.1355	0.622	0.667	3.95	0.3	2
κ	c_{v1}	c_{t1}	c_{t2}	c_{t3}	c_{t4}
0.41	7.1	1	2	1.2	0.5

Table 5.1: Constants for S-A turbulence model as given in Spalart and Allmaras (1994)

As mentioned, throughout most of the domain this 'S-A viscosity', $\tilde{\nu}$, is equal to the eddy viscosity as f_{v1} tends towards unity away from the wall. This function, f_{v1} will be covered in more detail later.

Taking into account the relevant turbulence mechanisms produces the following model equation for $\tilde{\nu}$:

$$\frac{D\tilde{\nu}}{Dt} = c_{b1}\tilde{S}\tilde{\nu} + \frac{1}{\sigma}\left[\nabla.((\nu+\tilde{\nu})\nabla\tilde{\nu}) + c_{b2}(\nabla\tilde{\nu})^2\right] - c_{w1}f_w\left[\frac{\tilde{\nu}}{d}\right] \tag{5.12}$$

Each of the terms in this equation serves a specific purpose. The left hand side of the equation is the substantive derivative and needs little explanation whilst the constants used are given in Table 5.1.

The first term on the right hand side $c_{b1}\tilde{S}\tilde{\nu}$ incorporates the suffix b to denote that it is a part of the basic model. This term is the main production term of the model and $\tilde{S}$ is the modified vorticity, given by:

$$\tilde{S} = S + \frac{\tilde{\nu}}{\kappa^2 d^2} f_{v2} \tag{5.13}$$

where the vorticity S and functions, f_{v1}, f_{v2} and χ are given by:

$$S = \left(\frac{\partial u}{\partial y} - \frac{\partial v}{\partial x} \right) \tag{5.14}$$

$$f_{v1} = \frac{\chi^3}{\chi^3 + c_{v1}^3} \tag{5.15}$$

$$f_{v2} = 1 - \frac{\chi}{1 + \chi f_{v1}} \tag{5.16}$$

$$\chi = \frac{\tilde{\nu}}{\nu} \tag{5.17}$$

The functions f_{v1} and f_{v2} are defined by Spalart and Allmaras (1994) in order to adjust the production term near the wall and hence the level of $\tilde{\nu}$. f_{v1} starts at zero when $\tilde{\nu}$ is small and increases, tending towards unity far away from the wall. f_{v2} starts at unity but as the value of $\tilde{\nu}$ increases, this function becomes negative to a value of the order of -1.5 and then tends towards zero. Thus away from the wall or for large values of $\tilde{\nu}$, f_{v2} tends towards zero and hence $\tilde{S}$ tends towards S. These functions are both shown in Figure 5.1.

The second term on the right denotes the diffusion of the eddy viscosity throughout the flow. Not only are the conventional second derivative terms included here, but there are also non-linear terms being controlled by the coefficient, c_{b2}. This term acts to diffuse $\tilde{\nu}$ away from the wall or other regions of high vorticity where the turbulence is being produced.

The third term on the right denotes the destruction term and is only necessary for the near wall parts of the model, hence the suffix 'w'. This term is dependent on the constant c_{w1}, the wall distance d, the eddy viscosity and the function f_w which is given by:

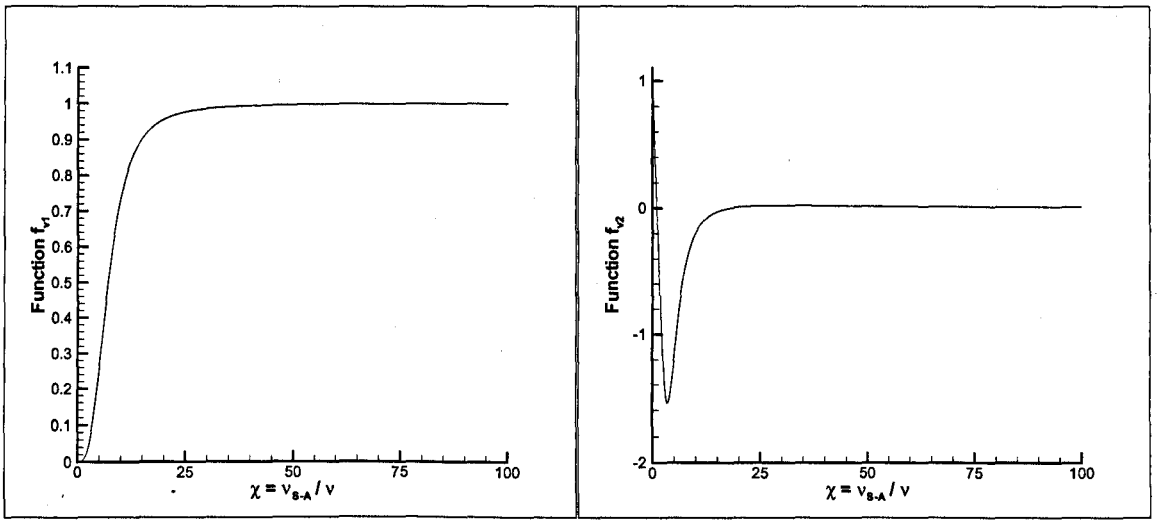

Figure 5.1: Model Functions f_{v1} and f_{v2} from Spalart and Allmaras (1994)

Note: $\nu_{S-A} = \tilde{\nu}$

$$f_w = g\left[\frac{1+c_{w3}^6}{g^6+c_{w3}^6}\right]^{1/6} \tag{5.18}$$

where g and r are defined as:

$$g = r + c_{w2}(r^6 - r) \tag{5.19}$$

$$r = \frac{\tilde{\nu}}{\tilde{S}\kappa^2 d^2} \tag{5.20}$$

All of these terms together constitute the S-A model minus laminar transition terms. A number of practical and numerical issues exist in the using of this model and so these will now be considered.

5.3.1 Practical & Numerical Aspects

Although the model is written with due regard to the mechanics of turbulence production and convection, when solving the model equations numerically, a number of issues have been encountered.

Firstly, the need for adequate inflow boundary conditions has been found to have a significant effect on the accuracy of the final results. This issue is covered is some depth in a number of works especially Spalart and Allmaras (1994) and Persson *et al.* (2006).

In particular, the inlet boundary conditions for an already developed boundary layer need to be defined reasonably accurately otherwise the further development of the boundary layer will be based on an inaccurate starting value. The effects of this boundary condition will be covered in more depth later in section 5.3.3 where a number of validation simulations are presented.

Other issues were also encountered with regard to the stability of certain terms within the model equation. In particular, the calculation of the vorticity produces very large values if the grid spacing in either coordinate direction is excessively small. This leads to numerical instabilities and so it may be prudent to provide under-relaxation when assessing this term.

Finally, an issue was observed regarding the differencing scheme used to solve the S-A model equation. As mentioned previously, the standard central differencing method is susceptible to instabilities when the local Peclet number is high. This was found to be the case for most of the simulations performed for the current work. A solution was found in always using the upwind differencing method to solve the S-A model equations. This was found to be successful in maintaining solution stability, and

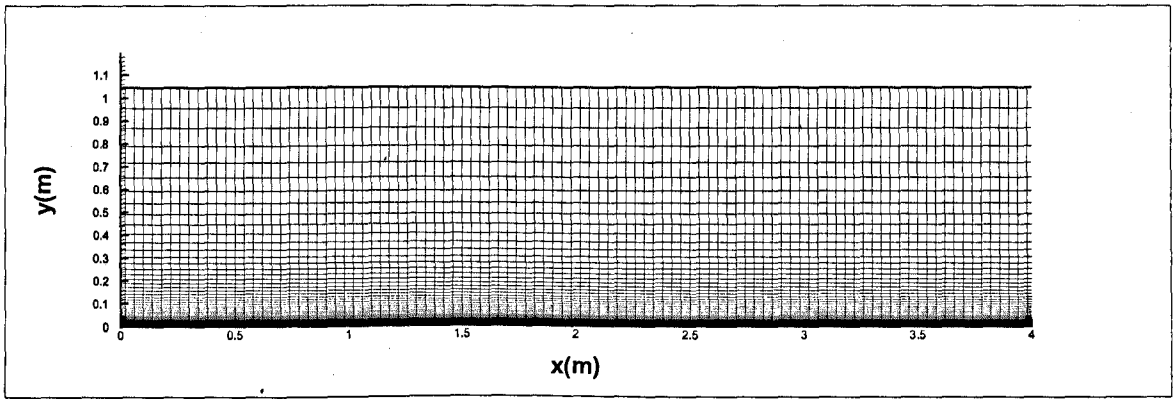

Figure 5.2: Domain & mesh set-up for S-A model flat plate boundary layer case

the excessive numerical diffusion associated with the method could be discounted as the model itself would be producing large amounts of diffusion by its very nature.

5.3.2 Validation of the basic S-A model

In order to assess the overall performance of the S-A model the test case is a flat plate boundary layer flow. The flat plate boundary layer domain and mesh are shown in Figure 5.2. The computational domain extends 20δ in the streamwise direction and is 5δ tall in the wall normal direction. The mesh divides the streamwise direction into 100 nodes whilst the wall normal direction consists of 100 nodes expanded to contain more nodes in the near-wall region. In the initial case, the grid expansion factor is a constant geometric factor of 1.1.

With regard to the set-up, a freestream velocity of $1.0m/s$ and a boundary layer thickness, δ, of $0.2m$ are used at the inlet with the boundary condition there being applied using a simple seventh-power law relation. These parameters effectively set the inlet position at $10.2m$ downstream of the start of the surface. This was calculated using

a mixed laminar-turbulent boundary layer growth assumption based on the seventh-power law as given in Houghton and Carpenter (2003). This, in turn, leads to the following parameters being implied at the inlet:

$$Re_\Theta = 1.34 \times 10^3 \quad (5.21a)$$

$$Re_x = 7.0 \times 10^5 \quad (5.21b)$$

$$\delta^* = 0.025m \quad (5.21c)$$

$$\Theta = 0.019m \quad (5.21d)$$

$$\tau_w = 2.47mPa \quad (5.21e)$$

The first plot of interest is the boundary layer velocity profile at the midplane (i.e. 10δ downstream of the inlet) shown in Figure 5.3. This is compared with the seventh power law and shows moderate agreement in the outer region of the boundary layer. Near the wall the profile shows less agreement although this is to be expected as the seventh power law assumes infinite velocity gradient and wall shear stress, and so a near wall plot is necessary to assess this region more completely.

This near wall velocity profile is given in Figure 5.4 and shows the accepted profiles $u^+ = y^+$ for the viscous sublayer (i.e. where $y^+ < 10$) and $u^+ = 2.2ln(y^+) + 5.5$ in the log-law region (where $y^+ > 10$). There is a good agreement between the simulated results using the S-A model and the accepted profiles.

The eddy viscosity distribution at the midplane shows a sensible profile following a roughly parabolic shape with the maximum being slightly lower than the middle of the boundary layer ($y = 0.5\delta$). This is shown in Figure 5.5 and the results are plotted against the profile given in Spalart and Allmaras (1994).

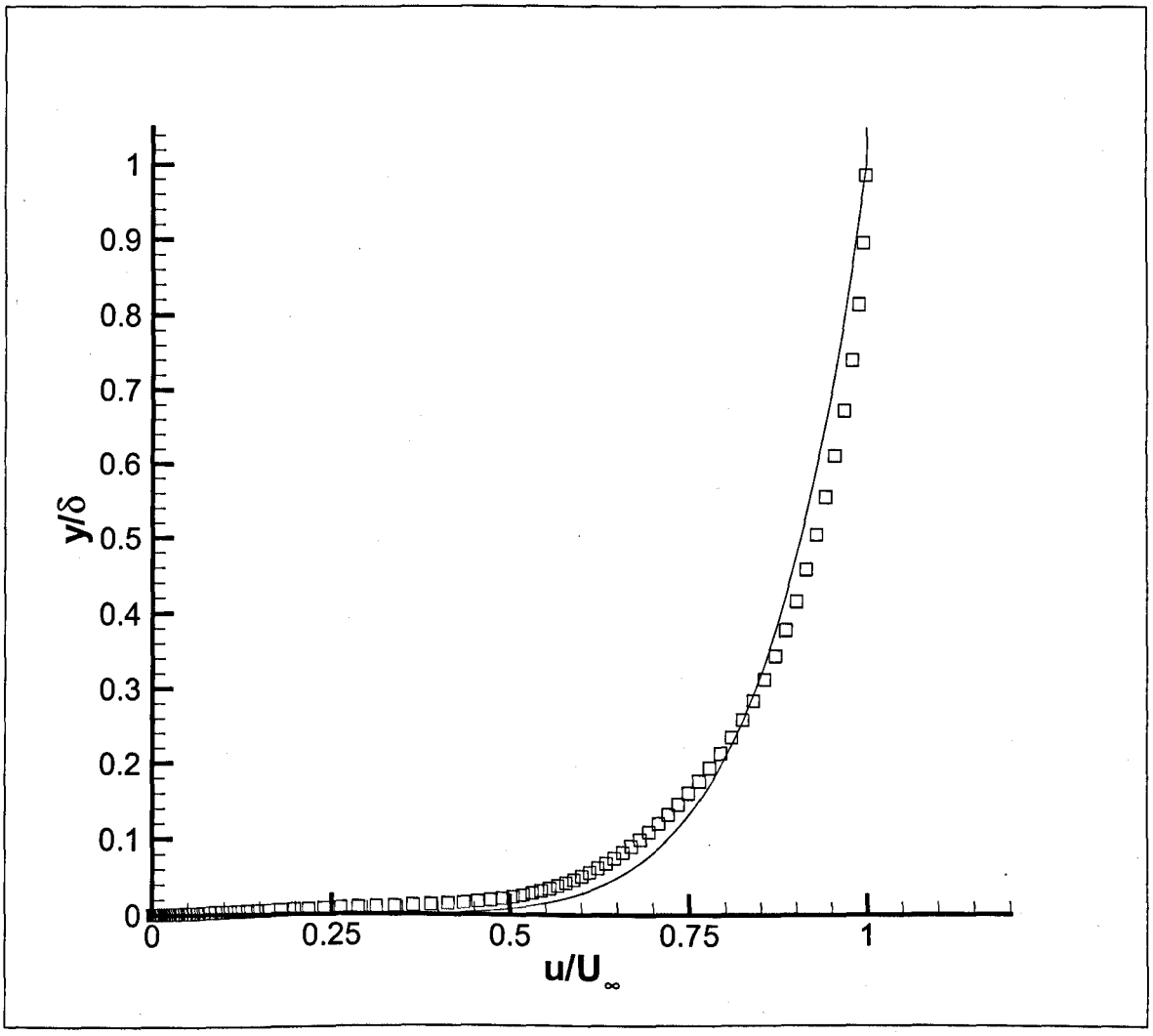

Figure 5.3: Velocity profile at $x = 10\delta$. □: Simulation, Line: Seventh power law profile

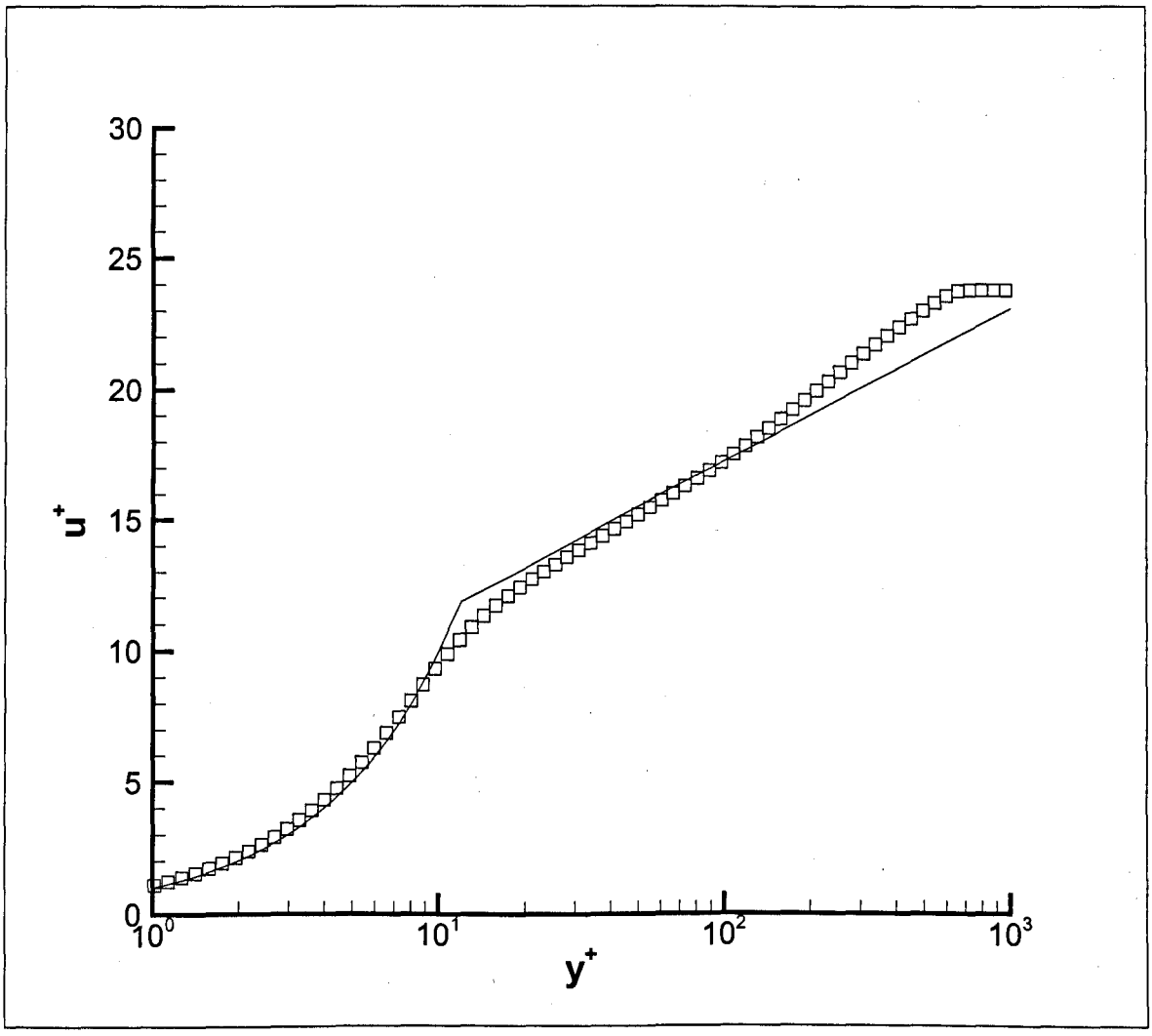

Figure 5.4: Law of the wall profile at $x = 2.0m$ □: Simulation, Line: $u^+ = y^+$ (below $y^+ = 10$) and $u^+ = 2.5ln(y^+) + 5.5$ (above $y^+ = 10$)

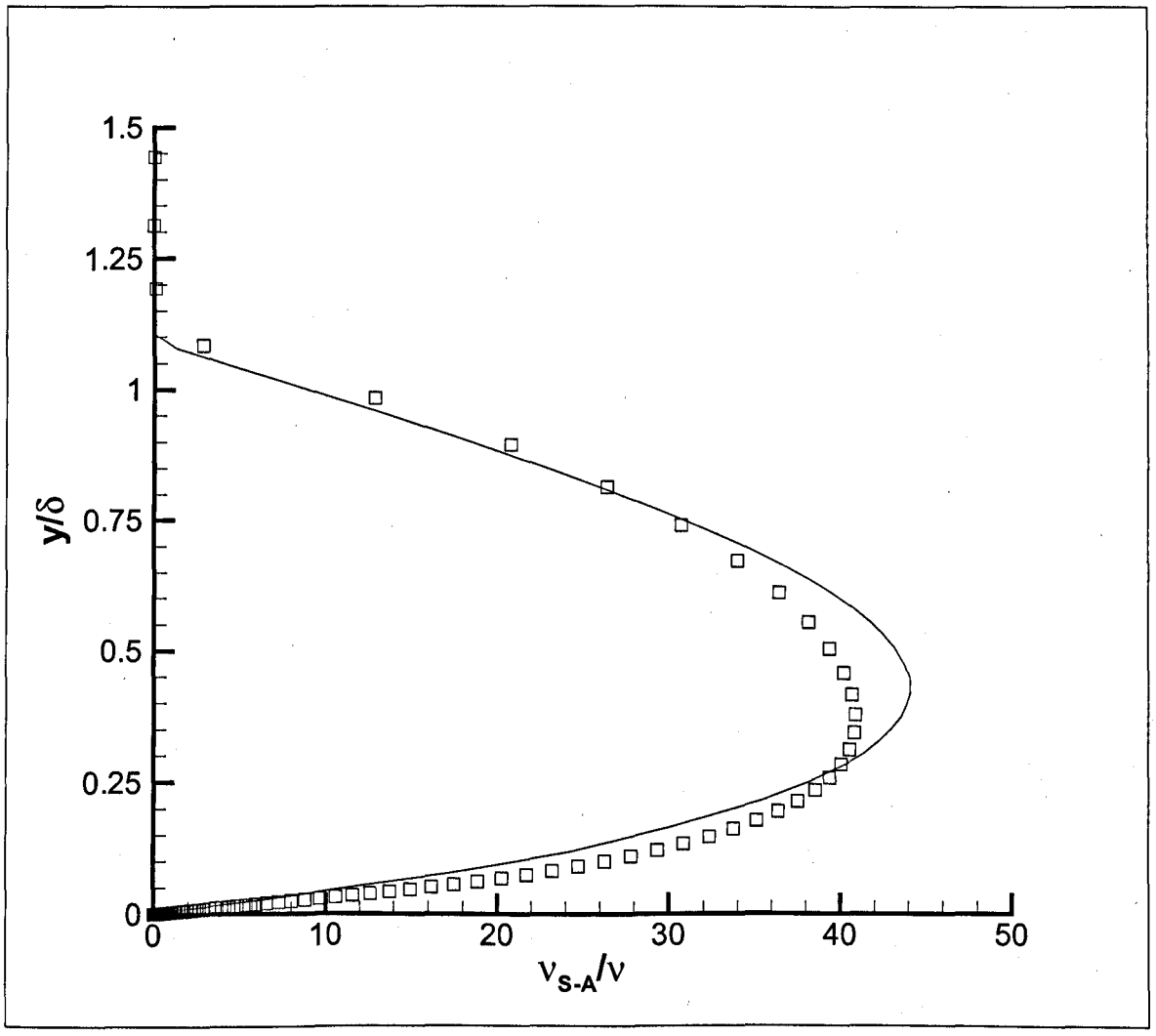

Figure 5.5: Modified Turbulent Viscosity Profiles at $x = 2.0m$. □: Simulation, Line: Results from Spalart and Allmaras (1994)

Table 5.2: Boundary Layer Properties at $x = 2.0m$

	Simulation	Theory	Error
Displacement Thickness, δ^*	0.0318	0.0305	4.3%
Momentum Thickness, Θ	0.0226	0.0237	-4.6%
Shape Function, H_{12}	1.41	1.28	10.2%
Wall Shear Stress, $\tau_w(mPa)$	2.34	2.38	-1.7%
Reynolds Number based on x, Re_x	8.38×10^5	8.5×10^5	-1.4%
Reynolds Number based on Θ, Re_Θ	1.55×10^3	1.63×10^3	-4.9%

With regard to the streamwise development of the boundary layer, Figures 5.6 and 5.7 show the displacement and momentum thicknesses along the domain. At the midplane, the errors for both displacement and momentum thickness are around 4.4% and -4.9% respectively.

The wall shear stress is shown in Figure 5.8 and whilst there is an over-estimation at the inlet as a result of the seventh power law profile applied there, the wall shear stress quickly recovers within 2.5δ of the inlet. There is a slight under-estimation at the mid-plane resulting in a value of 2.34mPa as opposed to the predicted value of 2.38mPa.

In summary, Table 5.2 shows the values of various boundary layer properties at the plane $x = 2.0m$.

The inaccuracies here are most likely due to the boundary conditions used at the top surface of the domain which is often a problematic area in simulating boundary layer flows. The velocity at the top face is set as shown in Eqns. (5.22a)-(5.22b) below:

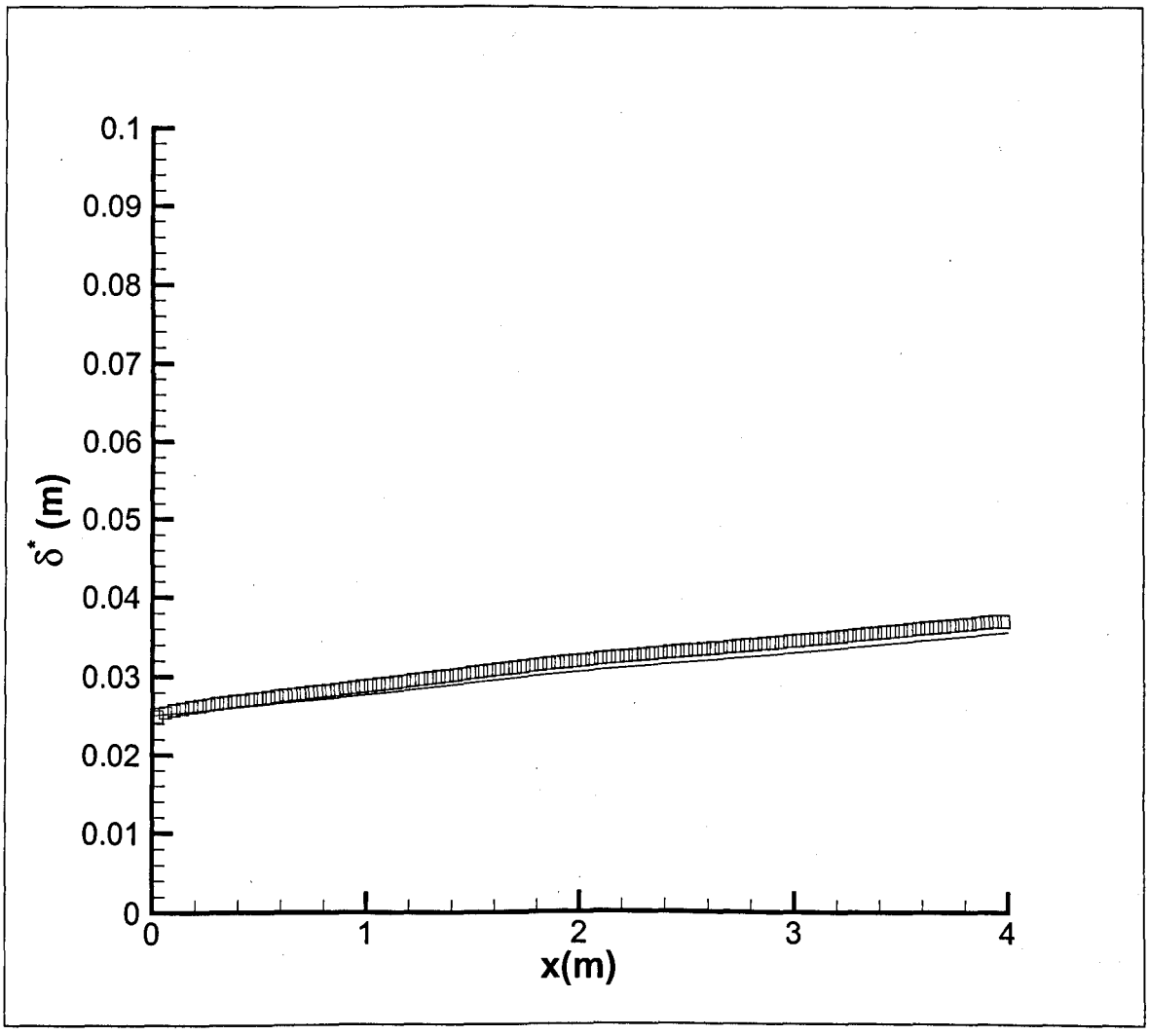

Figure 5.6: Displacement Thickness, δ^* along the domain. □: Simulation, Line: Boundary layer theory

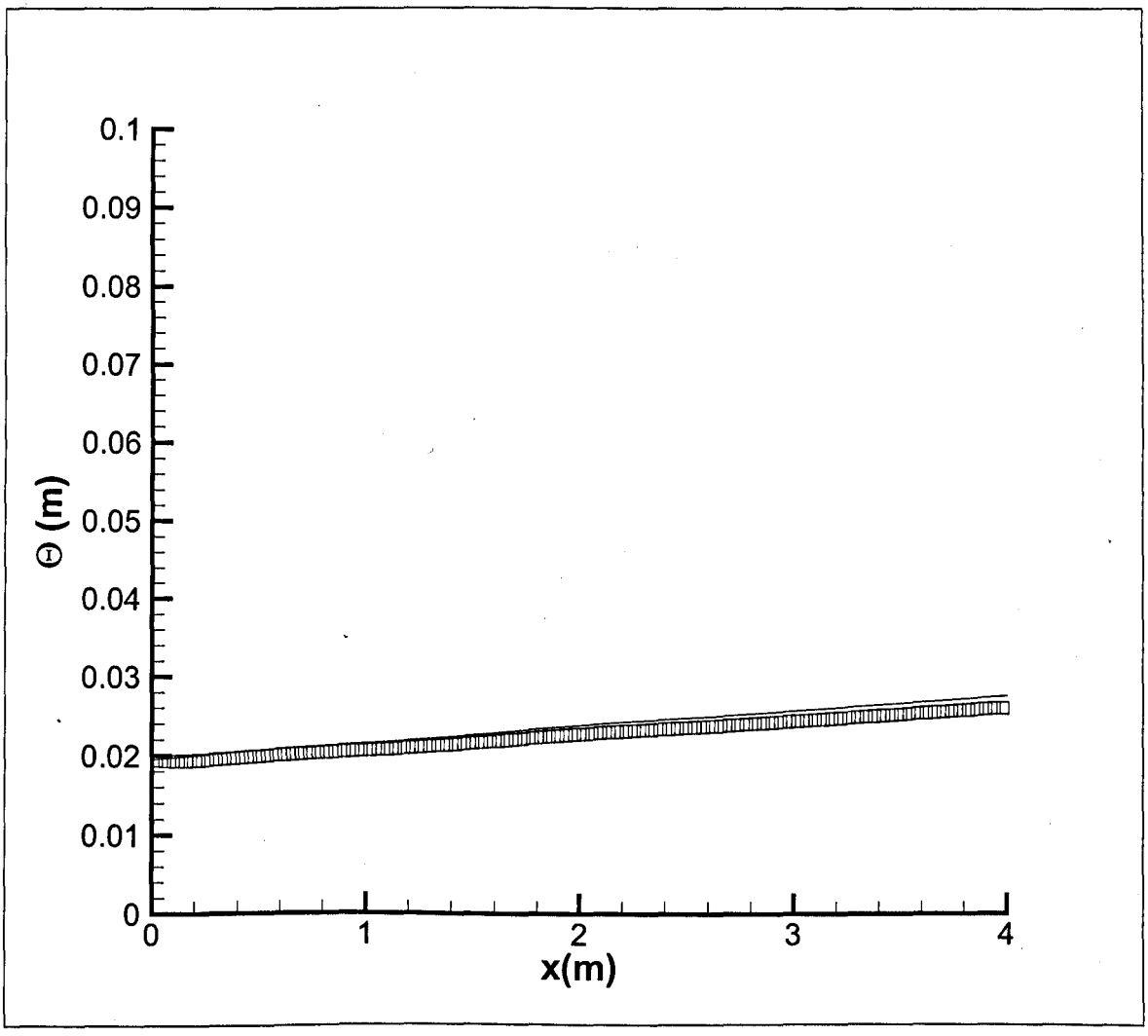

Figure 5.7: Momentum Thickness, Θ along the domain. □: Simulation, Line: Boundary layer theory

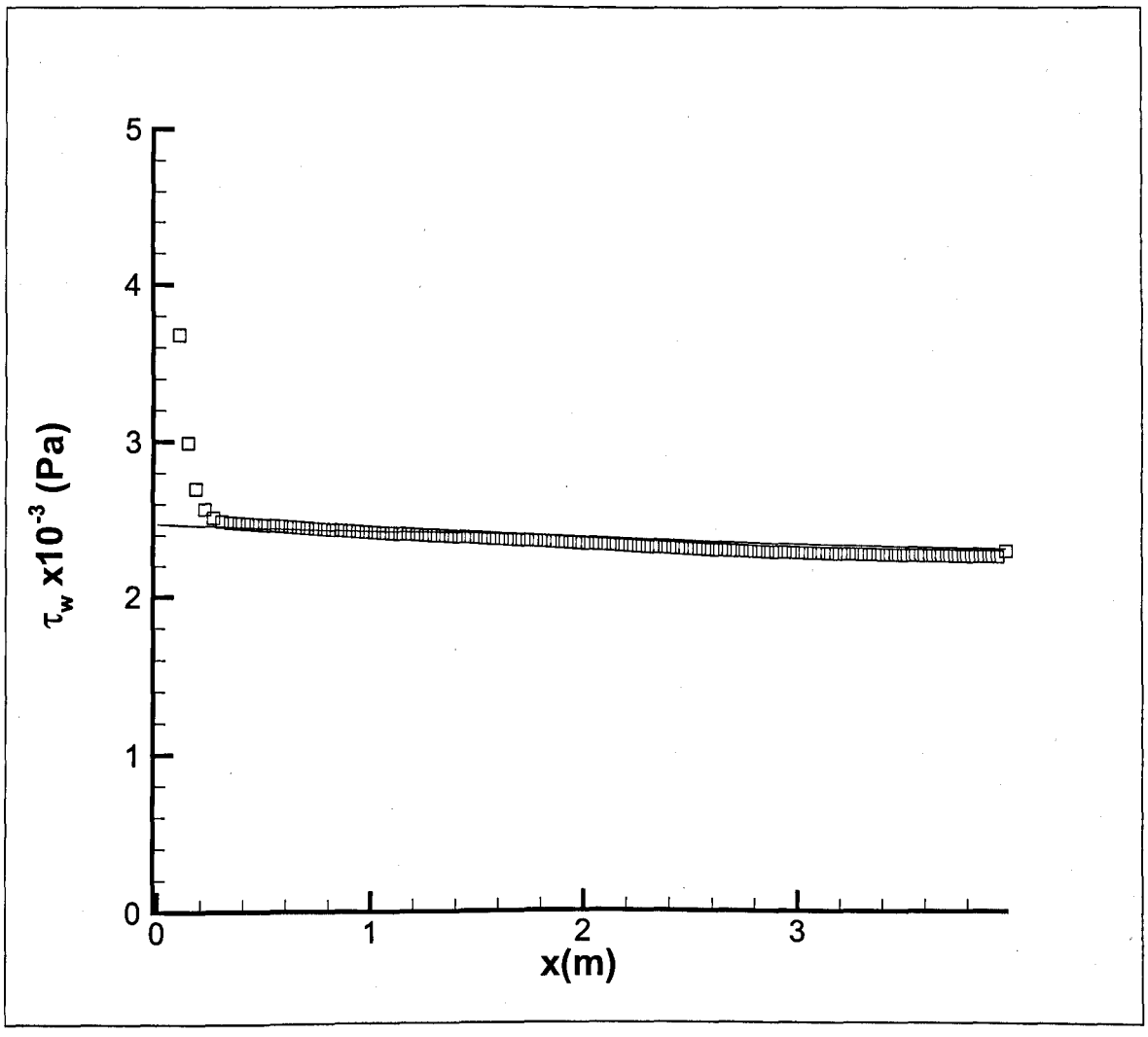

Figure 5.8: Wall shear stress, τ_w, along the domain. □: Simulation, Line: Boundary layer theory

$$\frac{\partial u}{\partial y} = 0 \tag{5.22a}$$

$$v = 0 \tag{5.22b}$$

Overall, the basic S-A model appears to function correctly and provides a reasonable approximation of the development and growth of a typical turbulent boundary layer. However, there are a number of parameters which affect this accuracy, and these will now be considered.

5.3.3 The effect of the inlet eddy viscosity boundary condition

Although the S-A model is able to model the development of the boundary layer along a flat plate, if a simulation is required to be pre-developed before the simulation inlet, then an adequate boundary condition for the eddy viscosity needs to be applied at the inlet. It makes sense that this eddy viscosity should closely match the eddy viscosity observed in the original derivation. As detailed previously, Figure 4 in Spalart and Allmaras (1994) shows that the eddy viscosity follows a roughly parabolic distribution across the boundary layer with a maximum value of $0.021 U_\infty \delta^*$ around $y/\delta^* = 3.5$. This figure has been reproduced here in Figure 5.9. Assuming that the boundary layer thickness is eight times larger than the displacement thickness, this means the maximum should be around $y/\delta = 0.44$ rather than around $y/\delta = 0.5$.

Three simulations have been run in order to test the effect of this inlet boundary condition. These simulations consider a boundary condition extending only across the boundary layer (i.e. reducing to zero by $y/\delta = 1$), a similar condition extending out

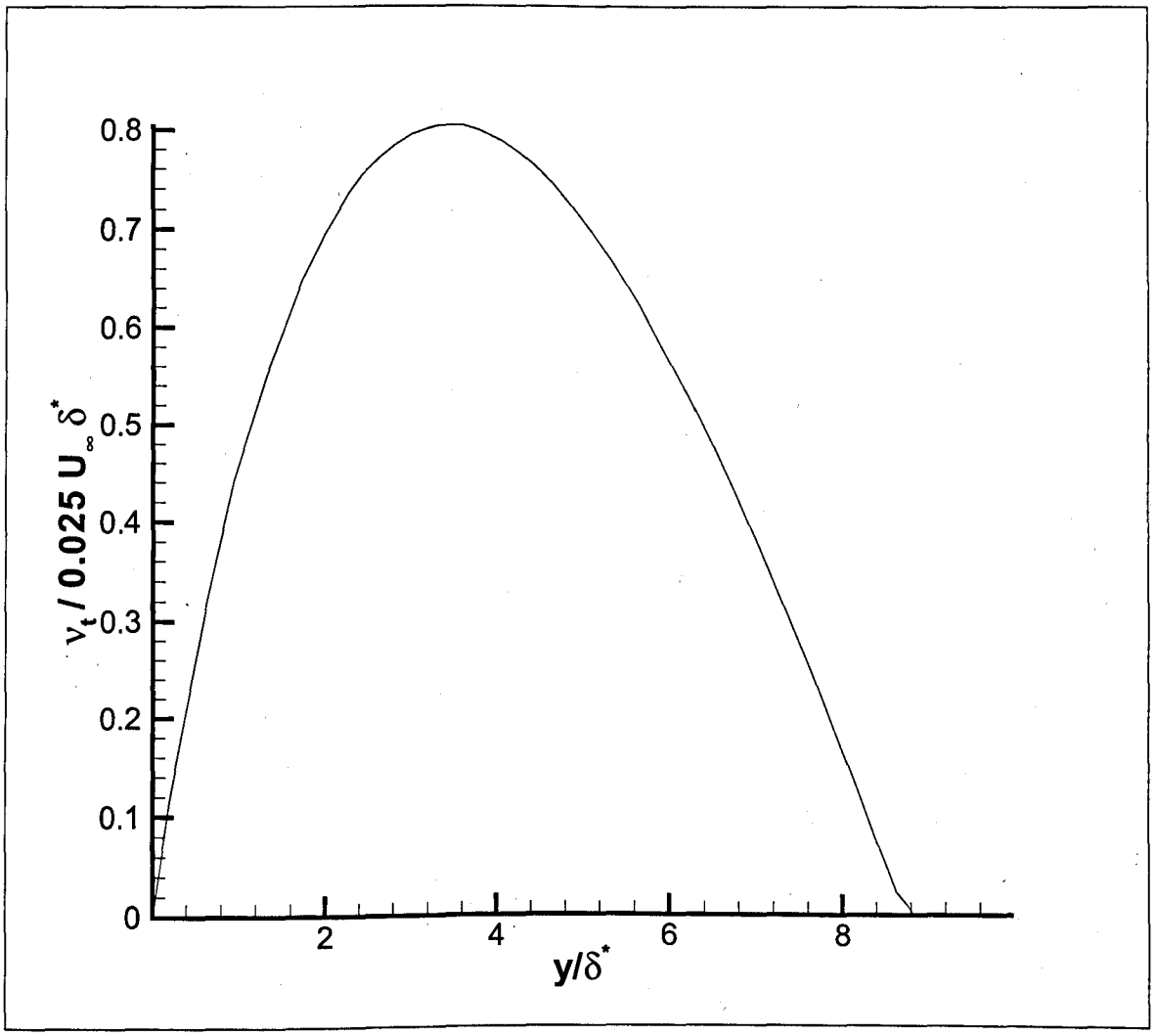

Figure 5.9: Figure 4 from Spalart and Allmaras (1994)

to $y/\delta = 1.2$ as implied in Spalart and Allmaras (1994) and finally, no inlet boundary condition at all. These conditions are shown in Figure 5.10.

The overall velocity profile at the midplane for these three cases are shown in Figure 5.11 and the non-dimensional near-wall velocity profile is shown in Figure 5.12. It is clear from these velocity profiles that whilst there is a negligible difference in whether the boundary condition reduces to zero at $y/\delta = 1$ or $y/\delta = 1.2$ at the inlet, not using any boundary condition for $\tilde{\nu}$ at all produces far worse results. This is evidently because the eddy viscosity has not had sufficient time to develop over the solid wall and so the velocity profiles end up less turbulent than they should be.

This point is further proved by considering the $\tilde{\nu}$ distribution at the mid-plane as shown in Figure 5.13. Surprisingly, there is quite a significant difference in the eddy viscosity between the $y/\delta = 1$ and the $y/\delta = 1.2$ cases. This difference only exists above $y/\delta = 0.2$ by which point, the mean shear rate within the profile is much reduced and so the eddy viscosity has much less effect.

It is also significant to note that whilst the $y/\delta = 1$ case maintains an eddy viscosity which returns to zero at $y/\delta = 1$ even at the midplane, the $y/\delta = 1.2$ case has an eddy viscosity which returns to zero at $y/\delta = 1.125$ as seen in Spalart and Allmaras (1994).

This would indicate that it is actually better to over estimate the eddy-viscosity at the inlet and allow it to be brought down by the destruction term rather than under-estimate and try to get the production term to make up the difference. This is possibly due to the fact that in deriving the original model equation, Spalart & Allmaras probably decided to have a model that was more on the stable side than on the powerful side. This can be seen in Figure 6 of Spalart and Allmaras (1994) in which the destruction term peaks at around -4 near the wall whilst the production term never exceeds unity.

Returning to Figure 5.13 it is clear that a lack of inlet eddy viscosity boundary

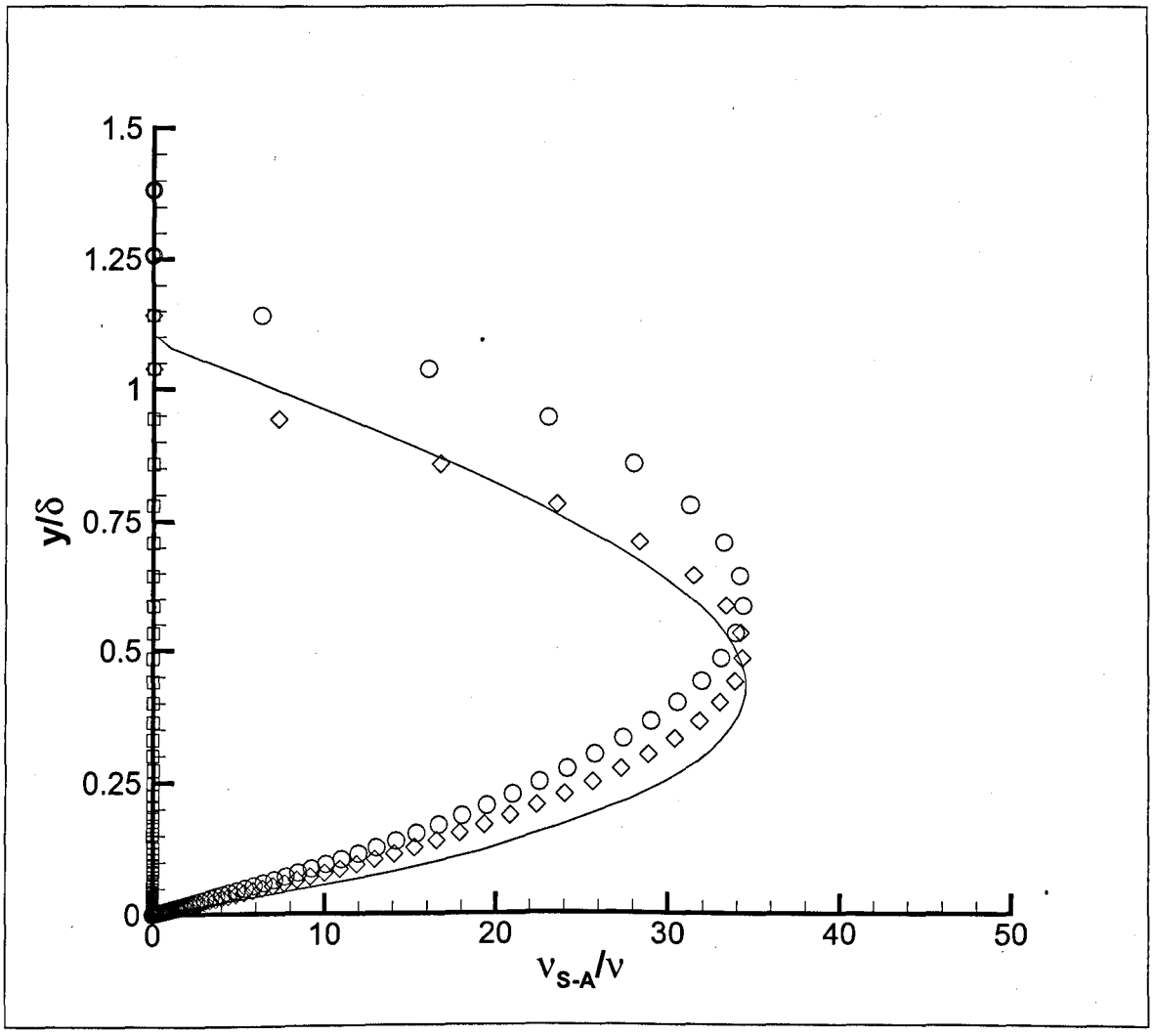

Figure 5.10: Inlet boundary conditions for modified eddy viscosity, $\tilde{\nu}$. □: No inlet condition, ◇: Inlet condition to $y/\delta = 1$, ○: Inlet condition to $y/\delta = 1.2$, Solid Line: Results from Spalart and Allmaras (1994) as reproduced in Figure 5.9 (Note:$\nu_{S-A} = \tilde{\nu}$)

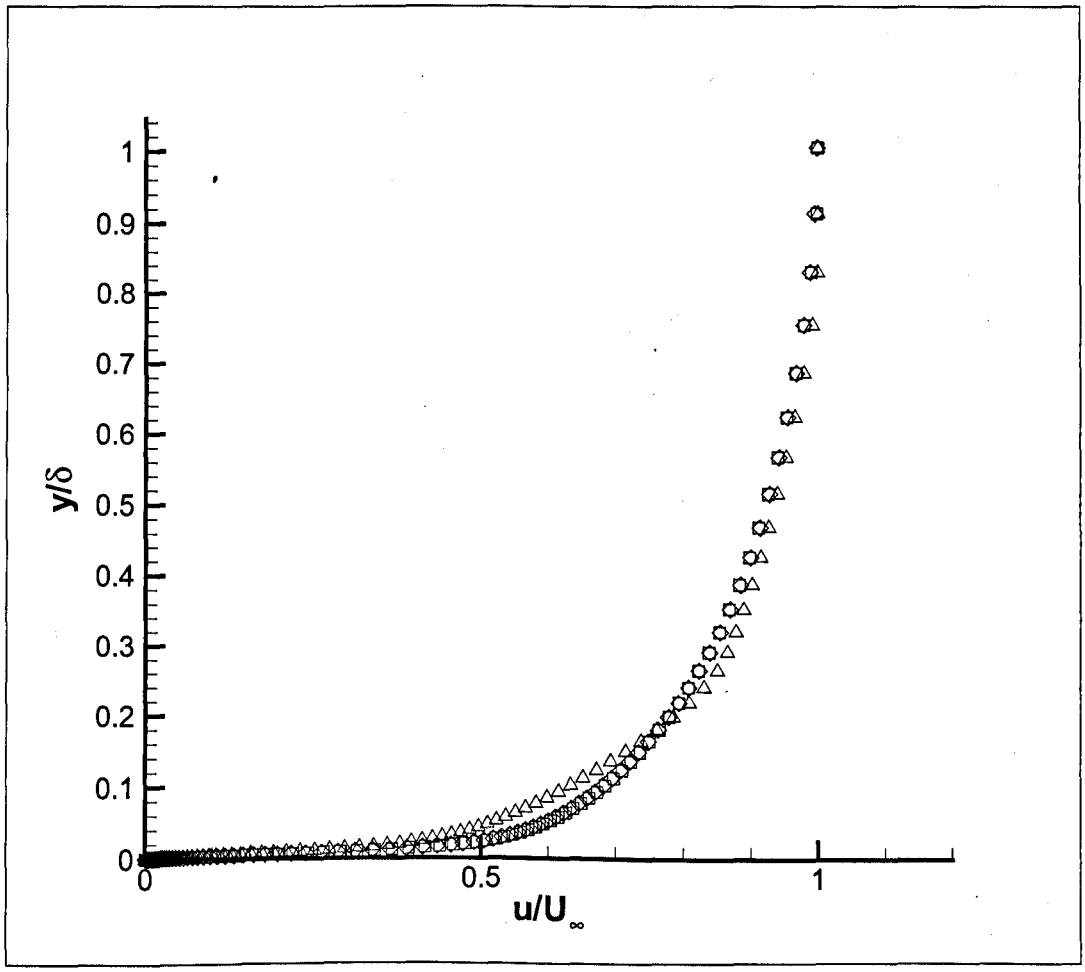

Figure 5.11: Overall velocity profile at x=2.0m: Parabolic $\tilde{\nu}$ inlet condition up to $y/\delta = 1$: $\square$, Parabolic $\tilde{\nu}$ inlet condition up to $y/\delta = 1.2$: $\diamondsuit$, No $\tilde{\nu}$ inlet condition: $\triangle$

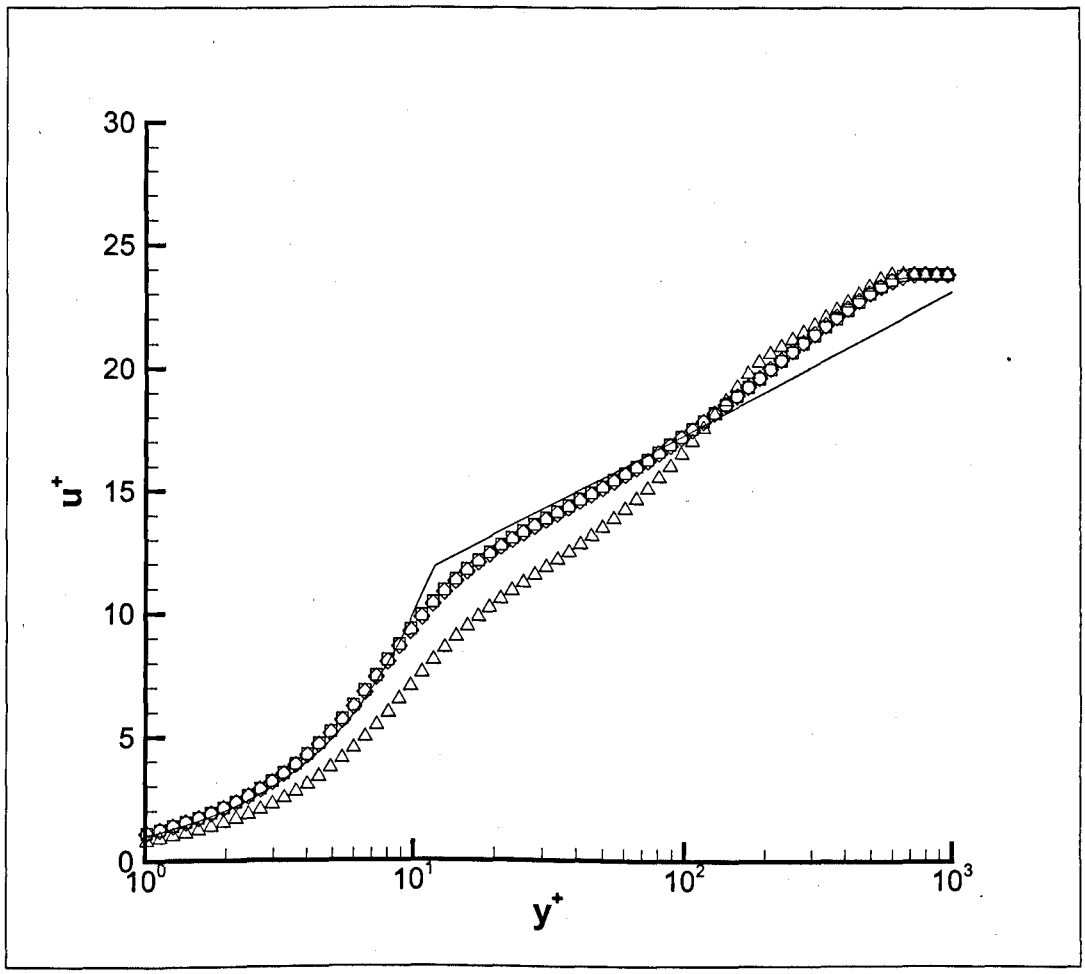

Figure 5.12: Near-wall velocity profile at x=2.0m: Parabolic $\tilde{\nu}$ inlet condition up to $y/\delta = 1$: $\square$, Parabolic $\tilde{\nu}$ inlet condition up to $y/\delta = 1.2$: $\diamondsuit$, No $\tilde{\nu}$ inlet condition: $\triangle$

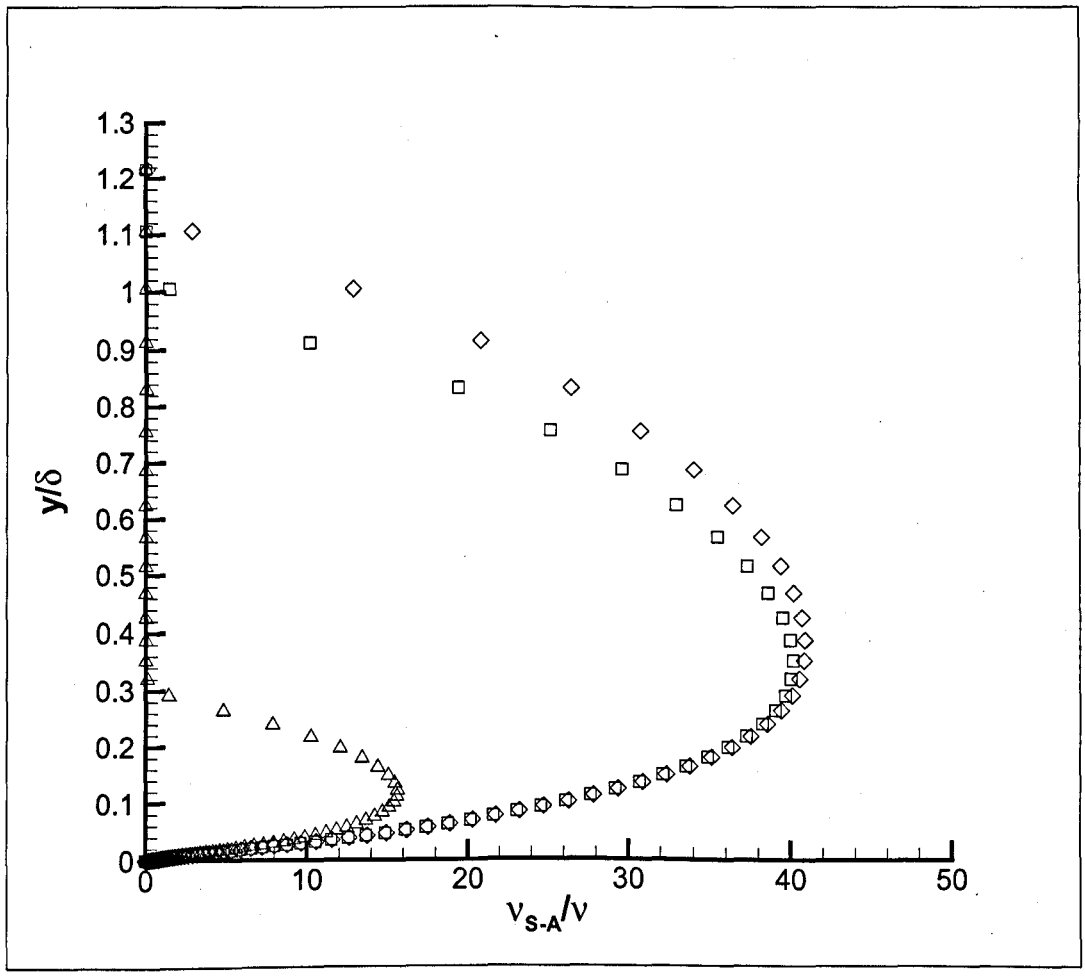

Figure 5.13: S-A Eddy Viscosity, $\tilde{\nu}$ at x=2.0m: Parabolic $\tilde{\nu}$ inlet condition up to $y/\delta = 1$: □, Parabolic $\tilde{\nu}$ inlet condition up to $y/\delta = 1.2$: ◇, No $\tilde{\nu}$ inlet condition: △

	δ^* (m)	Θ (m)	H_{12}	τ_w (mPa)
Inlet $\tilde{\nu}$ to $y/\delta = 1$	0.0318	0.023	1.383	2.34
Inlet $\tilde{\nu}$ to $y/\delta = 1.2$	0.0319	0.023	1.387	2.31
No inlet $\tilde{\nu}$ condition	0.0316	0.021	1.505	1.65

Table 5.3: Results at $x = 10\delta$ when changing the inlet $\tilde{\nu}$ conditions

conditions produces an inadequate distribution for the eddy viscosity far downstream, even (as is in this case) in excess of 10 boundary layer thicknesses downstream of the inlet. A correct boundary condition will improve the downstream results to a much greater extent. These downstream boundary layer properties are summarised in Table 5.3. Whilst the displacement thickness is largely the same across all three methods due to the fact that the mass flux being applied at the inlet is the same for all cases, the momentum thickness is significantly lower for the case without any inlet $\tilde{\nu}$ conditions. This is shown out in the increased shape factor showing that the profile for the no condition case is more laminar. The wall shear stress also shows a large drop (around 30%) for the case with no condition thus proving that the momentum transport in the y-direction is not being propagated into the boundary at the correct level.

5.3.4 The effect of the first off-wall node

One weak point of turbulence modelling is that the first off-wall grid node needs to be within the viscous sub-layer in order to correctly approximate the transfer of momentum to the boundary layer through the wall shear stress. This requirement can be difficult to achieve for engineering CFD. In order to test the effect of the position of the first off-wall node, a number of simulations were run with a variety of different grid expansions in

Table 5.4: Grid Properties

	Mesh Mesh Mesh $(nx \times ny)$	Expansion Ratio E_y	Position of First Off-wall node $y_1(mm)$	First Off-Wall grid spacing y_1^+
Grid 01	100×100	1.1	0.0073	0.011
Grid 02	100×100	1.05	0.383	0.553
Grid 03	100×100	1.025	1.156	3.340
Grid 04	100×100	1.0125	2.537	7.323

the wall normal direction. These grids are detailed in more depth in Table 5.4.

These grids have been selected with varying grid expansions allowing the position of the first off-wall node, y_1^+, to be adjusted. The first two grids, G01 and G02, were chosen to have positions for y_1^+ of much less than 1 in order to provide fully wall resolved solutions. Grids G03 and G04 were chosen to provide y_1^+ values of greater than 1 so being deliberately under-resolved.

Considering the overall velocity profile shown in Figure 5.14, it is clear that Grids 01 and 02 provide little difference as the first off-wall node lies well within the viscous sublayer for both grids. However, as the position of the first off-wall node moves out of this region as shown for Grids 03 and 04 the profile becomes less full as the wall shear stress becomes progressively under-estimated. This is also shown with the near-wall velocity profile given in Figure 5.15. These results simply show that if the first off-wall node is not within the viscous sub-layer, the wall shear stress is under-estimated and

so the profile ends up being under-estimated as a result of the reduction in momentum generation at the wall.

This presents a problem as it means the first off-wall node needs to be very close to the wall and this can present a problem if a complex geometry is used requiring a spread of fine nodes to be distributed over the surface. This is a particular problem for the Lille bump case as it would require wall normal grid spacings of less than $y^+ = 1$ over a large span in the y-direction in order to make sure that there is a node within the viscous sublayer near the wall all the way over the surface. One way around this problem is to relax the grid requirements in the wall normal direction and modify the momentum equations using a wall-function at the first off-wall node in order to take into account this discrepancy. This will be covered in more depth later in Section 5.4.

5.3.5 Conclusions to be drawn regarding the S-A model

In conclusion, it is clear, that in order to use the Spalart-Allmaras model correctly, two main factors must be taken into consideration. Firstly, the inlet boundary condition for the eddy viscosity must be set correctly if a pre-developed boundary layer simulation is to be run. This allows a reasonable guess as to what the boundary layer was doing as it developed before the inlet and so allows a more accurate boundary layer profile further downstream.

Secondly, the first off-wall grid node needs to lie within the viscous sub-layer in order to adequately resolve the wall shear stress and hence the transport of momentum away from the wall. This constraint means that the first off-wall node must lie within $y^+ = 1$ at the most and is a restrictive constraint if this is required over a significant span in y.

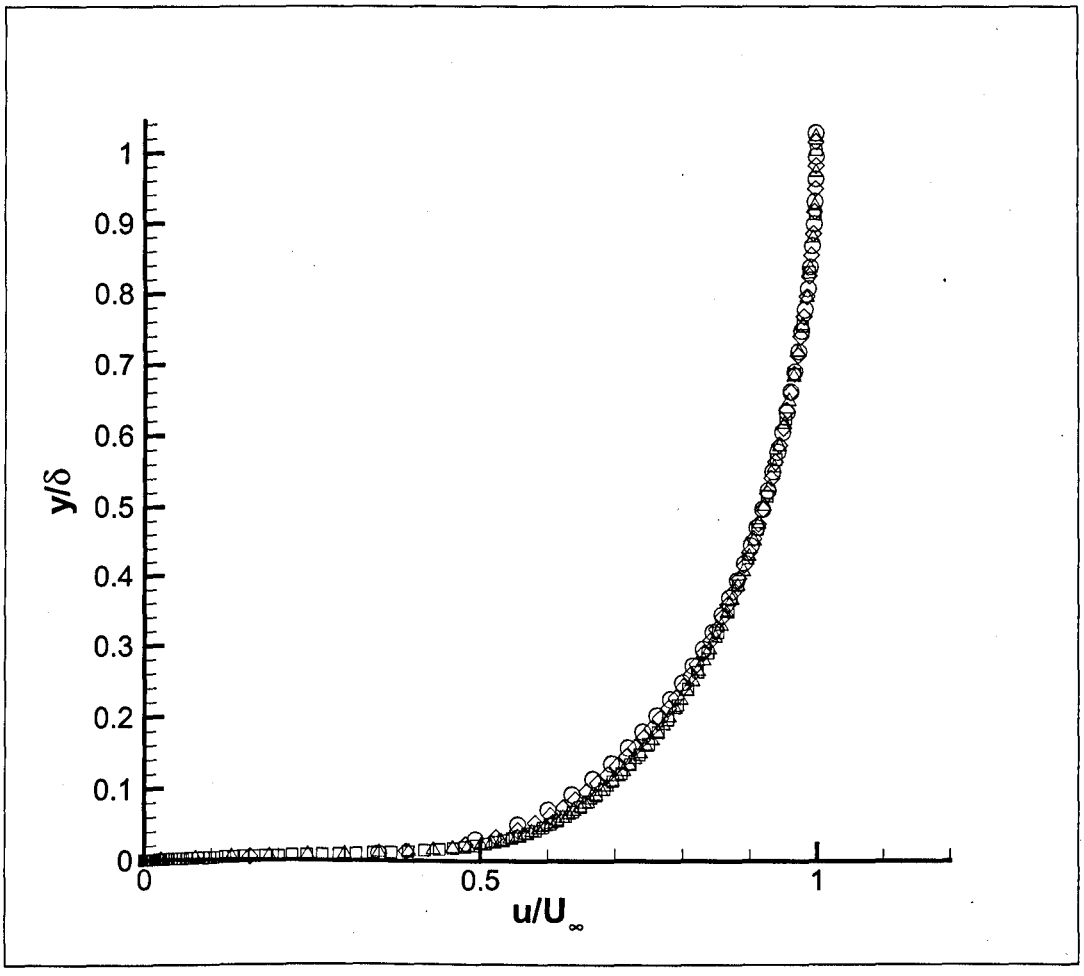

Figure 5.14: Overall velocity profile at x=2.0m: Grid 01 □, Grid 02 △, Grid 03 ◇, Grid 04 ○

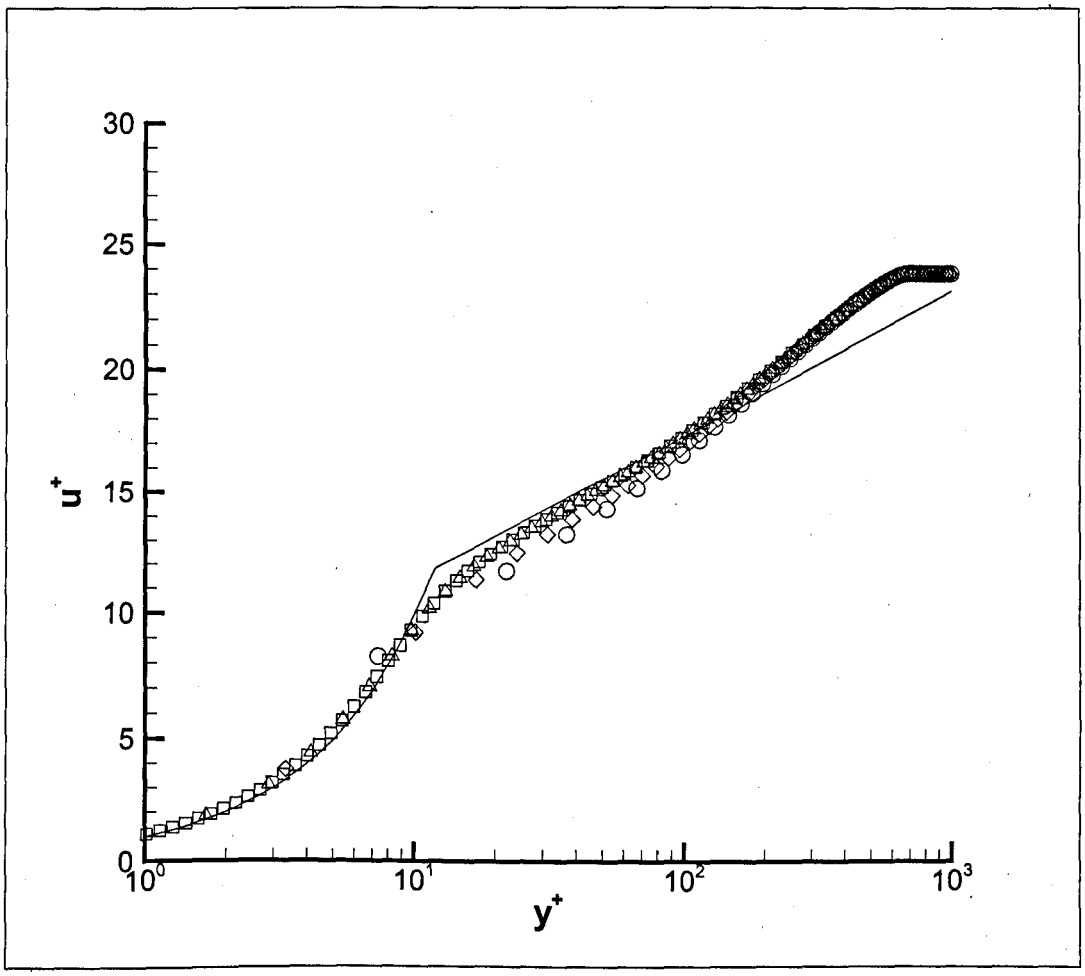

Figure 5.15: Non-dimensional near-wall velocity profile using wall units at x=2.0m: Grid 01 □, Grid 02 △, Grid 03 ◇, Grid 04 ○

5.4 Modifying the S-A Model using wall functions

5.4.1 Theory

As previously mentioned, if the first off-wall node does not lie within the viscous sub-layer (i.e. $y_1^+ < 1$) the wall shear stress is not adequately approximated and so the subsequent boundary layer profile is incorrectly developed. This is because the turbulence model assumes that the wall shear stress is simply a function of the velocity gradient between the first off-wall node and the wall. However, if the first off-wall node is outside the viscous sub-layer, the velocity gradient at the wall and hence the wall shear stress will be under-estimated. This is shown in Figure 5.16. Whilst there are many different ways of applying a wall function within a simulation, the present work uses a wall function method based on Kalitzin *et al.* (2005).

The process of applying a wall function can be divided into a number of stages that need to be addressed:

- Estimation of the friction velocity,
- Correction of the momentum equations at first off-wall node, and
- Correction of the eddy viscosity and turbulence variables at the first off-wall node.

Estimation of the friction velocity can be done in a straight-forward manner by completing a high-resolution simulation of a turbulent boundary layer in order to provide an accurate set of results of u^+ as a function of y^+. This can then be processed to produce a table of y^+ given a specific wall distance Reynolds number at the first off-wall node, Re_y defined as:

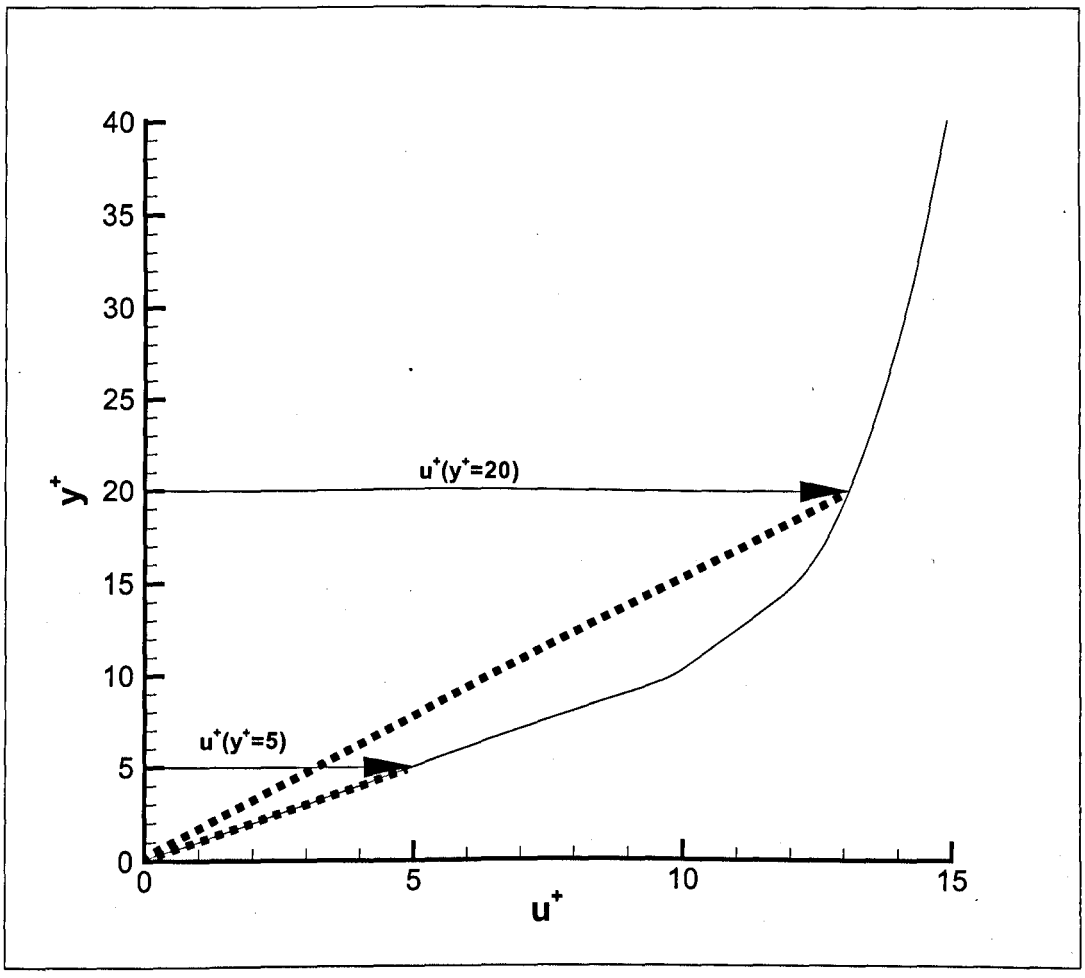

Figure 5.16: The need for wall functions: errors in wall shear stress estimation by a node too far away from the wall.

$$Re_y = \frac{Uy}{\nu} \tag{5.23}$$

The estimation of the friction velocity is then a simple process of calculating the Reynolds number, Re_y at the first off-wall node, looking up the corresponding value of y^+ at this point and calculating the friction velocity from the relation:

$$u_\tau = \frac{\nu y_1^+}{y_1} \tag{5.24}$$

This friction velocity can then be used to correct the momentum equations. This correction can be done in numerous ways but one straightforward way to do this is to consider the evaluation of the viscous diffusion terms at the first off-wall control-volume. Ordinarily, the viscous terms at the first off-wall node will only consist of the second derivative of the $u-$velocity with respect to y, that is $\partial^2 u/\partial y^2$. Using standard central differencing, this term would be approximated as follows:

$$\frac{\partial^2 u}{\partial y^2} = \frac{\left(\frac{\partial u}{\partial y}\right)_n - \left(\frac{\partial u}{\partial y}\right)_s}{y_n - y_s} \tag{5.25}$$

where $(\partial u/\partial y)_n$ and $(\partial u/\partial y)_s$ are the velocity gradients at the north and south faces respectively. Also using central differencing for these gradients means they can be written as:

$$\left(\frac{\partial u}{\partial y}\right)_n = \frac{u_N - u_P}{y_N - y_P} \tag{5.26a}$$

$$\left(\frac{\partial u}{\partial y}\right)_s = \frac{u_P - u_S}{y_P - y_S} \tag{5.26b}$$

However, if the first off-wall is not within the viscous sub-layer, the term $(\partial u/\partial y)_s$ can no longer be accurately approximated with a linear function as in Eqn. 5.26b.

To solve this issue, the velocity gradient at the south face can be calculated using the friction velocity from the relation:

$$\mu \frac{\partial u}{\partial y} = \rho u_\tau^2 \tag{5.27}$$

This can then be substituted into Equation (5.25) to give:

$$\frac{\partial^2 u}{\partial y^2} = \frac{\left(\frac{\partial u}{\partial y}\right)_n - u_\tau^2/\nu}{(y_n - y_s)} \tag{5.28}$$

To apply this relation the south coefficient needs to be set to zero (as the south point no longer has any influence on the gradient estimation) and an addition made to the source term of u_τ^2/ν.

Finally, corrections need to be made to the eddy viscosity, ν_t and the modified viscosity, $\tilde{\nu}$. As mentioned previously, whilst ν_t and $\tilde{\nu}$ are equal throughout most of the boundary layer, near the wall they differ and so the correction involved is different.

Corrections are made to the eddy viscosity, ν_t by using the look-up table which also contains values of ν_t^+ for a given Re_y and y^+ where:

$$\nu_t^+ = \frac{\nu_t}{\nu} \tag{5.29}$$

For the modified eddy viscosity, $\tilde{\nu}$, the relation is simpler as near the wall the following holds:

$$\tilde{\nu} = \kappa u_\tau y \tag{5.30}$$

and so this relationship can be applied explicitly to the first off-wall node.

These corrections to the momentum equations and the eddy viscosity are particularly useful as they allow correction to the first off-wall node alone rather than adjusting the node within the surface. This is preferable in the present work as the immersed boundary method already uses the first interior node for surface definition so using the first off-wall node for the wall function method should prevent any conflict between the two methods.

5.4.2 Validation

The validation of the wall functions approach has been done using eight different grid meshes as detailed in Table 5.5 with the first four grids being common to the previous section. Comparison of these meshes is also shown in Figure 5.17.

Each of these meshes were chosen to give a selection of first off-wall node positions. The first two grids have y_1^+ positions of less than 3 and so equate to wall resolved simulations. The next two grids have y_1^+ positions within the buffer layer. Finally, the remaining four grids have y_1^+ positions within the logarithmic law layer.

Overall, the boundary layer is still resolved with a sufficient number of nodes. As the boundary layer is around 0.25m thick, it is clear that even the coarsest grid still has a total of 10 nodes across the thickness.

The results for these boundary layer simulations are given in Figures 5.18-5.25 and allow the accuracy of the first off-wall node velocity to be assessed. It is clear that for Grids 01 and 02 (shown in Figures 5.18 and 5.19 respectively) the results differ very little as the simulation already has sufficient near-wall resolution and the first off-wall point has a velocity which lies close to the law of the wall profile. The results become less accurate for Grids 03 and 04 as shown in Figures 5.20 and 5.21 with the first off-

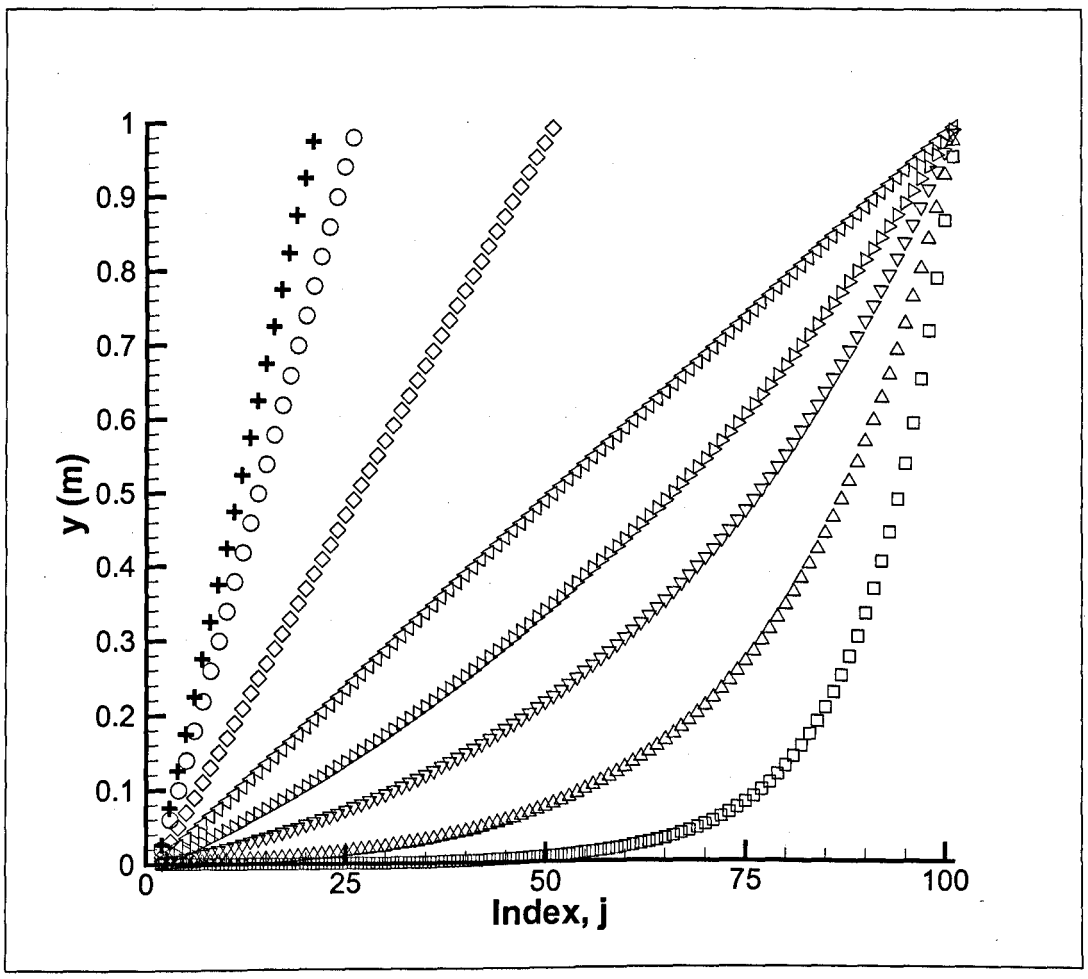

Figure 5.17: Grid node positions versus index for various validation cases. Grid 01 □, Grid 02 △, Grid 03 ▽, Grid 04 ▷, Grid 05 ◁, Grid 06 ◇, Grid 07 ○, Grid 08 +

Table 5.5: Grid Properties

	Mesh Mesh Mesh	Expansion Ratio	Position of First Off-wall node	First Off-Wall grid spacing
Grid 01	100 × 100	1.1	0.0073	0.011
Grid 02	100 × 100	1.05	0.383	0.553
Grid 03	100 × 100	1.025	1.156	3.340
Grid 04	100 × 100	1.0125	2.537	7.323
Grid 05	100 × 100	1.0	5.0	14.430
Grid 06	100 × 50	1.0	10.0	28.865
Grid 07	100 × 25	1.0	20.0	57.850
Grid 08	100 × 20	1.0	25.0	72.165

wall node under-estimated compared to the known profile. Finally, the results for Grids 05-08 are shown in Figures 5.22-5.25 and show a slight improvement over the Grids 03 and 04 results with the first off-wall node lying closer to the line.

These results are consistent with those found in Kalitzin *et al.* (2005) and can be simply explained. If a typical law of the wall profile is assessed with respect to first and second derivatives (as shown in Figure 5.26), then a number of significant points can be noted. Firstly, there is a trough in the second derivative around the position $y^+ = 8$ as shown in Figure 5.26(c). This is as a result of the profile here changing within the buffer layer from a linear viscous sub-layer profile near the wall to a logarithmic relationship away from the wall.

This causes problems in that the turbulence model assumes small changes in the velocity gradient so expecting small values for the second derivative. This means that if the first off-wall node is in this region of high second derivate then the assumptions are less accurate and result in a wider spread in the results. This can be seen in the previous figures and is confirmed on page 280 of Kalitzin *et al.* (2005).

In summary, the effect of using wall functions can be simply seen in Figure 5.27. Figure 5.27(a) shows the results without any wall function treatment. It can be seen that as the first off-wall node position shifts outwards, the results become more and more spread from the logarithmic law so being inaccurate. However, the results in Figure 5.27(b) show a significant improvement for all grids investigated as even for the first off-wall nodes well from the wall, the results maintain the law of the wall profile well.

5.5 Conclusions

In conclusion, the Spalart-Allmaras model of Spalart and Allmaras (1994) was shown to give an adequate simulation of a pre-developed turbulent boundary layer provided a number of factors were taken into consideration. The first of these was to make sure that a satisfactory inflow boundary condition for the eddy-viscosity was given for the subsequent development of the boundary layer.

The second factor considered the effect of the first off-wall node position and the inaccuracies caused by under-resolution. This issue was then addressed in greater depth with the wall-function approach detailed in Section 5.4. This wall-function was also found to improve the results significantly for first off-wall node positions of up to $y_1^+ = 72$. However, one area caution was found if the first off-wall node lay within the buffer layer around $y_1^+ = 8$.

Further turbulent treatment work will now be considering Chapter 6 in which Detached Eddy Simulation (DES) will be considered.

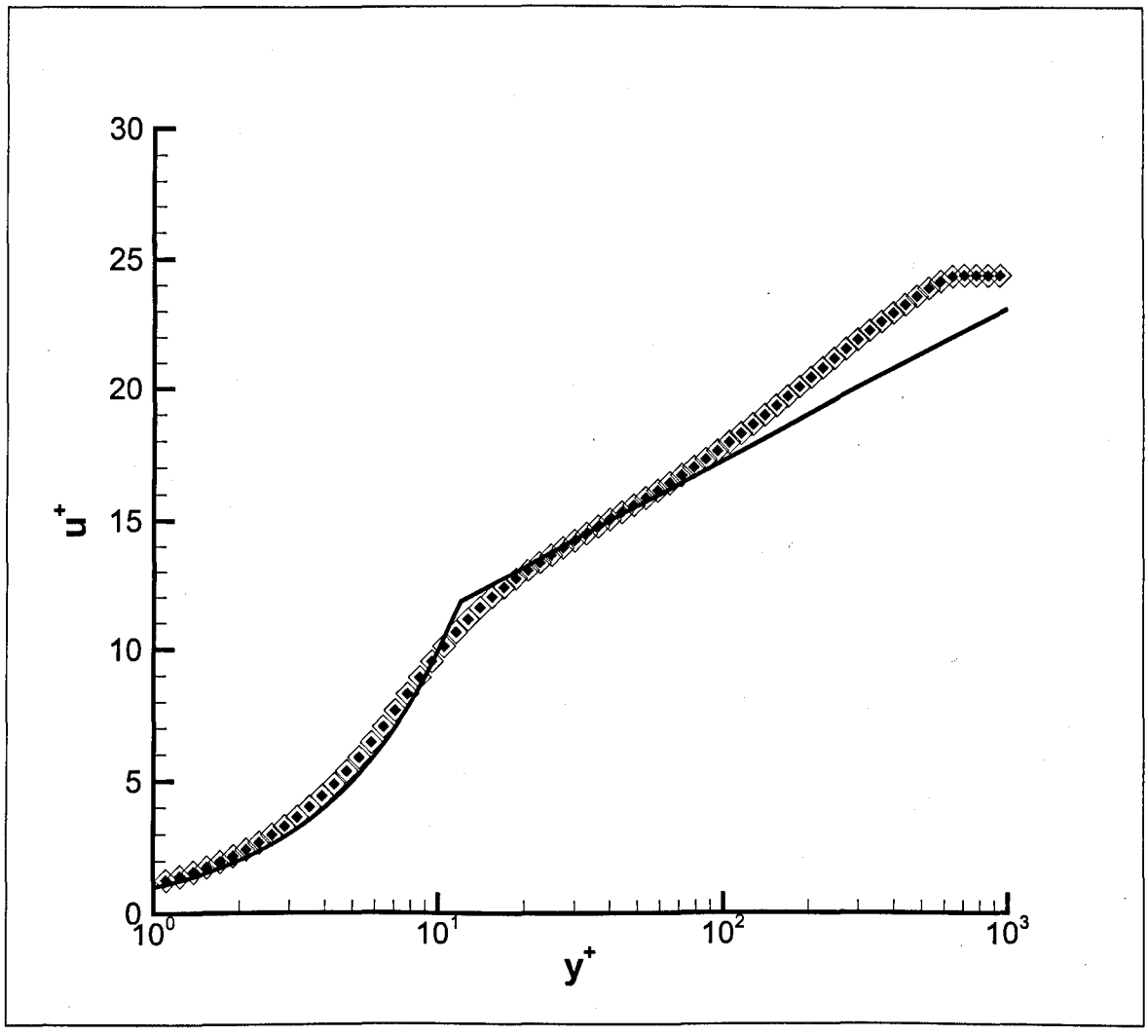

Figure 5.18: Wall function results for Grid 01 ($y_1^+ = 0.011$) ◇: No wall functions, •: With wall functions

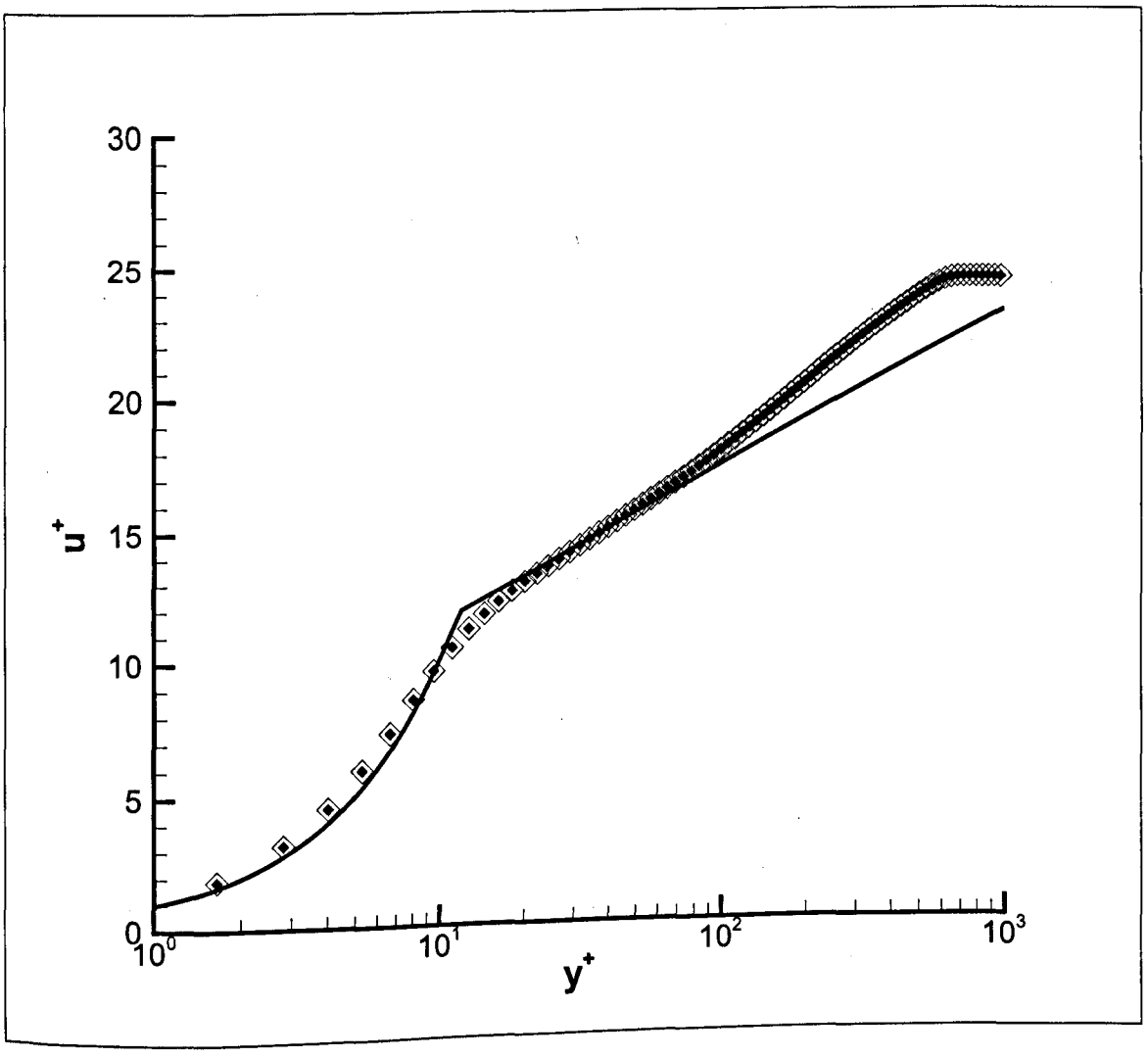

Figure 5.19: Wall function results for Grid 02 ($y_1^+ = 0.553$) ◇: No wall functions, •: With wall functions

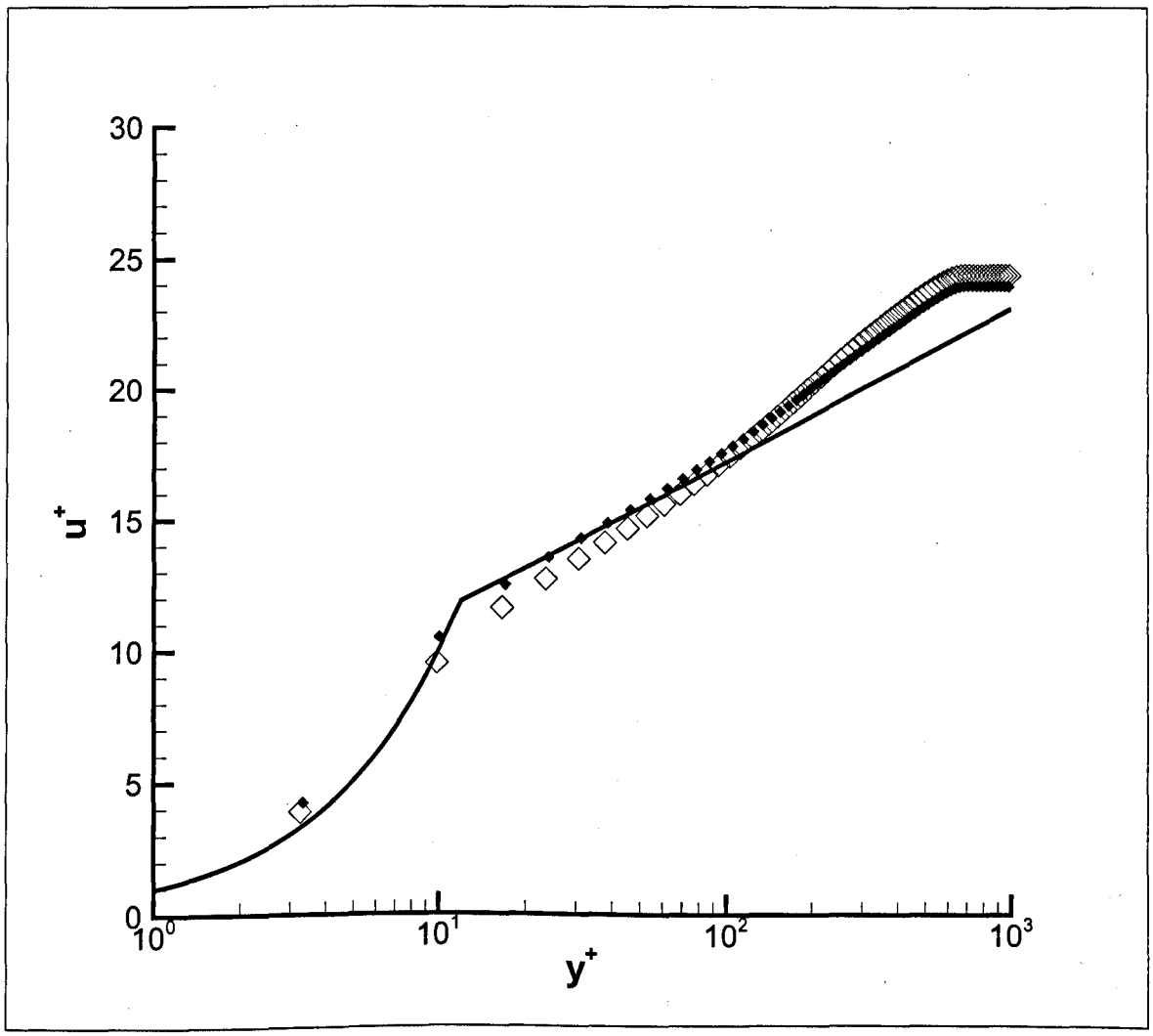

Figure 5.20: Wall function results for Grid 03 ($y_1^+ = 3.34$) ◇: No wall functions, •: With wall functions

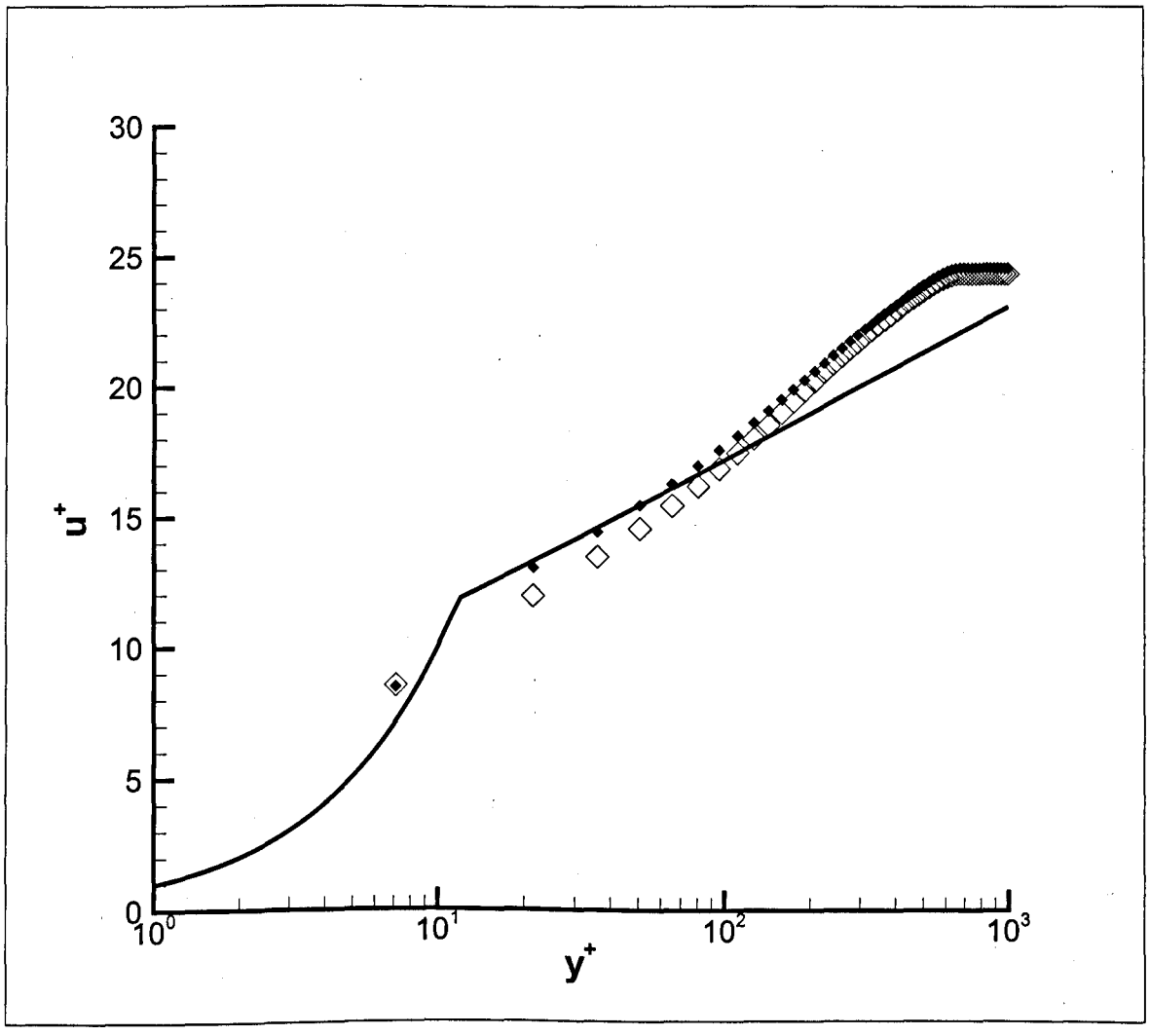

Figure 5.21: Wall function results for Grid 04 ($y_1^+ = 7.323$) $\diamond$: No wall functions, $\bullet$: With wall functions

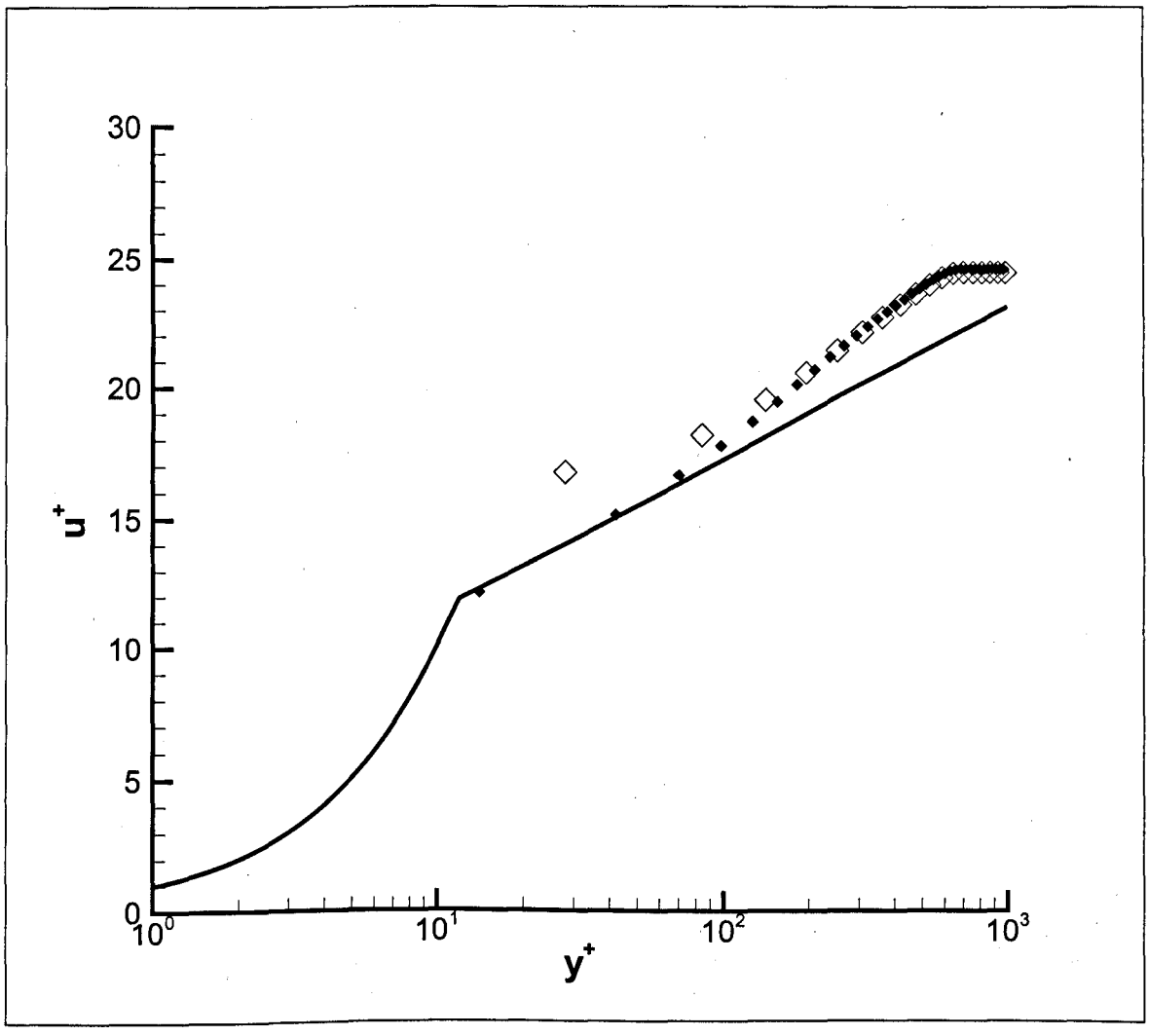

Figure 5.22: Wall function results for Grid 05 ($y_1^+ = 14.43$) ◇: No wall functions, •: With wall functions

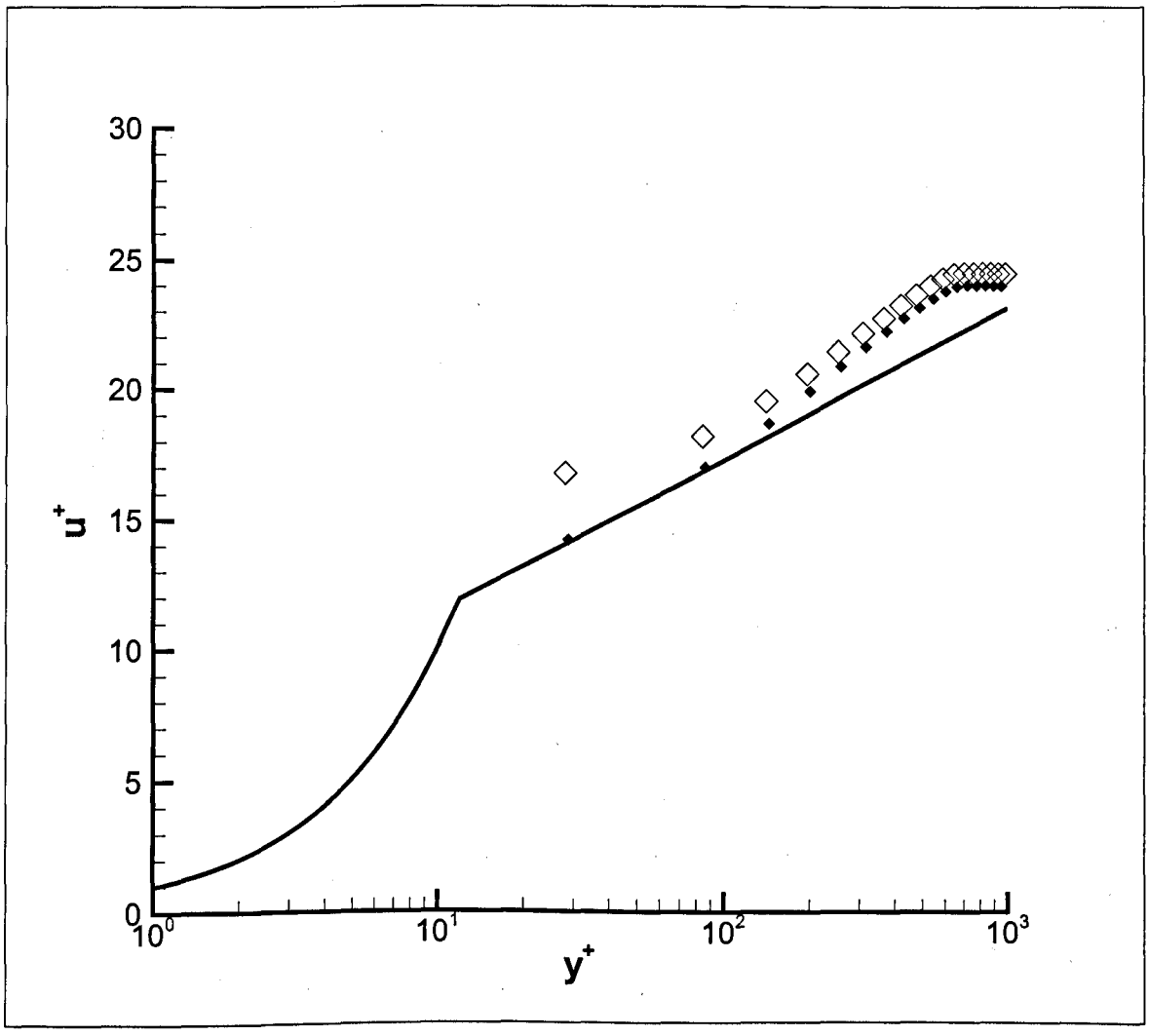

Figure 5.23: Wall function results for Grid 06 ($y_1^+ = 28.865$) ◇: No wall functions, •: With wall functions

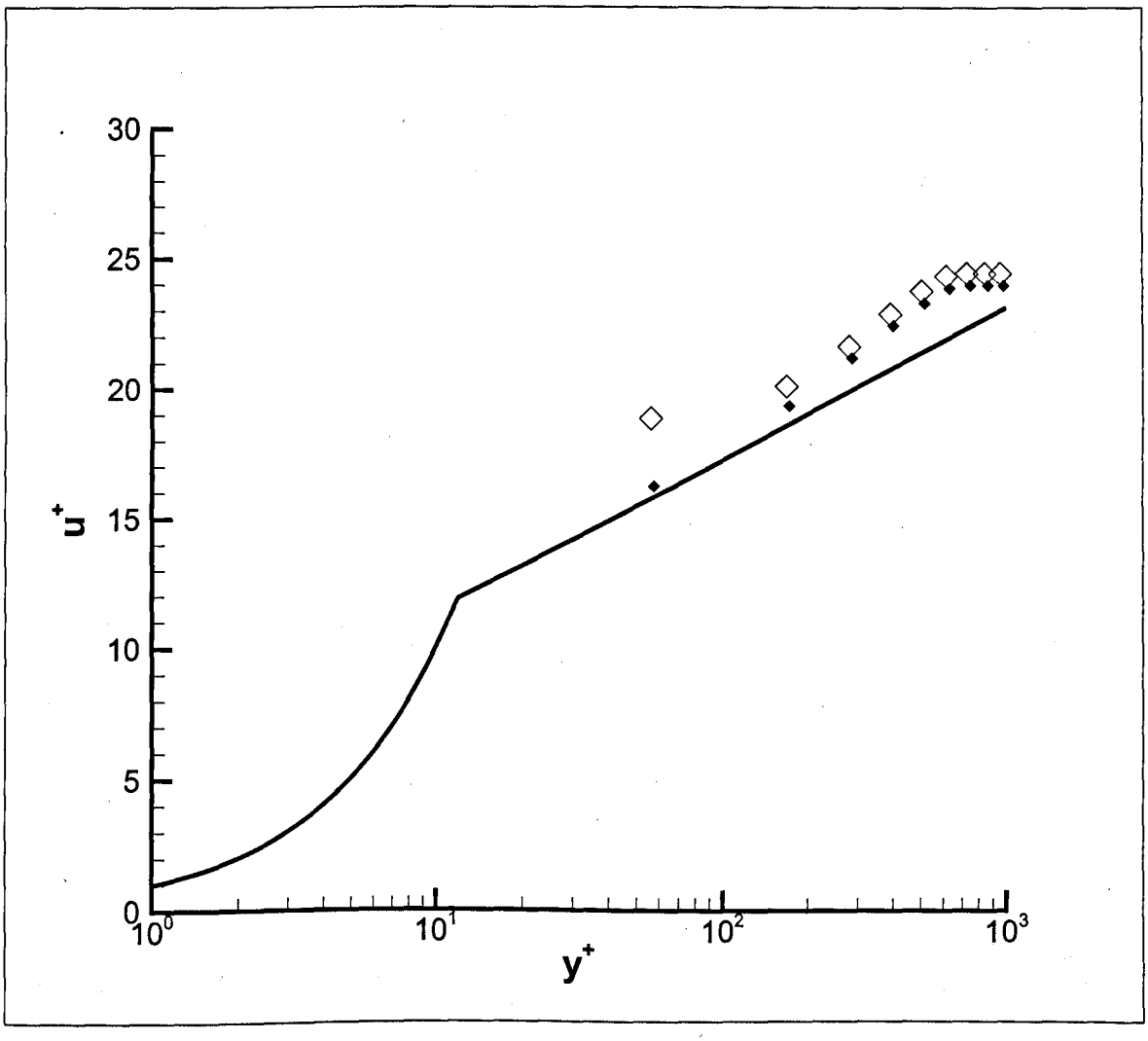

Figure 5.24: Wall function results for Grid 07 ($y_1^+ = 57.85$) ◇: No wall functions, •: With wall functions

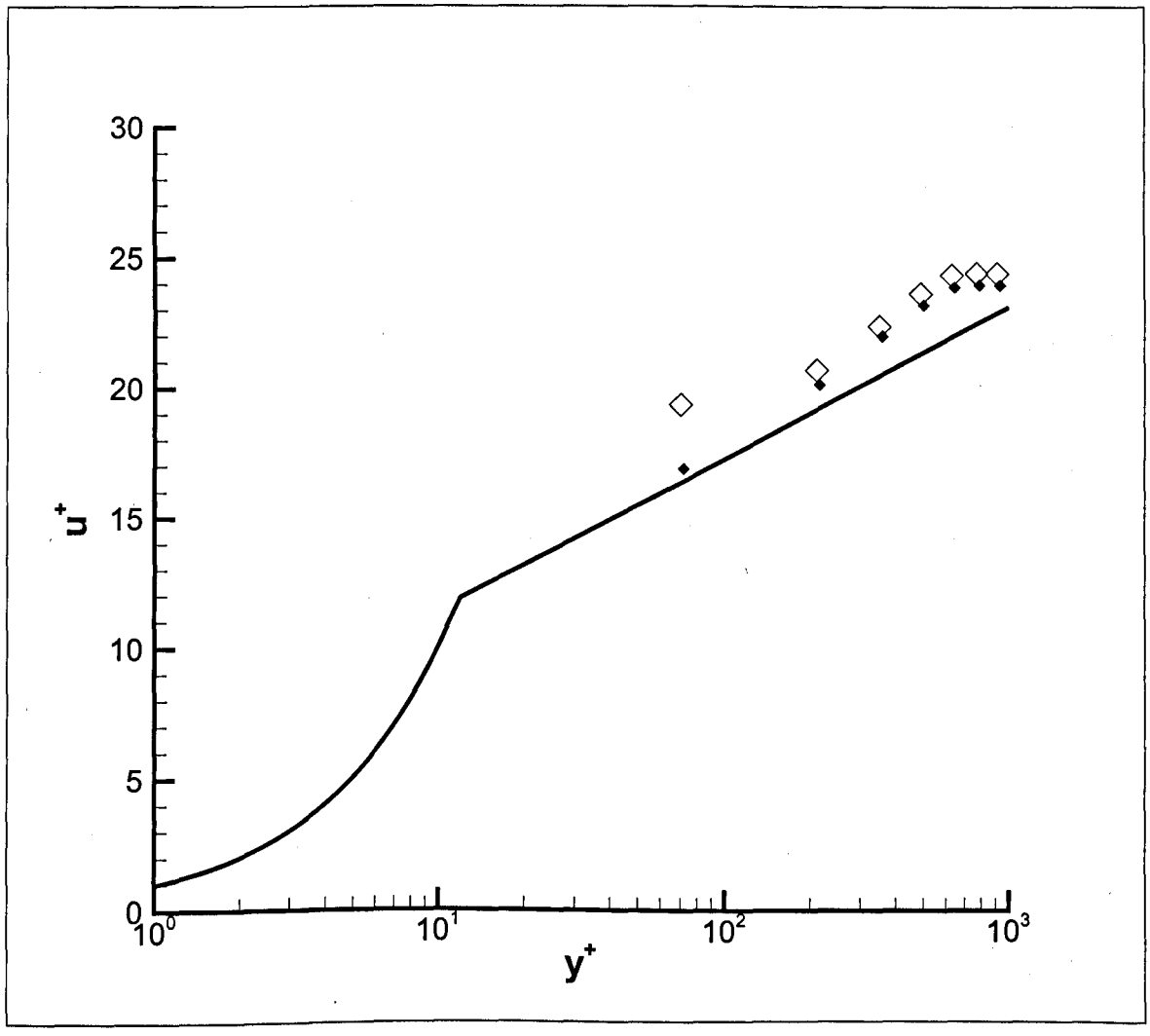

Figure 5.25: Wall function results for Grid 08 ($y_1^+ = 72.165$) ◇: No wall functions, •: With wall functions

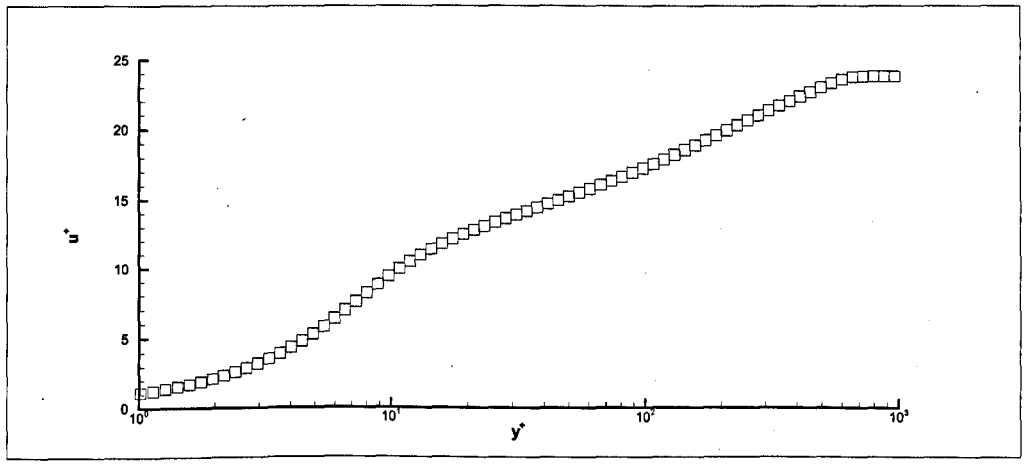

(a)

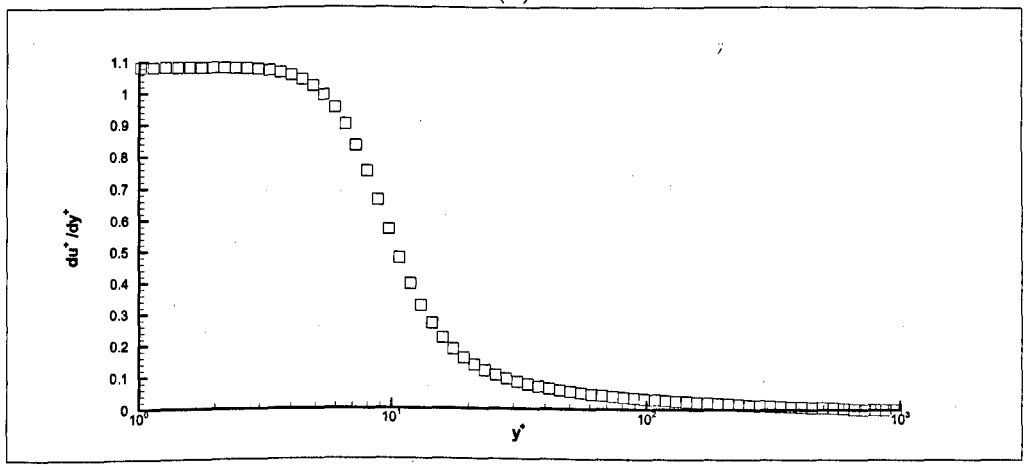

(b)

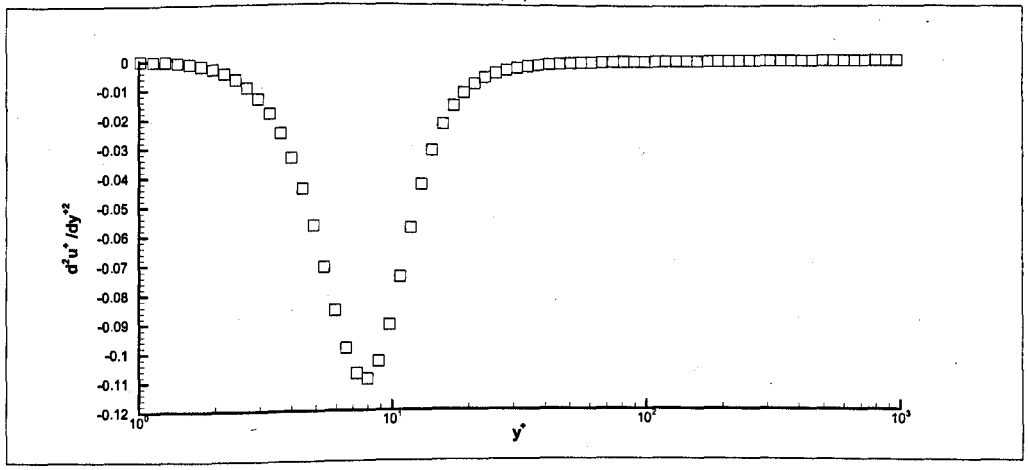

(c)

Figure 5.26: First and second derivatives for a typical law of the wall profile.

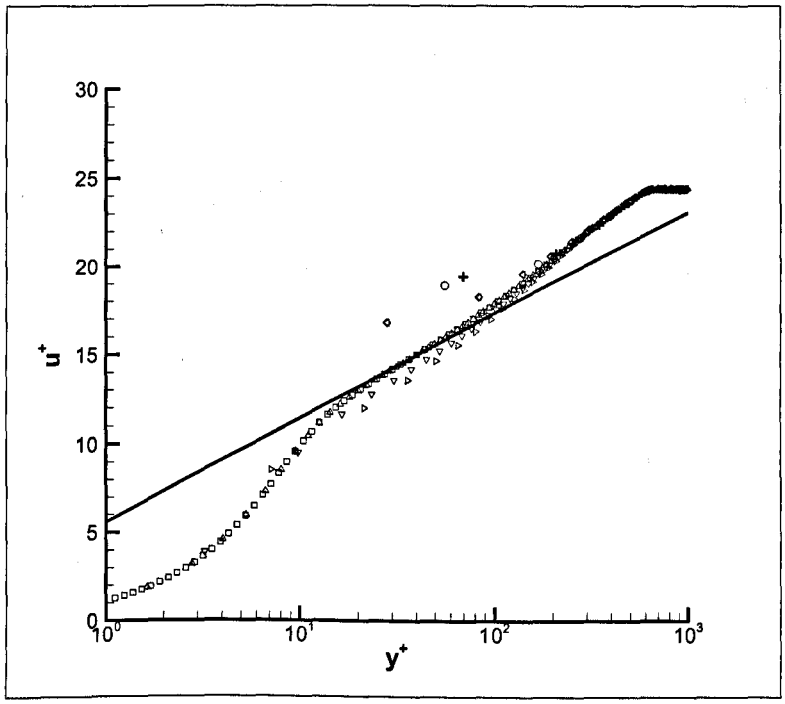

(a)

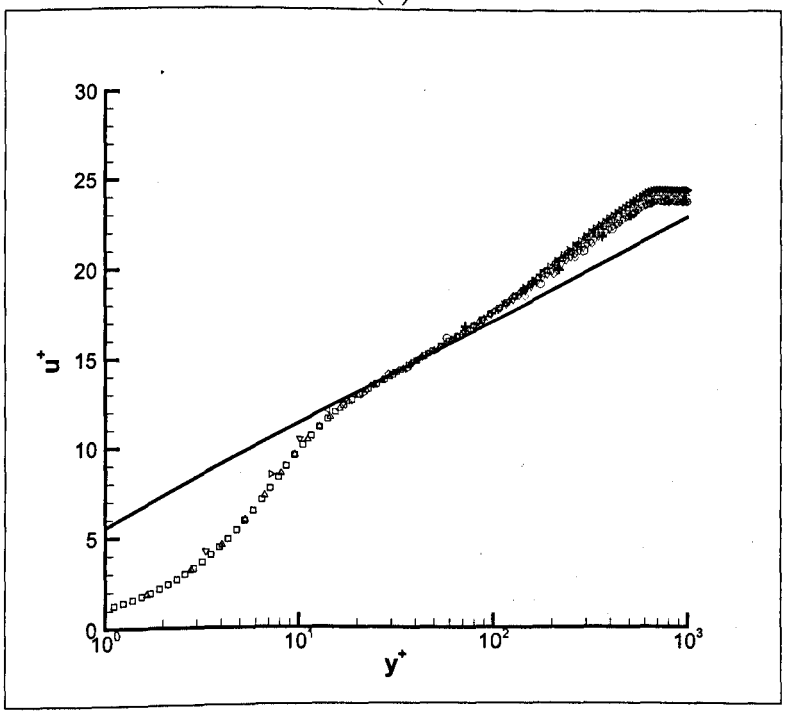

(b)

Figure 5.27: Summary of wall functions (a): Profiles without wall functions, (b): Profiles with wall functions, Grid 01 □, Grid 02 △, Grid 03 ▽, Grid 04 ▷, Grid 05 ◁, Grid 06 ◇, Grid 07 ○, Grid 08 +, Solid Line: Logarithmic Law as given in Eqn. 2.10

Chapter 6

Detached Eddy Simulation

As computing power has increased over the years, it was realised that a halfway house between full DNS and turbulence modelling could be reached. By using a very fine grid (although still not fine enough for DNS) and using RANS modelling to account for the turbulent effects missed by the coarseness of the grid, it was found that the unsteady turbulent behaviour could be better simulated. This method is known as Large Eddy Simulation and derives its name from the way in which the turbulent eddies much larger than the grid are completely resolved.

The problem with LES is that relatively fine grid resolutions are still required near the wall in all coordinate directions in order to resolve the near-wall structures which are key to turbulence production. For example, Tucker and Davidson (2004) proposes that LES requires grid resolutions of $\Delta x^+ \cong 100$, $\Delta y^+ \cong 1$ and $\Delta z^+ \cong 20$ are required.

Spalart *et al.* (1997) proposed a hybrid turbulence treatment method for reducing the overall cost of a turbulence simulation without sacrificing the large eddy resolution of LES methods. It was proposed that RANS modelling should be used near the wall

to reduce this grid requirement there but providing that resolution of the near-wall structures is not required. Such a method could reduce the grid requirement near the wall to $\Delta x^+ \cong 600$, $\Delta y^+ \cong 4$ and $\Delta z^+ \cong 200$.

Spalart *et al.* (1997) went on further to propose that this could be done using a single turbulence model and switching the turbulence length scale between the wall distance and the grid spacing accordingly. The following relation was given for the turbulent length scale:

$$d = min(d_{min}, C_{DES}\Delta) \tag{6.1}$$

where d_{min} is the wall distance, Δ is the maximum local grid spacing $max(dx, dy, dz)$, C_{DES} is an adjustable constant and d is the length scale in the destruction term of the S-A model (See the third term on the right hand side of Eqn. (5.12) in Chapter 5)

Although this method involves having regions of S-A RANS modelling and regions of LES (with S-A SGS modelling) it is not strictly a zonal model as the regions of RANS/LES are implicitly defined by the grid and not explicitly set. (See Spalart (2005)) This is known as Detached Eddy Simulation or DES.

An explanation can be sought by considering that for a true zonal method the regions of RANS and LES will always be fixed within the domain regardless of the grid resolution. This means that even if the grid is fine enough for an LES simulation, the RANS regions will still be modelled using RANS. However, for DES, the regions are flexible and dependent on the grid spacings. This has the effect of allowing a DES simulation to tend towards a fully LES simulation as the grid is made finer. Conversely an excessively coarse DES simulation will equate to a full RANS method.

The main advantage of using DES is that whilst a RANS method will always tend

towards a steady simulation regardless of the fineness of the grid and even if the flow is unsteady, a DES simulation will preserve the intrinsic flow unsteadiness by only using RANS modelling near the wall.

6.1 Validation of the DES Formulation

In order to test the DES formulation, the flow over a backward facing step has been simulated in order to give a qualitative study of the benefits of DES. There are a number of reasons for this. Firstly, this was the case used in the original proposal of the DES method as detailed in Spalart *et al.* (1997). In turn, Spalart chose this test case as experimental results for such a flow were given in Jovic and Driver (1995).

Secondly, there is much experimental and numerical data including the DNS work of Le *et al.* (1997). Finally and most importantly, this flow contains regions ideal for testing aspects of the formulation. There are areas of boundary layer flow near the wall to test the RANS regions of the simulation along with detached eddies shed from the step providing validation for the LES regions of the simulation.

The simulation set-up for this problem is shown in Figure 6.1. The flow domain is $30h$ long and $2h$ high with a step height, h, of 1m at $x = 10h$ thus giving an expansion ratio of 2. In order to achieve a turbulent Reynolds number, the inlet velocity was chosen as $0.074ms^{-1}$ resulting in a Reynolds number based on channel height of 5100. This ties in with the Reynolds number used by Spalart *et al.* (1997). The grid mesh was then chosen in order to provide compressed regions of the grid near to both the horizontal and vertical walls with uniform meshes in the streamwise direction given when further than one step height upstream or down stream of the step. This is similar to the simulations that were presented in Chapter 3.

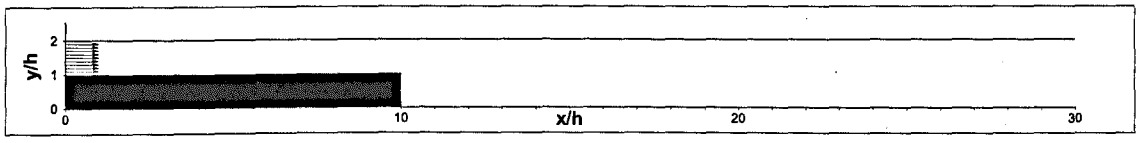

Figure 6.1: Set-up of the backward facing step simulations

For DES, the formulation given in Eqn. (6.1) is used to find the regions of RANS and the regions of LES. This is done by first finding the wall distance, d_{min} which is used by the RANS model to determine the maximum size of the eddies at any point in question and this is shown in Figure 6.2(a). The next stage is to calculate the value of $C_{DES}\Delta$ throughout the domain and a contour plot for this value is shown in Figure 6.2(b) assuming a grid similar to that in Figure 6.4. It can be seen that these contours are smallest where the grid is finest. Finding the destruction term length scale, d is then calculated by finding the minimum of these two parameters throughout the domain. Where the wall distance length scale is used, the turbulence model will effectively act as a pure-RANS model. However, if the grid spacing $C_{DES}\Delta$ is used, then the turbulence model acts as an LES sub-grid scale model. A representation of this for the coarse grid results is shown in Figure 6.3.

Two main grid meshes were chosen in order to illustrate the effect of grid mesh on a typical DES simulation. However, it should be noted that only two-dimensional simulations have been run here. Although this would appear to neglect the three-dimensionality of the flow, reasonable results can be obtained using such simulations. This is because the main motivation behind DES is to model the large scale detached eddies which may well be largely two-dimensional as a result of the two-dimensional step. Also, in this particular case the study is simply to illustrate the principles of DES and these can be done more than adequately using a simple two-dimensional simulation.

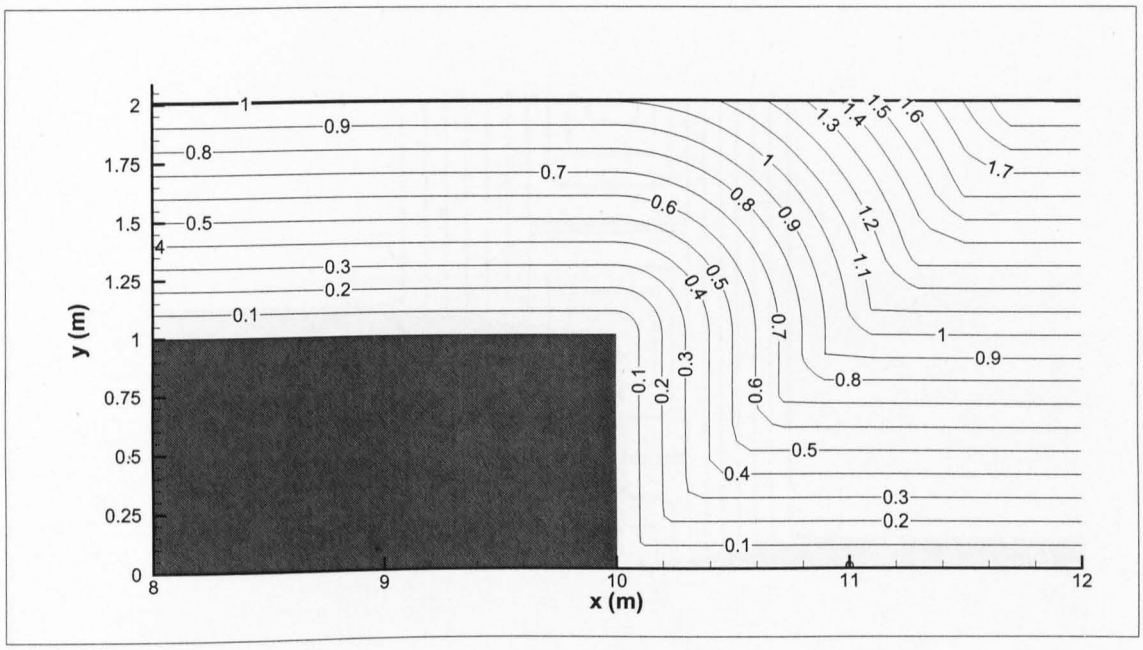

(a)

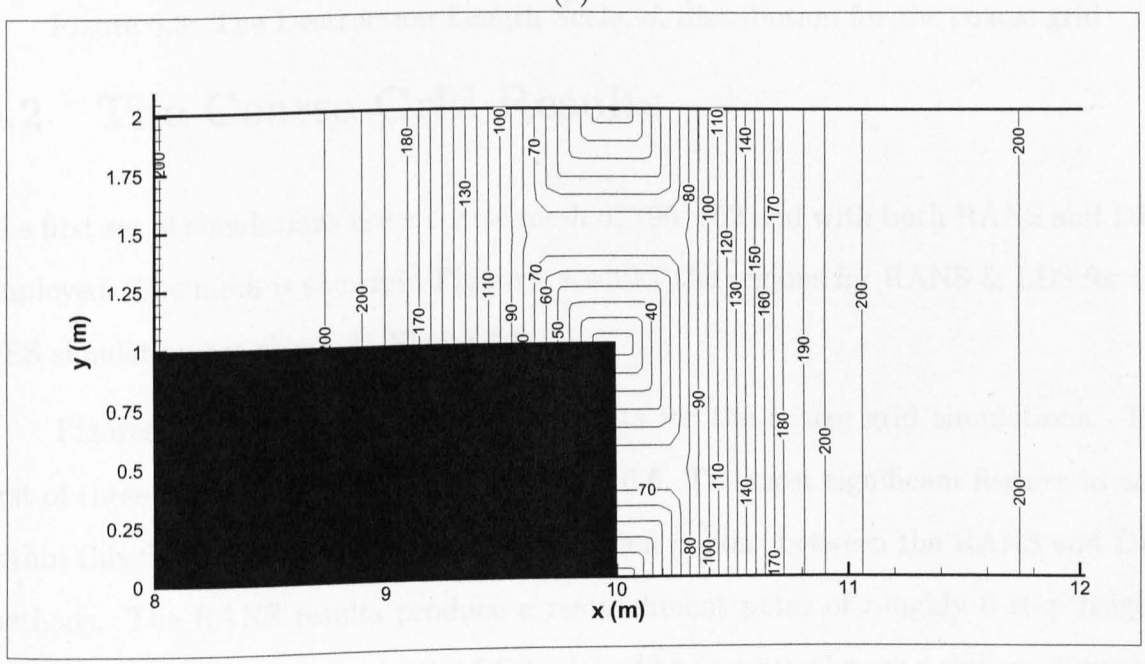

(b)

Figure 6.2: Distributions for (a) wall distance (m), d_{min} and (b) maximum grid spacing (mm), Δ for the coarse grid

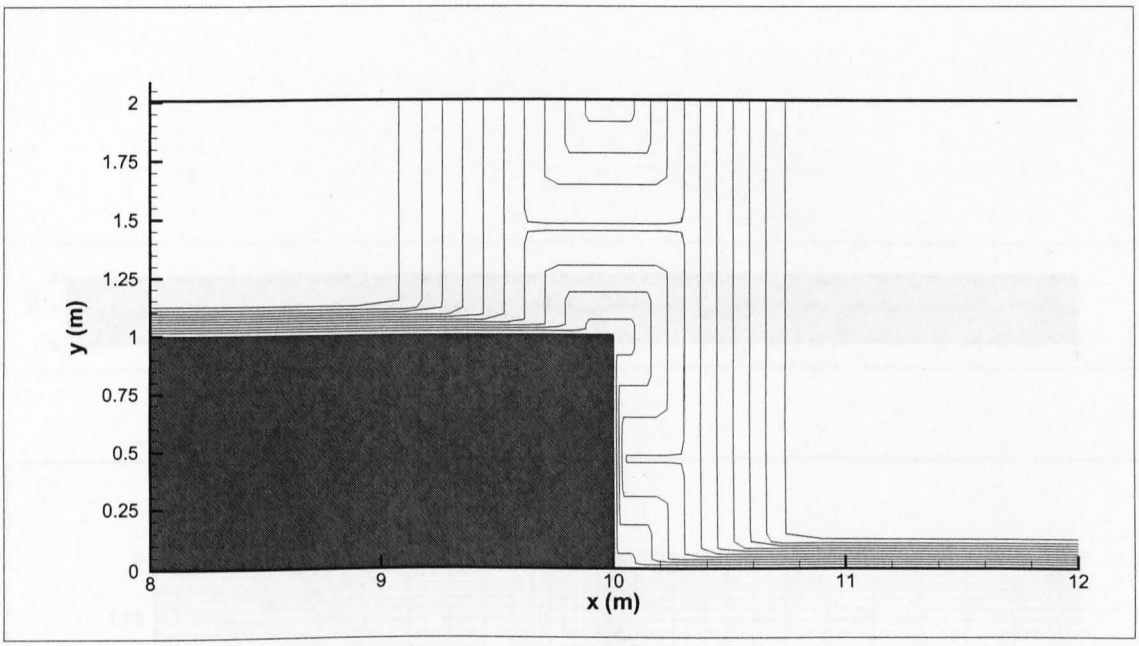

Figure 6.3: The Destruction Length Scale, d, distribution for the coarse grid

6.2 The Coarse Grid Results

The first set of simulations use a coarse mesh of 190×52 and with both RANS and DES employed. The mesh is shown in Figure 6.4 whilst the regions for RANS & LES for the DES simulation are shown in Figure 6.5

Figures 6.6-6.10 show a number of results for the coarse grid simulations. The first of these are the streamline plots in Figure 6.6. The most significant feature to note within this figure is the difference in recirculation regions between the RANS and DES methods. The RANS results produce a reattachment point of roughly 8 step heights downstream of the step whereas the DES method has a reattachment point much further downstream at nearer 14 step heights. Both of these values are significantly more than the value of 6 given in Jovic and Driver (1995) for a flow of this Reynolds number.

This is likely to be as a result of the reduced turbulent viscosity due to the DES

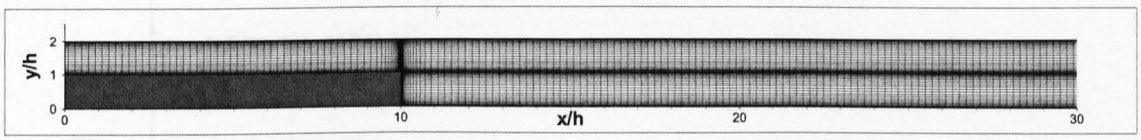

(a)

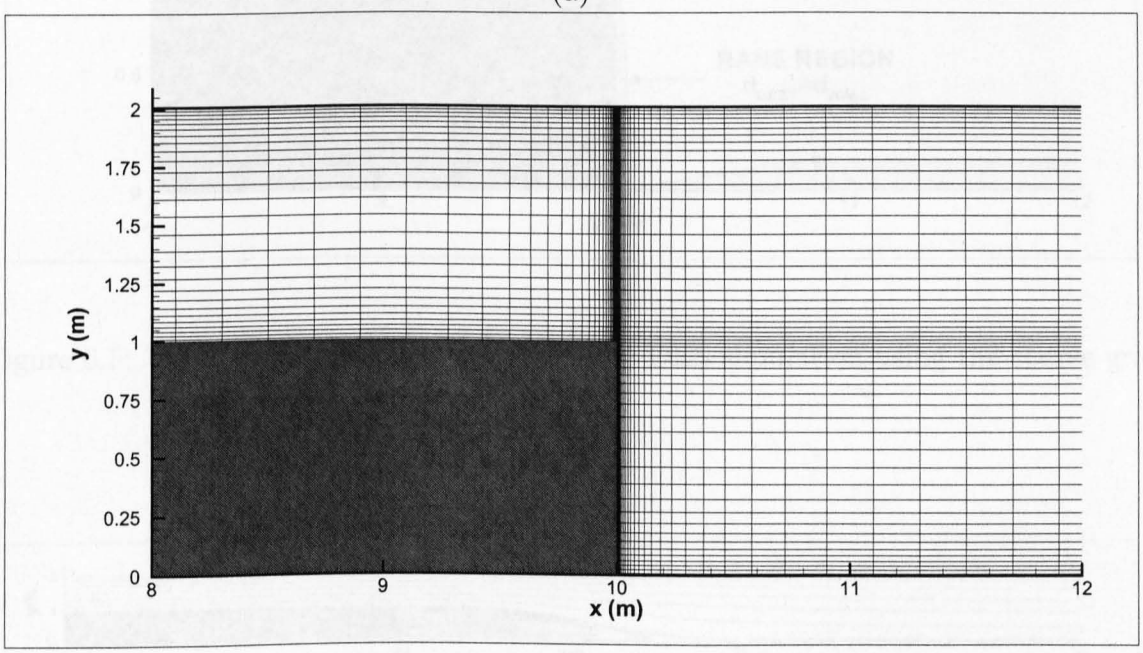

(b)

Figure 6.4: Coarse grid for the backward facing step simulations (a) Overall Grid, (b) Grid in the vicinity of the step

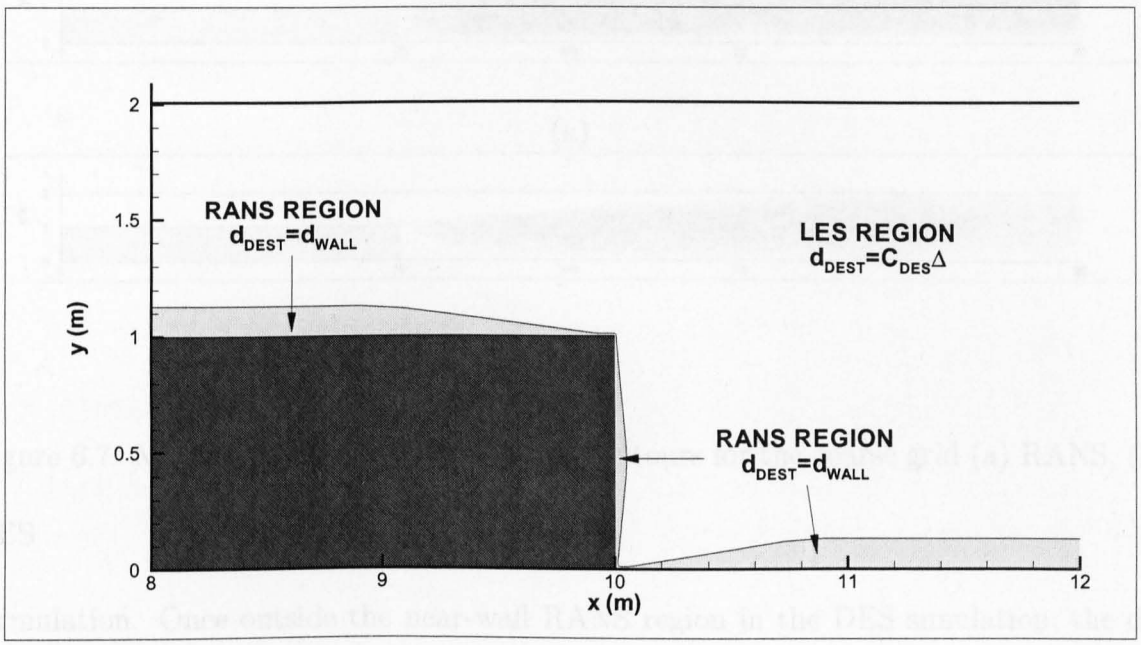

Figure 6.5: The RANS and LES regions for the DES simulation using the coarse grid

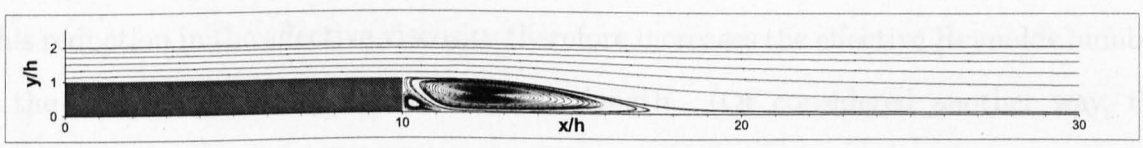

(a)

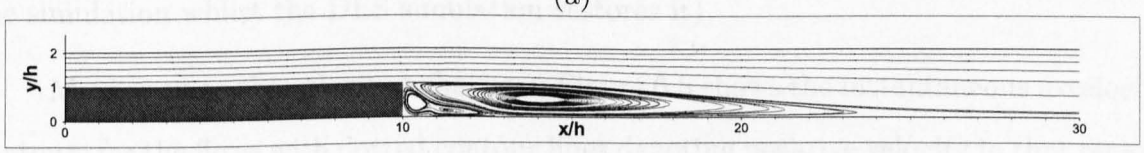

(b)

Figure 6.6: Streamtraces for the coarse grid (a) RANS, (b) DES

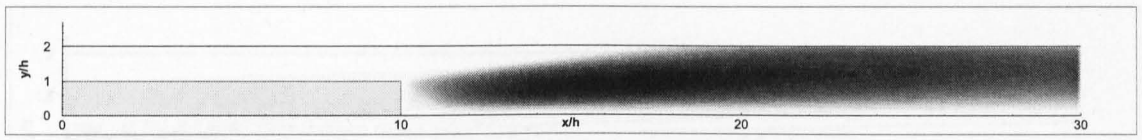

(a)

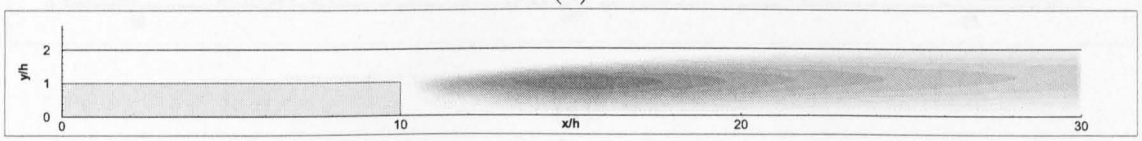

(b)

Figure 6.7: Modified turbulent viscosity, ($\tilde{\nu}$) contours for the coarse grid (a) RANS, (b) DES

formulation. Once outside the near-wall RANS region in the DES simulation, the destruction term is much higher than for a simple RANS simulation so reducing the overall eddy viscosity.

This can be seen in Figure 6.7 where the eddy viscosity is much less for the DES simulation even though both contour plots were produced with identical contour levels. This reduction in the effective viscosity therefore increases the effective Reynolds number of the flow so increasing the recirculation length. (Or considered another way, the increased viscosity of the RANS simulation decreases the effective Reynolds number of the simulation whilst the DES simulation restores it)

Moving on to the velocity behaviour, Figure 6.8 shows the instantaneous u-velocity contours for the flows with dotted contour lines denoting negative velocity in that region. These velocity plots are consistent with the streamtraces shown previously in that the negative velocity region extends further downstream for the DES simulation than for the RANS method results.

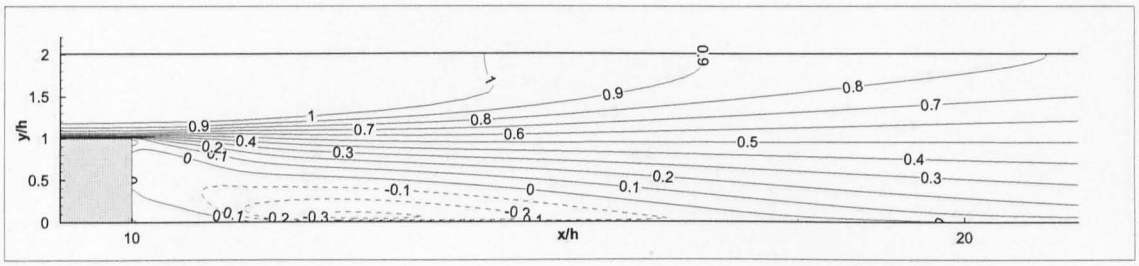

(a)

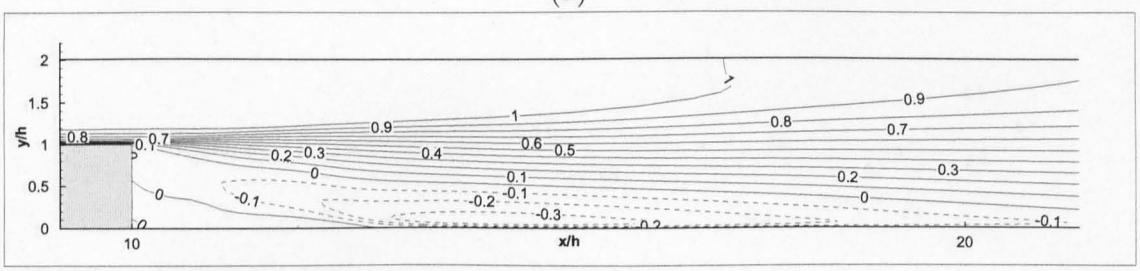

(b)

Figure 6.8: Instantaneous u-velocity contours for the coarse grid (a) RANS, (b) DES

However, the important point to note is when the instantaneous velocity contours of Figure 6.8 are compared with the mean velocity contour plots given in Figure 6.9. Both sets of contours are almost identical thus showing that the flows in both cases are steady with respect to time. This is unlikely as at the higher, turbulent Reynolds numbers, the flow is known to consist of unsteady shedding of eddies from the step downstream to the outlet. Here, it is clear that both the RANS and DES results are not showing this unsteady behaviour.

Finally, Figure 6.10 shows the vorticity contour plots for both methods. Here, the dotted contour lines denote anti-clockwise vorticity with the solid lines denoting clockwise vorticity. These plots confirm that there is no shedding and the regions of highest vorticity are restricted to the recirculation region immediately downstream of the step.

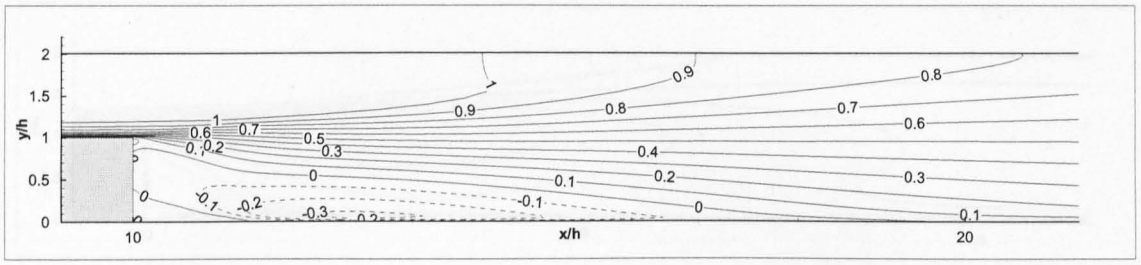

(a)

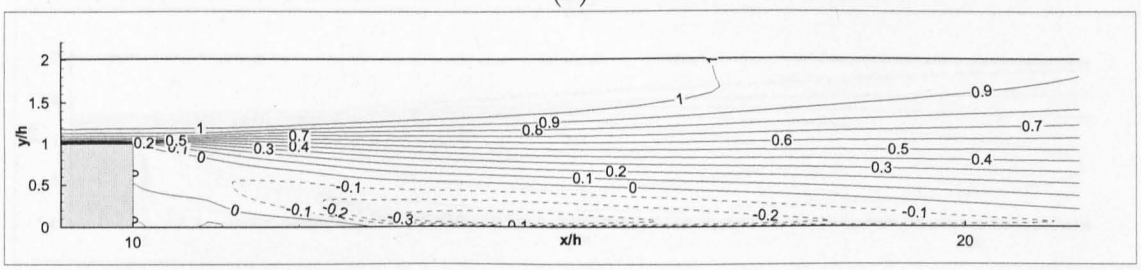

(b)

Figure 6.9: Mean u-velocity contours for the coarse grid (a) RANS, (b) DES

6.3 The Fine Grid Results

The fine grid results were produced by doubling the number of nodes in each coordinate direction to 380×100. This mesh is shown in Figure 6.11 whilst the regions for RANS and LES for the DES simulation are shown in Figure 6.12

The first results of interest consist of the instantaneous streamtrace plots given in Figure 6.13. From these plots, it is clear that there is a significant difference between these two methods. The RANS results given in Figure 6.13(a) are very similar to the previous, coarse grid results with a reattachment point of around 8 step heights downstream.

However, the DES results shown in Figure 6.13(b) are clearly unsteady with five eddies shown downstream of the bump on the top and bottom surfaces whilst a secondary

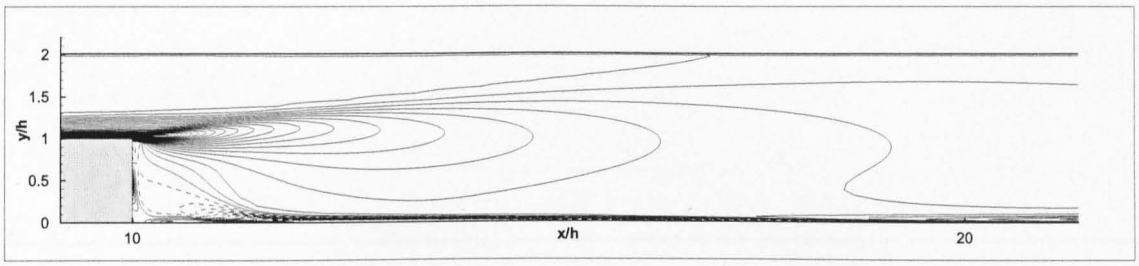

(a)

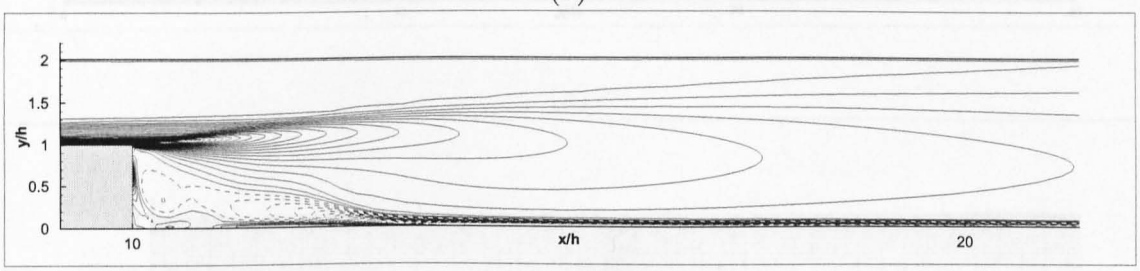

(b)

Figure 6.10: Instantaneous vorticity contours for the coarse grid (a) RANS, (b) DES

eddy is seen to be building next to the step. This difference of the flow behaviour is the single most important advantage of using DES. The unsteadiness of the flow regime is confirmed by the work of Armaly *et al.* (1983), Jovic and Driver (1995) and Spalart *et al.* (1997).

When considering the time averaged behaviour, it is clear that the RANS simulation, by its nature remains steady with respect to time whilst the DES results have an unsteady flow field. These are shown in Figures 6.14 (a) and (b). In these plots, the recirculation region for the RANS and DES simulations are seen to stretch to 8.5 and 3.5 respectively.

Whilst the RANS result is very similar to the previous, coarse grid results (a benefit of RANS in itself), the DES results are now under-estimated compared to the result given in Jovic and Driver (1995). This would propose that once the grid is fine

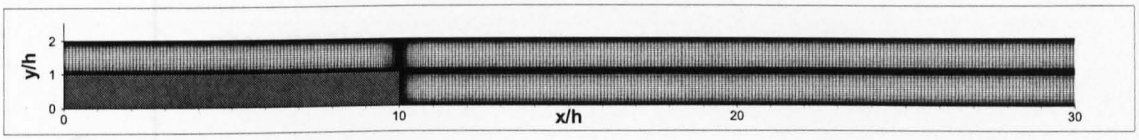

(a)

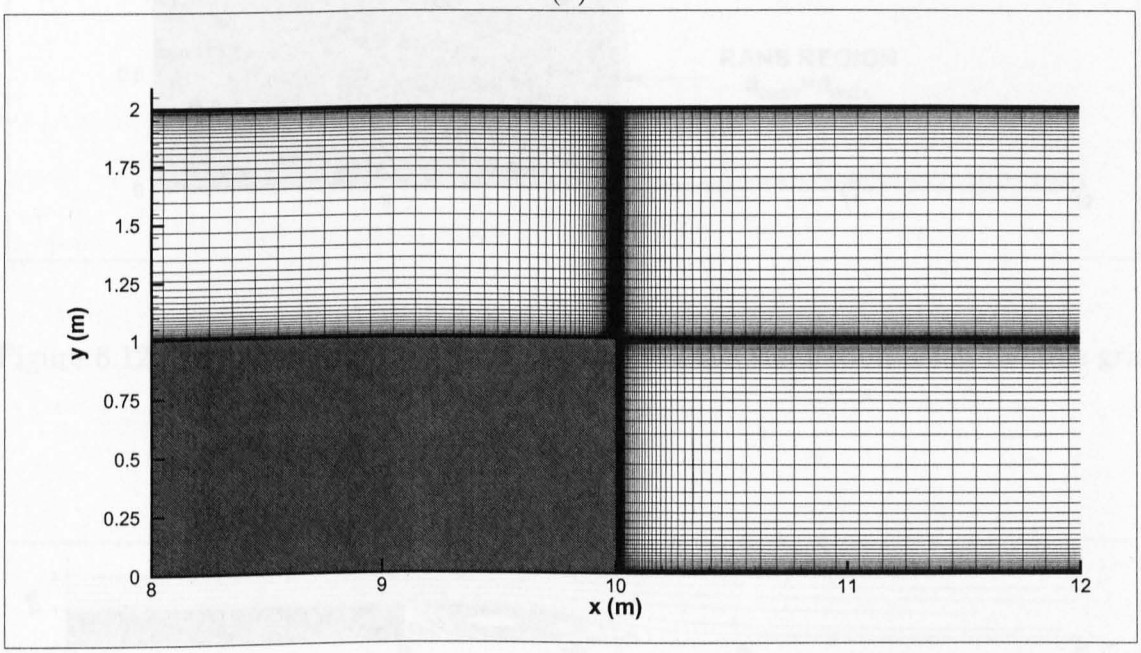

(b)

Figure 6.11: Fine grid for the backward facing step simulations (a) Overall Grid, (b) Grid in the vicinity of the step

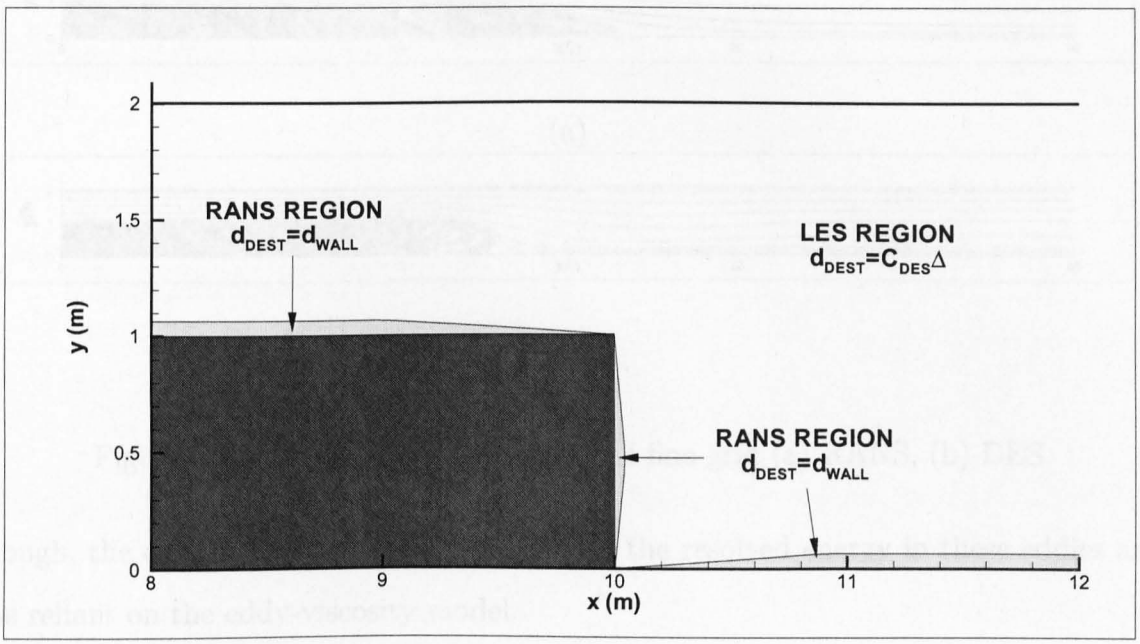

Figure 6.12: The RANS and LES regions for the DES simulation using the fine grid

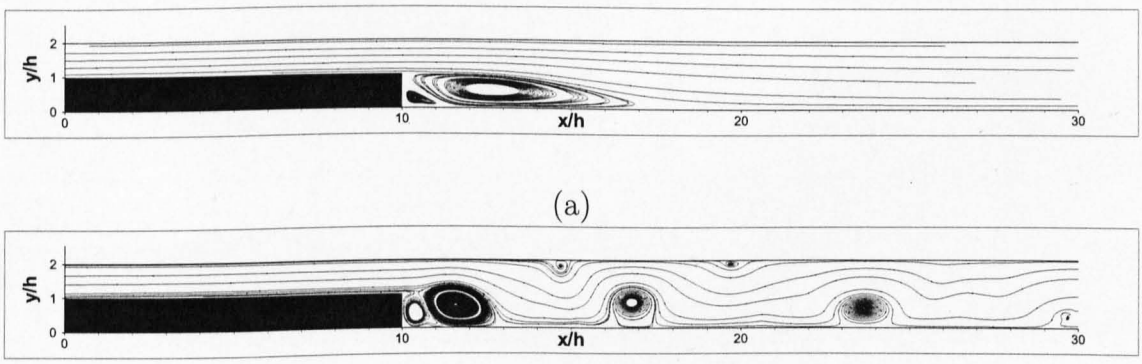

(a)

(b)

Figure 6.13: Instantaneous Streamtraces for the fine grid (a) RANS, (b) DES

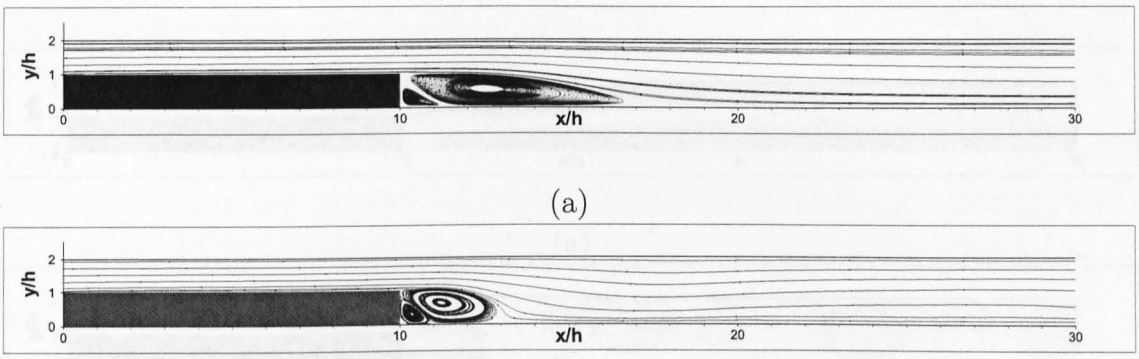

(a)

(b)

Figure 6.14: Mean Streamtraces for the fine grid (a) RANS, (b) DES

enough, the eddies become dependent more on the resolved energy in these eddies and less reliant on the eddy-viscosity model.

These results are also shown by the modified eddy viscosity plots shown in Figure 6.15 and the vorticity plots shown in Figure 6.16.

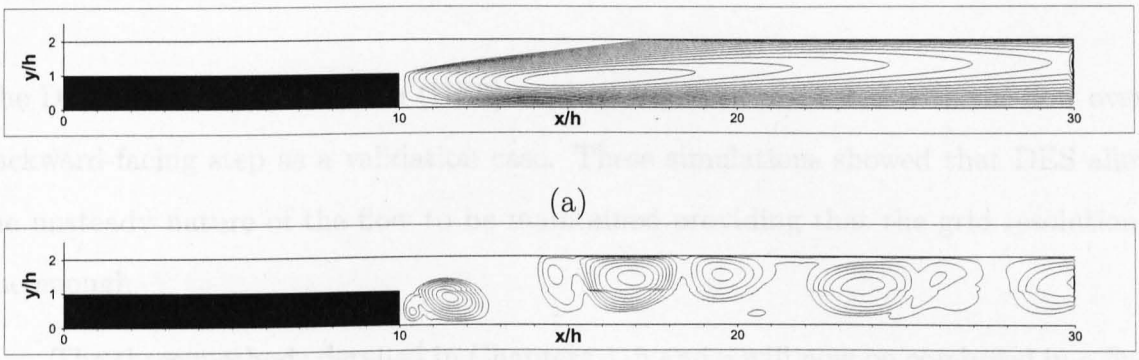

(a)

(b)

Figure 6.15: Modified turbulent viscosity, ($\tilde{\nu}$) contours for the fine grid (a) RANS, (b) DES

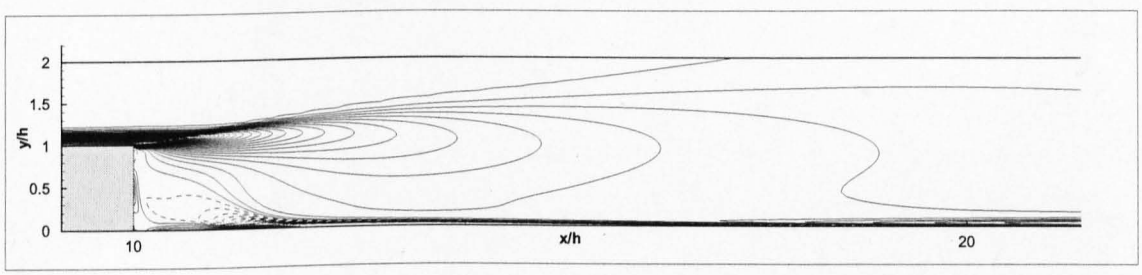

(a)

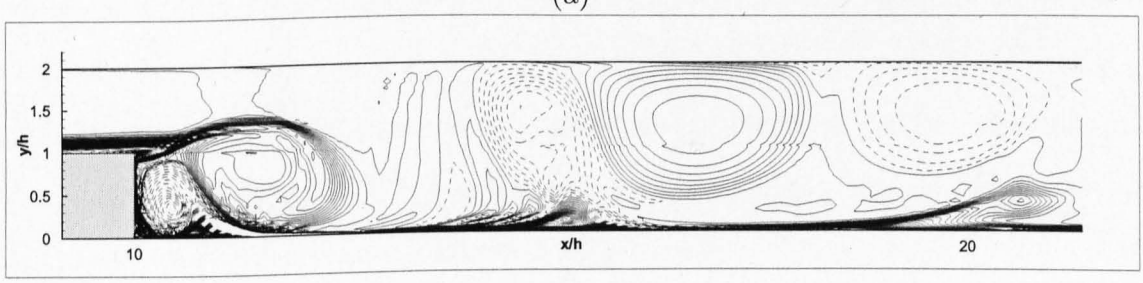

(b)

Figure 6.16: Vorticity contours for the fine grid (a) RANS, (b) DES

6.4 Conclusions

The Detached Eddy Simulation (DES) method has been presented with the flow over a backward-facing step as a validation case. These simulations showed that DES allows the unsteady nature of the flow to be maintained providing that the grid resolution is fine enough.

The three methods detailed in Chapters 4, 5 and 6 will now be combined in a final, feasibility study given in Chapter 7.

Chapter 7

Simulating Flow Control: A Feasibility Study

This final section brings together the separate studies described in Chapters 4, 5 and 6 and applies them to a typical turbulent separation control application with a view to using the methods in the field of engineering CFD. The purpose of this feasibility study is to assess the ability of the methods to work together without causing any numerical instability. This study has also been completed with the intention of observing any trends present in using the methods in isolation and in combination and, to the author's knowledge, is a study that has not been performed to date. To this end, the work within this chapter has been arranged into two distinct parts.

Firstly, simulations have been performed for the uncontrolled flow over the bump apparatus described in Bernard *et al.* (2003). These simulations are such that they compare each of the methods described separately and in conjunction and allows com-

parisons between the methods to be made.

Secondly, simulations of a steady-jet flow control application similar to the work detailed in Godard and Stanislas (2006b) has been performed. The main purpose of these simulations are to apply the described methods upon a typical flow control situation and compare the use of such methods to simulations without any special treatment.

Before considering these results, the set-up and parameters used for the simulations will now be covered in order to provide validation for the later sections.

7.1 Setting up the Lille simulations

7.1.1 The Uncontrolled Case of Bernard *et al.* (2003)

The work of Bernard *et al.* (2003) was begun under the framework of the European AEROMEMS-II project with the aim of considering the flow over the suction side of an aerofoil on the verge of separation. This was done using a two-dimensional bump within a wind-tunnel where a boundary layer had the opportunity to develop before flowing over the bump.

Due to the proposed size of such MEMS devices (of the order of $100\mu m$ to $1mm$) it was necessary to make the boundary layer and bump large in order to be able to use bigger jets whilst keeping the devices in proportion with the boundary layer on which they would be acting. For this reason, the windtunnel itself was 20m long with the bump occupying the final 5m of that length. The tunnel cross section was 1m (vertical) by 2m (spanwise) with the velocity used being 10m/s and a boundary layer thickness of 0.2m. This allowed Reynolds numbers based on momentum thickness of 7.5×10^3 to 2×10^4. Measurements were taken using hot-wire anemometry to characterize the flow velocity components, and micromanometer pressure transducers were used to estimate pressure information at the surface.

The results found were as to be expected for such a flow. The velocity increased up to around 15m/s over the apex of the bump with the pressure dropping to a minimum there. The pressure was also found to recover reasonably well after the bump although there is evidently a slight pressure loss across the bump overall.

The biggest feature observed is that the flow remains attached to the bump throughout the entire domain and this was a deliberate intention of the work. Com-

putations using a $k-\varepsilon$ model were performed by Dassault Aviation to this end and it was predicted that the flow would approach separation whilst not actually separating. The experimental results were found to be very close to the simulations of Dassault, certainly with respect to the pressure distribution over the bump.

The issues involved in applying the previous methods to this flow will now be considered.

7.1.2 Problem selection

Before beginning to define the simulation parameters, it was necessary to define the problem definition and domain limits. The first issue to address was the domain size and the position of the Lille bump within this domain. In the streamwise direction, a domain length of 8m was chosen as a longer domain with a length of 10m was seen to have little effect on the flow over the bump itself. In the wall normal direction, 1m was chosen as this was consistent with the experimental set-up.

Finally, the domain was reduced from 2m in the spanwise direction down to 0.5m. This was mainly in order to save on computational resources but was also chosen as the typical boundary layer thickness would be 0.2-0.3m so 0.5m seemed to comfortably contain any flow structures of comparable size to the boundary layer. This is consistent with the LES work of Nikitin *et al.* (2000).

In addition to this domain sizing, it was chosen to place the bump 1.5m downstream of the inlet as this would allow the flow sufficient time to develop its own structure before approaching the bump.

The next issue to address was that of Reynolds number. Although it would be ideal to run a simulation of the flow at Reynolds number as in the Lille case, it was soon

found that the grid requirements would be far too excessive. For example, the friction velocity at the apex of the bump (i.e. where it is at its greatest) is found to be around $0.535ms^{-1}$ and so employing the grid requirements in wall units of:

$$\Delta x^+ < 500 \tag{7.1a}$$

$$\Delta y^+ < 100 \tag{7.1b}$$

$$\Delta z^+ < 40 \tag{7.1c}$$

these would equate to the following limitations of:

$$\Delta x < 20.75mm \tag{7.2a}$$

$$\Delta y < 4.15mm \tag{7.2b}$$

$$\Delta z < 1.66mm \tag{7.2c}$$

Uniformly dividing the domain of $8m \times 1m \times 0.5m$ gives a total grid mesh of $386 \times 240 \times 301$ which equates to around 28 million nodes. Even given that this number could be reduced by using grid expansions to make the grid more economical, it would be unlikely that this mesh could be reduced down to the 1-2 million node mesh preferred. This is because although meshes larger than 2 million nodes are possible, in the field of engineering CFD design a large number of design simulations are desired so requiring a smaller mesh for quicker times.

For this reason, the Reynolds number was reduced by a factor of 10 with an inlet velocity from 10m/s to 1m/s. This resulted in an easier simulation to run whilst still being a high enough Reynolds number to produce useful results. It was also checked

that transition would occur well upstream of the bump at this reduced Reynolds number as given in Houghton and Carpenter (2003).

This choice in Reynolds number does have the disadvantage that the simulations will not be directly comparable with the experimental work of Bernard *et al.* (2003). However, as this current chapter is more about feasibility this is not critical. To this end, it is the author's desire to either obtain some lower Reynolds number experimental/computational results or to perform a full Reynolds number analysis using a finer grid. These proposals of further work will be expanded later in Chapter 8.

7.1.3 Selection of grids

In selecting the final grid, a number of factors needed to be considered. These factors were listed as follows:

- The boundary layer must have at least 10 nodes across its height to allow a realistic resolution of the layer
- The first off-wall grid node must be less than 1000 wall units from the wall (as covered in Chapter 5)
- The jet orifice must be approximated by no less than 10 nodes
- The grid spacing parallel to the wall should be less than 600 wall units in the streamwise (x) direction and 100 wall units in the spanwise (z) direction
- The grid must be less than 2 million nodes in total to allow reasonable engineering CFD to be performed

Grid expansion was used in the streamwise (x) direction and the spanwise direction (z) in order to achieve the fine grid spacings around the jet orifice. This produced something in the region of 13 nodes across the jet in x and 15 nodes across the jets in z. In total, there were 308 nodes in the x direction and 52 nodes in the z direction.

In the wall normal direction, the grid was left uniform as the bump took up around 30% of the domain height and any grid compressions/expansions would simply slow down the convergence of the solution in those areas. The wall normal grid spacing was chosen to be 0.05δ and this equated to the first off-wall grid spacing being roughly 100 wall units where the wall shear stress was largest. However, in the region of the bump itself this first off-wall node obviously varies as the surface intersects the cells at varying points in the y direction. This resulted in a grid count of 100 in the y direction. In total, the above grid results in 30,800 nodes in the x & y directions only (i.e. for a two-dimensional simulation) and 1.6 million nodes for a full three-dimensional simulation.

7.1.4 Boundary Conditions

At the inlet, a seventh-power law profile with a boundary layer thickness of 0.2m was applied in order to preserve the same boundary layer thickness to bump height ratio as would be expected for the full-Reynolds number case. Initially, unsteady fluctuations were also applied at the inlet to simulate turbulent flow structures but it was found that the flow was unable to sustain these structures and they quickly died away downstream. With regard to eddy viscosity boundary conditions, both $\tilde{\nu}$ and ν_t were set using a parabolic profile method detailed previously in Section 5.3.3.

On the top face of the domain, an impervious slip boundary condition was applied so that no flow could pass through this boundary whilst no boundary layer would develop

there. At the outlet, a simple differential boundary condition was chosen such that $(\partial u/\partial x) = 0$. This would have the effect of supressing any flow structures passing through the boundary but it was regarded that any separation would be likely to reattach so not causing a problem at the outlet. Finally, the span-wise faces were chosen to have periodic boundary conditions so allowing any flow structures pass out of one face to be bought back in to the other face. This is the same as running a number of jets one domain width apart. This means that although a single jet is modelled in the work that follows, the structures produced will be the same as for an infinite series of jets across the stream.

7.1.5 Numerical Methods

For the following simulations, either first order upwinding or the QUICK method of Hayase *et al.* (1992) were used as detailed in Chapter 3. For the given grid mesh and flow characteristics, standard central differencing was found to be unstable because of the high cell Peclet numbers within the majority of the domain. Other aspects of the flow solver used were as detailed in Chapter 3

7.2 The uncontrolled case

The uncontrolled case provides an excellent starting block for any subsequent flow control simulations as any issues relating to the high velocity flow surrounding any jet can be avoided until the uncontrolled base flow is validated. This section is arranged as follows. Firstly, a grid sensitivity analysis is performed to confirm that the mesh is adequate. Next, the simulation results are presented by comparing the velocity, pressure and boundary layer properties within the flow domain. Finally, conclusions regarding the comparison of the methods are covered.

7.2.1 The Simulation Parameters

A total of eighteen simulations were run testing a variety of grids, turbulence treatments, and immersed boundary methods. A summary of the parameters is given in Table 7.1. Firstly, the simulations are divided into two groups. A01-A09 which are performed without any immersed boundary methods and A10-18 which are performed with a full linear IBM in place. Next, the simulations are split between three different turbulence treatments, RANS modelling with a wall-resolved model, RANS modelling with a wall-functions model and Detached Eddy Simulation. Finally, the simulations are split between three different grid systems.

Table 7.1: Parameters for the uncontrolled Lille bump case (RS01)

Serial	Mesh ($nx \times ny$)	Turbulence	IBM
RS01-01-A01	307 × 100	RANS (WR)	None
RS01-01-A02	156 × 50	RANS (WR)	None
RS01-01-A03	78 × 25	RANS (WR)	None
RS01-01-A04	307 × 100	RANS (WF)	None
RS01-01-A05	156 × 50	RANS (WF)	None
RS01-01-A06	78 × 25	RANS (WF)	None
RS01-01-A07	307 × 100	DES (WF)	None
RS01-01-A08	156 × 50	DES (WF)	None
RS01-01-A09	78 × 25	DES (WF)	None
RS01-01-A10	307 × 100	RANS (WR)	Full Linear
RS01-01-A11	156 × 50	RANS (WR)	Full Linear
RS01-01-A12	78 × 25	RANS (WR)	Full Linear
RS01-01-A13	307 × 100	RANS (WF)	Full Linear
RS01-01-A14	156 × 50	RANS (WF)	Full Linear
RS01-01-A15	78 × 25	RANS (WF)	Full Linear
RS01-01-A16	307 × 100	DES (WF)	Full Linear
RS01-01-A17	156 × 50	DES (WF)	Full Linear
RS01-01-A18	78 × 25	DES (WF)	Full Linear

Note: WR=Wall Resolved model, WF=Wall functions model

7.2.2 The Effect of Grids

In order to justify the final grid selections a number of simulations showing grid sensitivity are now studied. The first of these is the pressure distribution for the simulations A01, A02 and A03 corresponding to the grid meshes given in Table 7.1. These simulations have been chosen as they incorporate no methods that are dependent on grid refinement meaning that the underlying grid independence can be investigated without any influence being produced by using wall functions, DES or IBM.

Considering Figure 7.1 the closeness of the fine and intermediate grid results (A01 and A02) show that these results are largely grid independent whilst the coarse grid results failed to predict the downstream pressure recovery correctly. The wall shear stress plots given in Figure 7.2 likewise show that the grid is reasonably independent for the fine (A01) and intermediate (A02) grids at least in the downstream portion of the flow. However, as the focus of the work is the downstream flow, then this is unlikely to cause any problems.

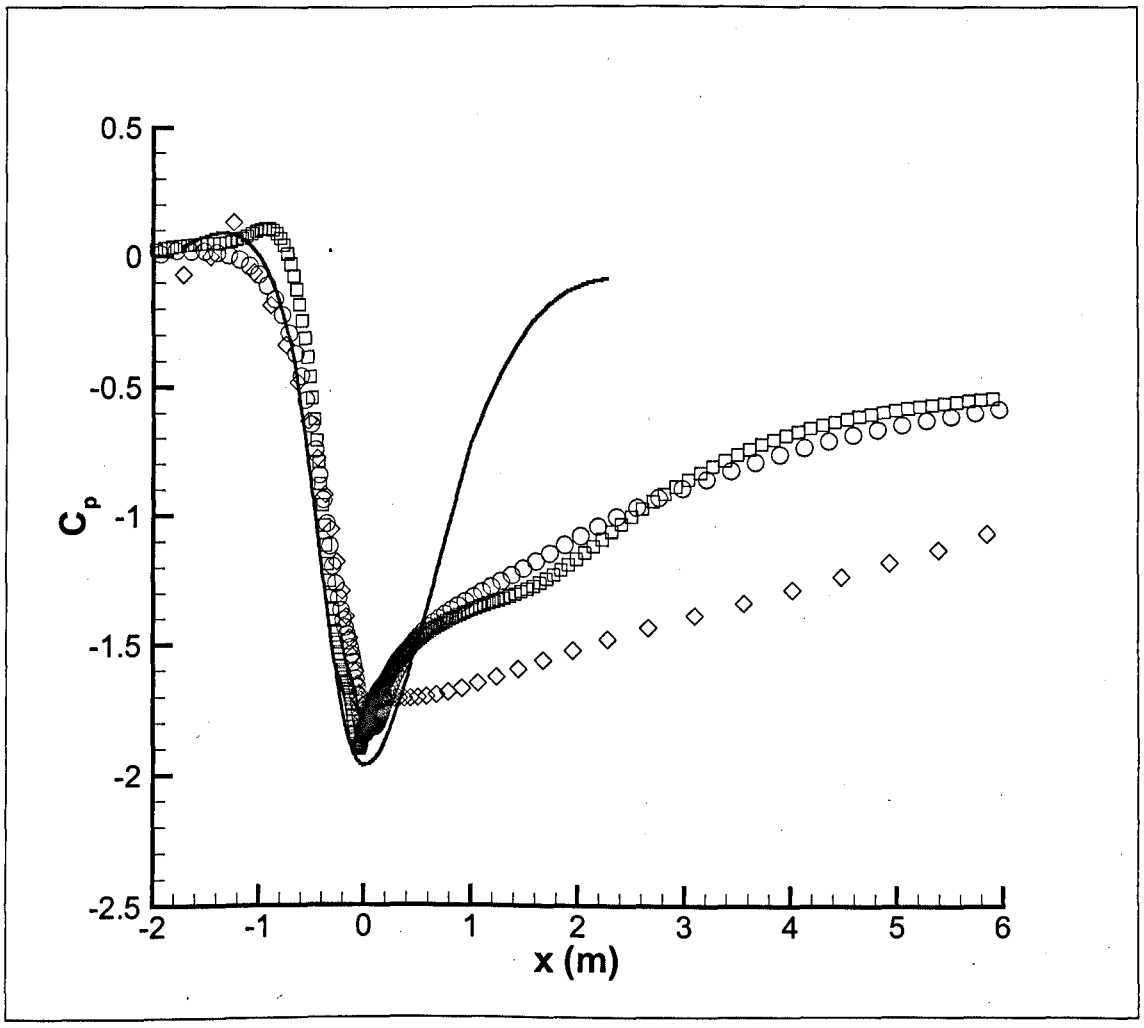

Figure 7.1: Pressure coefficient distribution for the uncontrolled case with three grid resolutions: □ = Fine Grid (A01), ○ = Intermediate Grid (A02), ◇ = Coarse Grid (A03), Solid Line = Higher Reynolds number results of Bernard *et al.* (2003)

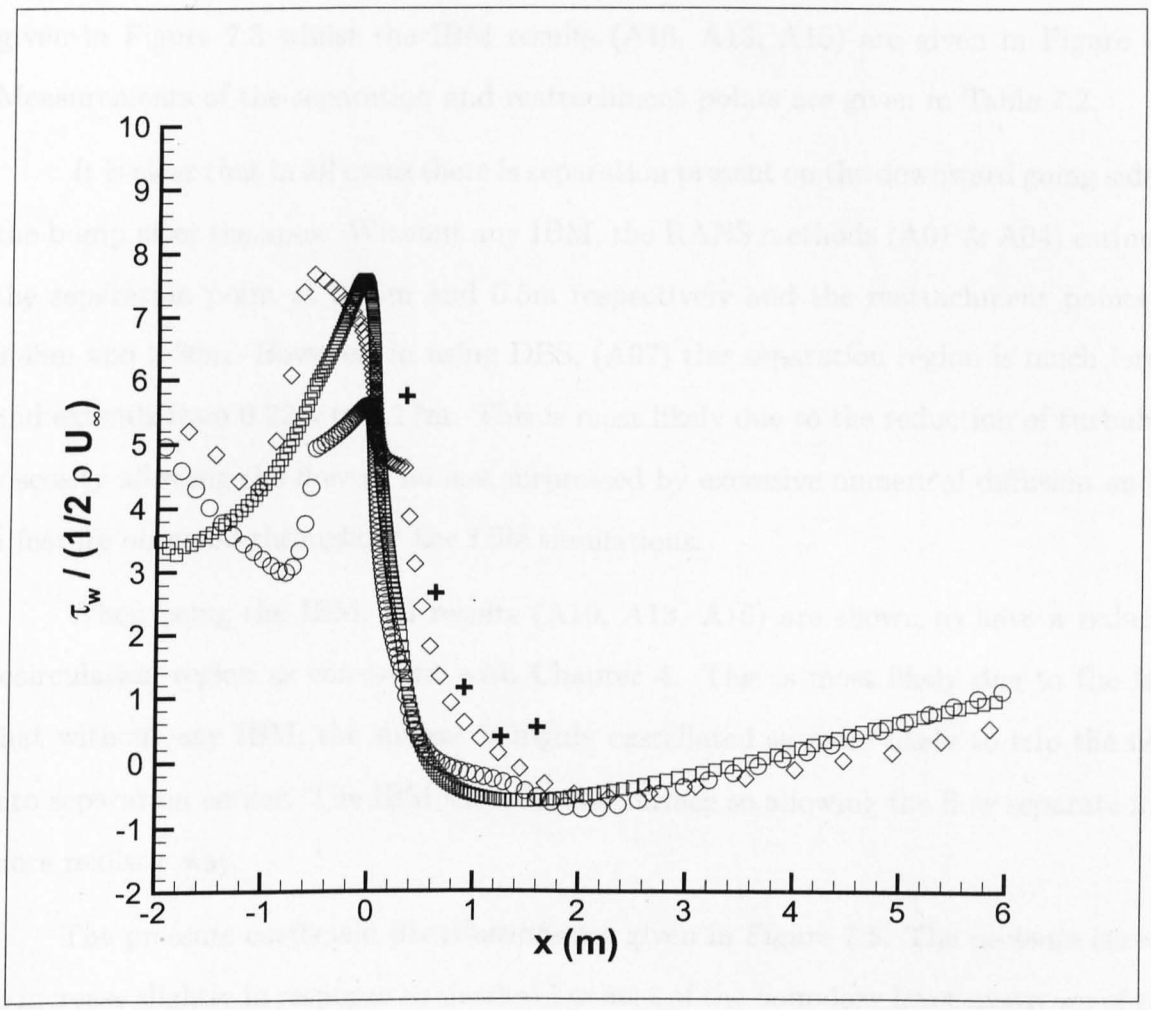

Figure 7.2: Wall shear stress distribution for the uncontrolled case with three grid resolutions: □ = Fine Grid (A01), ○ = Intermediate Grid (A02), ◇ = Coarse Grid (A03), + = Higher Reynolds number results of Bernard *et al.* (2003)

7.2.3 Comparison of the Methods

Initially, streamlines for the fine grid cases without any IBM (i.e. A01, A04, A07) are given in Figure 7.3 whilst the IBM results (A10, A13, A16) are given in Figure 7.4. Measurements of the separation and reattachment points are given in Table 7.2.

It is clear that in all cases there is separation present on the downward going side of the bump after the apex. Without any IBM, the RANS methods (A01 & A04) estimate the separation point at 0.35m and 0.5m respectively and the reattachment points at 3.48m and 3.36m. However, in using DES, (A07) this separation region is much larger and extends from 0.22m to 5.17m. This is most likely due to the reduction of turbulent viscosity allowing the flow to be less surpressed by excessive numerical diffusion and is a feature observed throughout the Lille simulations.

When using the IBM, all results (A10, A13, A16) are shown to have a reduced recirculation region as consistent with Chapter 4. This is most likely due to the fact that without any IBM, the surface is highly castellated so more likely to trip the flow into separation earlier. The IBM smooths the surface so allowing the flow separate in a more realistic way.

The pressure coefficient distributions are given in Figure 7.5. The pressure is seen to increase slightly in response to the development of the boundary layer upstream of the bump. After around 5δ upstream of the apex, the pressure begins to drop in response to the flow speeding up over the constriction. Minimum pressure is, as expected, reached over the apex itself where the velocity is greatest. However, the real area of interest is in the region of adverse pressure behind the bump.

Generally, the pressure results start to recover behind the bump but eventually they all exhibit a plateau which is present as a result of separation. This is due to

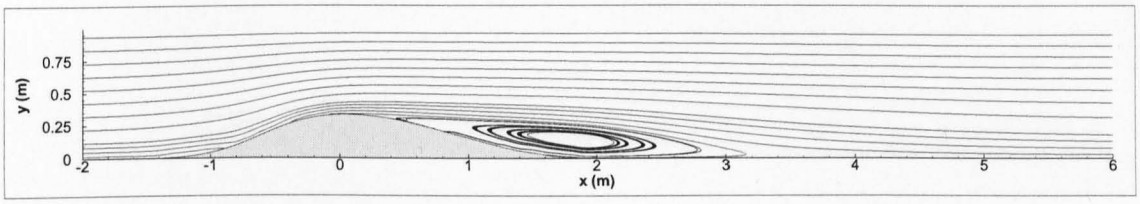

(a)

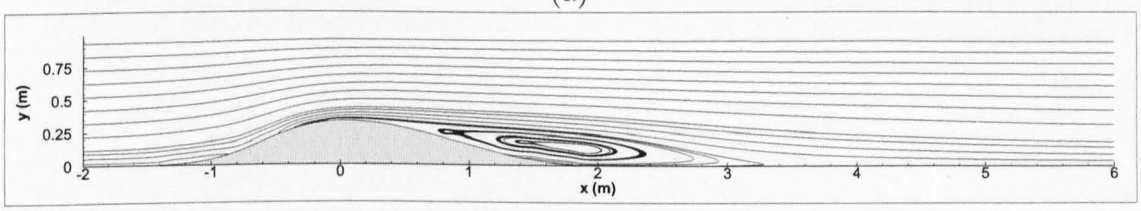

(b)

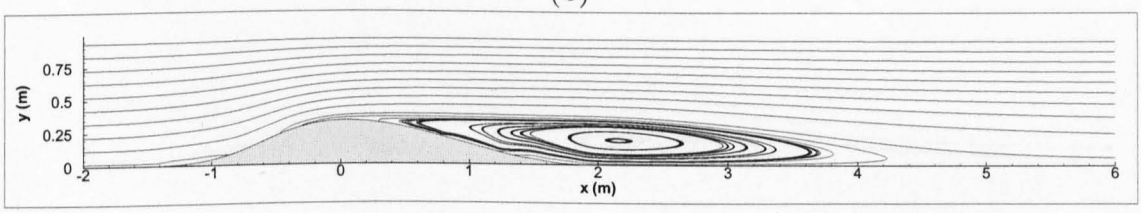

(c)

Figure 7.3: Streamtrace plots for the uncontrolled Lille bump case without Immersed Boundary Methods: (a) A01: RANS(WF), (b) A04: RANS(WF), (c) A07: DES

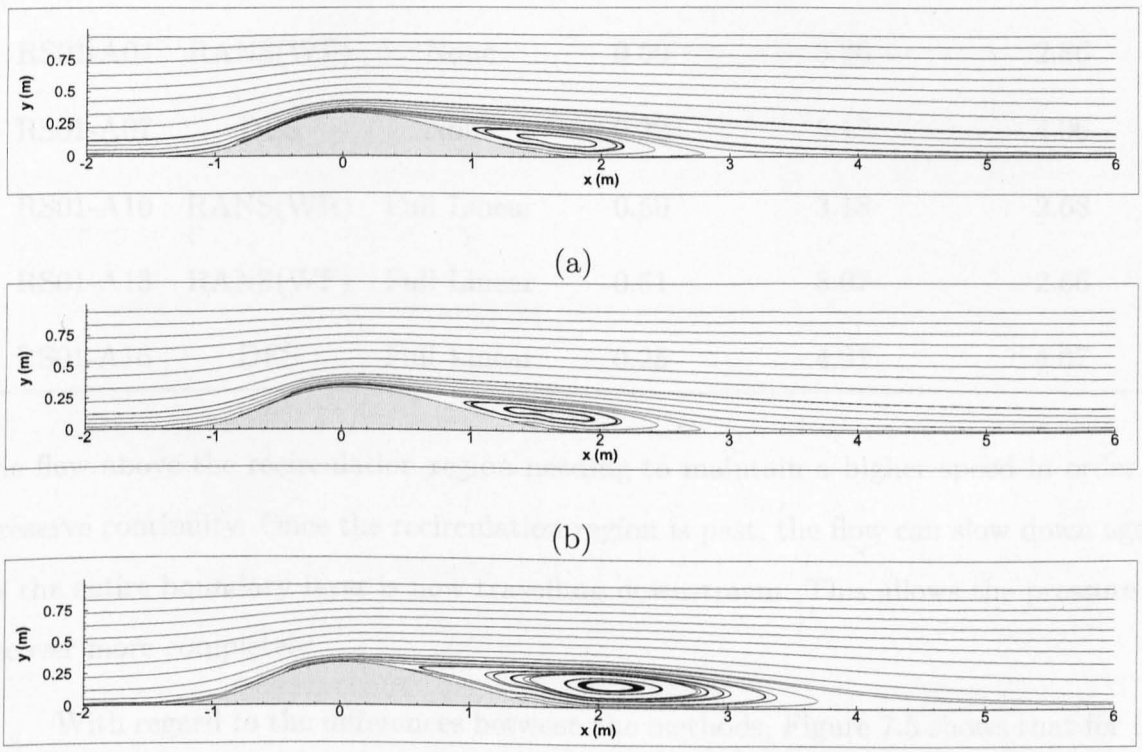

(a)

(b)

(c)

Figure 7.4: Streamtrace plots for the uncontrolled Lille bump case with Immersed Boundary Methods: (a) A10: RANS(WF), (b) A13: RANS(WF), (c) A16: DES

Table 7.2: Separation results for the uncontrolled Lille bump case

	Turbulence Treatment	IBM	Separation Point (m)	Reattachment Point (m)	Recirculation Length (m)
RS01-A01	RANS(WR)	None	0.35	3.48	3.13
RS01-A04	RANS(WF)	None	0.50	3.36	2.86
RS01-A07	DES	None	0.22	5.17	4.96
RS01-A10	RANS(WR)	Full Linear	0.50	3.18	2.68
RS01-A13	RANS(WF)	Full Linear	0.51	3.07	2.56
RS01-A16	DES	Full Linear	0.25	4.91	4.67

the flow above the recirculation region needing to maintain a higher speed in order to preserve continuity. Once the recirculation region is past, the flow can slow down again as the entire boundary layer is now travelling downstream. This allows the pressure to recover more completely.

With regard to the differences between the methods, Figure 7.5 shows that for the initial results using wall resolved RANS and without an IBM (A01) the flow separates as expected. When these results are improved using RANS with wall functions (as shown in A04) then the profile is seen to recover slightly more strongly although there is not a huge difference between the two results. This lack of difference is most likely due to the grid already being fine enough to produce reasonable results with wall resolved RANS alone. Finally, when incorporating DES (A07) the flow is much slower to recover which is consistent with the extended separation shown previously.

Figure 7.5 also shows the effect of using an IBM and these results are given in A10,

A13 & A16. The differences between the turbulence modelling results are the same as given previously although all results are shown to recover much more quickly than the results without IBM. This would be consistent as the smoother surface will allow the flow to get back to normal more quickly. Figure 7.6 shows the velocity at the edge of the boundary layer, U_e, and these results show similar trends to the pressure results although evidently the velocity changes in the opposite sense due to pressure coupling. For the Lille case, (shown with lines and +) both the pressure and edge velocity, show a much quicker recovery which is consistent with an unseparated flow as would be expected with a higher Reynolds number.

Looking at the flow in the vertical direction from the bump surface, a series of velocity profiles are detailed in Figure 7.7. Each plot shows the velocity profile at 1.0m intervals from 2m upstream of the bump to 5m downstream.

Up to the bump apex, the velocity profiles are almost identical due to the main influence there being the driving force of the main flow rather than any wall effects. As a point of interest, the IBM results show a slight negative velocity at the wall here and this is as a result of the method rather than an indication of any separation.

By 1m downstream of the apex, the flow is clearly separated (consistent with the separation point results in Table 7.2) and there starts to be a significant difference in the results. The DES results with and without IBM are both the most reversed so indicating the most separated profile. For the RANS simulations, the IBM results are seen to be the most positive showing they are stongest whilst the non-IBM results with RANS are in between the two extremes. Examining the flow downstream, these profiles exhibit similar trends.

Turning one's attention to the turbulent viscosity ratio, ν_t/ν, as shown in Figure 7.8 a similar trend is seen and there is little difference between methods up to the apex.

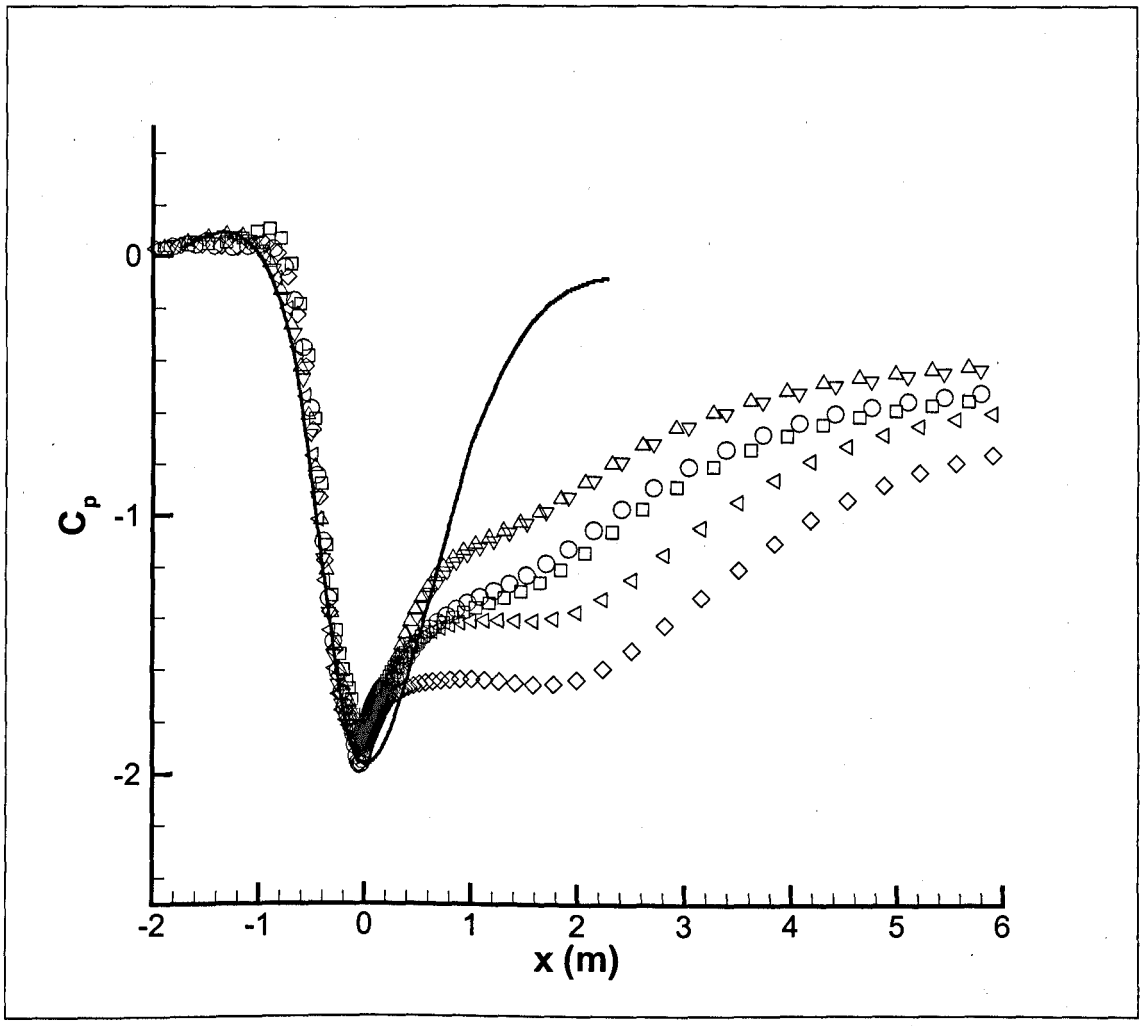

Figure 7.5: Pressure coefficient distribution for the uncontrolled case: □ = A01, ○ = A04, ◇ = A07, △ = A10, ▽ = A13, ◁ = A16, Solid Line= Higher Reynolds number results of Bernard *et al.* (2003)

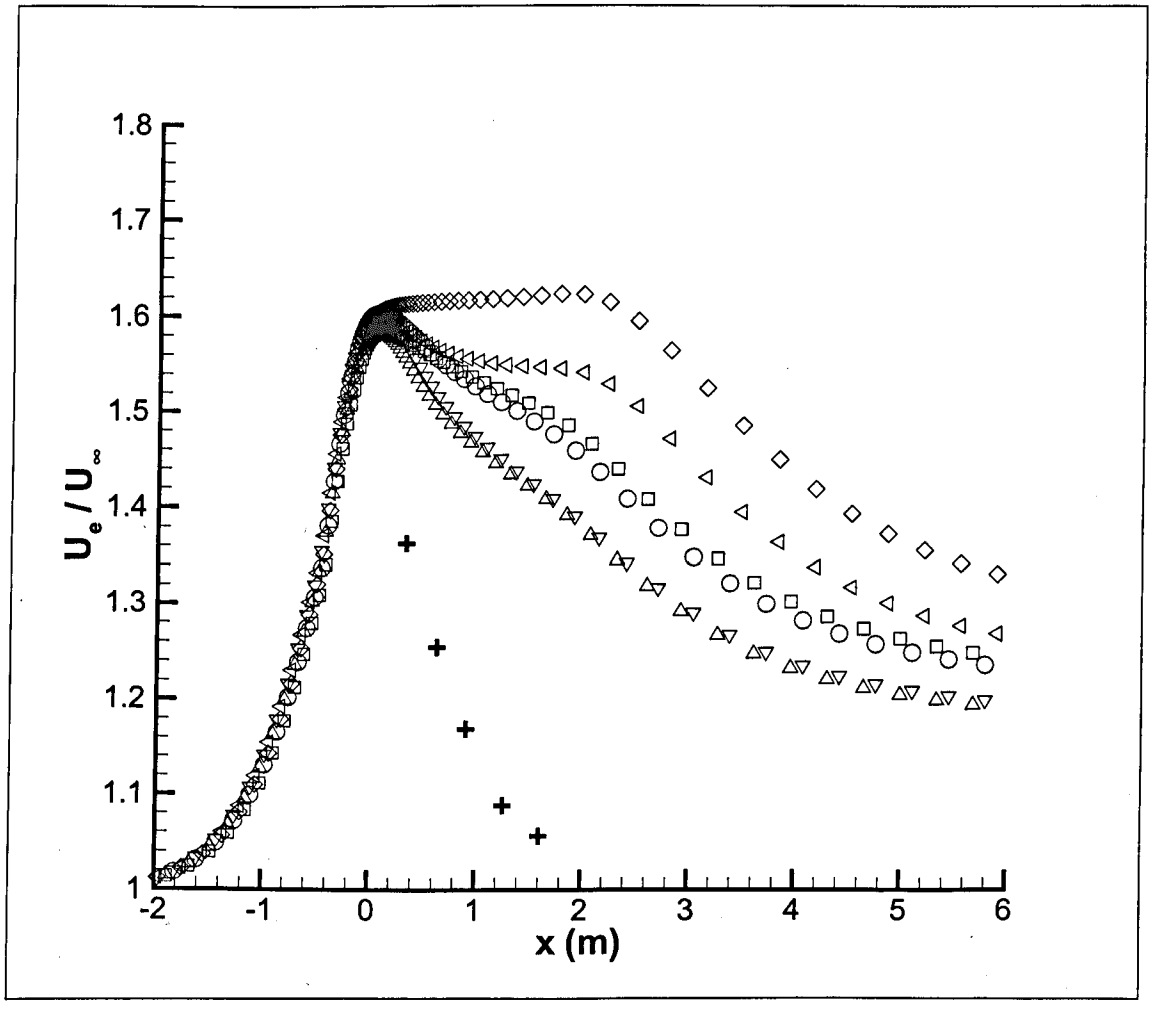

Figure 7.6: Velocity at the edge of the boundary layer for the uncontrolled case: □ = A01, ○ = A04, ◇ = A07, △ = A10, ▽ = A13, ◁ = A16, += Higher Reynolds number results of Bernard *et al.* (2003)

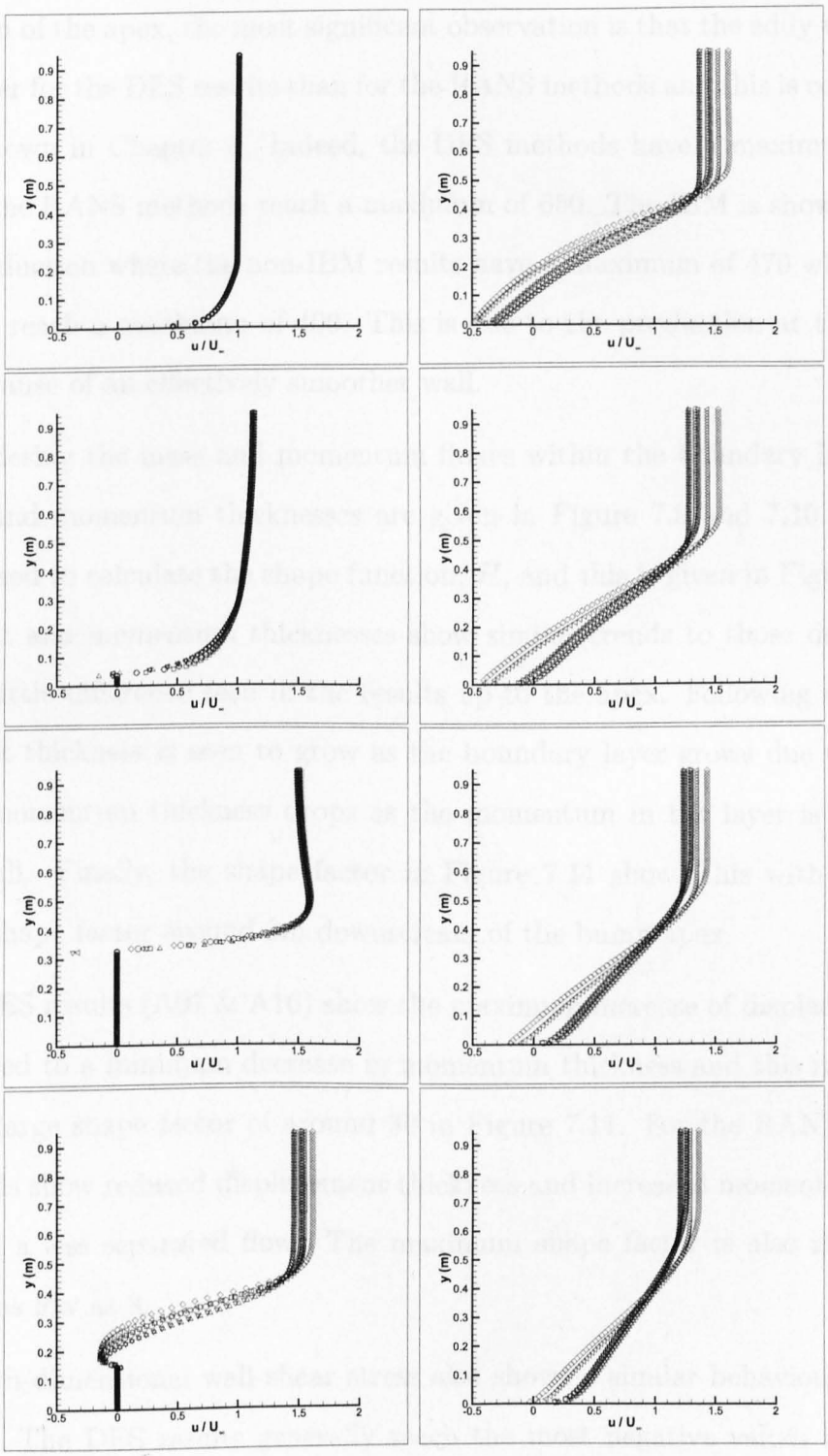

Figure 7.7: Velocity profiles (u/U_∞) for the uncontrolled case at -2m, -1m, 0m, 1m, (left) and 2m, 3m, 4m, 5m (right) from the bump apex: □ = A01, ◯ = A04, ◇ = A07, △ = A10, ▽ = A13, ◁ = A16

Downstream of the apex, the most significant observation is that the eddy viscosity ratio is much lower for the DES results than for the RANS methods and this is consistent with the work shown in Chapter 6. Indeed, the DES methods have a maximum of around 450 whilst the RANS methods reach a maximum of 650. The IBM is shown to produce a further reduction where the non-IBM results have a maximum of 470 whilst the IBM results only reach a maximum of 400. This is due to the production at the wall being reduced because of an effectively smoother wall.

Considering the mass and momentum fluxes within the boundary layer, the displacement and momentum thicknesses are given in Figure 7.9 and 7.10. These have then been used to calculate the shape function, H, and this is given in Figure 7.11. The displacement and momentum thicknesses show similar trends to those detailed previously with little difference seen in the results up to the apex. Following the apex, the displacement thickness is seen to grow as the boundary layer grows due to separation whilst the momentum thickness drops as the momentum in the layer is shifted away from the wall. Finally, the shape factor in Figure 7.11 shows this with a significant increase in shape factor around 2m downstream of the bump apex.

The DES results (A07 & A16) show the maximum increase of displacement thickness compared to a minimum decrease in momentum thickness and this ratio is shown in the very large shape factor of around 30 in Figure 7.11. For the RANS results, the IBM methods show reduced displacement thickness and increased momentum thickness indicative of a less separated flow. The maximum shape factor is also much reduced with values as low as 8.

The non-dimensional wall shear stress also shows a similar behaviour as given in Figure 7.12. The DES results generally reach the most negative values in the region behind the bump whilst the RANS results exhibit less separated values. Again, the

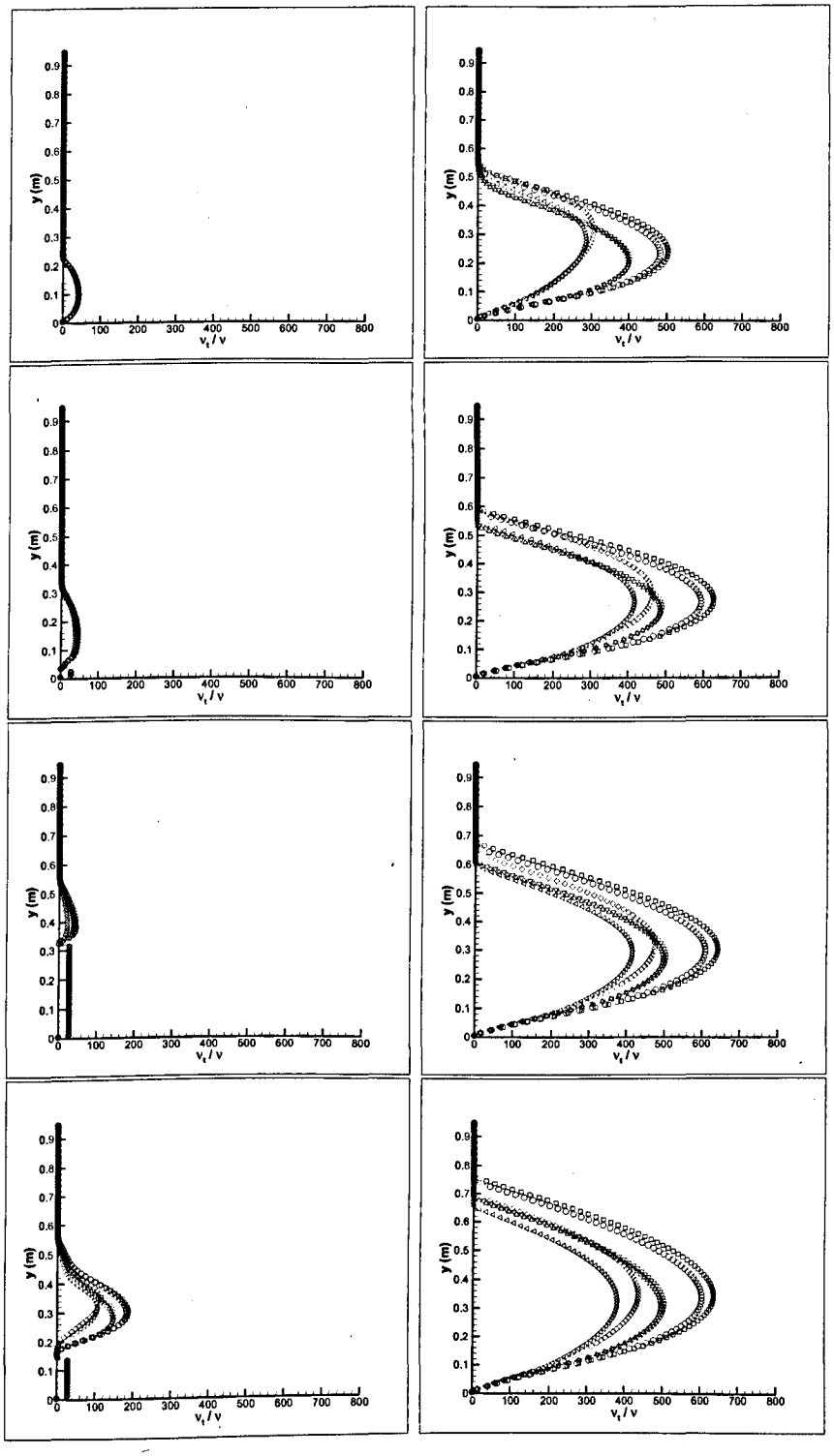

Figure 7.8: Turbulent Viscosity ratio profiles (ν_t/ν) for the uncontrolled case at -2m, -1m, 0m, 1m, (left) and 2m, 3m, 4m, 5m (right) from the bump apex: □ = A01, ○ = A04, ◇ = A07, △ = A10, ▽ = A13, ◁ = A16

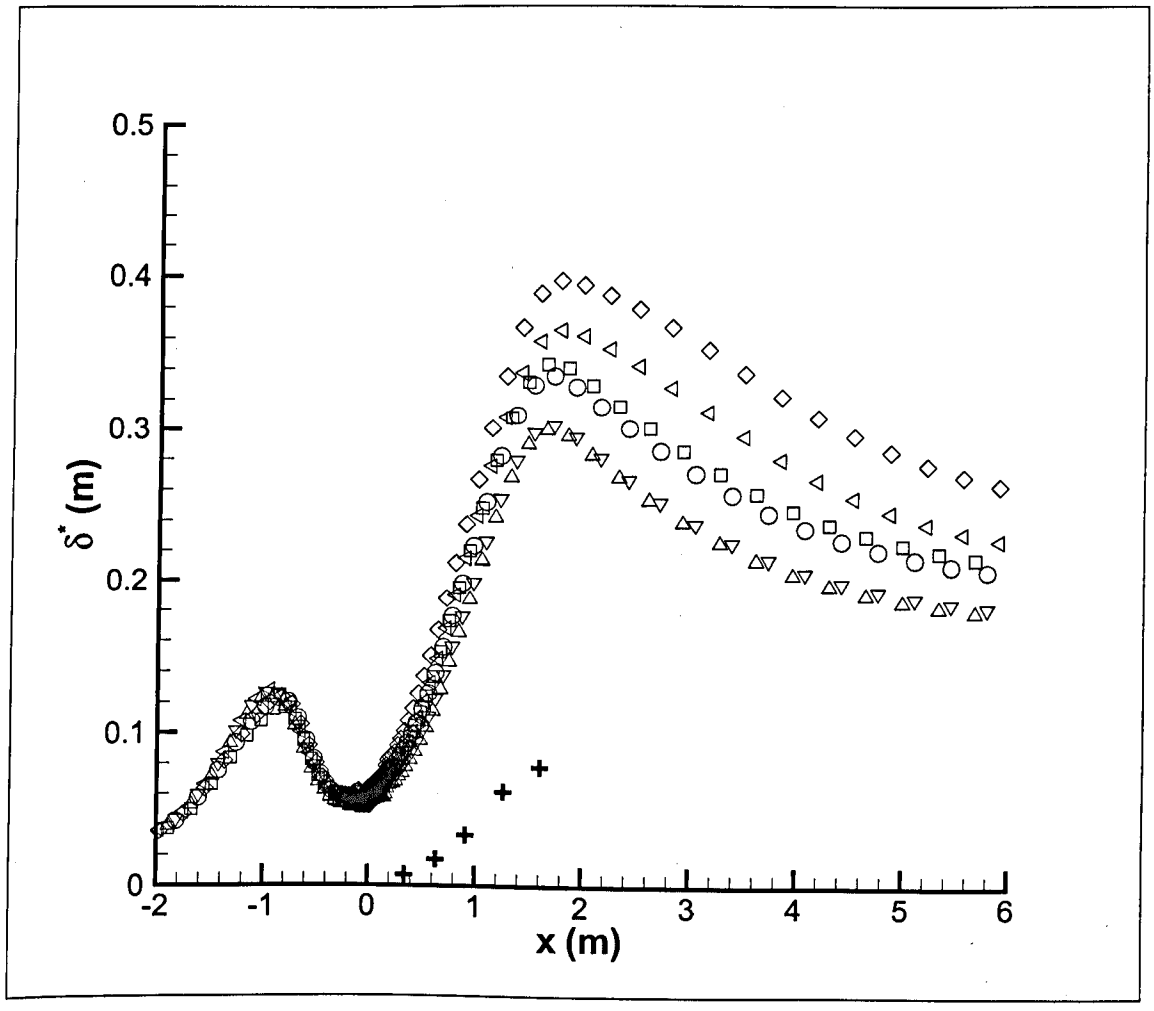

Figure 7.9: Displacement thickness for the uncontrolled case: □ = A01, ○ = A04, ◇ = A07, △ = A10, ▽ = A13, ◁ = A16, += Higher Reynolds number results of Bernard *et al.* (2003)

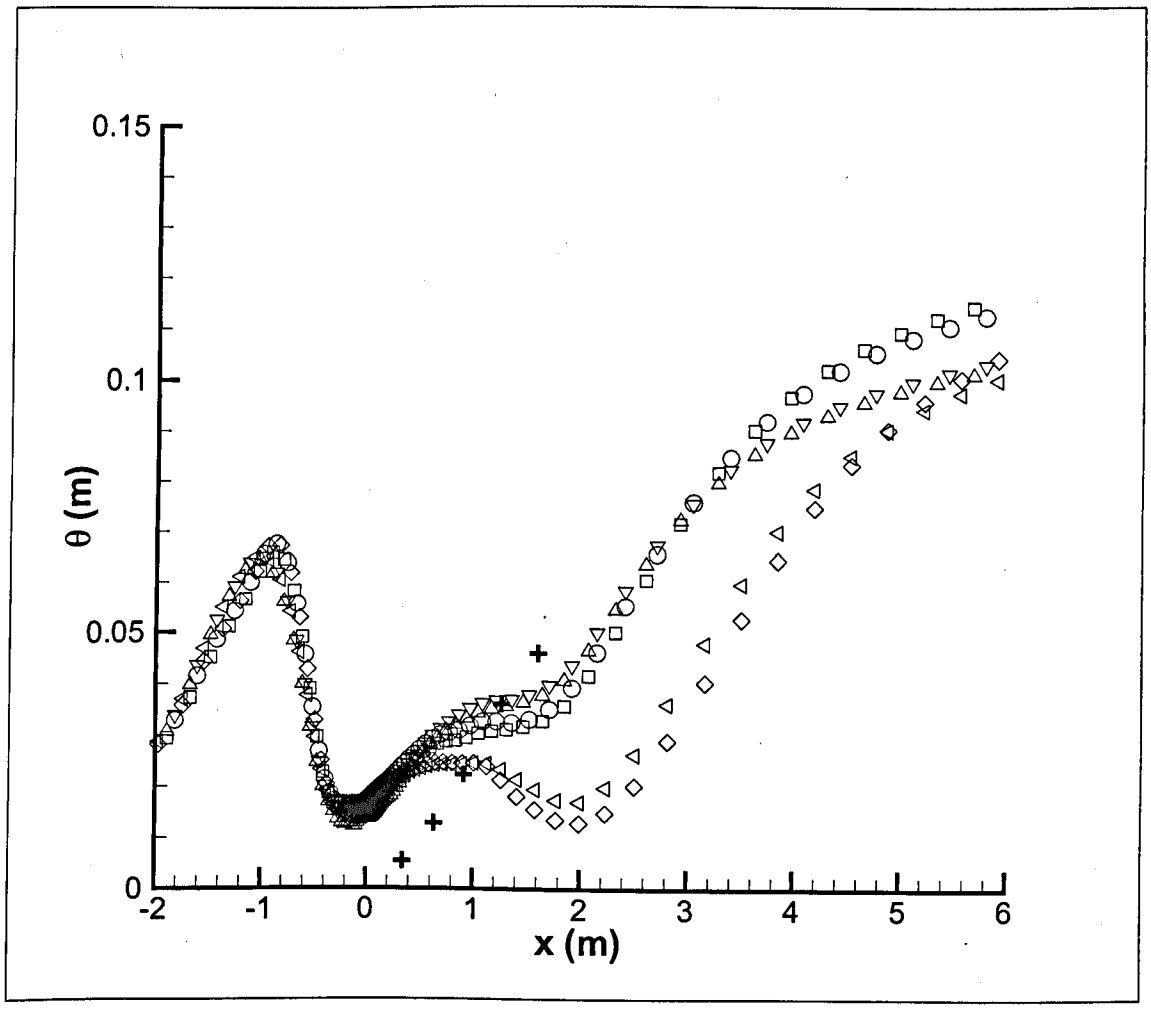

Figure 7.10: Momentum thickness for the uncontrolled case: □ = A01, ○ = A04, ◇ = A07, △ = A10, ▽ = A13, ◁ = A16, += Higher Reynolds number results of Bernard *et al.* (2003)

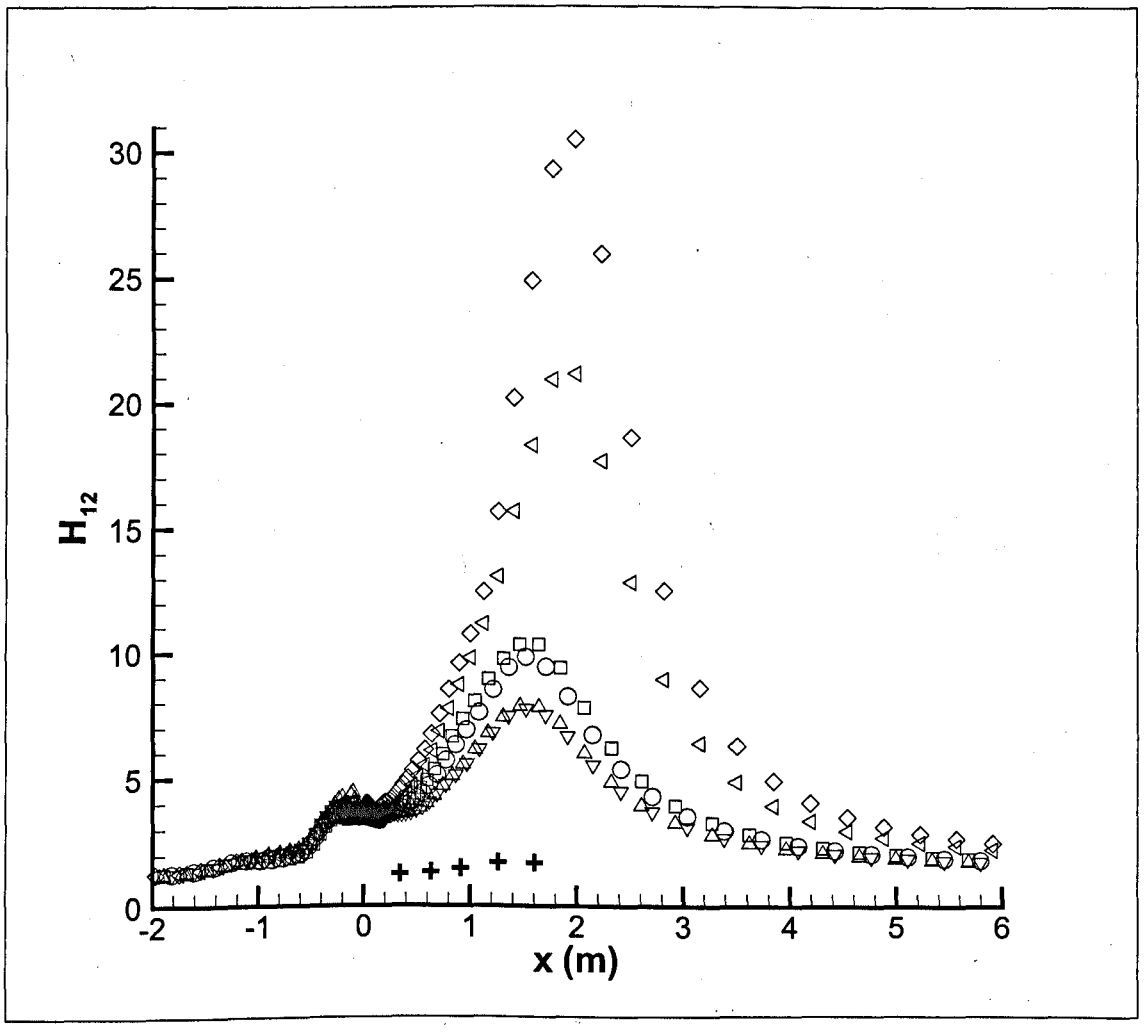

Figure 7.11: Shape factor H for the uncontrolled case: □ = A01, ○ = A04, ◇ = A07, △ = A10, ▽ = A13, ◁ = A16, += Higher Reynolds number results of Bernard *et al.* (2003)

IBM simulations show even stronger results indicative of a smaller separation region.

In summary, the simulations given show a variety of results depending on the method used and a number of points can be concluded by comparing these methods with one another. As these results cannot be compared to any experimental or computational results, concluding which method is best is difficult. However, a number of features can be noted below.

In general, the DES method produced more separated results than using RANS and this is most likely as a result of the reduced levels of turbulent viscosity in the simulation. One way to look at this is that whilst the DES simulation is more separated it is probably more sensible as the RANS models supress the separation artificially. The wall function RANS methods showed slightly less separation than the wall resolved RANS cases and this is due to the wall resolved RANS model underestimating the wall shear stress if the grid is too coarse in the wall normal direction.

Finally, the IBM always reduces any separation shown. This is consistent with the work of Chapter 4 as it corresponds to the surface being made smoother by the IBM. Any castellations in the non-IBM simulations only serve to trip the flow into separation prematurely and thus increase the recirculation region.

In summary, estimates for the drag forces on the bump, both due to pressure and due to skin friction effects, are given in Table 7.3. In general, the IBM simulations produce lower pressure drag values whilst the DES method tends to increase them due to the larger separation region. Conversely, the DES method tends to reduce skin friction drag as there is a larger recirculation region. However as the skin friction drag is an order of magnitude smaller than the pressure drag, this has little effect overall.

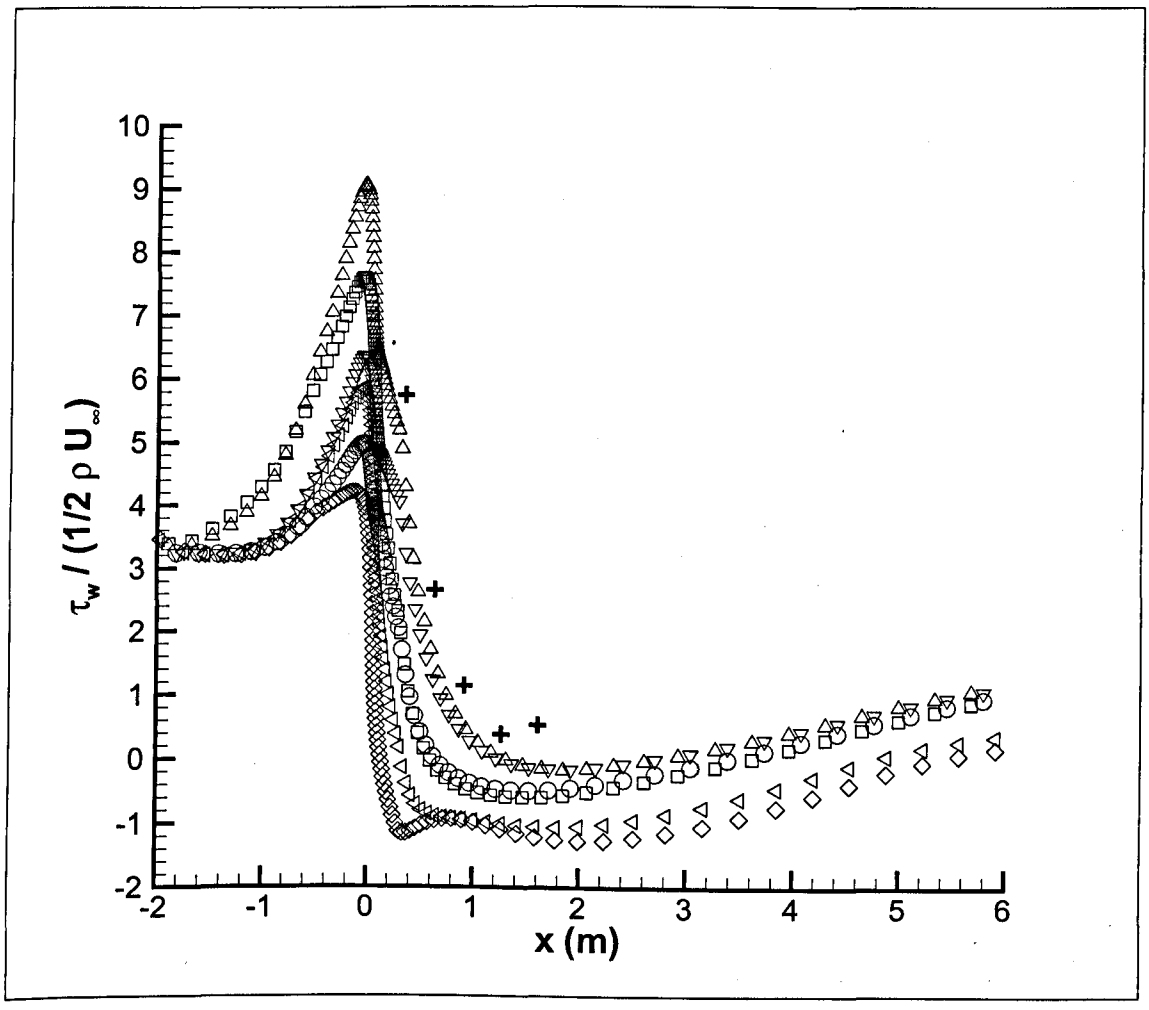

Figure 7.12: Wall shear stress distribution for the uncontrolled case: □ = A01, ○ = A04, ◇ = A07, △ = A10, ▽ = A13, ◁ = A16, += Higher Reynolds number results of Bernard *et al.* (2003)

Serial	F_{PD} (N)	F_{SF} (N)	C_{PD}	C_{SF}
A01	0.191	0.0115	0.943	0.057
A04	0.169	0.0093	0.831	0.0457
A07	0.225	0.0057	1.110	0.028
A10	0.123	0.0145	0.607	0.0713
A13	0.125	0.012	0.614	0.0577
A16	0.171	0.0075	0.843	0.0367

Table 7.3: Forces and coefficients on the bump for the uncontrolled case

7.3 Simulating the steady jet case

Now that the methods have been adequately tested, the case of using a round steady jet for flow control is now considered. These simulations are based on the work of Godard and Stanislas (2006b) in which the effect of using round jets on flow control is assessed.

In a similar manner to the Lille work, a jet diameter of 10mm was used with a velocity ratio of 5.0 leading to a a maximum jet velocity of 5m/s. The velocity profile of the jet was set to follow a seventh power law. The jet direction was chosen to have a pitch of 45 degrees and acted in the cross-stream direction, 90 degrees to the mainstream flow. The jet was positioned on the bump apex and this is consistent with Godard and Stanislas (2006b) where the jets are placed just downstream of the apex.

Whilst every combination of grid mesh, turbulence treatment and immersed boundary method were presented in the previous section on the uncontrolled case, this section will simply consider a simulation without any methods applied at all with a simulation

Table 7.4: Parameters for the steady-jet bump case (RS02)

Serial	Mesh ($nx \times ny$)	Turbulence	IBM
RS02-A01	307×100	RANS (WR)	None
RS02-A16	307×100	DES (WF)	Full Linear

incorporating all of the methods applied together. A summary of the parameters for these cases are given in Table 7.4.

7.3.1 The Cross-stream Flow-field

Figures 7.13, 7.14 and 7.15 present the streamwise velocity contours in a y-z plane produced downstream of the jet. Figure 7.13 shows the velocity at 0.5m downstream of the bump apex and the jet. It should be noted that the jet is positioned at 0.25m in the z direction and is acting at 45 degrees in the direction of the positive y and z axes. The jet is also skewed such that its axis is directly across the stream so lying within the $y - z$ plane.

It is clear that there is a significant difference as compared to the uncontrolled case. Although there are still areas of negative flow near the wall, in other areas higher levels of velocity have been brought down closer to the wall. This is likely as a result of a vortex induced by the jet which is anti-clockwise and roughly centred on the jet. (i.e. on $z = 0.25m$) Moving to 1m downstream, Figure 7.14 shows this structure growing outwards from the wall with the effects becoming more diffuse. However, it is clear that some effect is still being felt as the streamwise velocity is, over a spanwise average, being reduced to lower levels than the uncontrolled case. The results at 1.5m downstream show this structure becoming increasingly weak (Figure 7.15).

Considering the streamwise vorticity within the flow, as given in Figures 7.16-7.18 a vortex is being produced as expected with a large area of positive (i.e. anti-clockwise) vorticity being positioned at 0.25m in the cross-stream direction by the time the structure has reached 0.5 downstream. By 1.0m downstream, the structure has started to convect slightly in the positive z direction as a result of vortex interaction. By 1.5m downstream, the vortex has left the surface and now resides within the outer boundary layer.

Figures 7.19-7.21 give the eddy viscosity ratio ν_t/ν, the area of increased vorticity

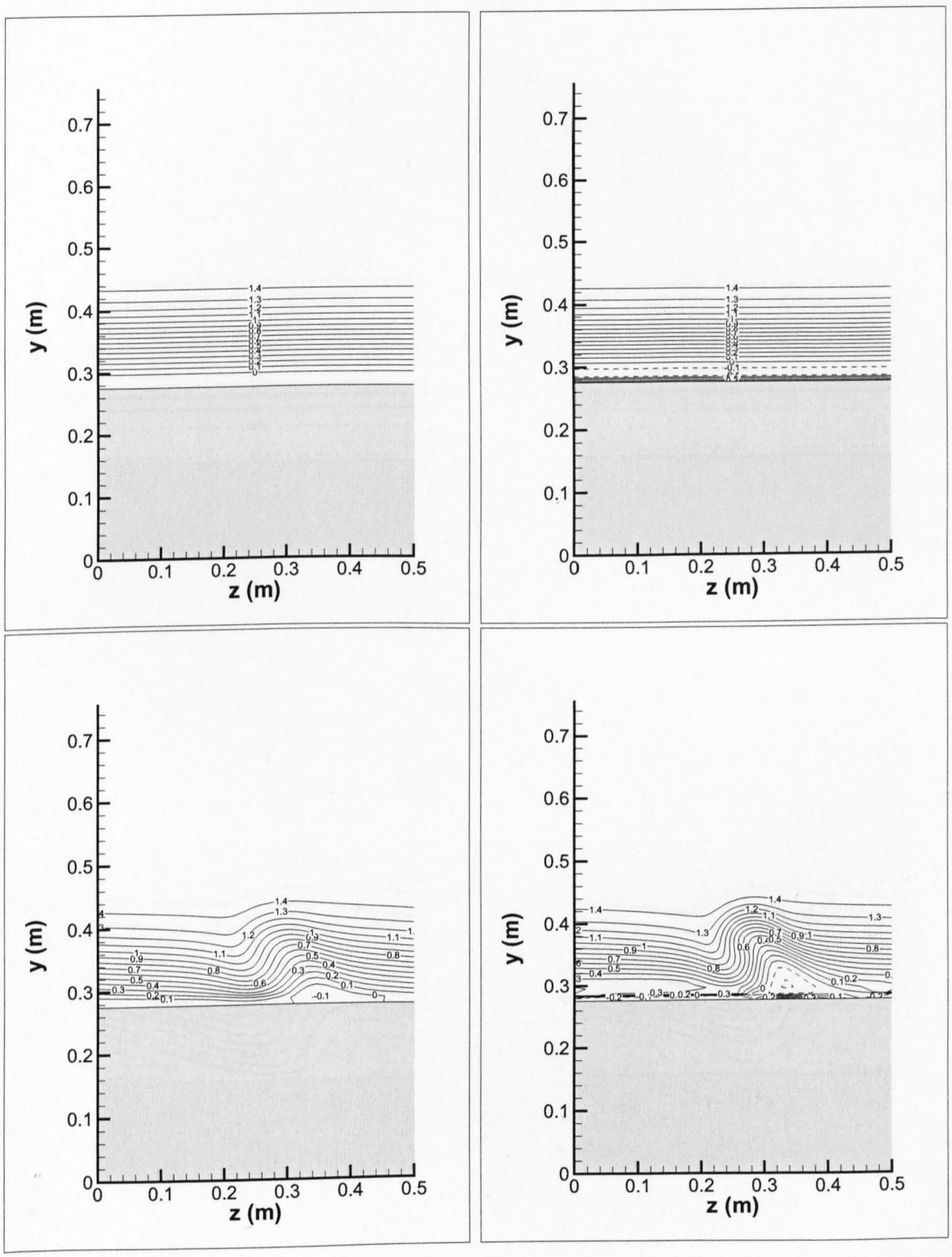

Figure 7.13: u-velocity contours at $x = 0.5m$ downstream of the apex for the steady-jet control case. Top row: Uncontrolled case, Bottom row: Steady-jet case, Left column: Simulation without methods, Right column: Simulation with all methods employed

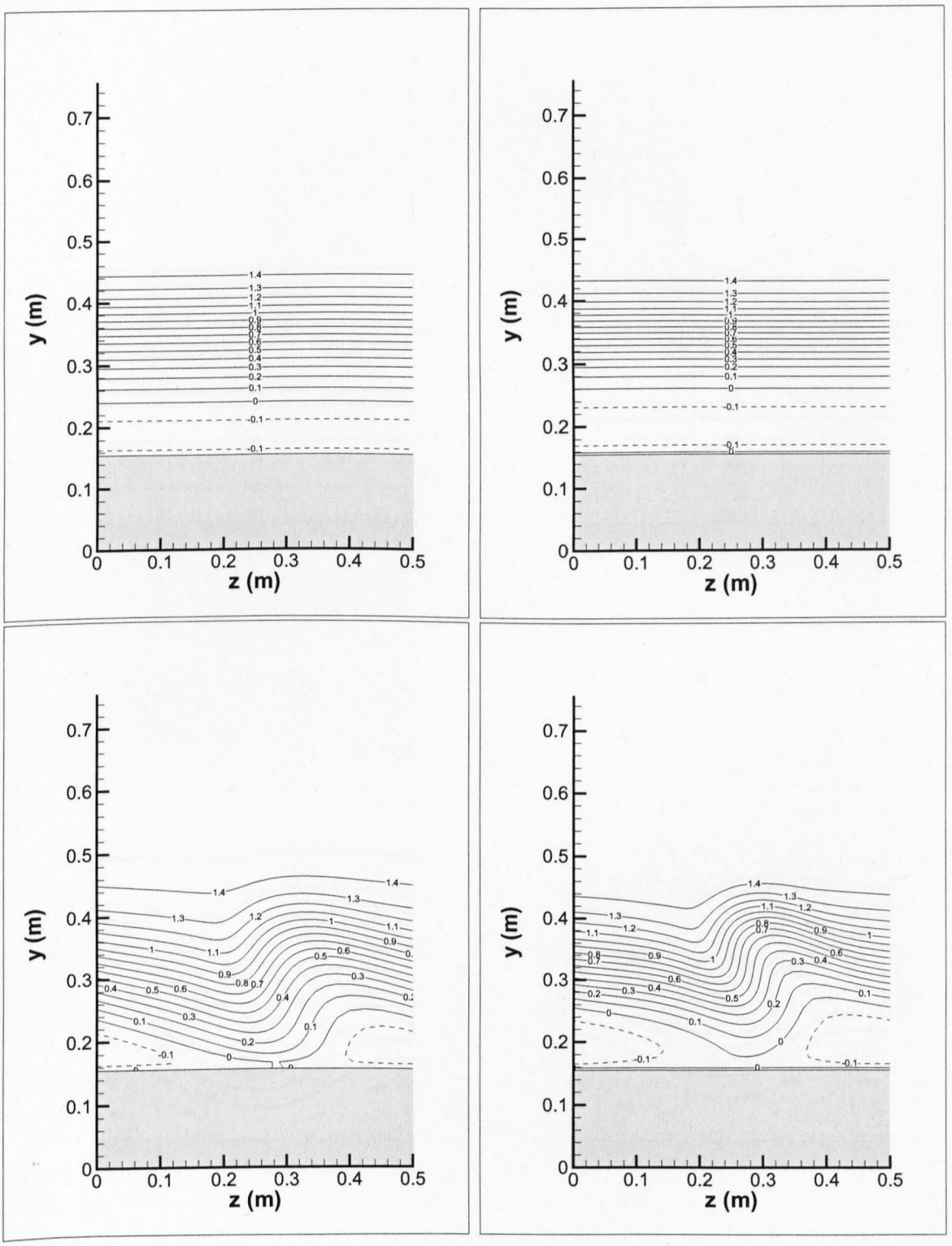

Figure 7.14: u-velocity contours at $x = 1.0m$ downstream of the apex for the steady-jet control case. Top row: Uncontrolled case, Bottom row: Steady-jet case, Left column: Simulation without methods, Right column: Simulation with all methods employed

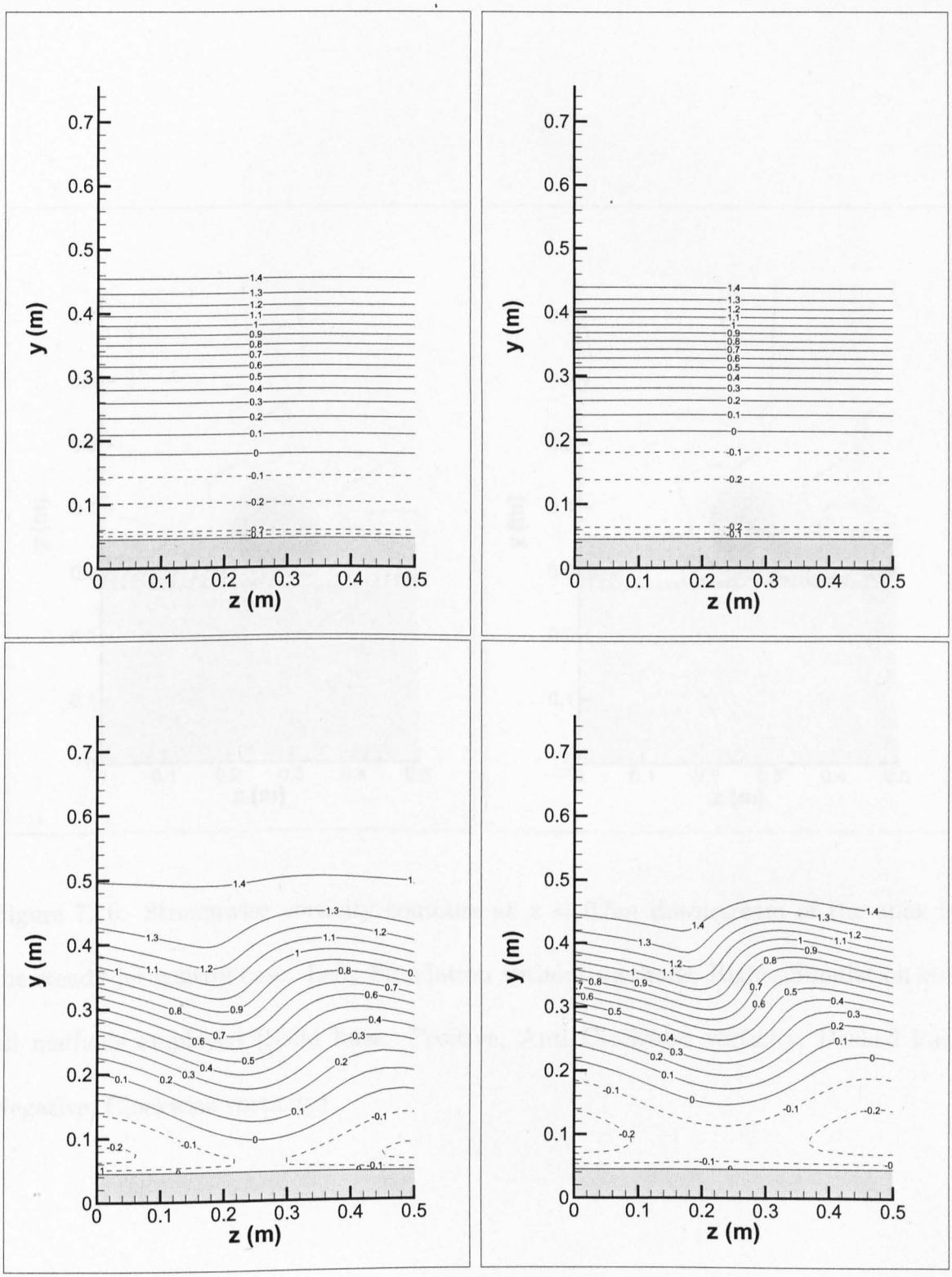

Figure 7.15: u-velocity contours at $x = 1.5m$ downstream of the apex for the steady-jet control case. Top row: Uncontrolled case, Bottom row: Steady-jet case, Left column: Simulation without methods, Right column: Simulation with all methods employed

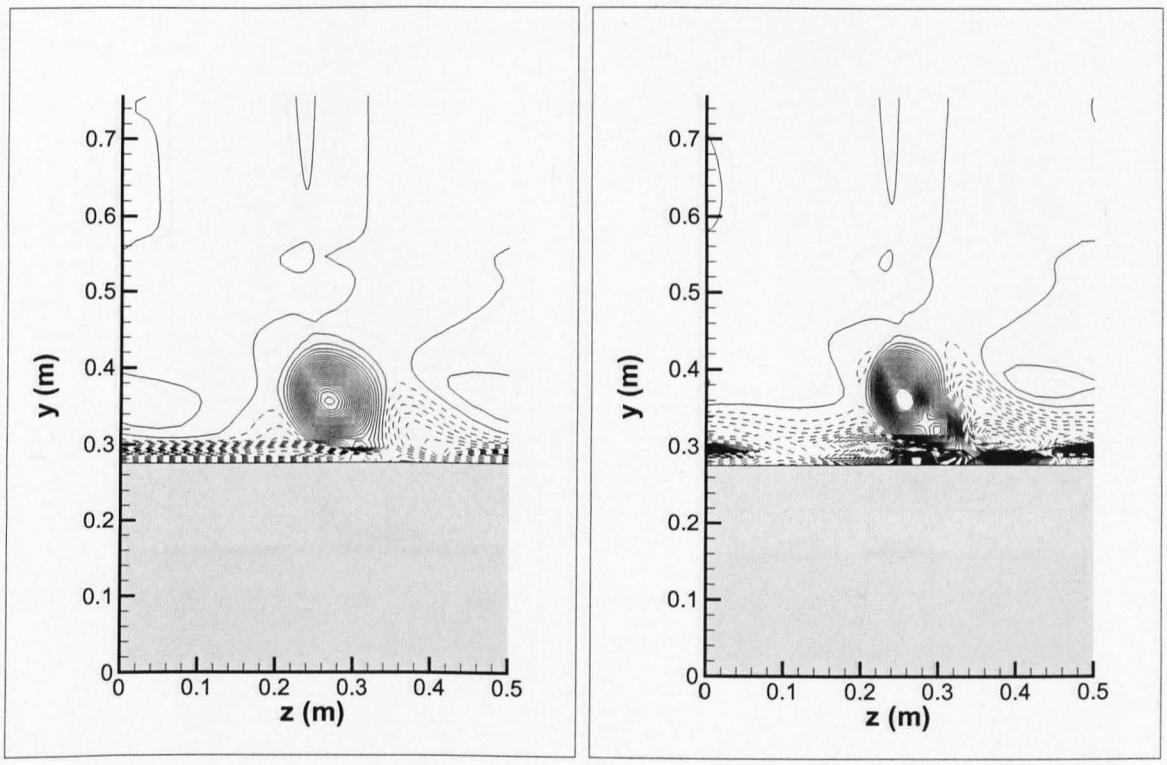

Figure 7.16: Streamwise vorticity contours at $x = 0.5m$ downstream of the apex for the steady-jet control case. Left: Simulation without methods, Right: Simulation with all methods employed (Solid lines: Positive, Anti Clockwise vorticity, Dashed lines: Negative, Clockwise vorticity)

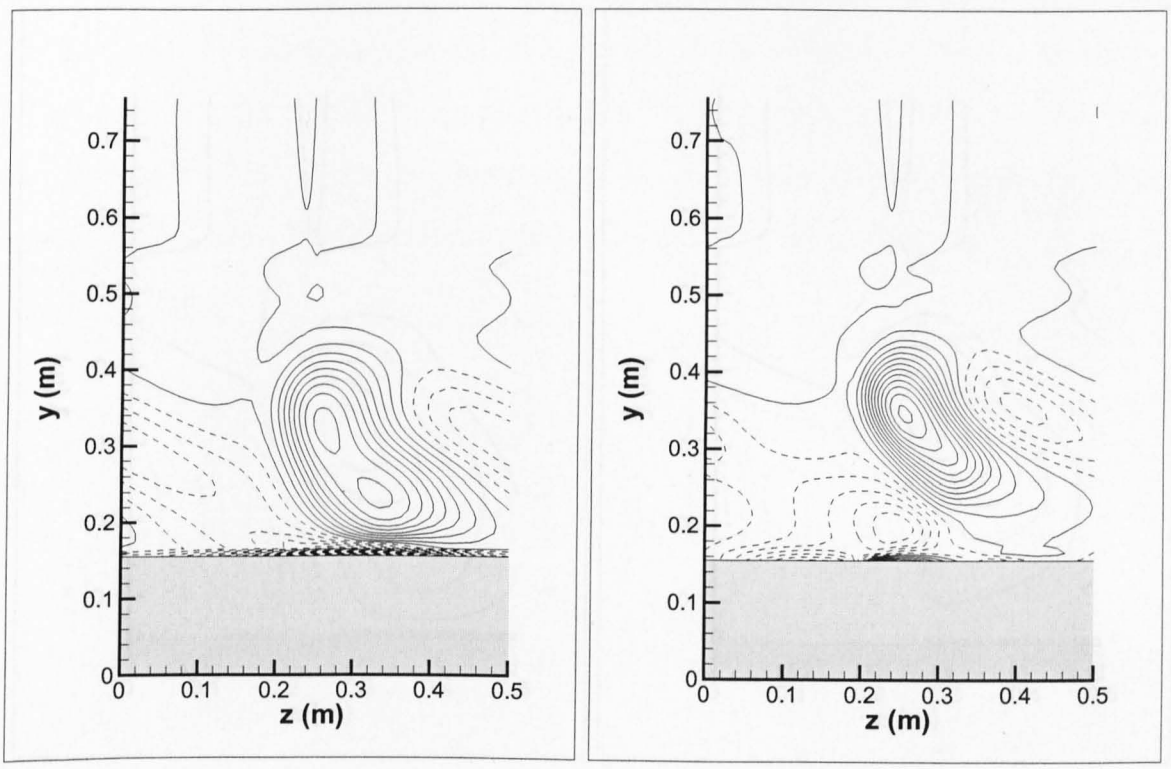

Figure 7.17: Streamwise vorticity contours at $x = 1.0m$ downstream of the apex for the steady-jet control case. Left: Simulation without methods, Right: Simulation with all methods employed (Solid lines: Positive, Anti Clockwise vorticity, Dashed lines: Negative, Clockwise vorticity)

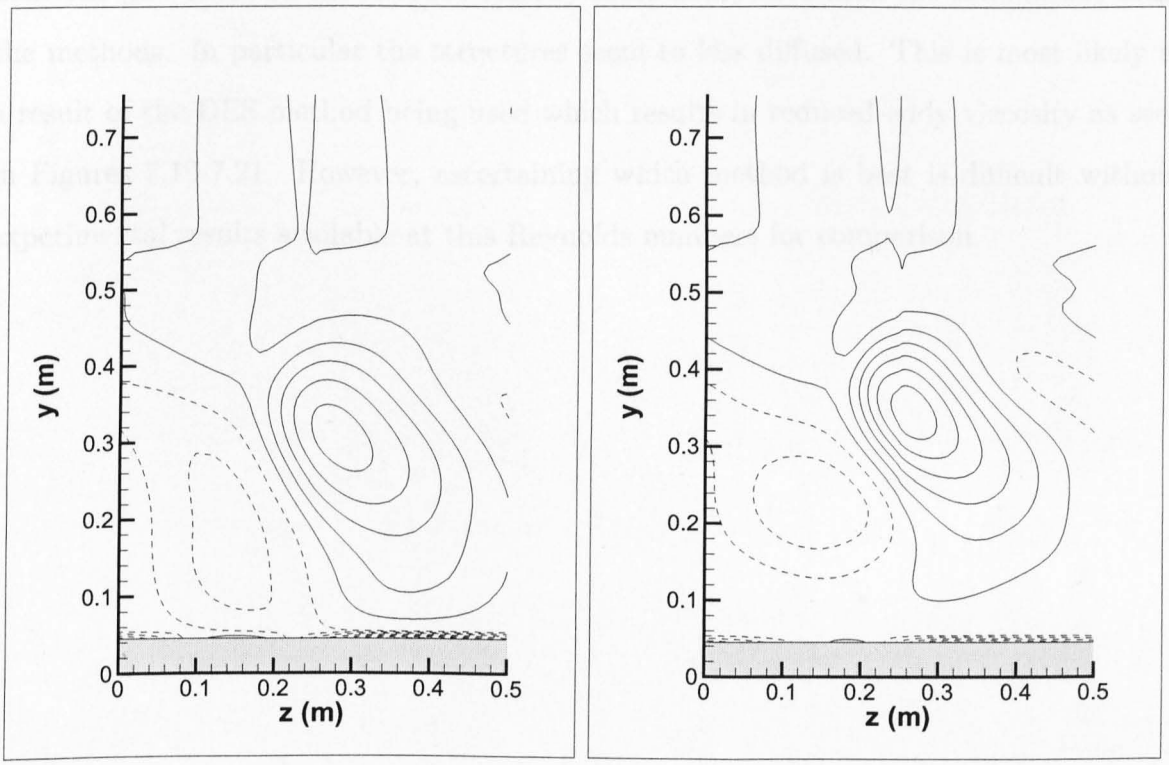

Figure 7.18: Streamwise vorticity contours at $x = 1.5m$ downstream of the apex for the steady-jet control case. Left: Simulation without methods, Right: Simulation with all methods employed (Solid lines: Positive, Anti Clockwise vorticity, Dashed lines: Negative, Clockwise vorticity)

is seen to correspond to increased eddy-visocity. This is as a result of the source term within the model equations which is dependent on the vorticity.

Comparing the different methods, it is clear that the simulations without any methods (i.e. those on the left) are slightly more dissipative than the simulations using the methods. In particular the structures seem to less diffused. This is most likely as a result of the DES method being used which results in reduced eddy viscosity as seen in Figures 7.19-7.21. However, ascertaining which method is best is difficult without experimental results available at this Reynolds numbers for comparison.

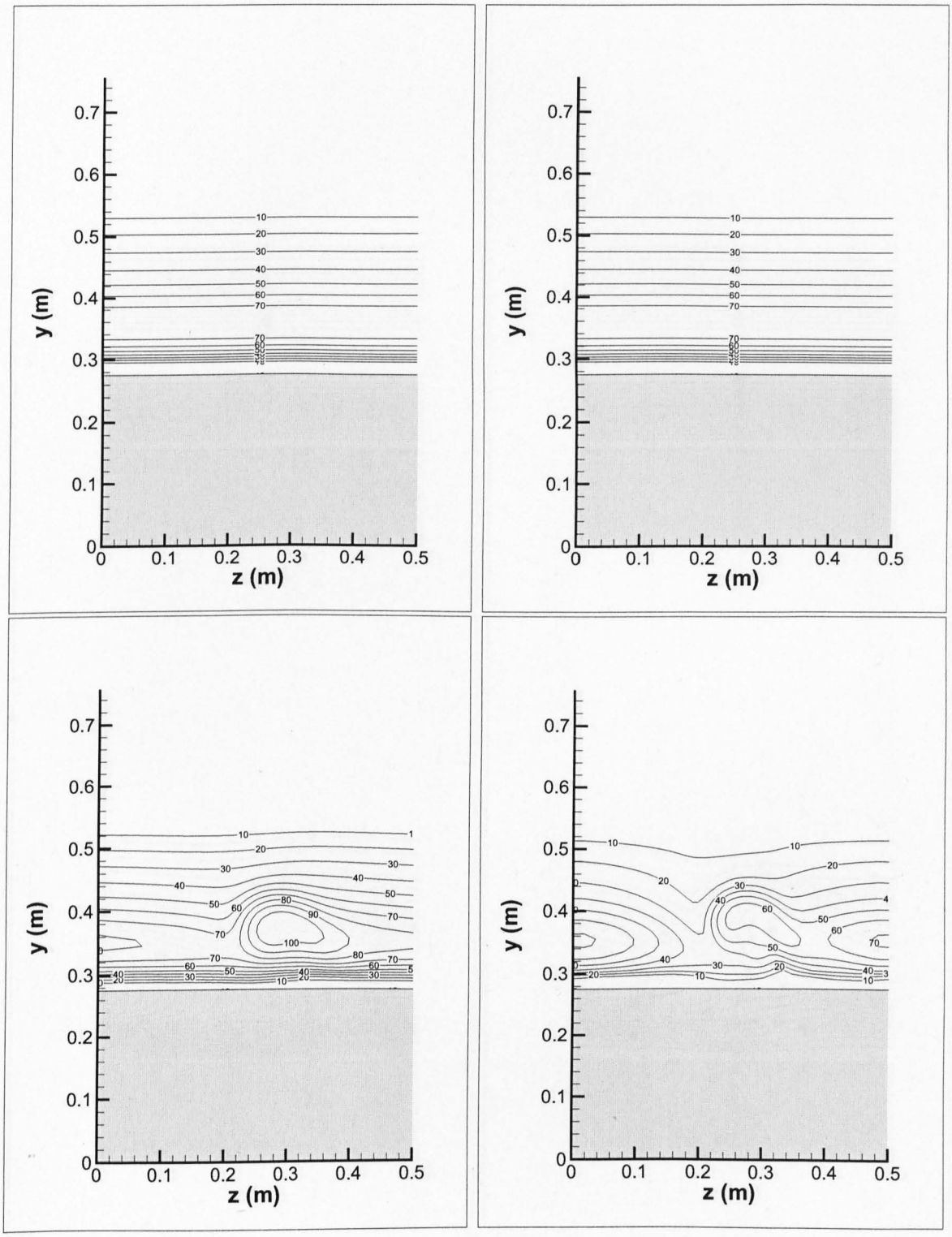

Figure 7.19: Eddy-viscosity ratio contours (ν_t/ν) at $x = 0.5m$ downstream of the apex for the steady-jet control case. Top row: Uncontrolled case, Bottom row: Steady-jet case, Left column: Simulation without methods, Right column: Simulation with all methods employed

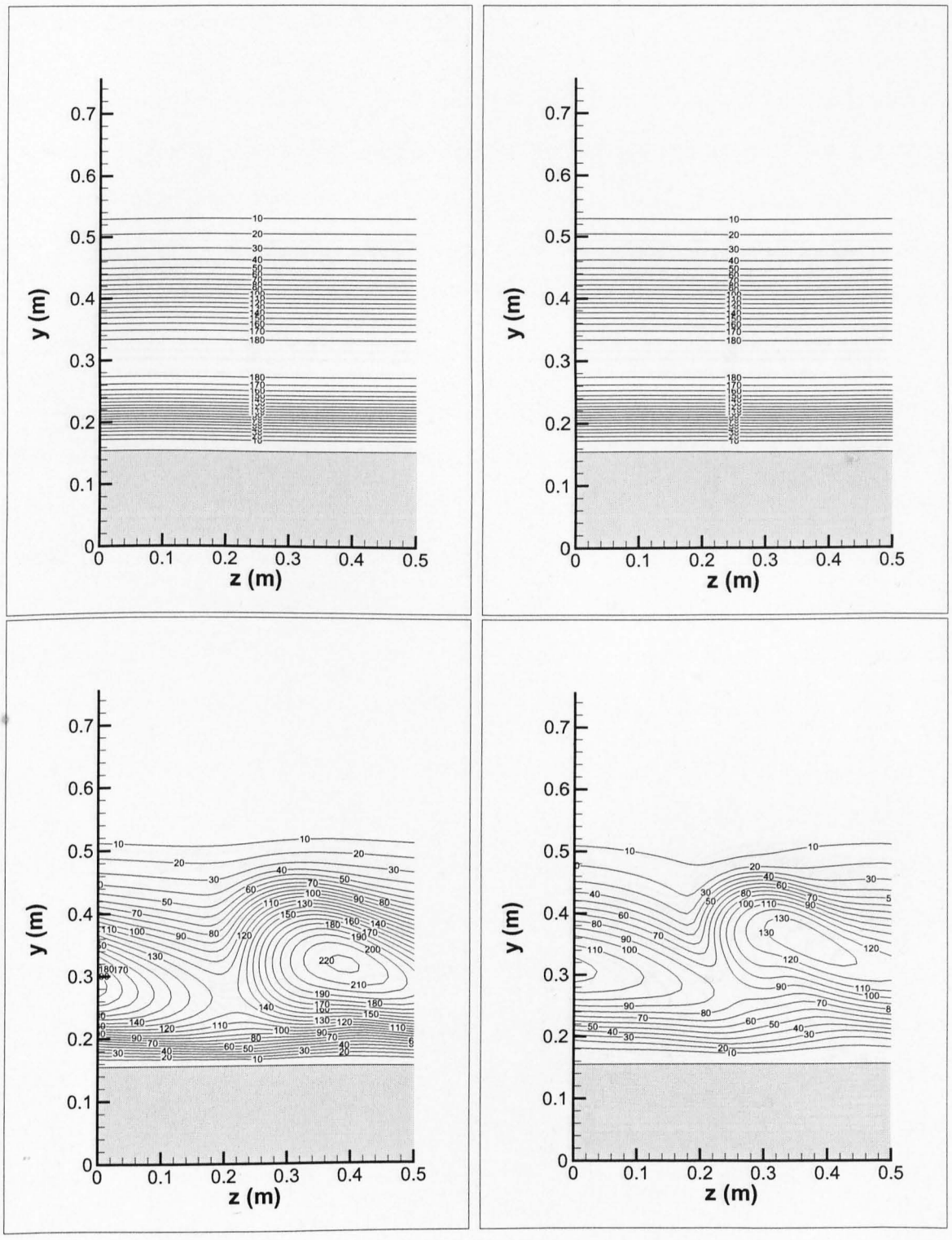

Figure 7.20: Eddy-viscosity ratio contours (ν_t/ν) at $x = 1.0m$ downstream of the apex for the steady-jet control case. Top row: Uncontrolled case, Bottom row: Steady-jet case, Left column: Simulation without methods, Right column: Simulation with all methods employed

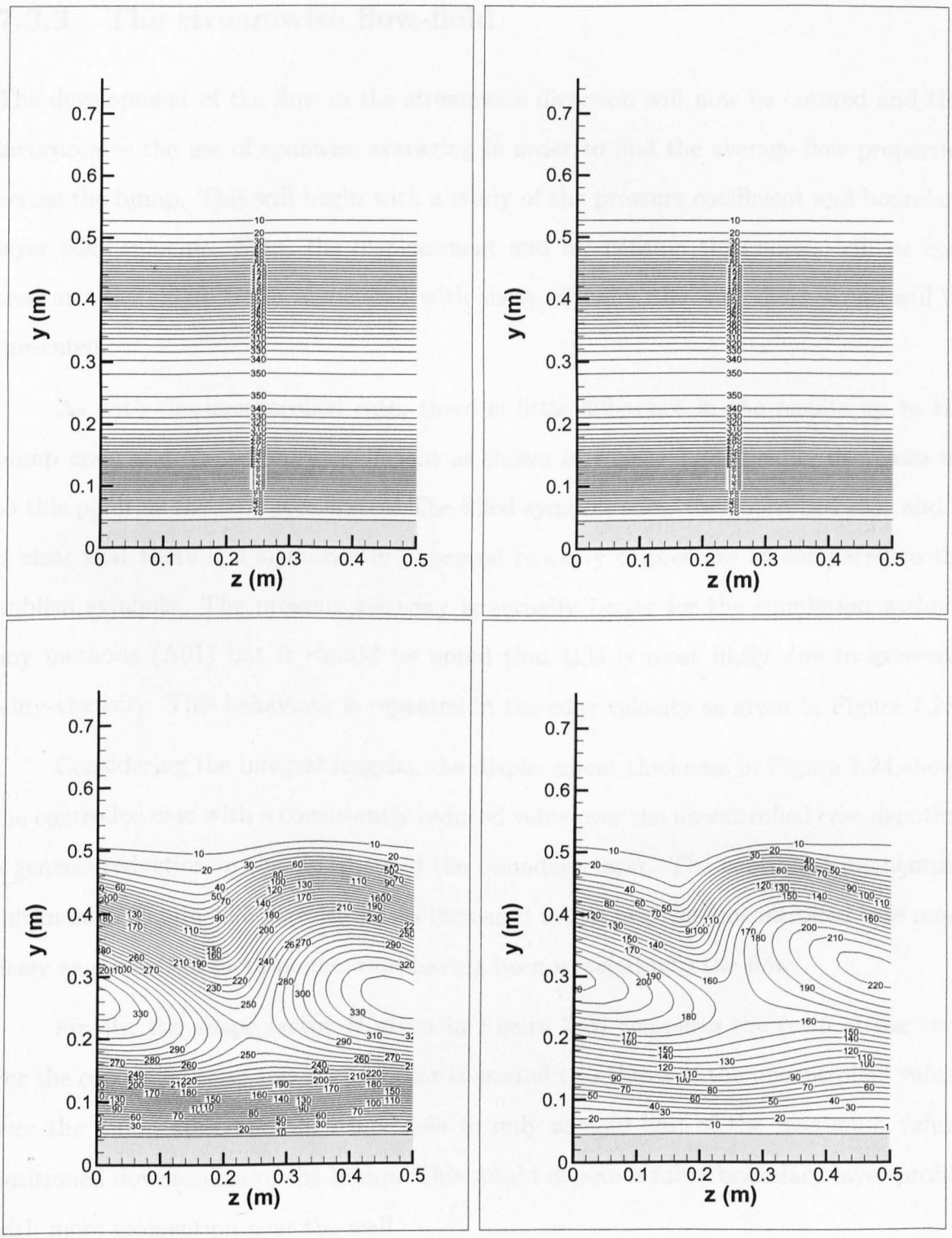

Figure 7.21: Eddy-viscosity ratio contours (ν_t/ν) at $x = 1.5m$ downstream of the apex for the steady-jet control case. Top row: Uncontrolled case, Bottom row: Steady-jet case, Left column: Simulation without methods, Right column: Simulation with all methods employed

7.3.2 The streamwise flow-field

The development of the flow in the streamwise direction will now be covered and this incorporates the use of spanwise averaging in order to find the average flow properties across the bump. This will begin with a study of the pressure coefficient and boundary layer edge velocity. Next, the displacement and momentum thicknesses will be covered and the shape factor associated with them. Finally, the wall shear stress will be presented.

As with the uncontrolled case, there is little difference in the results up to the bump apex and the pressure coefficient as shown in Figure 7.22 steadily decreases up to this point as the flow accelerates. The filled symbols show the controlled case and it is clear that there is a significantly improved recovery of pressure as compared to the unfilled symbols. The pressure recovery is actually better for the simulation without any methods (A01) but it should be noted that this is most likely due to excessive eddy-viscosity. This behaviour is repeated in the edge velocity as given in Figure 7.23.

Considering the integral lengths, the displacement thickness in Figure 7.24 shows the controlled case with a consistently reduced value over the uncontrolled case denoting a general reduction in the thickness of the boundary layer. The controlled momentum thickness in Figure 7.25 likewise shows increased values over the uncontrolled case most likely as a result of more momentum having been injected into the flow.

Finally, the shape factor H given in Figure 7.26 compares the ratio of the two. For the controlled case, this shape factor is around two-thirds of the uncontrolled values over the bump apex and then increases to only around half of the maximum values positioned downstream of the bump. This would denote a fuller boundary layer profile with more momentum near the wall.

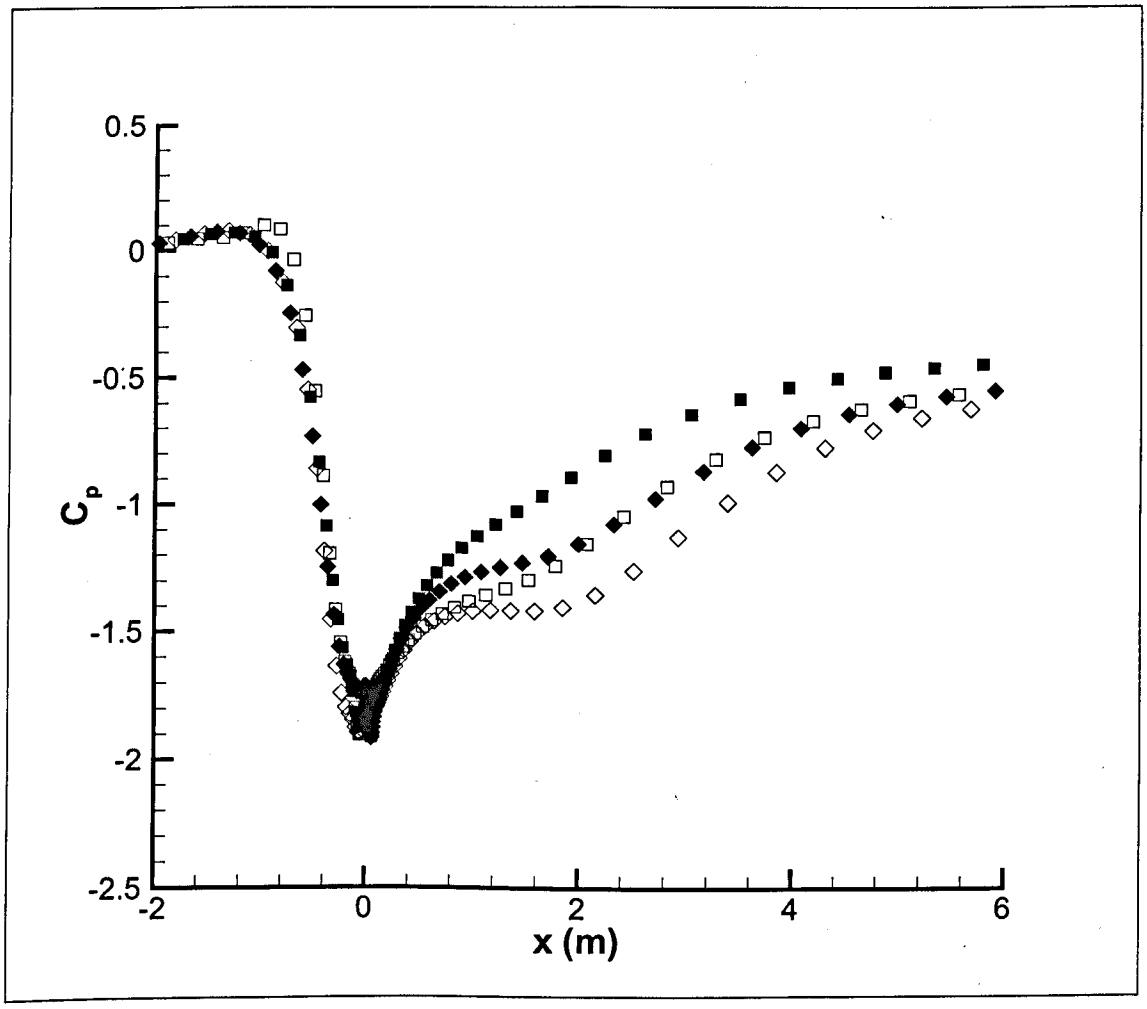

Figure 7.22: Spanwise averaged pressure coefficient distribution for the steady jet controlled case: □ = No Methods, ◇ = All Methods employed, *Unfilled* = Uncontrolled, *Filled* = Steady-jet controlled

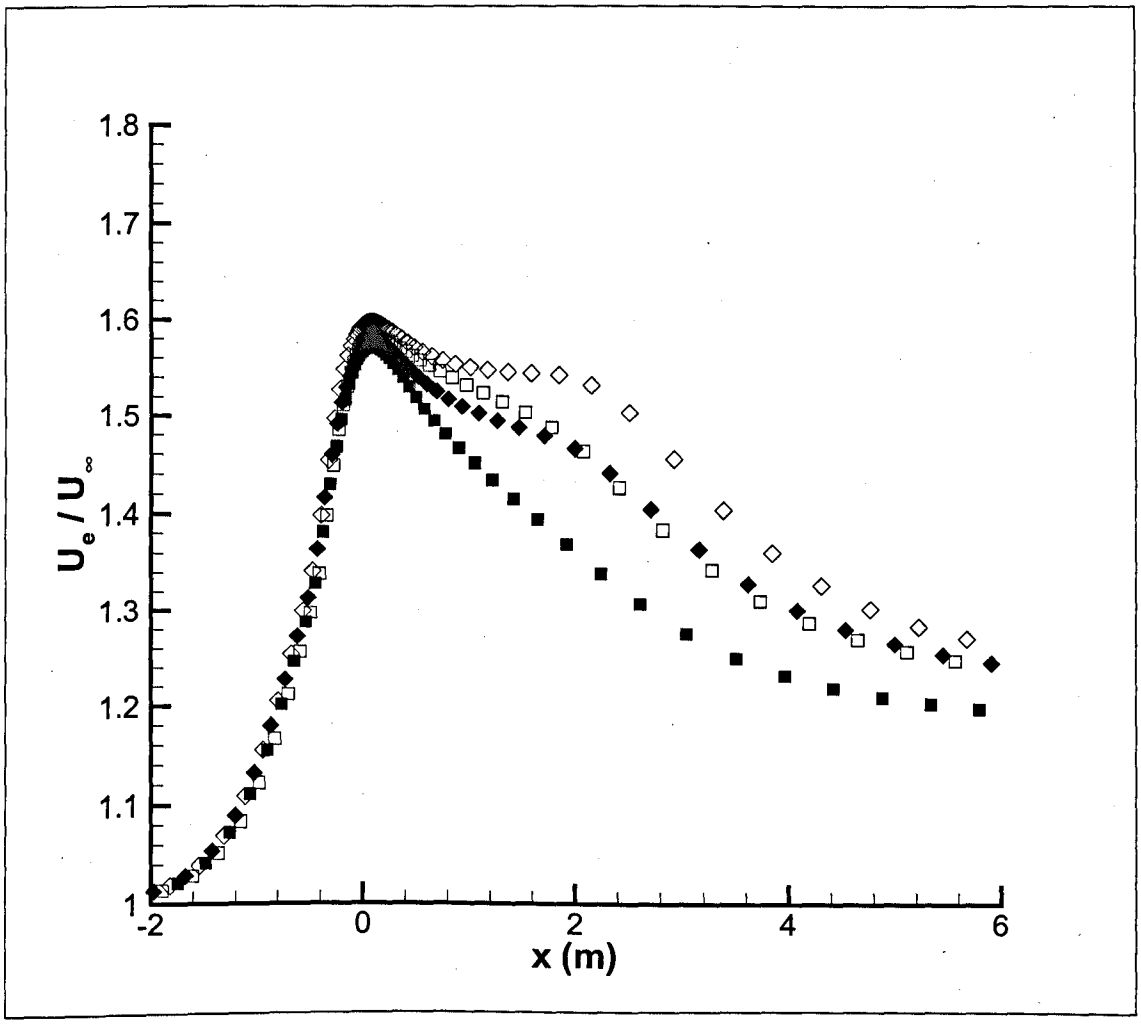

Figure 7.23: Spanwise averaged edge velocity distribution for the steady jet controlled case: □ = No Methods, ◇ = All methods employed, *Unfilled* = Uncontrolled, *Filled* = Steady-jet controlled

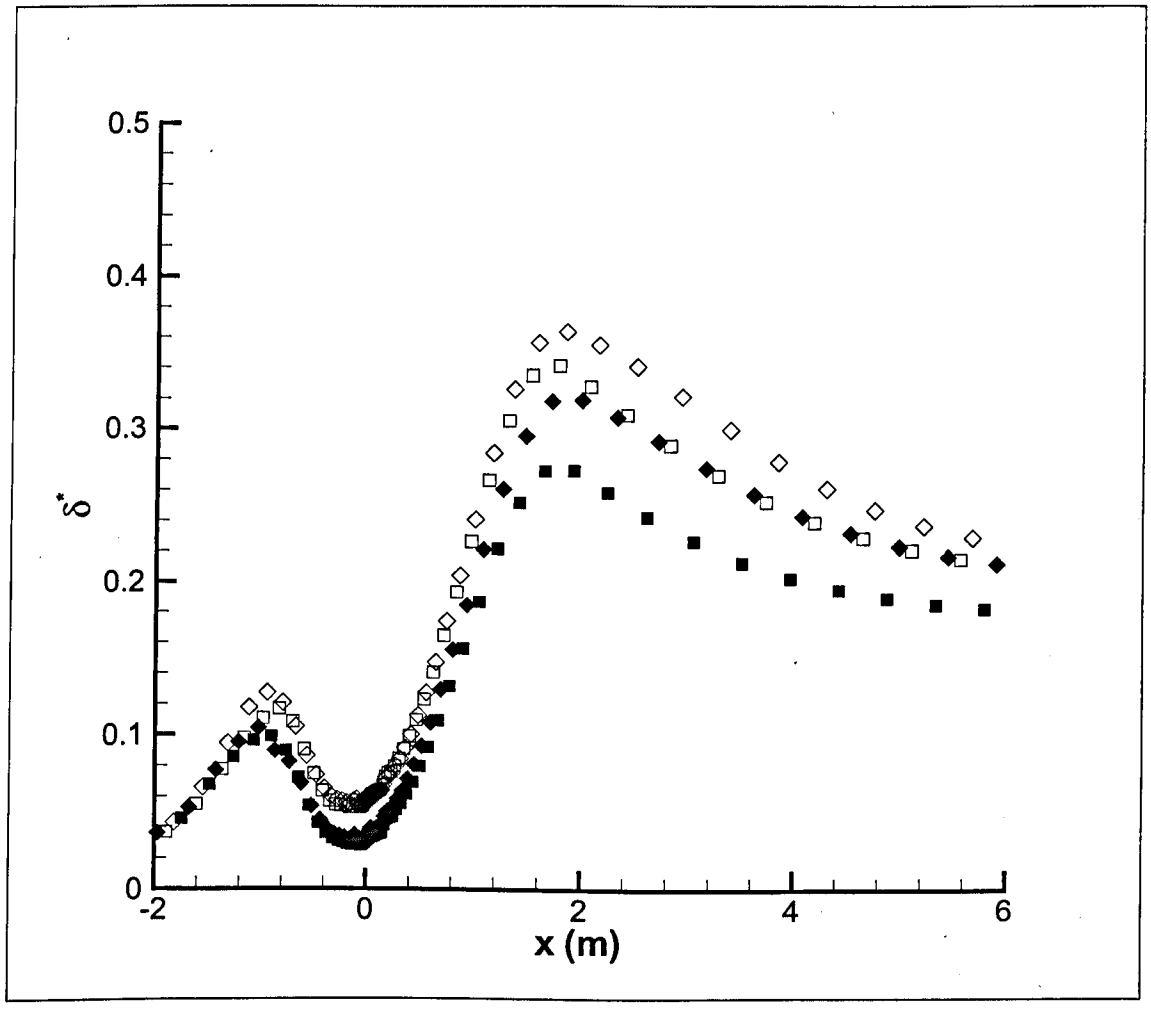

Figure 7.24: Spanwise averaged displacement thickness distribution for the steady jet controlled case: □ = No Methods, ◇ = All Methods employed, *Unfilled* = Uncontrolled, *Filled* = Steady-jet controlled

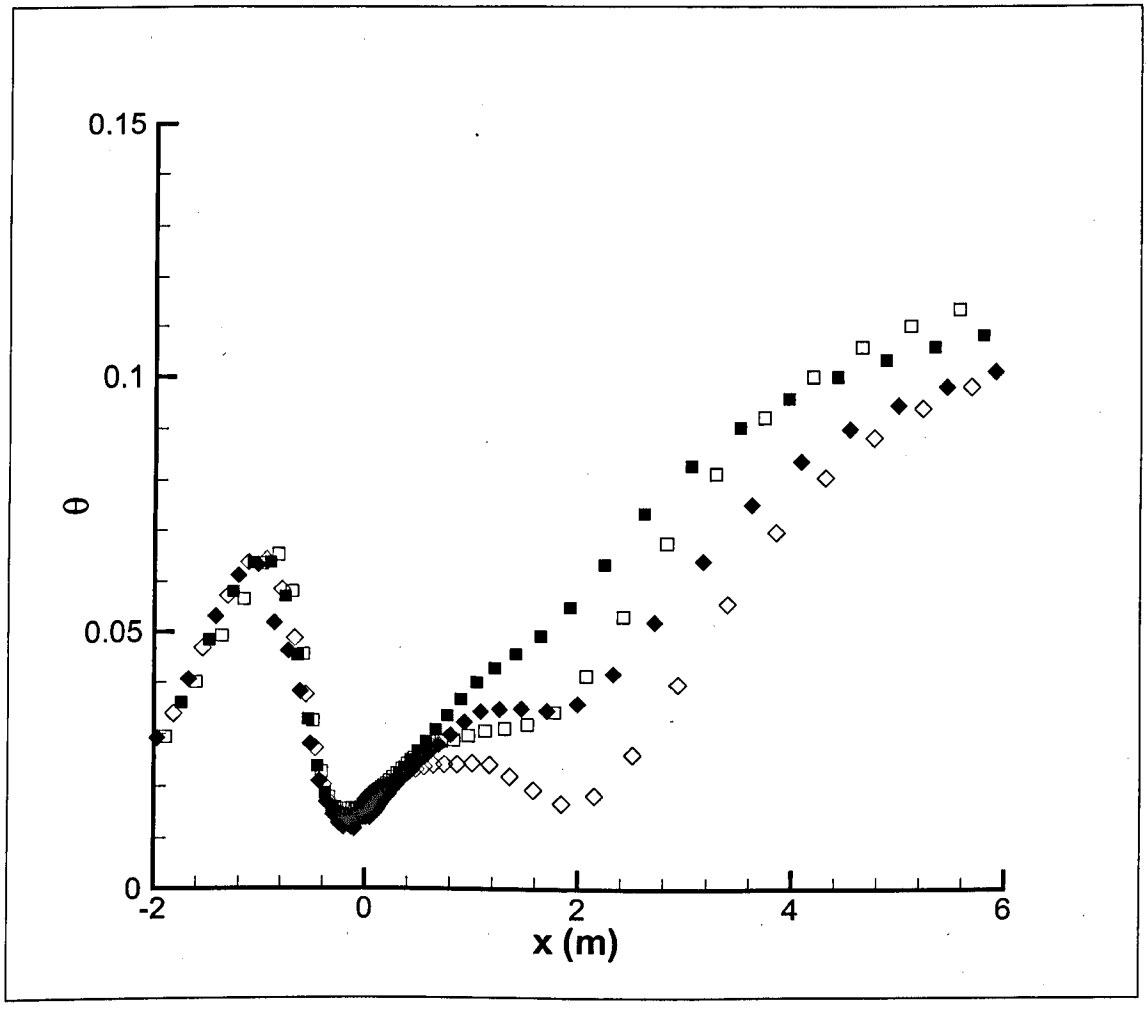

Figure 7.25: Spanwise averaged momentum thickness distribution for the steady jet controlled case: □ = No Methods, ◇ = All Methods employed, $Unfilled$ = Uncontrolled, $Filled$ = Steady-jet controlled

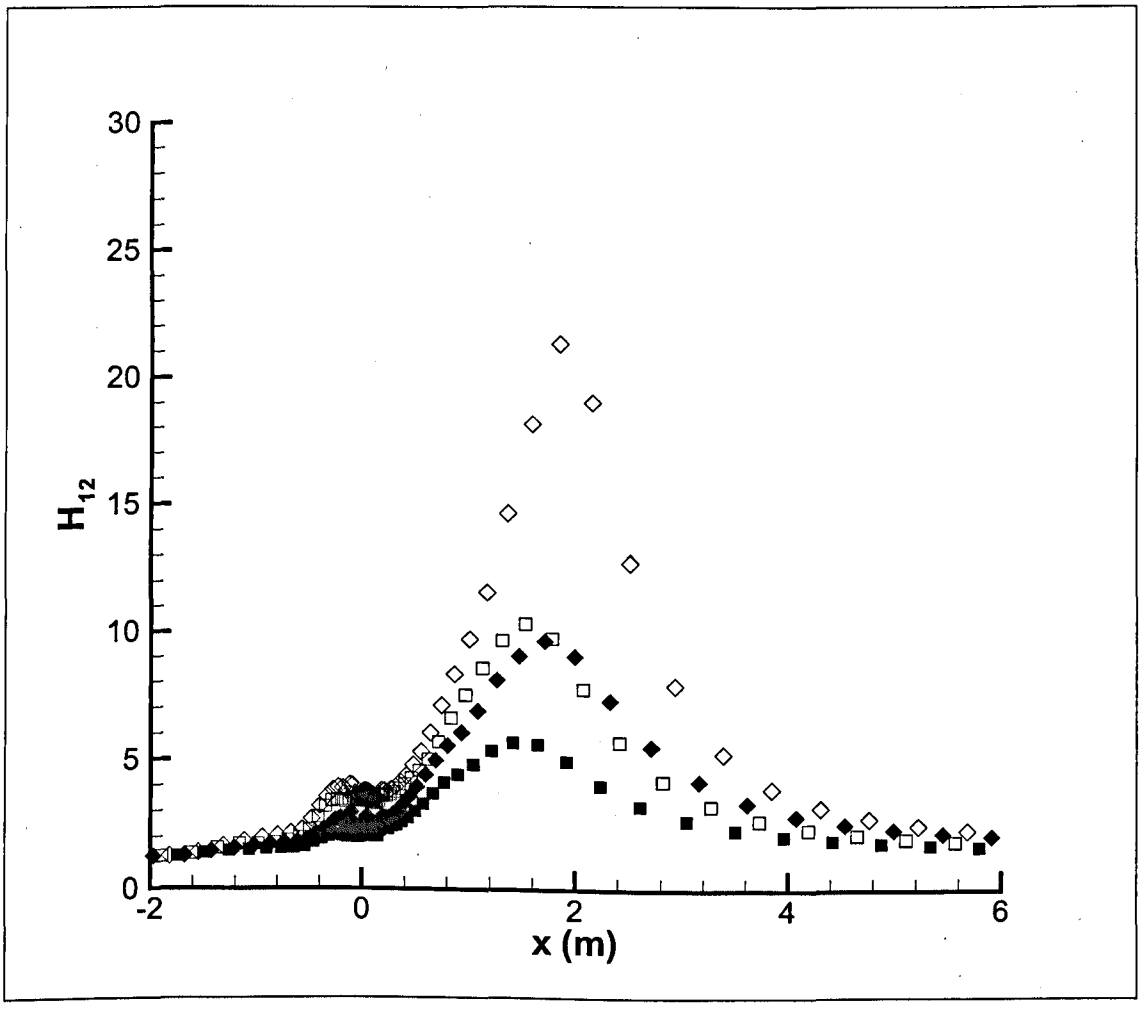

Figure 7.26: Spanwise averaged shape function H distribution for the steady jet controlled case: □ = No Methods, ◇ = All Methods employed, *Unfilled* = Uncontrolled, *Filled* = Steady-jet controlled

The spanwise averaged wall shear stress for the controlled case is shown in Figure 7.27 and a significant reduction in separation can be seen here. Although the uncontrolled case is clearly separated as indicated by the negative wall shear stress downstream of the bump, the controlled case is clearly positive throughout the flow-field. Another significant point is that there is a secondary peak in the wall shear stress at around 2m for the simulation incorporating special methods (A16) and this is likely to indicate a coherent, steady and stationary structure producing increased levels of wall shear stress at this point downstream of the bump.

Finally, these results have been processed to produce the drag forces on the bump for the steady jet case. These are given in Table 7.5. It is clear from these results that the flow control case (RS02) produces a significant decrease in the pressure drag coefficients whilst the skin friction drag is slightly increased by using flow control.

From this table it is clear that using the flow control reduces the drag significantly regardless of the computational methods used. However, for the simulations with methods (A16), this drag reduction was much less than for those simulations performed without any methods (A01). This is due to the simulations without methods over predicting the drag as was found in Chapter 4.

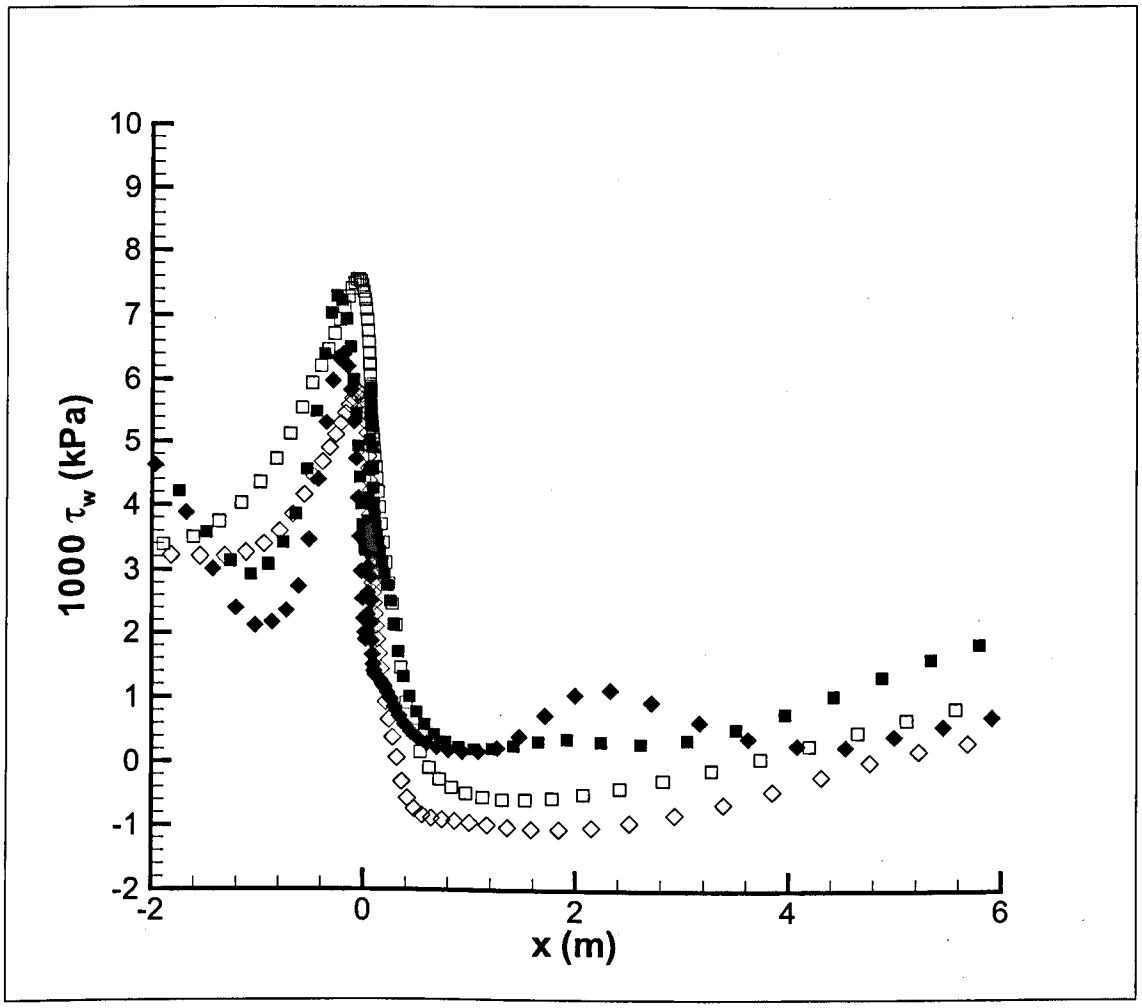

Figure 7.27: Spanwise averaged wall shear stress distribution for the steady jet controlled case: □ = No Methods, ◇ = All Methods employed, *Unfilled* = Uncontrolled, *Filled* = Steady-jet controlled

Serial	Summary	F_{PD} (N)	F_{SF} (N)	C_{PD}	C_{SF}
RS01-A01	Uncontrolled, no methods	0.1912	0.01154	0.943	0.057
RS02-A01	Controlled, no methods	0.1304	0.01267	0.643	0.0625
RS01-A16	Uncontrolled, all methods	0.1710	0.00745	0.843	0.0367
RS02-A16	Controlled, all methods	0.1451	0.01146	0.715	0.0565

Table 7.5: Forces and coefficients on the bump for the steady-jet case

7.4 Conclusions

In conclusion, using Immersed Boundary Methods (IBM), wall functions and Detached Eddy Simulation (DES) leads to significant changes compared to simulations performed without using any such methods. For the uncontrolled case it was seen that the IBM and wall functions resulted in a reduction in the recirculation region behind the Lille bump. This is due to the IBM smoothing the surface and the wall functions improving the transport of shear stress from the wall into the near-wall region. These both have the effect of energising the flow and hence reducing overall separation as was shown in Chapters 4 and 5. On the other hand, the DES approach had the effect of increasing the recirculation region by virtue of there being less diffusion present in the form of eddy viscosity. This was consistent the findings in Chapter 6.

Overall, an assessment of which method is better is difficult without any experimental results for comparison. However, the trends of using the assorted methods can be assessed to give an idea of how such methods would impact on a simulation improved by such methods. A comparison of the above work with experimental methods is a desired

next step and will be covered in more detail in Chapter 8.

Chapter 8

Conclusions & Further Work

The previous chapters have presented a number of computational methods and their implementations.

Chapter 4 considered immersed boundary methods and presented a novel implementation of the method within a SIMPLE pressure-correction based method. These methods were then tested against the circular cylinder and three main features were observed.

Firstly, an immersed boundary method will make the simulation less grid dependent so allowing results of reasonable accuracy to be maintained even for quite coarse grids. In reality this meant that even if their were only 10 nodes across a typical object, reasonable estimates were still found for the pressure drag and separation region. These results were comparable with the results found by solid block approximation but with the order of 20 nodes across the object. Secondly, the smoothing effect on the surface as a result of the immersed boundary method had the beneficial effect of making separation more realistic and less likely to be induced by steps on the surface as a result of

using solid blocks. Finally, the novel implementation used was found to be as stable as the base simulation in almost all cases unlike other immersed boundary methods which were found to be unstable in certain situations.

Turbulence modelling with wall functions was covered in Chapter 5 and focussed on the modification of one turbulence model in particular, that of Spalart and Allmaras (1994). When using the basic model without wall functions, a number of features were observed. Firstly, if a flow has been pre-developed or there is already a level of turbulence within the flow at the inlet, then an adequate boundary condition for the eddy viscosity needs to be provided there. Another issue was that the position of the first off-wall node needed to be chosen such that it was well within the viscous sub-layer of any boundary layer (i.e. within $y^+ = 1$) in order for the shear stress at the wall to be propagated correctly. This leads to very restrictive grid requirements and so prompted the development of the wall function method. This method was also presented in Chapter 5 and tested against a typical turbulent boundary layer flow. It was found that the first off-wall node could be as far away from the wall as $y^+ = 72$ without reducing the accuracy of the velocity profile appreciably.

Chapter 6 considered the investigation of detached eddy simulation and considered the use of such a formulation in qualitative terms. A study of using DES for a backward facing step flow was examined and it was found that whilst simple RANS methods were prone to make unsteady flows more steady, DES would allow flow unsteadiness to remain to a greater extent. This would be of benefit in a flow control situation where any structures produced by a flow control device would be able to remain without being damped out.

Finally, Chapter 7 provided a feasibility study of bringing all three methods together and examining any trends produced. The methods were applied to the case of the

Lille bump in both the uncontrolled and steady jet controlled case as given in Bernard *et al.* (2003) and Godard and Stanislas (2006b) respectively. Consistent with Chapters 4 and 5, the immersed boundary method and wall functions were seen to reduce flow separation as they smoothed out the surface and allowed the wall shear stress to be propagated into the flow at the correct level. On the other hand, the DES formulation covered in Chapter 6 increased the size of the recirculation region as a result of reduced levels of turbulent viscosity within the flow.

Combining all three methods together, the pressure drag was found to be reduced in the uncontrolled case as compared to the simulation without methods. For the steady jet controlled case, the drag was always seen to be reduced compared to the uncontrolled case although the drag reduction for the simulations without any methods was much larger than for the simulations with methods. However, this is most likely that the drag for the uncontrolled case without any methods (RS01-01) was over estimated as is consistent with Chapter 4.

In conclusion, each of the three methods was found to work well on its own to reduce the grid requirement needed and aid the modelling of unsteady turbulent flow structures. Combining the three methods met with success but the next key step would be to compare the combined methods with actual experimental results or high resolution computations. It is also the author's wish to start using the above methods to simulate flow control using synthetic jets as this is an area of active research.

Bibliography

Alving, A. and Fernholz, H. (1996). Turbulent measurements around a mild separation bubble and downstream of reattachment, *Journal of Fluid Mechanics* **322**: 297–328.

Amitay, M. and Glezer, A. (2002). Controlled transients of flow reattachment over stalled airfoils, *International Journal of Heat and Fluid Flow* **23**: 690–699.

Amitay, M. and Glezer, A. (2006). Flow transients induced on a 2d airfoil by pulse-modulated actuation, *Experiments in Fluids* **40**: 329–331.

Amitay, M., Smith, D., Kibens, V., Parekh, D. and Glezer, A. (2001). Aerodynamic flow control over an unconventional airfoil using synthetic jet actuators, *AIAA Journal* **39**: 361–370.

Amitay, M., Washburn, A., Anders, S. and Parekh, D. (2004). Active flow control on a stingray uninhabited air vehicle: transient behaviour, *AIAA Journal* **42**(11): 2205–2215.

Armaly, B., Durst, F., Pereira, J. and Schonung, B. (1983). Experimental and theoretical investigation of backward-facing step flow, *Journal of Fluid Mechanics* **127**: 473–496.

Bernard, A., Foucaut, J., Dupont, P. and Stanislas, M. (2003). Decelerating boundary layer: A new scaling and mixing length model, *AIAA Journal* **41**(2): 248–255.

Boussinesq, J. (1877). Essai sur la theories des eaux courantes., *Memoires presentes par divers savants a lAcademic des Sciences de lInstitut National de France* **23**(1).

Chung, Y., Tucker, P. and Roychowdhury, D. (2003). Unsteady laminar flow and convective heat transfer in a sharp 180 bend, *International Journal of Heat and Fluid Flow* **24**(1): 67–76.

Coles, D. (1956). The law of the wake in the turbulent boundary layer, *Journal of Fluid Mechanics* **1**: 191–226.

Compton, D. and Johnston, J. (1992). Streamwise vortex production by pitched and skewed jets in a turbulent boundary layer, *AIAA Journal* **30**(3): 640–647.

Dengel, P. and Fernholz, H. (1990). An experimental investigation of an incompressible turbulent boundary layer in the vicinity of separation, *Journal of Fluid Mechanics* **212**: 615–636.

Dias, A. and Majumdar, S. (1999). Numerical computation of flow around a circular cylinder, *Technical Report, PS II Report, BITS Pilani, India* .

Fadlun, E., Verzicco, R., Orlandi, P. and Mohd-Yusof, J. (2000). Combined immersed-boundary finite difference methods for three-dimensional complex flow simulations, *Journal of Computational Physics* **161**: 35–60.

Gatski, T. and Speziale, C. (1993). On explicit algebraic stress models (easm) for complex turbulent flows, *Journal of Fluid Mechanics* **254**: 59–78.

Glezer, A. and Amitay, M. (2002). Synthetic jets, *Annual Reviews of Fluid Mechanics* **34**: 503–529.

Glezer, A., Amitay, M. and Honohan, A. (2005). Aspects of low- and high-frequency actuation for aerodynamic flow control, *AIAA Journal* **43**(7): 1501–1511.

Godard, G. and Stanislas, M. (2006a). Control of a decelerating boundary layer. Part 1: Optimization of passive vortex generators, *Aerospace Science and Technology* **10**(3): 181–191.

Godard, G. and Stanislas, M. (2006b). Control of a decelerating boundary layer. Part 3: Optimization of round jets vortex generators, *Aerospace Science and Technology* **10**(6): 455–464.

Harlow, F. and Welch, J. (1965). Numerical calculation of time-dependent viscous incompressible flow of fluid with free surface, *Physics of Fluids* **8**: 2182–2189.

Hassan, A. and JanakiRam, R. (1998). Effects of zero-mass 'synthetic jets' on the aerodynamics of the naca-0012 airfoil, *Journal of the American Helicopter Society* pp. 303–311.

Hayase, T., Humphrey, J. and Greif, R. (1992). A consistently formulated quick scheme for fast and stable convergence using finite-volume iterative calculation procedure, *Journal of Computational Physics* **98**: 108–118.

Houghton, E. and Carpenter, P. (2003). *Aerodynamics for Engineering Students*, Elsevier Butterworth Heinemann.

Huang, W. and Sung, H. (2005). Improvement of mass source/sink for an immersed boundary method. To be published.

Johnston, J. (1999). Pitched and skewed vortex generator jets for control of turbulent boundary layer separation: a review, *Proceedings of 3rd ASME/JSME Joint Fluids Engineering Conference July 18-23, 1999, San Francisco, California* .

Johnston, J., Mosier, B. and Kham, Z. (2002). Vortex generating jets: effects of jet-hole inlet geometry, *International Journal of Heat and Fluid Flow* **23**: 744–749.

Johnston, J. and Nishi, M. (1990). Vortex generator jets- means for flow separation control, *AIAA Journal* **28**(6): 989–994.

Jouvray, A. and Tucker, P. (2005). Computation of the flow in a ventilated room using non-linear RANS, LES and hybrid RANS/LES, *International Journal for Numerical Methods in Fluids* **48**(1): 99–106.

Jovic, S. and Driver, D. (1995). Reynolds number effect on the skin friction in separated flows behind a backward-facing step, *Experiments in Fluids* **18**: 464–467.

Kalitzin, G., Medic, G., Iaccarino, G. and Durbin, P. (2005). Near-wall behaviour of rans turbulence models and implications for wall functions, *Journal of Computational Physics* **204**: 265–291.

Kim, J., Kim, D. and Choi, H. (2001). An immersed boundary finite-volume method for simulations of flow in complex geometries, *Journal of Computational Physics* **171**: 132–50.

Kim, K. and Moin, P. (1985). Application of a fractional-step method to incompressible Navier-Stokes equations, *Journal of Computational Physics* **59**: 308–323.

Kostas, J., Foucaut, J. and Stanislas, M. (2007). The flow structure produced by pulsed-jet vortex generators in a turbulent boundary layer in an adverse pressure gradient, *Flow Turbulence and Combustion* **78**: 331–363.

Lai, M. and Peskin, C. (2000). An immersed boundary method with formal second-order accuracy and reduced numerical viscosity, *Journal of Computational Physics* **160**: 705–719.

Launder, B. and Spalding, D. (1974). The numerical computation of turbulent flows, *Computational Methods applied to mechanical engineering* **3**: 269–289.

Le, H. and Moin, P. (1991). An improvement of fractional step methods for the incompressible Navier-Stokes equations, *Journal of Computational Physics* **92**: 369–379.

Le, H., Moin, P. and Kim, J. (1997). Direct numerical simulation of turbulent flow over a backward-facing step, *Journal of Fluid Mechanics* **330**: 349–374.

Leonard, B. (1979). A stable and accurate convective modelling procedure based on quadratic upstream interpolation, *Computational Methods applied to mechanical engineering* **19**: 59–98.

Liu, C., Zheng, X. and Sung, C. (1998). Preconditioned multigrid methods for unsteady incompressible flows, *Journal of Computational Physics* **139**: 35–57.

Ludwieg, H. and Tillmann, W. (1949). Untersuchungen über die Wandschubspannung in turbulenten Reibungsschichten, *Ing.-Arch* **17**: 288–299.

Melton, L. and Yao, C. (2006). Active control of separation from the flap of a supercritical airfoil, *AIAA Journal* **44**(1): 34–41.

Mohd-Yusof, J. (1997). Combined immersed boundary/b-spline methods for simulation of flow in complex geometries, *Annual Research Briefs, Centre for Turbulence Research, Stanford University, CA* pp. 317–28.

Morgan, P., Rizzetta, D. and Miguel, R. (2006). High-order numerical simulation of turbulent flow over a wall-mounted hump, *AIAA Journal* **44**(2).

Nikitin, N., Nicoud, F., Wasistho, B., Squires, K. and Spalart, P. (2000). An approach to wall modelling in large-eddy simulations, *Physics of Fluids* **12**(7): 1629–1632.

Patankar, S. (1980). *Numerical Heat Transfer and Fluid Flow*, 1st edition edn, HPC.

Patankar, S. and Spalding, D. (1972). A calculation procedure for heat, mass and momentum transfer in three-dimensional parabolic flows, *International Journal of Heat and Mass Transfer* **15**: 1787.

Persson, T., Liefvendahl, M., Bensow, R. and Fureby, C. (2005). Numerical investigation of the flow over an axisymmetric hill using LES, DES and RANS, *Proceedings of DESider Meeting on Detached Eddy Simulation, Stockholm, 14th-15th July 2005* .

Persson, T., Liefvendahl, M., Bensow, R. and Fureby, C. (2006). Numerical investigation of the flow over an axisymmetric hill using LES, DES and RANS, *Journal of Turbulence* **7**(4): 1–17.

Peskin, C. (1972). *Flow patterns around heart valves: a digital computer method for solving the equations of motion*, PhD thesis, Albert Einstein College of Medicine, Yeshiva University, New York.

Prandtl, L. (1904). Über Flüssigkeitsbewegung bei sehr kleiner Reibung, *Proc. 3rd Inter. Math. Congr. Heidelberg; Reprinted in: View Abhandlungen zur Hydrodynamik und Aerodynamik, Göttingen, 1927; see also Coll. Works II, 575-584; English translation: NACA Technical Memorandum (TM) 452 (1928)* pp. 484–491.

Preece, A., Tucker, P. and Liu, Y. (2004). Modelling synthetic jets using cubic $k-\epsilon$ and EASM, *Proceedings of the NASACFDVAL04 Validaton Conference, Williamsburg, Virginia, USA* **1**: 1.6.1–1.6.3.

Ruderich, R. and Fernholz, H. (1986). An experimental investigation of a turbulent shear flow with separation, reverse flow, and reattachment, *Journal of Fluid Mechanics* **163**: 283–322.

Rumsey, C., Gatski, T., Sellers III, W., Vatsa, V. and Viken, S. (2006). Summary of the 2004 computational fluid dynamics validation workshop on synthetic jets, *AIAA Journal* **44**(2): 194–207.

Samuel, A. and Joubert, P. (1974). A boundary layer developing in an increasingly adverse pressure gradient, *Journal of Fluid Mechanics* **66**(3): 481–505.

Schlichting, H. (1979). *Boundary Layer Theory*, McGraw-Hill.

Seifert, A., Bachar, T., Koss, D., Shepshelovich, M. and Wygnanski, I. (1993). Oscillatory blowing: A tool to delay boundary layer separation, *AIAA Journal* **31**(11): 2052–2060.

Seifert, A. and Pack, L. (2002). Active flow separation control on wall-mounted hump at high Reynolds numbers, *AIAA Journal* **40**(7).

Simpson, R., Chew, Y. and Shivaprasad, B. (1981). The structure of a separating turbulent boundary layer: Part 1. mean flow and Reynolds stresses, *Journal of Fluid Mechanics* **113**: 23–51.

Song, S., DeGraff, D. and Eaton, J. (2006). Experimental study of a separating, reattaching, and redeveloping flow over a smoothly contoured ramp, *International Journal of Head and Fluid Flow* **21**: 512–519.

Spalart, P. (2000). Strategies for turbulence modelling and simulations, *International Journal of Heat and Fluid Flow* **21**: 252–263.

Spalart, P. (2005). The use of DES: natural, extended, and improper, *Symposium on Hybrid RANS-LES Methods* .

Spalart, P. and Allmaras, S. (1994). A one-equation turbulence model for aerodynamic flows, *La Recherche Aerospatiale* **1**: 5–21.

Spalart, P., Jou, W., Strelets, M. and Allmaras, S. (1997). Comments on the feasibility of LES for wings & on a hybrid RANS/LES approach, *First AFOSR International conference on DNS/LES* .

Spalart, P. and Watmuff, J. (1993). Experimental and numerical study of a turbulent boundary layer with pressure gradients, *Journal of Fluid Mechanics* **249**: 337–371.

Suzuki, T. (2006). Effects of a synthetic jet acting on a separated flow over a hump, *Journal of Fluid Mechanics* **547**: 331–359.

Taneda, S. (1956). Experimental investigation of the wakes behind cylinders and plates at low Reynolds numbers, *Journal of the Physical Society of Japan* **11**(3): 302–307.

Tritton, D. (1977). *Physical Fluid Dynamics*, Van Nostrand Reinhold.

Tseng, Y. and Ferziger, J. (2003). A ghost-cell immersed boundary method for flow in complex geometry, *Journal of Computational Physics* **192**: 593–623.

Tucker, P. (2001). *Computation of Unsteady Internal Flows*, Kluwer Academic Publishers.

Tucker, P. (2003). Differential equation-based wall distance computation for des and rans, *Journal of Computational Physics* **190**: 229–248.

Tucker, P. and Davidson, L. (2004). Zonal $k-l$ based large eddy simulations, *Computers and Fluids* **33**: 267–287.

Tucker, P., Liu, Y., Chung, Y. and Jouvray, A. (2003). Computation of an unsteady complex geometry flow using novel non-linear turbulence models, *International Journal for Numerical Methods in Fluids* **43**(9): 979–1001.

Versteeg, H. and Malalasekera, W. (1995). *An Introduction to Computational Fluid Dynamics*, Prentice-Hall.

Warsop, C. (2005). Advanced aerodynamic flow control using mems: Aeromems ii project summary, *Technical Report G4RD-CT-2002-00748*, EU.

Williamson, C. and Brown, G. (1998). A series in $1/\sqrt{Re}$ to represent the Strouhal-Reynolds number relationship of the cylinder wake, *Journal of Fluids and Structures* **12**: 1073–1085.

Ye, T., Mittal, R., Udaykumar, H. and Shyy, W. (1999). An accurate cartesian grid method for viscous incompressible flows with complex immersed boundaries, *Journal of Computational Physics* **156**: 209–240.